Angélica Díaz

# CRYSTALLIZATION, PROCESSING AND APPLICATIONS OF NEW POLYESTERS

Doctoral Thesis Supervised by:
Prof. Dr. Jordi Puiggalí
Dr. María Teresa Casas

Barcelona, 2015


Departament d'Enginyeria Química
Escola Tècnica Superior d'Enginyeria Industrial de Barcelona (ETSEIB)
Universitat Politècnica de Catalunya (UPC)

*“Acepta la responsabilidad de hacer*

*de tus sueños una realidad”.*

*Les Brown.*

# ABSTRACT

Poly(alkylene dicarboxylate)s constitute a family of biodegradable polymers with increasing interest for both commodity and speciality applications. The most of these polymers can be prepared from biobased diols and dicarboxylic acids. In the present thesis two different groups of poly(alkylene dicarboxylate)s were synthesized by thermal policondensation.

The first group concerns to polymers derived from 1,9-nonanediol and different ratios of pimelic and azelaic acids. Different techniques such as OM, DSC, SAXS and FTIR were used in order to characterize the copolymers. The crystalline structure of these polyesters has been investigated by means of electron and X-ray diffraction. Single crystal of homopolymers and the copolymer with the intermediate composition were easily degraded by enzymes.

The second group is constituted by poly(alkylene dicarboxylate)s derived from 1,4-butanediol and succinic and azelaic acids. Physicochemical techniques were combined to understand the thermal properties and the different factors that influenced the crystallization process. Morphological changes occurring during crystallization were evaluated by time resolved SAXS/WAXD experiments using synchrotron radiation. Lauritzen and Hoffman analysis was performed from spherulite growth rates and also considering overall crystallization rates determined from DSC experiments. Enzymatic degradability was clearly dependent on the composition and logically on the crystallinity. Interestingly constituent spherulites of copolymer samples were highlighted during degradation.

Ultrasounds technology has been proved as an useful method to mould biodegradable polylactide and poly(nonamethylene azelate). Minimum material loss and degradation was found when materials were processed under appropriate operating conditions (i.e. time, amplitude and force). The technology was also appropriate to prepare nanocomposites, being assayed the use of clay and silica nanoparticles. In the first case, the achievement of exfoliated structures was clearly demonstrated by X-ray diffraction and TEM observations and using N757, C20A, C25A, and N848 clays. Crystallization behavior of exfoliated PLA nanocomposites was evaluated, being

found a highly peculiar behavior since clay particles had an antinucleating effect. The contrary effect was observed for nanocomposites derived from the poly(alkylene dicarboxylate) sample.

The possibility of using ultrasound micro-molding to get materials with a homogeneous dispersion of particles has also been explored considering both, micro and nano-sized silica particles using poly(nonamethylene azelate) as a matrix. No degradation was detected for the different assayed percentages of silica nanoparticles. These had a significant influence on the crystallization process even at the low content of 3 wt-%.

The wide versatility of polyesters and their derivatives provides advantageous technological applications as those for example reported in the biomedical field. Three different applications for polyesters have been specifically evaluated in this work.

The first was the study of polyester derivatives that incorporate urea groups. These poly(ester urea)s showed good properties and were highly soluble in most organic solvents, an interesting feature that facilitated the electrospinning process and the effective incorporation of drugs with bactericide activity, enzymes and bacteriophages. Electrospun scaffolds of new polymers could be applied in tissue engineering since they were biocompatible as demonstrated by adhesion and proliferation assays.



In the second application, polyethylene glycol grafted poly(lactide-*r*-trimethylene carbonate) copolymers were employed to prepare homogenous drug loaded microspheres. New polymers were degradable and biocompatible. Furthermore, the hydrophilicity given by the PEG segments increased the enzymatic degradability in lipase medium and the proliferation of both epithelial-like and fibroblast-like cells.

Finally, crystallization of multiarm star polymers was studied due to their wide applications (for example the development of epoxy coatings). Specifically, the study was focused on multiarm star systems constituted by a commercial core of poly(ethyleneimine) and arms of poly(ε-caprolactone) with degrees of polymerization of 50, 30 and 10. The study of the influence of the arm length on factors that determine the crystallization process like morphology, primary nucleation density, crystal growth and secondary nucleation constant was performed. Crystallization process of star mixtures having different PCL lengths was also determined.

# ACKNOWLEDGEMENTS

Antes de agradecer a las personas que de alguna manera han contribuido durante el desarrollo y culminación de este trabajo me gustaría dar gracias a Dios y a La Virgen, quienes me han guiado durante toda mi vida, poniendo las personas indicadas en mí camino.

En primer lugar quiero agradecer al Profesor Jordi Puiggalí su labor en la dirección de la presente tesis, así como su tiempo de dedicación, confianza, paciencia y apoyo durante todos estos años. Sus valiosos consejos y sugerencias.

Deseo agradecer a mi codirectora María Teresa Casas que desde el primer momento me ofreció su amistad. Por ayudarme en todo lo que fuera posible, tanto para los análisis de microscopia como con cualquier otro tema.

A todos los miembros del grupo, en especial a Lourdes y Lucho por siempre tener tan buena disposición para ayudarme con cualquier problema o duda, también por los ratos amenos y por siempre estar dispuestos a escuchar.

A todos mis compañeros que han formado parte de esta etapa, tanto a los del grupo de PSEP como los de la planta uno, Ana, Elena, Laura, Cristina Lavilla, Ainhoa, Javier, Alberto, Elena Llorens, Sara, Yani, Neudys, Yolanda, Giuseppe, Sejin, Ilaria, Vanessa, con los que he compartido muy buenos momentos y a muchos de ellos los considero grandes amigos.

A mis amigas Cristiana y Mayka no puede encontrar mejores personas con quien compartir esta etapa, tanto en la vida personal como profesional. Han sido años llenos de alegrías, risas y otros momentos no tan gratos pero juntas los hemos superado.

También quiero agradecerles al Dr. Abdelilah Alla y al Dr. Antxon Martinez de Llarduya por su gran amabilidad y por ayudarme siempre que lo necesite.

A Irene y Francina, muchas gracias por hacer todos los trámites administrativos más sencillos, por siempre ayudarme en todo lo que estaba en sus manos.

Al profesor Francisco López Carrasquero (pancho), por haberme iniciado en el mundo de los polímeros.

A mis amigos de siempre Luz Mary, Johanna, Patty, David, Maggy, Enrique, Johan, Luis, que al estar lejos de casa, somos una gran familia.

A mi familia, porque todo lo que soy se lo debo a ellos, son el mejor ejemplo de amor, constancia y dedicación. A pesar de la distancia me han apoyado en todo momento y han creído en mí.

A mi nueva familia, Mayte, Cristian, Leidy y la Nona, por sus ánimos y mostrar interés en el desarrollo y culminación de este trabajo.

A mi esposo Josep Camps, por todo el apoyo que me da cada día. Por ayudarme en todo lo que ha podido. Por entender todas las horas extras de trabajo sin protestar. Por lo que cada día resulta mucho más fácil. Gracias por compartir tu vida conmigo.

A la Agencia de gestión de ayudas universitarias y de investigación, Generalitat de Catalunya, FI-AGAUR que ha financiado el trabajo presentado en esta tesis.

# PUBLICATIONS

**Work from this thesis has been published by the autor:**

**A. Díaz,** L. Franco, A. Rodríguez-Galán, J. Puiggalí. Study on the crystallization of poly(alkylene dicarboxylate)s derived from 1,9-nonanediol and mixtures with different ratios of azelaic acid and pimelic acid units. Submitted

**A. Díaz,** M. T. Casas, J. Puiggalí. Preferential incorporation of pimelic acid units into the crystalline phase of copoly(alkylene dicarboxylate) derived from 1,9-nonanediol and an equimolar mixture of pimelic and azelaic acids. Submitted

**A. Díaz,** L. Franco, J. Puiggalí. Study on the crystallization of poly(butylene azelate-co-butylene succinate) copolymers. Thermochimica Acta 575 (2014) 45–54.

**A. Díaz,** L. Franco, F. Estrany, L. J. del Valle, J. Puiggalí. Poly(butylene succinate-co-azelate) copolymers: crystalline morphologies and degradation. Polymer Degradation and Stability 99 (2014) 80-91.



**A. Díaz,** L. Franco, MT. Casas, L. J. del Valle, J. Aymamí, C. Olmo, J. Puiggalí. Preparation of micro-molded exfoliated clay nanocomposites by means of ultrasonic technology. Journal Polymer Research 21 (2014) 584-596.

**A. Díaz,** MT. Casas, J. Puiggalí. Dispersion of functionalized silica micro and nanoparticles into poly(nonamethylene azelate) by ultrasonic micro molding. Submitted

**A. Díaz,** LJ. del Valle, D. Tugushi, R. Katsarava, J. Puiggalí. New poly(ester urea) derived from L-leucine: Electrospun scaffolds loaded with antibacterial drugs and enzymes. Materials Science and Engineering C 46 (2015) 450-462.

**A. Díaz,** LJ. del Valle, D. Tugushi, R. Katsarava, J. Puiggalí. Incorporation of bacteriophages in electrospun fibres of a poly(ester urea) derived from L-leucine. Preparation.

**A. Díaz,** LJ. del Valle, L. Franco, JR. Sarasua, F. Estrany, J. Puiggalí. Anhydric maleic functionalization and polyethylene glycol grafting of lactide-co-trimethylene carbonate copolymers. Materials Science and Engineering C 42 (2014) 517-528.

**A. Díaz,** A. Bacaicoa, A. Serra, L. Franco, J. Puiggalí. Study on the crystallization of multiarm stars with a poly(ethyleneimine) core and poly(ε-caprolactone) arms of different length. Thermochimica Acta. Accepted

**A. Díaz,** R. Katsarava, J. Puiggalí. Synthesis, properties and applications of biodegradable polymers derived from diols and dicarboxylic acids: from polyesters to poly(ester amide)s. International Journal of Molecular Sciences 15 (2014) 7064-7123.

**Collaborations in other publications**



L. del Valle, R. Camps, **A. Díaz,** L. Franco, A. Rodríguez-Galán, J. Puiggalí. Electrospinning of polylactide and polycaprolactone mixtures for preparation of materials with tunable drug release properties. Journal of Polymer Reserch 11 (2011) 1903-1917

L. del Valle, **A. Díaz,** M. Royo, A. Rodriguez-Galán, J. Puggalí. Release behavior of biodegradable polyesters reinforced with triclosan loaded polylactide micro/nanofibers. Express Polymer Letters 6(2012) 266-282.

L J. Del Valle, M Roa, **A Díaz,** MT. Casas, J Puiggalí, A. Rodriguez. Electrospun nanofibers of a biodegradable poly(ester amide). Scaffolds loaded with antimicrobial agents. Journal Polymer Resarch 19 (2012) 9792-9805.

H-H. Su, H-L. Chen, **A. Díaz,** M T. Casas, J. Puiggalí, JN. Hoskins, SM. Grayson, RA. Pérez, AJ. Müller. New insights on the crystallization and melting of cyclic PCL chains on the basis of a modified ThomsoneGibbs equation. Polymer 54 (2013) 846-859.

# GLOSSARY

| | |
|---|---|
| **AFM** | Atomic Force Microscopies |
| **AMPS** | (3-aminopropyl) triethoxysilane |
| **BPO** | benzoyl peroxide |
| **CA** | Contact Angle |
| **Cloisite 20A** | Dimethyl dihydrogenated-tallow ammonium montmorillonite |
| **Cloisite 25A** | Dimethyl hydrogenated-tallow 2-ethylhexyl ammonium montmorillonite |
| **DIC** | Diisopropylcarbodiimide |
| **DMAP** | 4-Dimethylaminopyridine |
| **DSC** | Differential Scanning Calorimetry |
| **DTGA** | Derivative Thermogravimetric Analysis |
| **FTIR** | Fourier transform infrared spectroscopy |
| **GPC** | Gel Permeation Chromatography |
| **HFIP** | 1,1,1,3,3,3-Hexafluoroisopropanol |
| **LA** | L-lactide |
| **$M_n$** | Number-average molecular weight |
| **MTT** | 3-(4,5-Dimethylthiazol-2-yl)-2,5-diphenyl-2H-tetrazolium bromide |
| **$M_w$** | Weight-average molecular weight |
| **Nanofil 757** | Sodium montmorillonite |
| **Nanofil 848** | Organoclay octadecyl ammonium montmorillonite |

| | |
|---|---|
| **NMR** | Nuclear Magnetic Resonance |
| **PBS** | Polybutylene succinate. |
| **PBS** | Sodium phosphate buffer |
| **PCL** | Poly(ε-caprolactone) |
| **PDI** | Polydispersity index |
| **PE4,9/4 *x*** | Polyester (PE) derived from 1,4-butanediol (4) and having azelate (9) and succinate (4) units. (*x*) the molar ratio of azelate units |
| **PE49** | Polyester (PE) derived from 1,4-butanediol (4) and azelate (9) units. |
| **PE99** | Poly(nona-methylene azelate) |
| **PEG** | Poly(ethylene glycol) |
| **PEG-*g*-PLA** | Polyethylene glycol grafted polylactides |
| **PEI** | Poly(ethyleneimine) |
| **PEI-PCL *x*** | Multiarm star, *x* accounts for the degree of polymerization |
| **PEI-PCL *x/y*** | Multiarm star mixtures |
| **PLA** | Polylactide |
| **PLA-*r*-PTMC** | Poly(lactide-*r*-trimethylene carbonate |
| **PTMC** | Polytrimethylene carbonate |
| **PVA** | Polyvinyl alcohol |
| **RCS** | Refrigerated Cooling System |
| **SAXS** | Small Angle X-ray Scattering |
| **SEM** | Scanning Electron Microscope |

| | |
|---|---|
| **$Sn(Oct)_2$** | Tin (II) bis-(2-ethylhexanoate) |
| **TEM** | Transmission Electron Microscopy |
| **TEOS** | Tetraethoxysilane |
| **TGA** | Thermogravimetry |
| **THF** | Tetrahydrofurane |
| **TMC** | Trimethylene carbonate |
| **WAXD** | Wide Angle X-ray Diffraction |
| **XPS** | X-ray Photoelectron Spectroscopy |

# TABLE OF CONTENTS

# *Chapter 1.*

# *Introduction*

## I. Biodegradable Polymers

In the last 25 years the interest in the study of the biodegradable polymers has been increased primarily due to their potential use in the medical field, especially in the drug delivery area, sutures, artificial tissues and several medical devices.[1-4] Also they are very important as safe materials for the environment, reducing “the white pollution” caused by polymers coming from fossil resources. Synthetic polymers are recognized as major solid waste environmental pollutants. In 2009, around 230 million tonnes of plastic were produced and around 25 per cent of these plastics were used in the EU.[5] This global figure has been increasing by an average rate of 9 per cent since 1950 to a peak of 245 million tonnes in 2008, after which there was a slight drop in production. The financial recession may be responsible for this slight decline in plastic production, (see Figure 1). The presence of these substances in the environment brings about important problems, including a challenge to wastewater treatment plants and pollution of groundwater and surface water. There is a world-wide research effort to develop biodegradable polymers as a waste management option for polymers in the environment.[6]



**Figure 1.** World plastics production 1950-2008 and victims of pollution of plastics. Photos: Unknown.

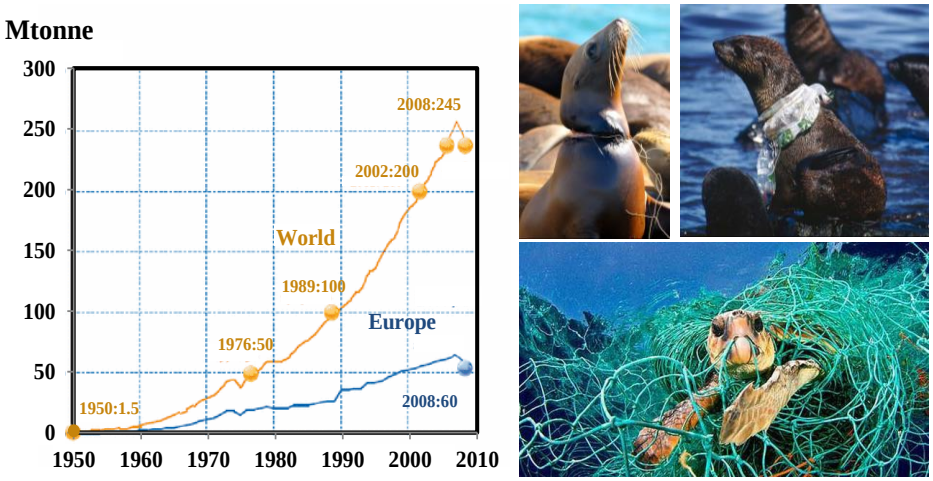

The growing interest in the study of the biodegradable polymers is easily appreciated for example, in the high number of publications on biodegradable polymers and in the great number of citations in the recent years, as it is shown in the Figure 2 obtained from the ISI web of Sciences.

**Figure 2.** (a) Evolution of the number of publications, and (b) citations on biodegradable polymers in the last four years.

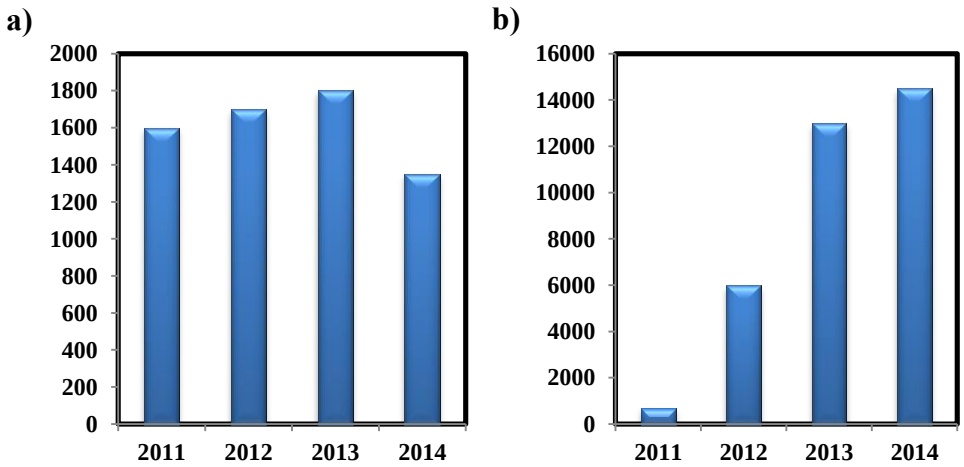




## 1. Biodegradation of polymers

The biodegradation of polymers is a process carried out in two steps. In the first one, the long repetitive chains of the polymer are shortened by hydrolysis, oxidation or temperature effect, which produces loss of chemical and physical properties mainly as a consequence of the molecular weight decrease. This part is a preliminary degradation process which is followed by a second step when the true biodegradation is produced by the enzymatic action of microorganisms such as bacteria, fungi, and algae in appropriate environments, and ending with the production of carbon dioxide, water, methane (under anaerobic conditions), biomass, etc. (Figure 3).[7]

**Figure 3.** Scheme of polymer degradation under aerobic and anaerobic conditions.[7]

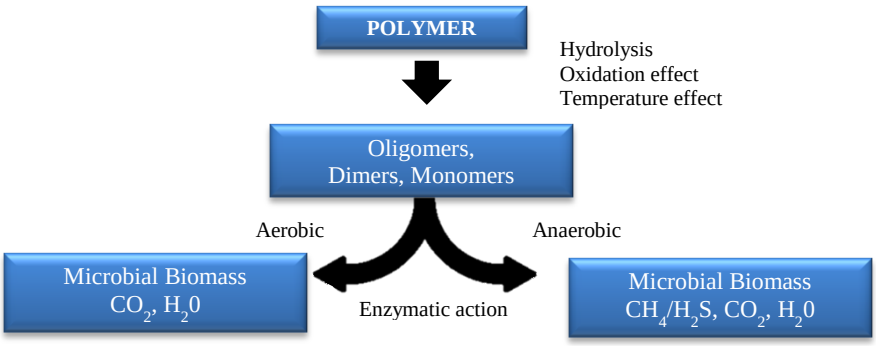


## 2. Factors affecting biodegradability

Biodegradability of polymers has been extensively studied and consequently different factors can be pointed out:

(1) Water solubility of polymers, as biodegradation requires water permeability across a microbial cell membrane; (2) Structural complexity, as more complex polymers require more effort from microorganisms to degrade them. This point includes also the molecular structure since biodegradability depends on chain-branching and cross-linking, and (3) Availability of reactional chemical sites in the structure. These should also be responsible for stability, hydrophilicity and swelling behaviour.



Other factors are also being highly significant: physical properties, molecular weight, porosity, elasticity, crystalline/amorphous morphology, additives, methods of synthesis and environmental conditions.

## 3. Classification of biodegradable polymers

Biodegradable polymers are generally divided into two groups, natural and synthetic based on their origin. In this work we focus on synthetic polymers.

### 3.1. Synthetic Polymers

Synthetic polymers offer advantages over natural polymers since they are more versatile and may cover a wide spectrum of applications. In fact, synthetic polymers offer a great capability to tailor mechanical properties and altering the rate of degradation according to the need. On the other hand, natural polymers seem to be attractive due to their excellent biocompatibility.

There are many polymers available for different applications (Figure 4) where the choice of the polymer is dependent on the requirements that a particular biomaterial demands. For example, with respect to drug delivery, it is the time of release that governs the type of polymer, size and shape of the device.[8] Clinically approved polymers such as lactide, glycolide and their copolymers are currently the samples most employed for the different applications.

#### 3.1.1. Polyesters



Polyesters are most extensively investigated for biomedical applications due to their excellent biocompatibility and tunable degradation properties. In fact, polyesters are considered the most competitive biodegradable polymers commercialized up to now. Poly(alkylene dicarboxylate)s constitute a specific family of polyesters that offer great possibilities especially considering that most of them can be obtained from renewable resources. The extensive application of such polymers could not only mitigate the negative effect of non-degradable plastics on the environment but also reduce the dependence on fossil resources.[9-11] Poly(butylene succinate) (PBS) is probably nowadays the most significant poly(alkylene dicarboxylate) due to the unusual combination of good properties and the successful efforts carried out to solve typical problems of this family such as the limited molecular weight attained by polycondesation reactions. Biodegradability of poly(alkylene dicarboxylate)s can be clearly improved by preparing random copolymers with low crystallinity and melting point, whereas incorporation of rigid units like biobased carbohydrates and even aromatic dicarboxylates may lead to better mechanical properties.

**Figure 4.** Classification of biodegradable polymers.[18]

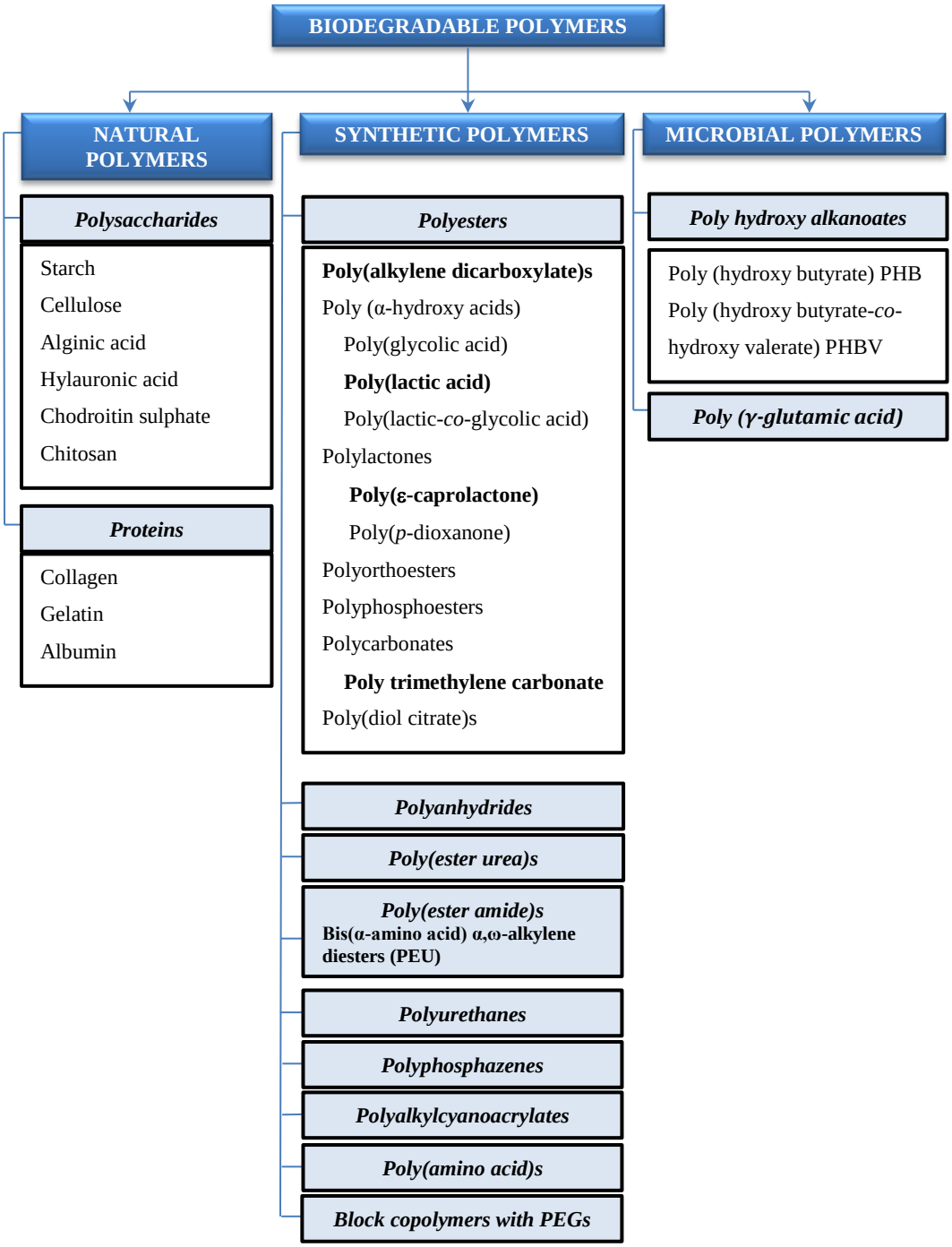

#### 3.1.1.1. Poly(alkylene dicarboxylate)s

Aliphatic polyesters derived from diols and dicarboxylic acids are crystalline and biodegradable materials that can be used as an alternative of more conventional biodegradable polyesters prepared by ring opening polymerization of lactones (*e.g.*, polyglycolide, poly(lactic acid) and poly(ε-caprolactone)). Poly(alkylene dicarboxylate)s can be easily prepared by thermal polycondensation of diols and dicarboxylic acids or either their diesters or dichlorides. Nevertheless, these syntheses have problems associated to the use of solvents, high vacuum and temperature conditions required to favour condensation reactions and the removal of water or alcohol by-products. In general, the average molecular weight of poly(alkylene dicarboxylate)s is limited ($M_n$ lower than 30,000 g/mol) if conventional polycondensation chemistry is used and toxic catalysts are avoided.[12-14]

The synthesis of these polymers also can be made by polycondensation catalysts and ring opening polymerization.



Polycondensation of diols with dicarboxylic acids can also be performed by employing nonspecific lipases,[15,16] but in this case final cost is also increased due to the expensive enzyme and even for the subsequent separation process that is required to eliminate the enzyme. Nevertheless, some advantages should be indicated since it is an eco-friendly method, that could proceed without any environmental pollution and effectively avoid both phase separation of the reactants and the use of toxic solvents. For example, the synthesis of poly(butylene sebacate) has been reported by a lipase-catalyzed synthesis in absence of organic solvents.[17]

Ring opening polymerization (ROP) has several advantages over polycondensation, but the low availability and high manufacturing costs of cyclic ester oligomers (CEOs) at industrial scale has prevented its general application for the synthesis of poly(alkylene dicarboxylate)s. Nevertheless, several efforts have been focused to develop CEOs by enzymatic synthesis since mild reaction conditions are usually required and high selectivity is obtained.

Furthermore, biodegradable poly(alkylene dicarboxylate)s derived from biobased monomers have an additional interest as above indicated and specifically those obtained from diols like 1,3-propanediol, 1,4-butanediol and 1,10-decanediol, and dicarboxylic acids such as those based on carbohydrates and succinic acid, adipic acid, sebacic acid and fatty acids. Thus, succinic acid and 1,4-butanediol can be fully synthesized using sugar-based feedstock by bacterial fermentation.[19,20] Specifically, succinic acid can be obtained with high yield by *A. succiniciproducens* using glycerol as substrate whereas 1,4-butanediol can be easily prepared by the reduction of succinic acid. The indicated monomers are employed to get a fully bio-based PBS, which is one of the most investigated degradable polyesters because of its relatively high melting point ($T_m$ = 103 °C) and favorable mechanical properties. In fact PBS could be a very interesting substitution for polyolefins in some applications.

### a. Crystalline structure of poly(alkylene dicarboxylate)s



Structural studies on poly(alkylene dicarboxylate)s indicate variability on the molecular conformation. Kink conformations can be found in polymers with a low number of methylene groups, such as polyesters 2 4,[21] 2 6,[22] 2 8,[23] 4 4,[24] 4 6[25] and 6 6[26] (digits indicate the number of carbon atoms in the diol and the dicarboxylic acid units). In fact, quantum mechanical calculations on small diesters[27] showed the tendency of methylene units to adopt gauche conformations when a short aliphatic segment was placed between two carbonyl groups. On the other hand, an extended conformation was postulated for polyesters with long polymethylene sequences.[28] In general, all the above referred polyesters crystallize according to monoclinic or orthorhombic unit cells,[29] the dimensions of the chain axis projected unit cell being similar to that reported for polyethylene when the polyester has an extended conformation. In this case, energy calculations suggested a packing structure where molecular chains had an orientation of methylene segments similar to that of polyethylene (*i.e.,* a setting orientation angle close to ±45º).[30]

Polymorphism has been determined for some polyesters having short polymethylene sequences (*i.e.,* poly(ethylene succinate), poly(butylene succinate) and poly(butylene adipate))[31] since an extended conformation (β-form) was found in addition to the indicated kink conformation (α-form) (Figure 5). In general, the transition from the α-form to the β-form occurred reversibly under the application and release of tension.

**Figure 5.** Crystal structures for the α-form (a) and the β-form (b) of PBS on the *a*-*b* (bottom) and *b*-*c* (top) base planes. All hydrogen atoms are omitted.[32]

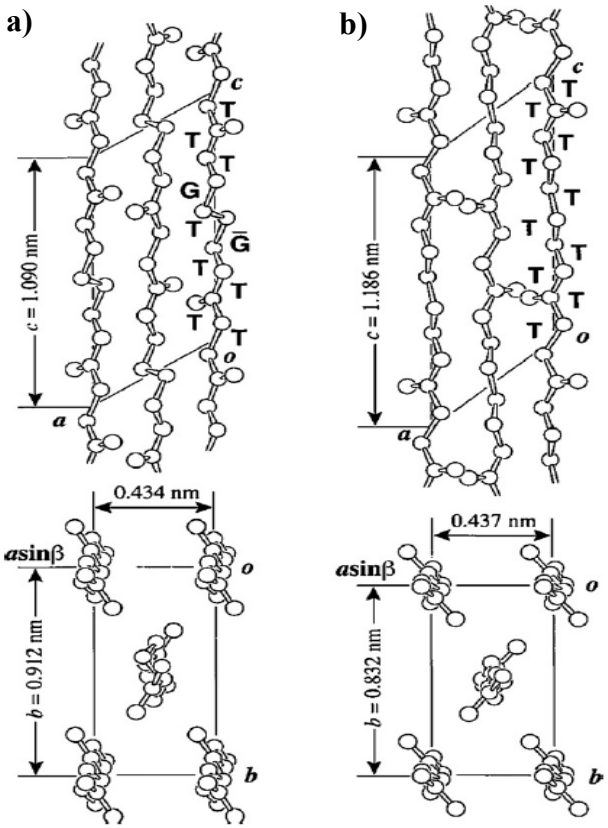


Electron diffraction patterns of polyesters with the extended zig-zag conformation indicated that the unit cells projected along the chain axis were rectangular, the parameters being

close to *a* = 0.500–0.504 nm, and *b* = 0.73–0.75 nm. These cells contained as indicated two molecular segments, but recent works on some 1,4-butanediol (*i.e.*, polyesters 4 8, 4 10 and 4 12)[33] and 1,6-hexanediol (*i.e.*, polyesters 6 8 and 6 12)[34] derivatives have revealed the existence of unit cells where the *b*-axis parameter was doubled. These more complex structures were characterized by the fact that neighboring molecules along the *b*-axis were only equivalent in chain axis projection. Complex structures were also determined for polyesters 6 6[35] and 6 4[36] (Figure 6) since the corresponding unit cells contained eight molecular segments.

**Figure 6.** View parallel to the *c*-axis direction showing the packing of polyester 6 4 assuming a large unit cell with *a* and *b* parameters of 1.612 nm and 1.464 nm, respectively. In projection this packing can be defined by a conventional rectangular cell containing only two chain segments (dotted lines).[36]

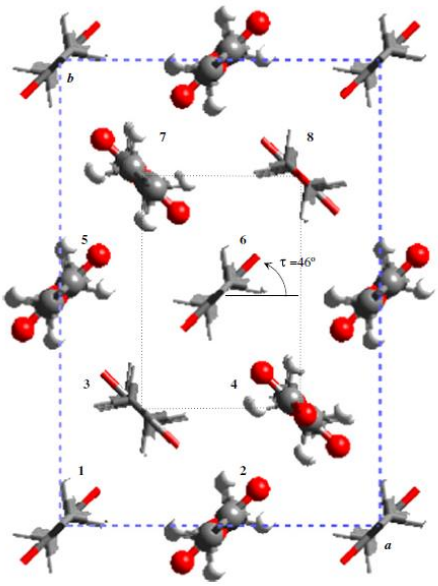

### b. Copolymers constituted by different diol or/and dicarboxylic acid units

Preparation of new copoly(alkylene dicarboxylate)s offers a key opportunity to increase the range of degradable materials and even to generate a set of products with easily tunable properties. Thus, different types of PBS copolymers and blends have recently been developed to increase biodegradability, decrease costs, increase commercial offer and even modify final properties.

Incorporation of comonomers has also a great influence on melting behaviour, sample crystallinity, lamellar surface morphology, and consequently enzymatic degradability.[37,38] Several works have recently been addressed to study the crystallization process of random copoly(alkylene dicarboxylate)s. This kind of studies is significant not only because of the processability and applicability of the materials, but also for its strong correlation with the biodegradation process.[39]



The processability of PBS is not excellent due to its low crystallization temperature and slow crystallization rate. This problem may be solved by using nucleating agents or alternatively by modifying the chemical structure with, for example, branching agents. Incorporation of comonomers has also a great influence on melting behavior, sample crystallinity, lamellar surface morphology, and consequently enzymatic degradability.[36,37] The studied copolymers are mainly constituted by even units, and specifically poly(butylene succinate-*co*-ethylene succinate),[40] poly(hexamethylene succinate-*co*-hexamethylene adipate),[41] poly(hexamethylene sebacate-*co*-hexamethylene adipate),[42,43] poly(hexamethylene sebacate-*co*-hexamethylene suberate)[9] and poly(hexamethylene suberate-*co*-hexamethylene adipate)[44] are representative examples. An understanding of the relationship between structure, morphology and properties is crucial to design these new materials with enhanced physical and chemical properties.

It seems now interesting to get insight into the crystallization behaviour of copolyesters constituted by differentiated units and parity (*e.g.*, Polyester 49). This study is important not only due to its strong correlation with the biodegradation process, but also because the good processability of such materials. On the other hand, the study of the crystallization process and degradability of odd-odd polyesters has not been developed, appearing again interesting to extend the range of available materials. Furthermore, some of this polymers can be derived from natural resources, as for example 1,9-nonanediol, pimelic and azelaic acids, which constitutes an additional advantage. Copolymers derived from similar units (*e.g.*, azelaic and pimelic acid units) may meet requirements of isomorphism,[45] that can allow to control of thermal properties and influence characteristics like biodegradability.

### c. Degradation of poly(alkylene dicarboxylate)s

Besides biodegradability, thermal stability and thermal degradation behaviour of biodegradable polymers are important for their processing, application, and thermal recycling and in general are crucial for the development of safe materials. Therefore, thermal degradation of aliphatic polyesters based on dicarboxylic acids and diols has extensively been studied.[46-51] In general, these polyesters can be well-processed since start to decompose at temperatures significantly higher than their melting point. Decomposition has been described to take place, mainly, through β-hydrogen bond scission and secondarily by α-hydrogen bond scission (Figure 7). Thermal degradation under an oxidative environment may proceed according to a different mechanism and for example α-H abstraction mechanism that led to the formation of a hydroperoxide intermediate was characteristic of PBS thermal oxidation.[47]

**Figure 7.** Schemes showing the β- and α-hydrogen bond scissions for aliphatic polyesters derived in this case from 1,3-propanediol and azelaic acid, based on.[51]

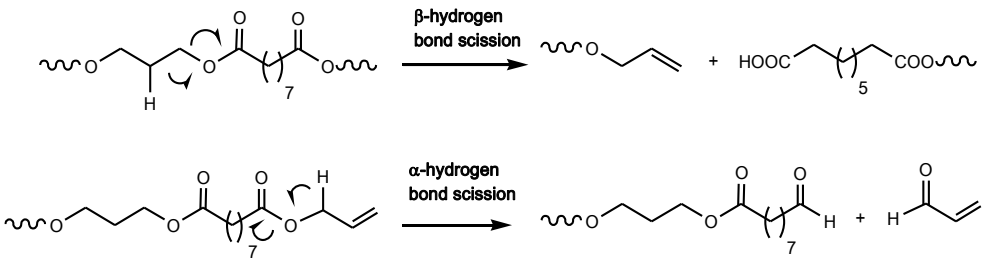


Aliphatic polyesters can be easily enzymatically degraded and constitute nowadays an important group of polymers to solve white pollution. Enzymatic degradation studies suggested that biodegradation rate was faster for polyesters made from moieties containing around six carbon atoms, whereas increasing or decreasing the spacing between ester groups made the polymers less susceptible to enzymatic degradation.[52]



Nevertheless, biodegradation rate is highly influenced by the degree of crystallinity, spherulite size and lamellar structure. Furthermore, melting temperature plays an important role since a polymer having a lower melting temperature is more susceptible to biodegradation due to the higher flexibility of their polymeric chains that allows fitting more easily into the active sites of enzymes.[53]

Enzymatic degradation studies performed with high molecular weight poly(butylene succinate-*co*-ethylene succinate)s indicated that the degree of crystallinity was the dominant factor upon the degradation rate, whereas the sequence distribution of butylene and ethylene succinate subunits had little effect upon lipase activity.[40]

Degradation of semicrystalline polymers must also occur in the crystalline phases mainly, during the later stages of decomposition despite the closely-packed crystalline regions hinder the enzymatic attack. Single lamellar crystals obtained by crystallization from dilute solutions are ideal systems to detect how enzymatic degradation proceeds. Extensive studies

have been performed with single crystals of polyesters such as poly([R]-3-hydroxybutyrate)[54,55] poly(ε-caprolactone)[56] (PCL), poly(L-lactide),[57] poly(ethylene succinate)[58] and poly(tetramethylene adipate).[59] Recognition of the position of ester bonds in the molecular chain is required by the active site of the enzyme for cleavage of the molecular chain and consequently it seems very important that these groups were accessible either on the folding surface or on the lateral faces of lamellar crystals.

Usually, enzymatic degradation progressed mainly from the edges of lamellar crystals without a decrease in molecular weight and lamellar thickness. However, the central portion of poly(butylene adipate) crystals was also degraded by enzymatic attacks, suggesting the existence of loosely-packed chain regions inside lamellae.[59] Enzymatic degradation studies performed with poly(octametylene suberate) showed that in this case the main attack was on the lamellar surfaces.[63] Interestingly, crystal sectors had different susceptibility to enzymatic attack and furthermore degradation was observed to progress preferentially along a crystalline direction (Figure 8). It was concluded that both molecular packing and the nature of molecular folds play a crucial role in the enzymatic degradation process.



**Figure 8.** Lamellar crystals of poly(octamethylene suberate) after exposure to the enzymatic medium containing lipase for 2 (a), 2.5 (b), 3 (c) and 3.5 h (d).[63]

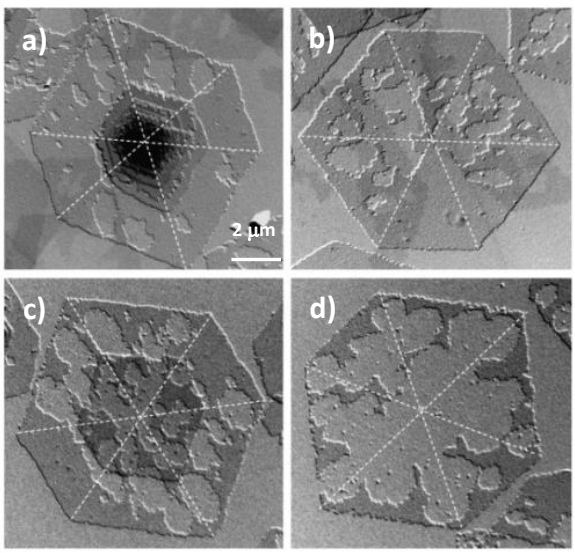

### d. Applications of poly(alkylene dicarboxylate)s

- **Biomedical applications**

Development of antimicrobial packaging films has logically interest in hospital environments where sterile conditions are required for the medical equipment, but also in the food industry in order to increase the safety of food products. Antimicrobial agents can be added to films and also chemically bounded to its surface. In the first case, activity is linked to the migration of the agent which can alter properties of the food product (*e.g.*, taste and quality). This problem does not exist in the second case, but the lack of functional groups in the polymer chains and also the demanding reaction conditions become restrictive points that may limit its application. Functionalization of polyesters can be easily performed by copper catalyzed azide-alkyne 'click' chemistry,[60,61] a reaction that can be carried out under mild conditions that do not alter the chain length of the polyester backbone. In this way, alkyne-containing poly(butylene adipate) was effectively functionalized with a quaternary phosphonium group, known for their antimicrobial properties (Figure 9).[62] The resulting polyester showed great antimicrobial activity through direct contact without freely available active groups and consequently with potential application for food or medical purposes.



**Figure 9.** Synthetic of poly(butylene adipate) functionalized with quaternary phosphonium groups.

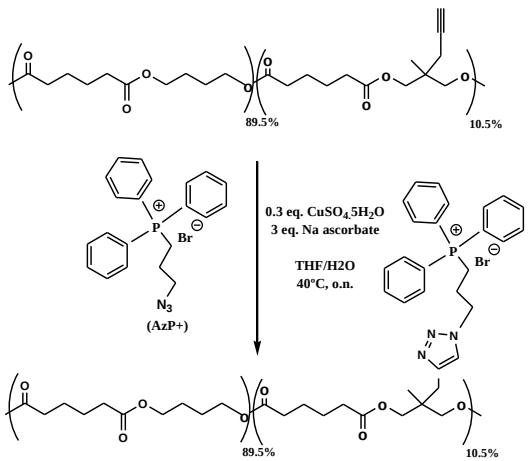

- **Electrospun materials**

Electrospun fibers are broadly applied in biomedical applications, as tissue engineering scaffolds(due to their small diameters which are able to mimic natural extracellular matrix), in wound healing, filtration, as affinity membrane, in immobilization of enzymes, small diameter vascular graft implants, healthcare, biotechnology, and environmental engineering.

The electrospinning process is governed by many parameters, which can be classified into solution parameters, process parameters, and ambient parameters.

The electrospining equipment basically consists of a syringe to hold the polymer solution, two electrodes and a DC voltage supply in the kV range (Figure 10). The electrospinning process generally consists of three stages:

(1) Jet initiation and elongation of the charged jet along a straight line.

(2) Growth of electrical bending instability and further elongation of the jet, which may or may not be accompanied with the jet branching and/or splitting.

3) Solidification of the jet into micro/nanofibers and deposition on a collector.



**Figure 10.** Schematic diagram of the electrospinnig process.

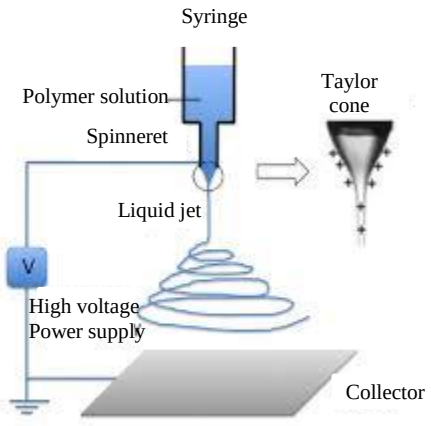

The electric force has been identified as the driving force for initiating an electrospinning process. The charged solution droplet at the needle tip reduces its size so that the force balance is maintained. With an increase in the applied voltage, the shape of the solution droplet evolves from the hemisphere to a cone shape (Taylor cone) with a high electric force concentrated at the tip of the Taylor cone. When the electric field reaches a critical voltage *Vc*, the droplet at the cone tip overcomes its surface tension to eject into the electric field, and a solution jet is thus generated. During the process of jet elongation, the solvent evaporates, leaving behind a charged polymer fiber. Mass and volume of the fluid jet decreased due to evaporation and solidification. Cross-sectional radius of the dry fiber could be $1.3 \times 10^{-3}$ times of that of the initial fluid jet. An increase of relative humidity when hydrophilic polymers are electropun from aqueous solutions may delay the solidification process, allowing elongation of the charged jet to continue longer and thereby to form thinner fibers.



Solid polymer fibers are finally deposited on a grounded collecting screen. During the fiber deposition process, a characteristic instability termed as buckling instability may occur due to the longitudinal compressive force from jet impingement on a solid flat surface. This instability usually results in bending fibrous structures with sinuous folding and overlapping figures-of-eight and circles.

In general the influence of main processing paarmeters can be summarized as follows:

(a) Initial jet/orifice radius: decreasing orifice radius tends to decrease the average fiber diameters (*e.g.*, average fiber diameters of 250, 150 and 125 nm for orifices of radii 0.59, 0.42 and 0.29 mm, respectively).

(b) Flow rate: increasing flow rate tends to increase fiber diameter.

(c) Distance from nozzle to collector: average fiber diameters tend to decrease with increase in collector distance. For example, Nylon 6 fiber diameters decrease from 230

to 140 nm with spinning distance changing from 4 to 18 cm, holding other parameters constant.

(d) Polymer concentration: Fiber diameters increase when increasing initial polymer concentration (*e.g.*, nylon 6 from 80 to 230 nm when concentration changed from 10 to 25%).

(e) Applied voltage: in general, a higher applied voltage ejects more fluid in a jet, resulting in a larger fiber diameter. However, an initial decrease in diameter has in some case been reported (*e.g.*, from 900 to 450 nm with an increase of applied voltage from 8 to 10 kV).

(f) Vapor diffusivity: lower evaporating solvent allowing for longer stretching process before jet solidification taking place, and thus for thinner fibers.

(g) Relative humidity: as the relative humidity increases, the solidification process becomes slower, allowing elongation of the charged jet to continue longer and thereby to form thinner fibers.



(h) Solution conductivity: increasing solution conductivity tends to decrease fiber diameter due to increase in electrical charge carried by the jet and thus tensile force in the presence of an electric field.

(i) Surface tension: the effect of surface tension is negligibly small for most properly chosen electrospun solutions, where the viscoelastic forces completely dominate the surface tension. However, beaded fibers tend to form higher surface tension solvents like water, low viscosity and low conductivity/charge density systems.

Electrospinning process provides a simple way to:

**a) Encapsulate drugs** within a micro/nanofiber matrix that can lead to a controlled and sustained release [64,65] A number of researchers have successfully encapsulated drugs within electrospun fibers by mixing the drugs in the polymer solution to be electrospun.[66,67] A variety of

solutions containing low molecular weight drugs have been electrospun, including lipophilic drugs such as ibuprofen,[68] cefazolin,[69] rifampin, and hydrophilic drugs such as mefoxin [67] and tetracycline hydrochloride.[66]

**b)** Prepare **conducting composites**. Conducting polymer such polyaniline can be blended with other polymers.[70] Materials can be employed as biosensors after embedding, for example, specific antibody molecules. Metal particles can also be added to the polymer matrix to produce conductive polymer composites, which can be used to provide shielding for electromagnetic interference and electrostatic discharge.

**c) Get copolymer samples by reactive blending**. This appears as an efficient and easy method to obtain new copolymers displaying modulated final properties. To this end, bioresorbable poly(butylene/diethylene glycol succinate) multiblock copolymers were specifically synthesized[71,72] starting from the parent homopolymers (i.e. PBS and poly(diethylene glycol succinate) (PDGS)) and used to fabricate biomimetic electrospun scaffolds. Interestingly, new materials supported cell growth and had a more pronounced elastomeric behaviour and a faster degradation rate than PBS.[73]



Scaffolding materials have also been developed from elastomeric polyesters constituted by citric acid and sebacic acid.[74-77] These monomers are considered biocompatible since participate in different metabolic cycles in the human body [78,79] and can react with multifunctional alcohols (e.g. glycerol and octanediol) to yield hydrophilic and elastic hydrogels. Poly(octanediol citrate) and poly(glycerol sebacate) (Figure 11) are polyesters with pendant -COOH and –OH functional groups that brings hydrophilicity and allows also the formation of physical crosslinks between polymer chains that are characteristic of elastomeric materials. Interestingly, poly(glycerol sebacate) and poly(octanediol citrate) have been employed to get biphasic systems ideal for blood vessel tissue engineering where poly(glycerol sebacate) is used as an inner non-porous phase and poly(octanediol citrate) constitutes the porous outer layer. [80]

**Figure 11.** Chemical structures of linear poly(octanediol citrate) and poly(glycerol sebacate) with pendant hydroxyl and carboxyl groups.

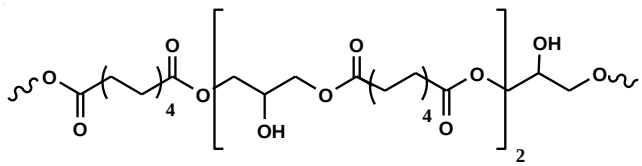

Polyglycerol sebacate (PGS)

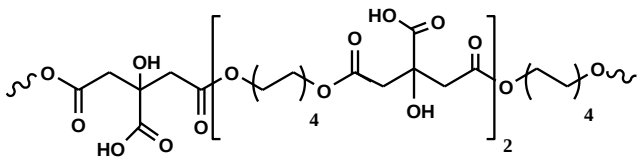

Polyoctanediol citrate (POC)



- **Tissue engineering applications of electrospinning in drug delivery**

Tissue engineering scaffolds can be easily prepared by the electrospinning technique, which is able to produce nanonofibers from a wide range of polymers.[81,82] Furthermore, many kinds of drugs can be incorporated into such nanofibrous mats and then successfully released from them without a significant loss of their activity. Different examples can be mentioned about the specific use of electrospinning to render scaffolds from poly(alkylene dicarboxylate)s.

First attempts to get biodegradable PBS nanofibers were reported by Jeong *et al.* when different solvent mixtures were assayed.[83] PBS fibers had average diameters in the range of 125–315 nm and were highly crystalline (Figure 12).

Electrospun 1,6-diisocyanatohexane-extended PBS fiber mats appeared suitable as bone scaffolds since supported the grown and proliferation of bone cells.[84] A novel PBS/wollastonite/apatite composite scaffold useful for bone tissue an application was fabricated

via electrospinning and biomimetic processes. The microstructure of these scaffolds could be adjusted by controlling the wollastonite content and the incubation time in simulated body fluid.[85]

**Figure 12.** SEM images of the ultrafine PBS electrospun fibers from various solvents: (a) chloroform/2-chloroethanol (6/4), (b) N,N-dimethyl formamide-dichloromethane/2-chloroethanol (6/4), (c) chloroform/3-chloro-1-propanol (9/1), and (d) N,N-dimethyl formamide-dichloromethan/1-chloro-2-propanol (9/1).[85]

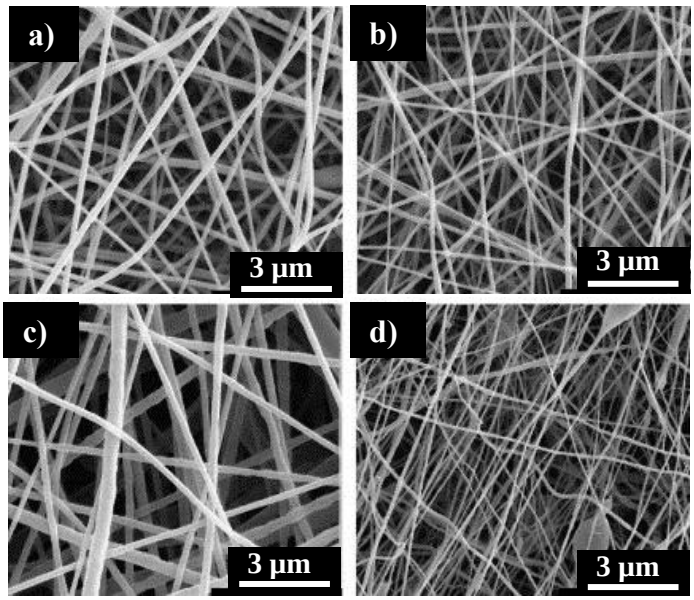




Reactive blending of PBS and poly(diethylene glycol succinate) rendered multiblock bioresorbable copolyesters with an elastomeric behaviour and able to be processed as electrospun scaffolds. These were found to support the growth and preserve the cardiac phenotype markers of cardiomyocyte $H_9C_2$ cells, demonstrating its potential utility in soft tissue engineering applications.[73]

Biodegradable PBS fiber mats containing silver nanoparticles were prepared by the electrospinning process. Bacterial growth was found to be inhibited for a long period of time due

to the long-term release performance of Ag from these fiber mats.[86] Drug-loaded PBS microspheres useful for wound treating were also prepared by electrospinning. Diameters of these microspheres could be controlled within the 5 to 25 μm range.[87]

#### 3.1.1.2. Poly (α-hydroxy acids)

##### Poly(lactic acid) (PLA)

The category of poly (α-hydroxy acids) includes poly (glycolic acid), poly (lactic acid) and a range of their copolymers (*e.g.*, poly (lactic-*co*-glycolic acid). These polymers are synthesized by ring opening or condensation polymerizations depending on the starting monomer units.[88-90]

PLA is a thermoplastic, high-strength, high-modulus polymer that can be made for annually renewable resources to yield articles for use in either the industrial packaging field or the biocompatible/bioabsorbable medical device market. It is easily processed on standard plastics equipment to yield molded parts, films, or fibers.



Polylactides unlike polyglycolide are present in many forms due to the optical isomerism of lactic acid (see Figure 13). Polymerization of isomers of lactide (L-lactide and D-lactide) results in crystalline polymers with about 40% crystallinity, whereas polymerization of the racemic mixture (DL-lactic acid) results in amorphous polymers with lower mechanical strength. Poly (L-lactic acid) and poly (DL-lactic acid) are more preferred for biomedical applications in which the former is used for bone fixation devices (Bio Interference Screw®, BioScrew®, Bio-Anchor®) and the latter is suitable candidate as a drug delivery vehicle.[91] PLLA is considered as a promising material in the medicine field, for instance wound closure, surgical implants,[92,93] drug delivery system,[94,95] and tissue culture.[96]

**Figure 13.** Stereoforms of lactides.

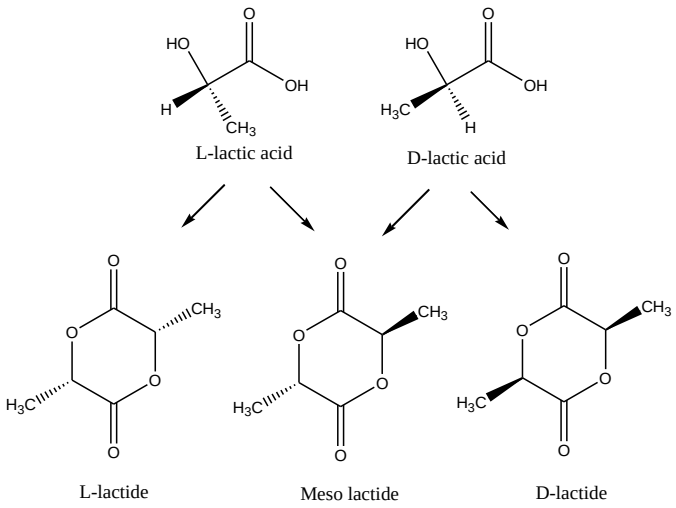




### a. Crystalline structure of poly(lactic acid)

The mechanical, thermal, and optical properties of polymorphic polymers strongly depend on the crystalline form and morphology.[97,98] Besides, biodegradability is also influenced by the crystalline form in the case of biodegradable polymers including PLLA.[99] PLLA is able to crystallize in three main crystalline forms (α, β and γ) (see Figure 14) as has been widely reported.[100-105] The α form, is the most predominant structure when crystallization proceeds from the melt or solution The structure is defined by a $10_3$ helical chain conformation [102-104] and an orthorhombic $P2_12_12_1$ space group. The β form corresponds to $3_1$ helices that are packed in a trigonal lattice.[106] This form is obtained from stretching the α form under high drawing and high temperature.[105,106] The γ form of PLLA, produced by epitaxial growth on a hexamethylbenzene substrate, has been reported by Cartier *et al.*[107] More recently, α disordered crystal named as the α' form was produced when PLLA samples were crystallized below 120 ºC.[107-110]

**Figure 14.** (a) *ab* projections of the optimized packing of PLLA in the $P2_12_12_1$ and $P222_1$ space groups, the first one was chosen considering packing energy calculations and structural refinements.[118] (b) Crystal structure of the β-phase of PLLA, shown here with three parallel helices. Below, computed diffraction pattern of the β-phase of PLLA, and corresponding indexing.[106] (c) Chain axis projection of the crystal structure determined for the γ-phase of PLLA produced by epitaxial crystallization on HMB at 140 ºC. Below, computed fiber diffraction pattern of the γ-phase of PLLA.[105]

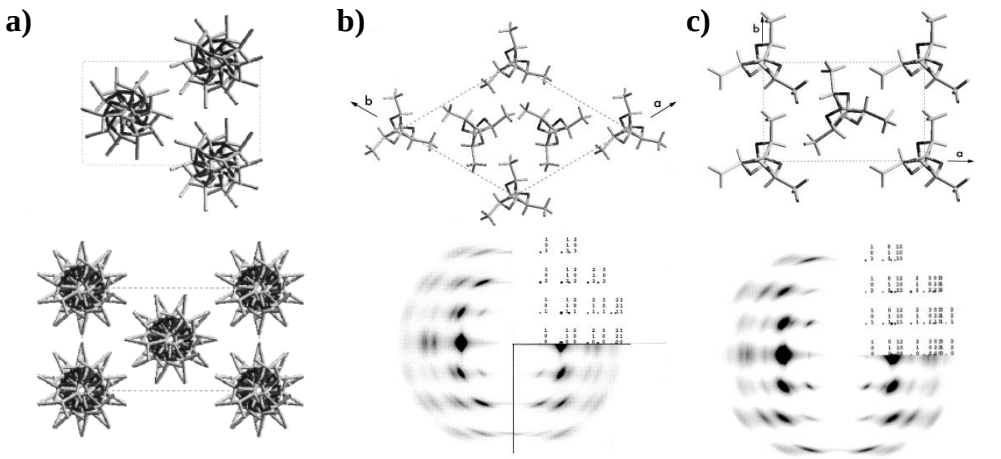




### b. Poly(lactic acid) modifications

The ability to make PLA polymers in two different ways, namely polycondensation and ring opening polymerization, leads to a wide variety of copolymers for improving or changing the final properties. The use of direct condensation leaves open the use of any hydroxy acid, diol, or diacid, with which to form random or nearly random copolymers, mostly with increased flexibility and modified solubility. The use of ring opening polymerization yields the ability the form random, block, or pseudo block copolymers to produce polymers with a wide range of mechanical properties.

There is a growing interest in increasing the hydrophilicity and flexibility of PLA in order to get materials more attractive for biomedical uses. The most frequently synthesized and most largely exploited copolyesters of lactic acid, as far as biomedical application is concerned, are those constituted by lactic and glycolic acid units.[111-115] The high melting point (228 ºC), relatively low glass transition temperature (37 ºC) and high hydrophilicity of polyglycolic acid leads to an improvement of toughness and changes on solubility and degree of crystallinity that depend also on the block distribution in the polymer backbone. Thus for example, incorporation of 30 mol-% or glycolic acid may lead to insoluble copolymers in non-polar aprotic solvents and more easily degradable materials than pure PLA.

Direct dehydropolycondensation of bis-carboxyl-terminated PLA with PEG yielded multiblock copolymers, in which PLA and PEG blocks were phase separated and the properties of one block were affected by the block length of the other.[116] The longer the PLA block the lower the crystallinity and melting temperature of the PEG block. These copolymers showed different crystallization behavior in melt and solution casting crystallization process, even though the chemical structures and molecular weights were the same in both cases. The capability to crystallize of the PLA block was more affected by the crystallization method than that of the PEG block. Such alternating multiblock copolymers formed interesting hydrogels, which were thermoplastic in nature.[117] They offer potential for application in drug delivery and various other biomedical projects.



Di- and triblock copolymers of PEG with aliphatic polyesters like PLA showed thermo-reversible gelation because of the hydrophilicity-hydrophobicity balance between the two block components.[119,120] Such block copolymers formed micelle in water at lower concentrations while at higher concentrations the gel to sol transition was observed as temperature was increased up to a certain temperature beyond which the polymer precipitated. With increasing block length of the hydrophobic aliphatic ester block, the gel to sol transition is observed at lower concentrations

and with a broad temperature range from 0 ºC to 90 ºC. Such properties are worth exploitation in the drug delivery industry.

Polyethylene glycol grafted polylactides (PEG-*g*-PLA) have also been considered to improve the ductility of PLA. In fact, PEG has excellent plasticizing abilities, although the amount introduced in PLA must be lower or equal to 20 wt-% to avoid phase separation.[121-124] Reactive blending of a maleic anhydride grafted PLA with hydroxyl functionalized PEG has been proposed as an easy way to prepare PEG-*g*-PLA copolymers, which should create more interactions between the so-functionalized polyester matrix and non-grafted PEG.[125] In situ reactive grafting of hydroxy terminated poly(ethylene glycol) (PEG) plasticizer onto maleic anhydride modified PLA in PLA/PEG blends had a positive impact on mechanical properties and lowered the glass transition temperature significantly compared to the blends where no grafting could occur (neat PLA + PEG).

### c. Degradation of poly(lactic acid)



PLA is degraded by simple hydrolysis of the ester bond and does not require the presence of enzymes to catalyze this hydrolysis. However, prolonged exposure of PLA to water is needed in order to initiate the hydrolysis process. The rate of degradation depends on the molecular weight of polymer, crystallinity and porosity of the matrix, the isomer ratio and the temperature of hydrolysis.[126,127] It has been shown that crystalline PLA will take months, sometimes years, to hydrolyze fully to lactic acid, whereas an amorphous sample is degraded in weeks. This is due to the impermeability of crystalline region.[128]

Copolymer composition also affects polymer degradation, since degradation kinetics is highly influenced by the change on crystallinity and the reduction of steric effects that are caused by the incorporation of additional monomers.[129] The rate of chain cleavage has been found to be for example accelerated with increasing glycolide portion. Conversely, copolymerization of L-lactide with D,L-lactide increases the degradation time since oligomers of D-lactic acid are

unlikely to be naturally degraded by the body's enzymes. Nevetheless, this approach helps to prolong the functionality of PLA implants in the human body. PCL, a biopolymer consumable by bacteria and fungi but not by mammalian bodies due to the lack of suitable enzymes, is polymerized with lactide to yield a copolymer with a prolonged degradation time. This biopolymer undergoes hydrolytic degradation in the early stage, and proceeds to surface and bulk degradation pathways. Manipulation of copolymer composition is very important to get a controlled drug release in a selected medium.[129]

#### 3.1.1.3. Polylactones

**Poly(ε-caprolactone) (PCL)**

Poly(ε-caprolactone) (PCL) is an aliphatic polyester with great interest due its biodegradability and biocompatibility. PCL is a semicrystalline polymer with low melting point and high solubility in common solvents, which make easy its processability. Hydrolytically labile ester linkages are responsible for its degradation although it is relatively slow (2–3 years). PCL and its blends have been suggested for use in a wide range of applications.[130-132] For medical purposes, it may be used in release systems for drug delivery to the human body,[133,134] as a material for surgical device[135] or in orthopedics for confection of splint.[136] Outside the medical field, PCL based products can be used as soil degraded container material, as water resistant laminate on paper[137] and latent heat storages as a substitute of polyethylene [138-140] and polyethylene glycols.[141,142] In this area, aliphatic polyesters are interesting because of the possibility to change the crystallization characteristics by altering the number of ethylene units between the ester groups. Material characteristics such as the latent heat, drug permeability, and biodegradability depend on the crystallinity and, thus, on the crystallization procedure.

Recently, star-shaped PCL with well-defined architectures have been extensively investigated by different research groups using multifunctional small molecules and/or dendritic

molecules.[143-145] In general, the maximal melting point, the cold crystallization temperature, and the degree of crystallinity of PCL polymers decrease with the increasing number of polymer arms, while crystalline structure is kept. The variation trend of overall crystallization rate over the number of polymer arms or the molecular weight of polymer was found be consistent with the analyses of both nonisothermal crystallization kinetics and the spherulitic growth rate.[146]

On the other hand, it is known that the use of block copolymers, with blocks of different miscibility, capable of self-assembling upon blending with uncured precursor, can lead to materials with phase-separated morphologies and a significant toughness enhancement.[147,148]

New amphiphilic polymers with hyperbranched polyester core and poly(ethylene glycol) (SP-PEG) or poly(ethylene glycol)/poly(ε-caprolactone) arms (SP-PEGPCL) (Figure 15) have been used as toughness modifiers of an epoxy/anhydride formulation. The selection of the core and arms aims to reach different phase-separated morphologies using star polymers with different flexibility and amphiphilicity.[149]



**Figure 15.** Synthetic steps for the preparation of SP-PEGPCL.

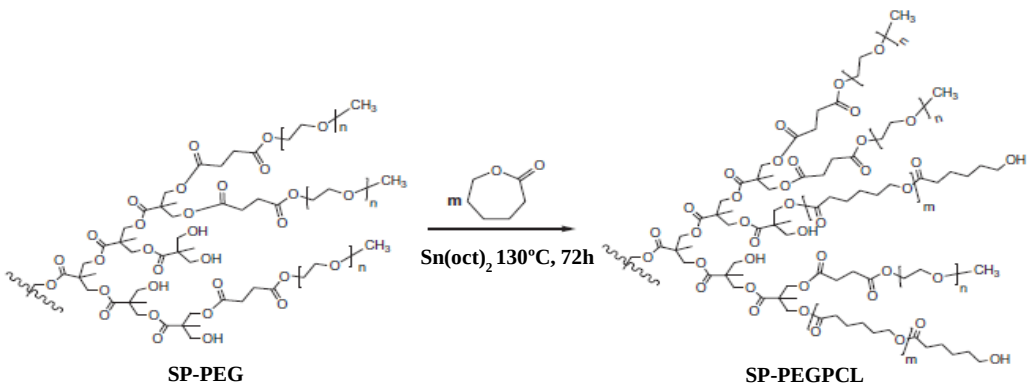


An important limitation in the use of biodegradable (bioresorbable) polymers as biomedical materials is the potential toxicity of the degradation products, and so, research

towards synthetic biodegradable polymers has mainly focused on materials entirely composed of naturally occurring and nontoxic ("physiological") building blocks. Among the physiological building blocks to be used for constructing biodegradable biomaterials naturally occurring α-amino acids are one of the most attractive ones due to their availability and versatile nature. Thus, several amino acids are produced in many thousand tones,[150] the global market is forecast to reach US$ 11.6 billion by the year 2015,[151] and almost all of 20 naturally occurring α-amino acids can be used for constructing biodegradable biomaterials that allows tuning their properties in the widest range. The α-amino acids that represent hetero-bifunctional compounds, allow to incorporate two of the most desirable hetero-links into the polymeric backbones, ester bond *via* C-terminus (carboxyl group) and H-bond forming links such as amide bond *via* N-terminus (amino group). The former, provides reasonable biodegradation (hydrolysis) rates, improves processability and decreases immunogenicity of α-amino acids-based polymers; the latter provides desired mechanical properties at lower molecular weights, increases hydrophilicity of the polymers and promotes their active interaction with the surrounding tissues in a desirable manner after implantation. All these features impart to poly(ester amide)s an obvious advantage over biodegradable polyesters.[152] It is reasonable to note here that pure polyamides made of α-amino acids (*i.e.*, poly(α-amino acid)s) have been proved to be less suitable as biodegradable materials for biomedical engineering use for many reasons, such as low rate of biodegradation and poor processability.[153]



#### 3.1.2.1. Poly(ester amide)s derived from the incorporation of natural α-amino acids to polyalkylene dicarboxylates

The three most important types of biodegradable α-amino acid derivatives correspond to polydepsipeptides that are the copolymers of α-hydroxy acids (mostly glycolic and lactic acids) and α-amino acids,[154-156] tyrosine dipeptide based polymers,[157] and polymers composed of α-amino acids and other nontoxic building blocks such as diols and dicarboxylic acids.[154,158] Only the

latter type of α-amino acids, called as amino acid based biodegradable poly(ester amide)s,[159] relates to the family of alkylene dicarboxylates

The amino acid based biodegradable poly(ester amide)s (Figure 16) can be considered as derivatives of alkylene dicarboxylates (AA-BB type polyesters) that are obtained by the insertion of α-amino acids residues among carbonyl group and ether oxygen in polyesters.

**Figure 16.** Schematic representation of amino acid based biodegradable poly(ester amide)s as products of the insertion of α-amino acids between ester bonds.

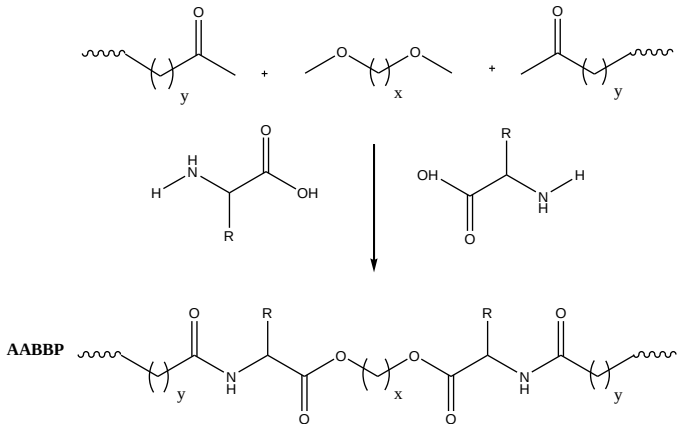


This kind of amino acid based biodegradable poly(ester amide)s can be prepared using two types of dimerized forms of α-amino acids as key monomers (Figure 17), either bis-(amino acid)-alkylene diesters or *N*,*N*'-diacyl-bis-amino acids.

**Figure 17.** Two types of α-amino acids based monomers bis-nucleophilic bis-(amino acid)-alkylene diesters and bis-electrophilic *N*,*N*'-diacyl-bis-amino acids.

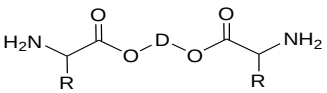

Bis-(amino acid)-alkylene diesters, **AAAD**

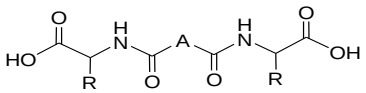

*N*,*N*'-diacyl-bis-amino acids, **DABA**

**R** = side chain of **AA**; **D** = diol residue; **A** = diacid residue.

### 3.1.2.2. Poly(ester urea)s derived from natural α-amino acids

Poly(ester urea)s (PEUs) have been proposed as a new class of α-amino acid-based polymers with bioabsorbable properties. These polymers can be easily prepared from bis(α-amino acid)-alkylene diester monomers, which can undergo either nonspecific (chemical) or specific (enzymatic) hydrolysis due to the presence of two ester linkages per elemental unit in the molecule. First syntheses were reported in the late 1970s by Huang *et al*.[160] and yielded low molecular weight powdery samples ($M_n$ close to 2,000 g/mol). Later, Yoneyama *et al.* synthesized high molecular weight PEUs by condensing the above diester-diamine monomers with non-physiological diisocyanates.[161] In order to avoid the use of diisocyanates, other syntheses based on polycondesation processes through active carbonates (*e.g.*, di-*p*-nitrophenyl carbonate) were investigated.[162] However, intramolecular cyclization led to low molecular weight polymers, which in turn led to hydantoin formation, and therefore, chain scission.



Problems were solved when an acid chloride of carbonic acid (phosgene, diphosgene, triphosgene) was entered into the polycondensation reaction with a di-*p*-toluenesulfonic acid salt of a bis(α-amino acid)-alkylene diester.[163] In the interfacial polycondensation reaction, the nucleophilic amino group was readily revealed by addition of an inorganic base, such as NaOH, $NaHCO_3$ and $Na_2CO_3$. This method provides high-yield, high-molecular weight PEUs potentially useful for biomedical applications because of their advantageous mechanical, chemical and biodegradation properties over well-known, chemically similar poly(ester amide)s also derived from α-amino acids.[164] For example, the PEU derived from carbonic acid, L-leucine, and 1,6-hexanediol (named 1L6 see Figure18) has tensile strength at yield, elongation at break and Young's modulus of 21 MPa, 114% and 622 MPa, respectively.[163] Its melting temperature is 114 ºC and its glass transition temperature 47 ºC. New PEUs were proposed to be useful as implantable surgical devices such as vascular stents and hard tissue replacement implants, and also for delivery of a variety of pharmaceutical and biologically active agents to humans and other mammals.

**Figure 18.** The PEU derived from carbonic acid, L-leucine, and 1,6-hexanediol (1L6).

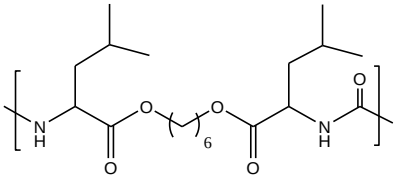

### a. Applications of amino acid based biodegradable poly(ester amide)s and poly(ester urea)s

Selected representatives of amino acid based biodegradable poly(ester amide)s were used for constructing biodegradable hydrogels, nanoformulations, drug eluting devices and coatings. Guo *et al.* used the unsaturated amino acid based biodegradable poly(ester amide)s for obtaining hybrid hydrogels through photochemical conjugation with PEG-diacrylate.[165] The biodegradable hybrid hydrogels are promising for many biomedical and pharmaceutical applications, such as drug delivery systems, tissue engineering, etc. Legashvili *et al.*[166] used brush-like *co*-amino acid based biodegradable poly(ester amide)s to obtain molecular complexes with PEG that are promising as nanocarriers of drugs. Yamanouchi *et al.*[167] evaluated complexation of a novel family of synthetic biodegradable L-arginine based amino acid based biodegradable poly(ester amide)s with DNA, for their capability to transfect rat vascular smooth muscle cells, a major cell type participating in vascular diseases.



Katsarava *et al.*[168] used amino acid based biodegradable poly(ester amide)s and their blends for constructing various medical biocomposites. One of them, registered as “Phago-BioDerm” in Republic of Georgia, is produced as elastic films (Figure 19a) and represents an innovative wound-dressing device (artificial skin) consisting of lytic bacteriophages, antibiotics, pain killer, and proteolytic enzymes. PhagoBioDerm showed an excellent therapeutic effect in the management of infected wounds and ulcers (of both trophic and diabetic origin) and in the complex treatment of infected local radiation injuries caused by the exposure. It is a successful

commercial example of phage entrapment. [169,170] Elastomeric functional *co*-amino acid based biodegradable poly(ester amide)s[171] of a high biocompatibility [172,173] revealed high elastic properties and excellent adhesion to stainless steel, and was used by MediVas, LLC (San Diego, CA, USA) for developing drug-eluting coating for vascular stent (Figure 19b). Some amino acid based biodegradable poly(ester amide)s show good mechanical characteristics and are promising as resorbable bone substitutes (Figure 19c). The amino acid based biodegradable poly(ester amide)s can also be made as viscos-flow mass (not shown) that could be impregnated with drugs and bioactive fillers and used, *e.g.*, to seal bone cavities and regenerate/reconstruct bone tissues.

The amino acid based biodegradable poly(ester amide)s form also microspheres (Figure 19d) suitable as resorbable containers for drug delivery purposes, porous materials (Figure 19e) promising as scaffolds for cell cloning, and electrospun nanofibers, medicated ones, including from non-toxic solvents like ethanol (Figure 19f) and appropiate as dressing for accelerated wound healing.



**Figure 19.** Some biomedical applications of AABBP as resorbable biomaterials: (a) an artificial skin PhagoBioDerm; (b) drug eluting vascular stent; (c) bone substitute; (d) microspheres for drug delivery; (e) porous scaffolds for cell cloning; (f) electrospun microfibers.

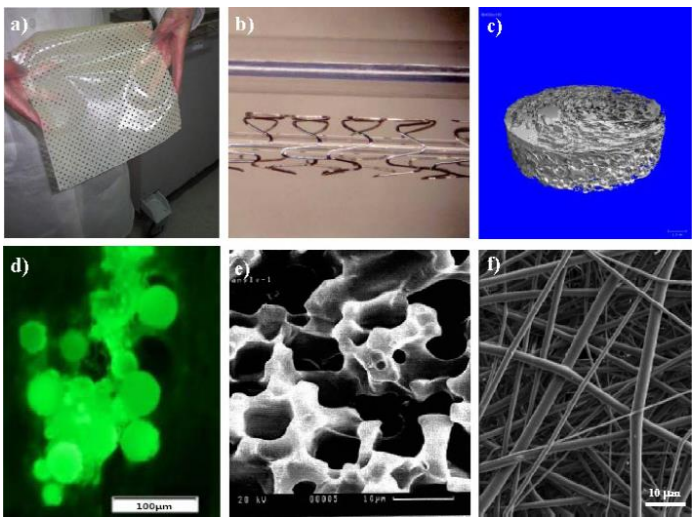

### b. Incorporation of Bacteriophages

The excellent properties of amino acid based biodegradable poly(ester urea)s may justify to explore their applications as a scaffold for supporting bacteriophages. This is an alternative to the usual addition of antibiotics for prevention of infections. It is well know that the emerge of pathogenic bacteria resistant to currently available antimicrobial agents has become a critical problem in modern medicine,[174] in this way the incorporation of bacteriophages into electrospun micro- nanofibers should give scaffolds with a clear added value. Phages has usually been adsorbed onto polymer nanofibers to design controlled released platforms.[175,176] Some cautions must be considered to kept the phage activity, namely care must be exercised to not compromise phage stability,[177] its lytic ability or its interaction with its target host/analyte[178,179] by the employed chemicals/polymers. Furthermore, some phages possess enzymes that degrade certain natural polymers (*e.g.*, alginate)[180] which complicate the use of these polymers as the main component of a protective porous matrix.[181]



Bacteriophages were “officially” discovered in 1910 by Felix d’Herelle, a French-Canadian microbiologist at the institute Pasteur in Paris,[182] while he was studying microbiologic means of controlling an epizootic of locusts in Mexico. Not long after phages were used to treat dysentery, in what was probably the first attempt to use bacteriophages for therapeutic purposes.

Bacteriophages (phages) are viruses that infect bacteria.[183,184] Phages are the most abundant biological entity on earth and, being obligate parasites, propagate themselves by hijacking the host machinery.[185] They can have a broad host range, infecting several strains or species of bacteria,[186] or infect a specific host, even down to a single bacterial strain.[187] A phage virion (morphologically complete viral particle and infectious) usually consists of a protein envelope (lipids can also be found in this envelope) encasing the genome, which can be a single or double stranded DNA or RNA molecule.[188] A phage virion may have a range of different shapes and sizes including tailed, filamentous, and icosahedral (Figure 20).[189]

**Figure 20.** Schematic representation of major phage groups.[188]

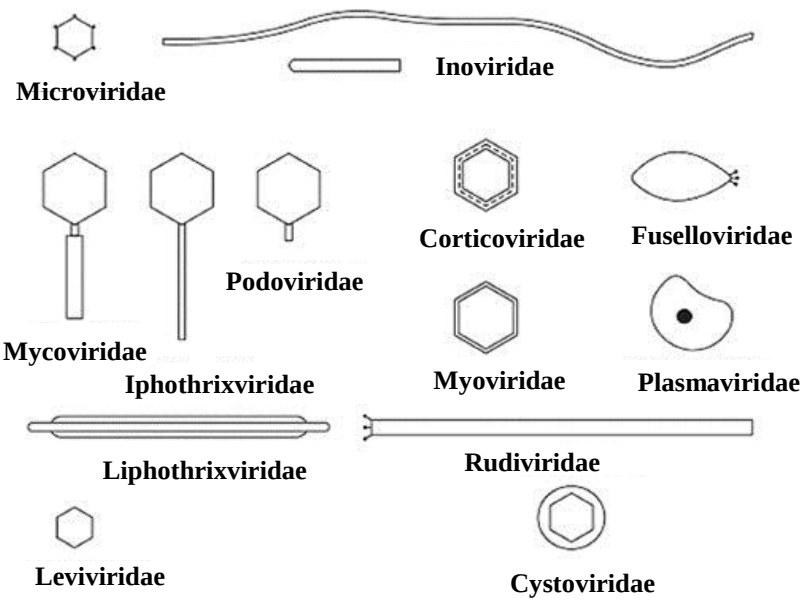




A phage infects its host bacterium by first attaching its "capture proteins" to specific receptors on the host cell surface (*e.g.*, lipopolysaccharide (LPS), pili, *etc.*).[190] Phage capture proteins can be located symmetrically all around the virion[191] or located asymmetrically on one vertex,[192] on a pole (filamentous phages)[193] or at the tip of tail fibers (tailed phages).[194] Once attached to the host bacterium, phage injects its genome into the host and either takes over host machinery immediately and starts propagating (lytic phage), or the viral genome gets incorporated into the host DNA and stays dormant (lysogenic or temperate phage) (Figure 21). The lytic life-cycle ultimately leads to host destruction, except for some filamentous lytic phage which only decrease host growth rate.[195] The genome of a temperate phage is passed on to daughter cells during bacterial replication, maintaining the lysogenic lifestyle. Certain environmental triggers (*e.g.*, heat, UV radiation, chemicals, *etc.*) can cause a switch from the lysogenic to the lytic lifestyle.[196,197]

**Figure 21:** Replication cycles of lytic and lysogenic phages. (A) Lytic phages: step 1, attachment; step 2, injection of phage DNA into the bacterial host; step 3, shutoff of synthesis of host components, replication of phage DNA, and production of new capsids; step 4, assembly of phages; step 5, release of mature phages (lysis). (B) Lysogenic phages: steps 1 and 2 are similar to those of lytic phages (i.e., attachment and injection, respectively); starting with step 3, lysogenic phages can, among other possibilities, initiate a reproductive cycle similar to that of lytic phages (a) or integrate their DNA into the host bacterium's chromosome (lysogenization) (b). Lysogenized cells can replicate normally for many generations (1b) or at some point undergo lysogenic induction (2b) spontaneously or because of inducing agents such as radiation or carcinogens, during which time the integrated phage DNA is excised from the bacterial chromosome and may pick up fragments of bacterial DNA.

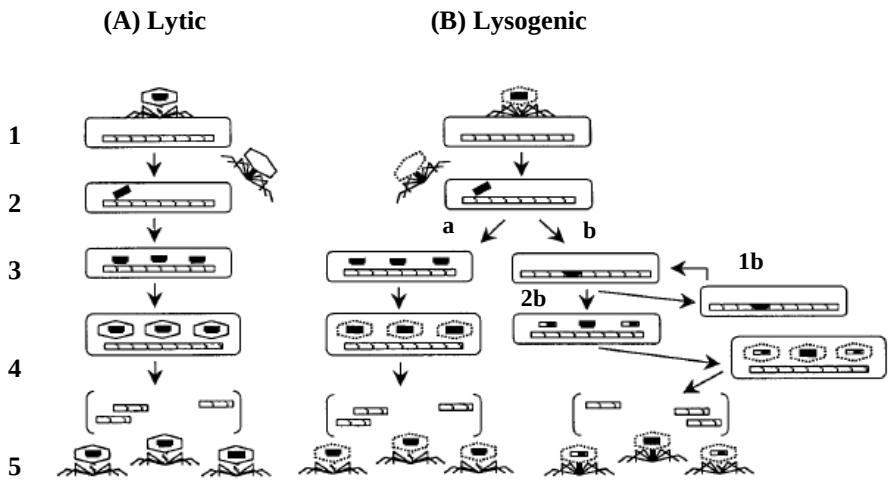




All phages have the potential to be used as specific recognition moieties in designing bioactive surfaces. Compared to other biological agents that provide similar specific interaction for pathogen capture/detection (*e.g.*, antibodies), phage offers the advantages an easy production and a long shelf life. Most lytic phage also offers the dual functionality of capture and destruction of the host. Compared to other bactericidal agents (*e.g.*, antibiotics, antimicrobial

peptides, silver nanoparticles, chemicals, *etc.*), phage offer the advantage of specificity, this characteristic could be very beneficial for many applications such as medical devices which must not disturb the body's microbiome, the collection of microorganisms living in our body that is responsible for maintaining physiological balance as well as the body's immunity towards infections.[198] Furthermore, phages are innocuous to humans, animals and plants, which is an added advantage over many biocides currently in use.[199,200]

Immobilization within a semi-solid and micro-porous matrix allows to structurally and functionally stabilize the phage particles, retaining their activity for extended periods of time. The immobilization of phage by entrapment within a porous matrix (*e.g.*, hydrogels, (bio)polymeric matrices of alginate and agar) is the method of choice for applications where the virions must be protected against harsh conditions.[201-203] Furthermore, entrapment could serve to retain humidity, which is critical for the infectivity of many phages, or protect the virions in lyophilized form.[204,205]

## II. Nanocomposites

A nanocomposite is a material in which nanoparticles are consolidated by the matrix and have an average size less than 100 nm at least in one direction. These materials have a great potential for application in mechanical engineering, astronautics, electrical engineering, medicine, and other fields. They are used for making barrier films, packaging material, conductors and cables, current conducting materials, car fuel systems, and many others.

Polymer nanocomposites are a class of materials that generally contain less than 6% of nanometer sized additives.[206] Typical forms of nanofillers are spherical (*e.g.* silica nanoparticles), laminar-like (e.g. layered silicate nanoclays like montmorrillonite (MMT)) or tubular (e.g., single (SWCNTs) and multiwalled carbon nanotubes (MWCNTs), respectively).

### 1. Layered silicate nanoclays

Layered silicates used in the synthesis of nanocomposites are natural or synthetic minerals, consisting of very thin layers that are usually bound together with counter-ions. Their basic building blocks are tetrahedral sheets in which silicon is surrounded by four oxygen atoms, and octahedral sheets in which a metal like aluminum is surrounded by eight oxygen atoms. Therefore, in 1:1 layered structures (e.g. kaolinite) a tetrahedral sheet is fused with an octahedral sheet, whereby the oxygen atoms are shared.[207] On the other hand, the crystal lattice of 2:1 layered silicates (2:1 phyllosilicates), consists of two-dimensional layers where a central octahedral sheet of alumina is fused to two external silica tetrahedron by the tip, so that the oxygen ions of the octahedral sheet also belong to the tetrahedral sheets, as shown in Figure 22. The layer thickness is around 1 nm and the lateral dimensions may vary from 30 nm to several microns, and even larger, depending on the particulate silicate, the source of the clay and the method of preparation (e.g. clays prepared by milling typically have lateral platelet dimensions of

approximately 0.1–1.0 μm). Therefore, the aspect ratio of these layers (ratio between length and thickness) is particularly high, with values greater than 1000.[208-210]

**Figure 22.** The structure of a 2:1 layered silicate

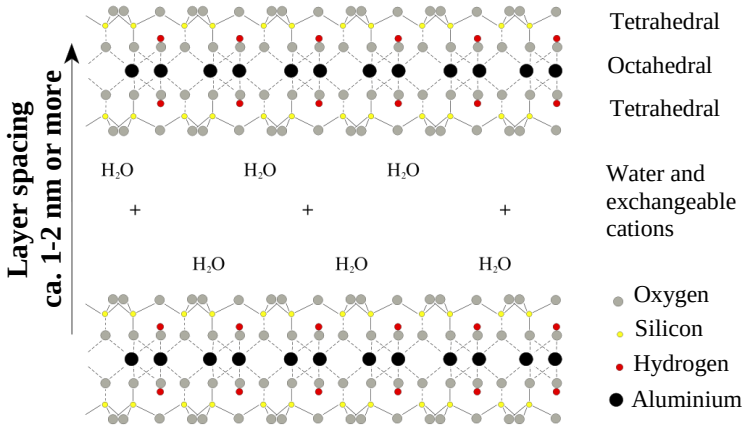




Along with montmorillonite, hectorite and saponite are the layered silicates that are most commonly used in nanocomposite materials. Their chemical formula is given in Table 1.[211]

**Table 1.** Chemical structure of commonly used 2:1 phyllosilicates[a]. [211]

| 2:1 Phyllosilicates | General formula |
|---|---|
| Montmorillonite | $M_x(Al_{4-x}Mg_x)Si_8O_{20}(OH)_4$ |
| Hectorite | $M_x(Mg_{6-x}Li_x)Si8O_{20}(OH)_4$ |
| Saponite | $M_xMg_6(Si_{8-x}Al_x)O_{20}(OH)_4$ |

[a] M: monovalent cation; *x*: degree of isomorphous substitution (between 0.5 and 1.3).

Depending on the strength of interfacial interactions between the polymer matrix and layered silicate (modified or not), three different types of layered silica nanocomposites are thermodynamically achievable (Figure 23):[212,213]

a) Intercalated nanocomposites: In intercalated nanocomposites, the insertion of a polymer matrix into the layered silicate structure occurs in a crystallographically regular fashion, regardless of the clay to polymer ratio. Intercalated nanocomposites are normally interlayer by a few molecular layers of polymer. Properties of the composites typically resemble those of ceramic materials.

b) Flocculated nanocomposites: Conceptually this is same as intercalated nanocomposites. However, silicate layers are some times flocculated due to hydroxylated edge-edge interactions of the silicate layers.

c) Exfoliated nanocomposites: In an exfoliated nanocomposite, the individual clay layers are separated in a continuous polymer matrix by an average distance that depends on clay loading. Usually, the clay content of an exfoliated nanocomposite is much lower than that of an intercalated nanocomposite.



**Figure 23.** Typical structures found in polymer-layered silicate composites.

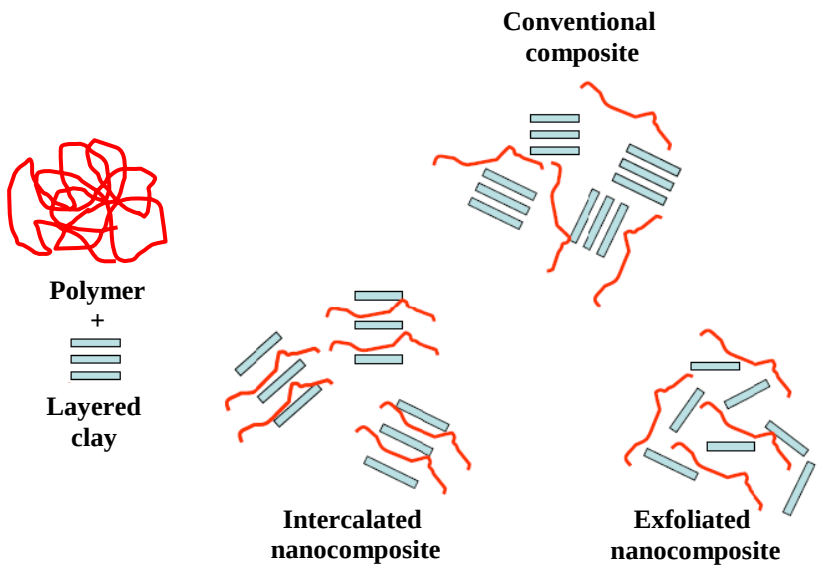

Alternatively a phase separated microcomposite can be attained when interactions are poor.

Polymer nanocomposites are characterized by a high modulus of elasticity, enhanced bending and tension strengths, heat resistance, reduced gas permeability, and such a unique property as controlled biodegradation.

### 1.1. Organic modification of layered silicates

The physical mixture of a polymer and layered silicate may not form a nanocomposite. This situation is analogous to polymer blends, and in most cases separation into discrete phases takes place. In immiscible systems, which typically correspond to the more conventionally filled polymers, the poor physical interaction between the organic and the inorganic components leads to poor mechanical and thermal properties. In contrast, strong interactions between the polymer and the layered silicate in nanocomposites lead to the organic and inorganic phases being dispersed at the nanometer level. As a result, nanocomposites exhibit unique properties not shared by their micro counterparts or conventionall filled polymers. Pristine layered silicates usually contain hydrated $Na^+$ or $K^+$ ions. Obviously, in this pristine state, layered silicates are only miscible with hydrophilic polymers, such as poly(ethylene oxide), or poly(vinyl alcohol). To render layered silicates miscible with other polymer matrices, one must convert the normally hydrophilic silicate surface to an organophilic one, making the intercalation of many engineering polymers possible. Generally, this can be done by ion-exchange reactions with cationic surfactants including primary, secondary, tertiary, and quaternary alkylammonium or alkylphosphonium cations.[214] These cations in the organosilicates lowers the surface energy of the inorganic host and improve the wetting characteristics of the polymer matrix, resulting in a larger interlayer spacing.[215] Additionally, the alkylammonium or alkylphosphonium cations can provide functional groups that can react with the polymer matrix, or in some cases initiate the polymerization of monomers to improve the adhesion between the inorganic and the polymer matrix.

Depending on the functionality, packing density, and length of the organic modifiers, the organo-modified layered silicates (OMLSs, organosilicates or organoclays) may be engineered to optimize their compatibility with a given polymer.[216] Table 2 summarizes the main organoclays modified with alkylammonium salts. Chain lengths and also used organophilic clay.

**Table 2.** Layered silica organoclays modified with alkylammonium salts.

| Layered silicate nanoclays | Chemical structure of the organic modifier[a] |
|---|---|
| **Nanofil 757** | Natural montmorrillonite ($Na^+$) |
| **Nanofil 848** | 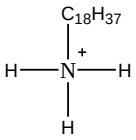 |
| **Cloisite 20A** | 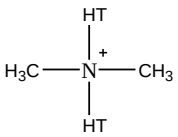 |
| **Cloisite 25A** | 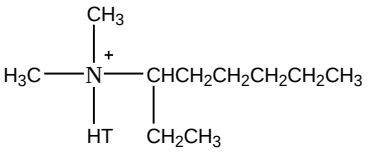 |

[a]T: (~65% C18, ~30% C16, ~5% C14); HT: hydrogenated Tallow



## 2. Silica nanoparticles

Silica was the first inorganic monodisperse colloidal particles prepared in solution and systematically characterized in 1968 by Stöber *et al*.[217] Modifications of the Stöber process currently remain the dominant route for the synthesis of monodisperse silica particles.[218-220] In general, the surfaces of the silica particles have two different types of functional groups, siloxane

groups (Si-O-Si) and (Si-OH) silanol groups whose relative concentrations depends on the preparation conditions and storage. Silanol groups behave as acids (-SiO-H +) being chemically active. According to available surface, these groups are classified as isolated, vicinal or geminal groups as illustrated in Figure 24.

The use of silica ($SiO_2$) nanoparticles is also highly interesting to provide materials with enhanced properties due to their intrinsic advantages (low cost, nontoxicity, high modulus and capability to modify the chemical surface characteristics).[221,222] Therefore, a considerable improvement of properties could be attained when materials are processed in a way that good silica nanoparticle dispersion is obtained and an appropriate surface functionalization is produced in order to improve interfacial interactions with the polymer matrix.[223-225]

**Figure 24.** General form of silica nanoparticles.

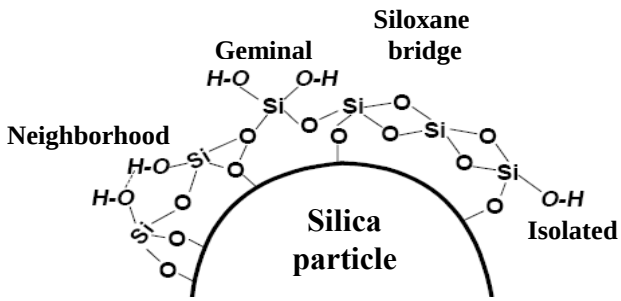




Properties of PBS/$SiO_2$ nanocomposites prepared by the *in situ* polymerization were carefully investigated to determine the potential interactions taking place between the hydroxyl end groups of PBS and the surface silanol groups of $SiO_2$.[226] It was found that at low concentrations the $SiO_2$ nanoparticles acted as chain extenders, increasing the molecular weight of PBS, while at higher loadings they resulted in extended branching and crosslinking reactions (Figure 25), leading to smaller hydrodynamic dimensions and an apparent decrease on the molecular weight. Silica nanoparticles acted as nucleating agents, increasing the crystallization rate of PBSu, although the degree of crystallinity was slightly reduced.

**Figure 25.** Cross-linked structures obtained by reaction between the hydroxyl end groups of PBS and the surface silanol groups of fumed silica nanoparticle.

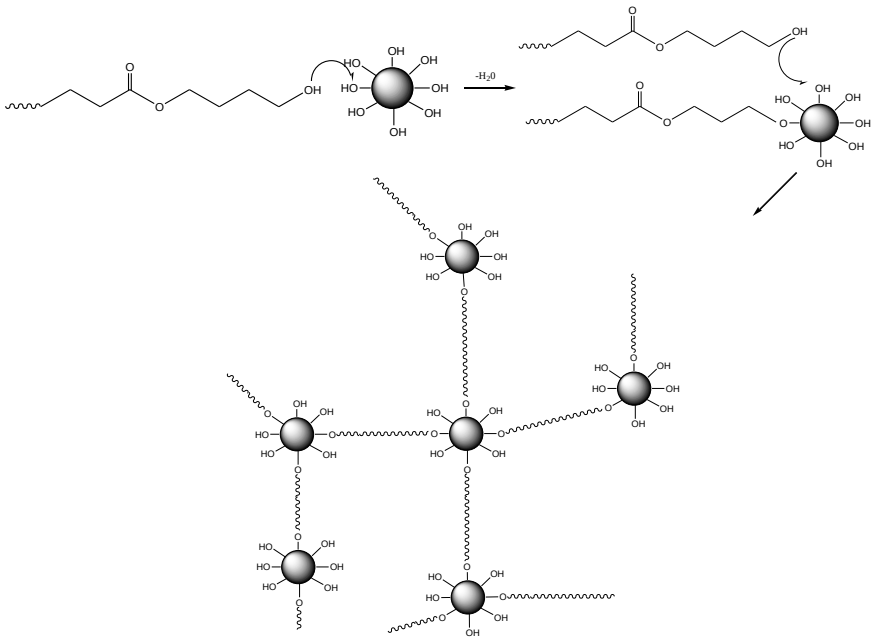



As layered silicates, nanosilica needs some modifications, because, the different nature of the nanofiller (inorganic) with respect to that of the polymeric matrix (organic), and their high adsorption surface energies are responsible for a strong nanofillers tendency to form aggregates. The surface modification of the nanosílica can be carried out either by chemical or physical treatment methods, having the first one a greater interest. Modification can be obtained using a coupling agent containing a double bond or an initiator moiety. This method has been followed by Caris *et al*.[227] with $TiO_2$ modified with a functional titanate coupling agent, and extended more recently by the same group for styrene polymerization.[228] Silane coupling agents have also been used either by first treating the inorganic surface with octadecyltriethoxysilane[229] or directly with a mixture of a silane initiator, monomers and inorganic particles.[230]

### 3. Degradation of nanocomposites

Studies on the biodegradation of nanocomposites based on aliphatic polyesters show contradictory results about the influence of nanoparticles. An enhanced degradation is postulated mainly due the presence of hydroxyl groups in the added nanoparticles (*e.g.*, the terminal hydroxylated edge groups of silicate layers).[231] Basically, the hydrolysis of polyester/clay nanocomposites seems to depend upon both the nature of the pristine layered silicate and the surfactant used for the modification of the layered silicate.[232] Furthermore, the hydrophilicity of the silica surface enhanced the susceptibility of the nanocomposite to microbial attack as demonstrated for PBS/silica nanocomposites.[233] In the same way, hydrophilic fillers may enhance the degree of swelling of the otherwise hydrophobic matrix.[234]

On the other hand, a decrease on the biodegradation rate has also been reported. In this case, arguments are based on the barrier properties of nanoparticles that should increase the difficulty for the micro-organism to reach the bulk matrix due to the more tortuous diffusion path.[235] Decrease on the biodegradation rate has also been related to interactions of the matrix with the nanofiller, water permeability, degree of crystallinity and anti-microbial property of the nano-filler.[236]



The comparative effect on the enzymatic hydrolysis of three nanocomposites prepared by *in situ* polymerization and based on a poly(propylene sebacate) matrix and a 2 wt. % content of either fumed silica nanoparticles ($SiO_2$), multiwalled carbon nanotubes (MWCNTs), or montmorillonite (MMT) has recently been reported.[237] A similar hydrolysis mechanism was determined, but in all cases nanoparticles hampered the action of the enzymes. It was postulated that the available surface area for hydrolysis was hindered and also that significant interactions took place between nanoparticles and the polymer matrix. The addition of MWCNTs and MMT was found to enhance the thermal stability of the polymer, while $SiO_2$ nanoparticles do not affect it.[238]

## III. New processing techniques

The need to produce very small plastics parts is growing, due to demands of electronics, biomedical, and other industries for such micro-devices and also for the production of components for complex micro-electromechanical systems (MEMS). These features have driven the development of advanced techniques for micro-fabrication of polymer products including micro-fluidic devices, micro-actuators, and optical components.

Micro-molding of thermoplastic polymers is therefore becoming a popular fabrication method for micro-devices (Figure 26). Most micro-molding techniques use heated molds to plasticize the thermoplastic polymer, which requires an increased cycle time and additional heating/cooling equipment. In addition several limitations were also reported: a) The production of micro-devices using conventional injection molding machines led to large wastes because the weight of the specimen represents only a few percent of the whole molded mass; b) Material degradation occurred during the different processing steps (plasticization, injection, holding); c) Hydraulic control of the metering size was not accurate enough for the replication of such small specimens. So there arose the need to introduce new process technologies, in terms of the minimization of energy and optimization of reaction control both microwave and ultrasound irradiation have now been proved as real options.[239]



**Figure 26.** Micro-molded polymer piece processed by ultrasonic radiation.

### 1. Ultrasonic radiation.

Ultrasound is most simply defined as a sound with a frequency that is too high to be detected by the human ear. This is generally considered to be above 20 kHz.

The potential of using acoustic cavitation to create changes in materials was identified in the USA in the late 1920s.[240-242] Over the following years after a great deal of pioneering work in sonochemistry, two reviews on the applications of ultrasound in polymer and chemical processing were published.[243,244] Yet there are very few references to ultrasound in chemistry from about 1955 to 1970 when a major renaissance in the subject began to occur. The subsequent revival of interest is undoubtedly due to the more general availability of commercial ultrasonic equipment. Now there are many publications and texts on a wide variety of applications.[245-247]

Ultrasonic waves are an energy source for melting and welding polymer samples that has been applied as an assembly procedure for over 40 years. This source has also been applied for the preparation of nanocomposites.[248] Recently, the possibility of using ultrasonic energy for micro-molding applications has also been studied with highly promising results. Specifically, it has been demonstrated that polylactide (PLA) can be well processed by this technology without an appreciable degradation.[249] It seems also that the ultrasonic energy may make feasible the delamination of a silicate structure and therefore may favor the attainment of an exfoliated structure when a polymer/clay powder mixture is processed.



There are many features of power ultrasound that make its use effective and different from other methods for the fabrication of nanomaterials.[250] These include: (a) The ability to produce nanomaterials in the amorphous state which is due to the very high cooling rates (>1011 K/s) obtained in the collapsing cavitation bubble during sonochemistry. The amorphous nature of the products is of importance in fields like catalysis, magnetism, coatings and others. (b) Sonication generally results in shorter reaction times. (c) The shock waves and microjets which

follow the collapse of a bubble near a solid surface is unique to sonochemistry, and is of great importance for the insertion and coating processes. These forces can be used for the insertion of nanoparticles into the pores of mesoporous materials (MSPM). The nanoparticles form a homogeneous monolayer on the inner walls of the MSPM and do not block the pores. The same effect is responsible for the formation of a smooth coating monolayer of nanoparticles on ceramic or polymeric surfaces.

In the present work we are interested in the study of ultrasonic energy as a new processing method to obtain micro-molded specimens from biodegradable polymers, and also in the evaluation of their capability to get appropriate dispersions from both silica nanoparticles and silicate nanoclays.

## IV. References


1. Middleton JC, Tipton AJ. Biomaterials 2000;21:2335.
2. Hacker M, Mikos A. Foundations of Regenerative Medicine: Clinical and Therapeutic Applications. , London: Academic Press; 2009. p. 336.
3. Luten J, van Nostrum CF, De Smedt SC, Hennink WE. J Control Release 2008;126:97.
4. Khan W, Hosseinkhani H, Ickowicz D, Hong PD, Yu DS, Domb AJ. Acta Biomater 2012;8:4224.
5. Mudgal S, Lyons L, Bain J. et al. (2011) Plastic Waste in the Environment – Revised Final Report for European Commission DG Environment. Bio Intelligence Service. France; 2011
6. Kyrikou J, Briassoulis D. J Polym Environ 2007;15:125.
7. Gu JD. Int Biodeter Biodegr 2003;52:69.
8. Shalini Verma KG, Mittal A, Kumar N, Biodegradable Polymers for Emerging Clinical Use in Tissue Engineering. New Jersey: Wiley; 2011.
9. Okada M. Prog Polym Sci 2002;27:87.
10. Sharma V, Kundu PP. Prog Polym Sci 2008;33:1199.
11. Di Lorenzo ML, Raimo M, Cascone E, Martuscelli E. J Macromol Sci B: Phys 2001;40:639.
12. Han YK, Um JW, Im SS, Kim BC. J Polym Sci: Part A1 2001;39:2143.
13. Zhu CY, Zhang ZQ, Liu QP, Wang ZP, Jin J. J Appl Polym Sci 2003;90:982.
14. Saulnier B, Coudane J, Garreau H, Vert M. Polymer 2006;47:1921.
15. Kobayashi S, Uyama H, Kimura S. Chem Rev 2001;101:3793.
16. Olson DA, Sheares VV. Macromolecules 2006;39:2808.
17. Liu W, Chen B, Wang F, Tan T, Deng L. Proc Biochem 2011;46:1993.
18. Doppalapudi S, Jain A, Khan W, Domb AJ. Polym Adv Technol 2014;24:427.
19. Hofvendahl K, Hahn-Hagerda B. Enzym Microb Technol 2000;26:87.
20. Zeikus JG, Jain MK, Elankovan P. Appl Microbiol Biotechnol 1999;51:545.
21. Ueda AS, Chatani Y, Tadokoro H. Polym J 1971;2:387.
22. Turner-Jones A, Bunn CW. Acta Crystallogr 1962;15:105.
23. Chatani Y, Hasegawa R, Tadokoro H. Meeting of the Society of Polymer Science. Japan: 1971. p. 420.
24. Minke R, Blacwell J. J Macromo Sci Phys 1979;B16:407.

25. Minke R Blacwell J. J Macromol Sci Phys 1980;B18:233.
26. Aylwin PA, Boyd RH. Polymer 1984;25:323.
27. Alemán C, Puiggalí J. J Org Chem 1997;62:3076.
28. Kanamoto T, Tanaka K. J. Polym Sci Part A-2 1971;9:2043.
29. Brandrup J, Immergut EH. In. Polymer Handbook; Wiley-Interscience: New York, 1989.
30. Liau WB, Boyd RH. Macromolecules 1990;23:1531.
31. Ichikawa Y, Kondo H, Igarashi Y, Noguchi K, Okuyama K, Washiyama J. Polymer 2000;41:4719.
32. Pan P, Inoue Y. Prog Polym Sci 2009;34:605.
33. Almontassir A, Gestí S, Franco L, Puiggalí J. Macromolecules 2004;37:5300.
34. Gestí S, Almontassir A, Casas MT, Puiggalí J. Polymer 2004;45:8845.
35. Gestí S, Almontassir A, Casas MT, Puiggalí J. Biomacromolecules 2006;7:799.
36. Gan Z, Abe H, Doi Y. Biomacromolecules 2000;1:713.
37. Gan Z, Abe H, Doi Y. Biomacromolecules 2001;2:313.
38. Iwata T, Doi Y. Macromol Chem Phys 1999;200:2429.
39. Gestí S, Casas MT, Puiggalí J. Polymer 2007;48:5088.
40. Mochizuki M, Mukai K, Yamada K, Ichise N, Murase S, Iwaya Y. Macromolecules 1997;30:7403.
41. Li X, Hong Z, Sun J, Geng Y, Huang Y, An H. J Phys Chem. 2009;113:2695.
42. Li X, Sun J, Huang Y, Geng Y, Wang X, Ma Z, Shao CG, An HN, Yan TZ, Li LB. Macromolecules 2008;41:3162.
43. Liang Z, Pan P, Zhu B, Dong T, Hua L, Inoue Y. Macromolecules 2010;43:2925.
44. Liang Z, Pan P, Zhu B, Inoue Y. Polymer 2011;52:2667.
45. Allegra G, Bassi W. Adv polym Sci 1869;6:549.
46. Shih YF, Chieh YC. Macromol Theory Simul 2007;16:101.
47. Rizzarelli P, Carroccio S. Polym Degrad Stab 2009;94:1825.
48. Chrissafis K, Paraskevopoulos KM, Bikiaris DN. Thermochim Acta. 2005;435:142.
49. Chrissafis K, Paraskevopoulos KM, Bikiaris DN. Polym Degrad Stab 2006;91:60.
50. Soccio M, Lotti N, Finelli L, Gazzano M, Munari A. Polymer 2007;48:3125.
51. Chrissafis K, Paraskevopoulos KM, Papageorgiou GZ, Bikiaris DN. J Anal Appl Pyrol 2011;92:123.

52. Dimitrio N, Bikiaris GZ, Papageorgiou DJ, Giliopoulos CA, Stergiou. Macromol Biosci 2008;8:728.
53. Tokiwa Y, Suzuki T. J Appl Polym Sci 1981;26:441.
54. Murase T, Iwata T, Doi Y. Macromolecules 2001;34:5848.
55. Kikkawa Y, Hirota T, Numata K, Tsuge T, Abe H, Iwata T, et al. Macromol Biosci. 2004;4:276.
56. Iwata T, Doi Y. Polym Int 2002;51:852.
57. Iwata T, Doi Y. Macromolecules 1998;31:2461.
58. Iwata T, Doi Y. Macromolecules 2001;34:7343.
59. Iwata T, Kobatashi S, Tabata K, Yonezawa N, Doi D. Macromol Biosci 2004;4:296.
60. Billiet L, Fournier D, Du Prez F. J Polym Sci Part A: Polym Chem 2008;46:6552.
61. Seyednejad H, Ghassemi AH, van Nostrum CF, Vermonden T, Hennink WE. J Control Release 2011;152:168.
62. Anthierens T, Billiet L, Devlieghere F, Du Prez F. Innov Food Sci Emerg 2012;15:81.
63. Casas MT, Puiggalí J. Polym Degrad Stab 2009;94:1941.
64. Llorens E, Del Valle LJ, Ferrán R, Rodríguez-Galán A, Puiggalí J. J Polym Res 2014;21:360.
65. Yang D, Li Y, Nie J. Carbohydr Polym 2007;69:538.
66. Kenawy ER, Bowlin GL, Mansfield K, Layman J, Simpson DG, Sanders EH, et al. J Control Release 2002;81:57.
67. Zong X, Fang D, Kim K, Ran S, Hsiao BS, Chu B, et al. Chem Soc Div Polym Chem 2002b;43:659.
68. Jiang HL, Fang DF, Hsiao D, Chu B, Chen WL. J Biomater Sci Polym Ed 2004b;15:279.
69. Katti DS, Robinson KW, Ko FK, Laurencin CT. J Biomed Mater Res 2004;70B:286.
70. Guo Y, Li My, Mylonakis A, Han JJ, MacDiarmid AG, Chen XS, Lelkes PI, Wei Y. Biomacromolecules 2007;8:3025.
71. Soccio M, Lotti N, Finelli L, et al. Eur Polym J 2008;44:1722.
72. Soccio M, Lotti N, Finelli L, et al. Eur Polym J 2009;45:3236.
73. Gualandi C, Soccio M, Govoni M, Valente S, Lotti N, Munari A, Giordano E, Pasquinelli G, Focarete ML. J Bioact Compat Polym 2012;27:244.
74. Wang Y, Kim YM, Langer R. J Biomed Mater Res A 2003;66:192.
75. Bettinger CJ, Weinberg EJ, Kulig KM, Vacanti JP, Wang Y, Borenstein JT, Langer R. Adv Mater 2006;18:165.

76. Qiu H, Yang J, Kodali P, Koh J, Ameer GA. Biomaterials 2006;27:5845.
77. Bat E, Plantinga JA, Harmsen MC, van Luyn MJA, Zhang Z, Grijpma DW. J Biomed Mater Res Part A 2010;95A:940.
78. Yang J, Webb AR, Ameer GA. Adv Mater 2004;16:511.
79. Bruggeman JP, De Bruin BJ, Bettinger CJ, Langer R. Biomaterials 2008;29:4726
80. Stammen JA, Williams S, Ku DN, Guldberg RE. Biomaterials 2001;22:799.
81. Reneker DH, Chun I. Nanotechnology 1996;7:216.
82. Frenot A, Chronakis IS. Curr. Opin Colloid Interface Sci 2003;8:64.
83. Jeong EH, Im SS, Youk JH. Polymer 2005;46:9538.
84. Sutthiphong S, Pavasant P, Supaphol P. Polymer 2009;50:1548.
85. Zhang D, Chang J, Zeng Y. J Mater Sci 2008;19:443.
86. Tian L, Wang P, Zhao Z, Ji J. Appl Biochem Biotech 2013;171:1890.
87. Xu L, Ren Z. J Polym Eng 2008;28:27.
88. Nair LS, Laurencin CT. Tissue Engineering I. Verlag Berlin Heidelberg: Springer; 2006. p. 47.
89. Gunatillake PA, Adhikari R. Eur Cell Mater 2003;5:1.
90. Gunatillake P, Mayadunne R, Adhikari R. Biotechnol Annu Rev 2006;12:301.
91. Gupta A, Kumar V. Eur Polym J. 2007;43:4053.
92. Hofmann GO, Wagner FD. Clin Mater 1993;14:207.
93. Russias J, Saiz E, Nalla RK, Gryn K, Ritchie RO, Tomsia AP. Mat Sci Eng C-Bio S 2006;26:1289.
94. Park TG, Cohen S, Langer R. Macromolecules 1992;25:116.
95. Mi FL, Shyu SS, Lin YM, Wu YB, Peng CK, Tsai YH. Biomaterials 2003;24:5023.
96. Mikos AG, Lyman MD, Freed LE, Langer R. Biomaterials 1994;15:55.
97. Kristiansen M, Tervoort T, Smith P, Goossens H. Macromolecules 2005;38:10461.
98. Libster D, Aserin A, Garti N. Polym Adv Technol 2007;18:685.
99. Furuhashi Y, Iwata T, Kimura Y, Doi Y. Macromol Biosci 2003;3:462.
100. Hoogsteen W, Postema AR, Pennings AJ, Ten Brinke G, Zugenmaier P. Macromolecules 1990;23:634.
101. Kobayashi J, Asahi T, Ichiki M, Okikawa A, Suzuki H, Watanbe T, Fukuda E, Shikinami Y. J Appl Phys 1995;77:2957.
102. Sasaki S, Asakura T. Macromolecules 2003;36:8385.

103. Sawai D, Takahashi K, Imamura T, Nakamura K, Kanamoto T, Hyon SH. J Polym Sci Polym Phys Ed 2002;40:95.

104. Sawai D, Takahashi K, Sasashige A, Kanamoto T, Hyon S H. Macromolecules 2003;36:3601.

105. Cartier L, Okihara T, Ikada Y, Tsuji H, Puiggali J, Lotz B. Polymer 2000;41:8909.

106. Puiggali J, Ikada Y, Tsuji H, Cartier L, Okihara T, Lotz B. Polymer 2000;41:8921.

107. Zhang J, Domb AJ, Sato H, Tsuji H, Noda I, Yan S, Ozaki Y. Macromolecules 2005;38:8012.

108. Zhang J, Tashiro K, Tsuji H, Domb AJ. Macromolecules 2008;41:1352.

109. Zhang J, Tashiro K, Tsuji H, Domb AJ. Macromolecules 2007;40:1049.

110. Pan P, Zhu B, Kai W, Dong T, Inoue Y. J Appl Polym Sci 2008;107:54.

111. Alemán C, Lotz B, Puiggali J. Macromolecules 2001;34:4795.

112. Reed AM, Gliding DK. Polymer 1981;22:494.

113. Cohn D, Younes H, Marom G. Polymer 1987;28:2018.

114. Ferruti P, Penco M, D'Addato P, Ranucci E, Deghenghi R. Biomaterials 1995;16:1423.

115. Mooney DJ, Baldwin DF, Suh NP, Vacanti JP, Langer R. Biomaterials 1996;17:1417.

116. Agrawal CM, Huang D, Schmitz JP, Athanasiou KA. Tissue Eng 1997;3:345.



117. Lee S-Y, Chin I-J, Jung J-S. Eur Polym J 1999;35:2147.

118. Huh KM, Bae YH. Polymer 1999;40:6147.

119. Jeung B, Lee DS, Shon J-I, Bae YH, Kim SW. J Polym Sci Part A: Polym Chem 1999;37:751.

120. Choi SW, Si YC, Jeong B, Kim SW, Lee DS. J. Polym Sci Part A: Polym Chem 1999;37:2207

121. Oh JK. Soft Matter 2011;7:5096.

122. Jacobsen S, Fritz HG. Polym Eng Sci 1999;39:1303.

123. Hu Y, Hu YS, Topolkaraev V, Hiltner A, Baer E. Polymer 2003;44:5681.

124. Hu Y, Rogunova M, Topolkaraev V, Hiltner A, Baer E. Polymer 2003;44:5701–5710.

125. Hassouna F. Raquez JM, Addiego F, Dubois P, Toniazzo V, Ruch D. Eur Polym J 2011;47:2134.

126. Auras RA, Lim LT, Selke SE, Tsuji H. Poly (lactic acid): synthesis, structures, properties, processing, and applications, Vol. 10. New Jersey: Wiley, Hoboken: 2011.

127. Gupta B, Revagade N, Hilborn J. Prog Polym Sci 2007;32:455.

128. Kharas GB, Sanchez-Riera F, Severson DK. in D. P. Mobley (Ed.), Plastics From Microbes. Munich: Hanser-Gardner; 1994. p. 93–137.

129. Hiemenz PC. Polymer Chemistry: The Basic Concepts. New York: Marcel Dekker; 1984.

130. Chiono V, Vozzi G, D'Acunto M, Brinzi S, Domenici C, Vozzi F, Ahluwalia A, Barbani N, Giusti P, Ciardelli G. Mater Sci Eng C 2009;29:2174.
131. Coombes A, Rizzi S, Williamson M, Barralet J, Downes S, Wallace W. Biomaterials 2004;25:315.
132. Dasaratha Dhanaraju M, Gopinath D, Rafiuddin Ahmed M, Jayakumar R, Vamsadhara C. J Biomed Mater Res A 2006;76:63.
133. Pitt CG. Drugs Pharmaceupt Sci 1990;71.
134. Pitt CG, Chasalow FI, Hibionada YM, Klimas DM, Schindler A. J Appl Polym Sci 1981;26:3779.
135. Yasin M, Tighe BJ. Biomaterials 1992;13:9.
136. Kaloustian J, Pauli AM, Pastor J. J Therm Anal1991;37:1767.
137. Akahori S, Osawa. Polym. Degrad. Stabil 1994;45:261.
138. Kamimoto M, Abe Y, Sawata S, Tani T, Ozawa T. J Solar Energy Eng 1986;108:282.
139. Kasza KE, Choi SU, Kaminsky J. AshraeTransact 1987;93:2.
140. Kasza KE, Chen MM. J Solar Energy Eng 1985;107:229.
141. Hayakawa K, Taoda H, Tazawa M, Yamakita H.Proc. Congress Int. Solar Energy Society. Kobe, Japan: 1990. vol. 3. p. 2281.
142. Vigo TL, Bruno JS. Proc. 26th Intersociety Energy Conversion Eng. Conference, Boston, MA: 1991 vol. 4. p.161.
143. Trollsas M, Hedrick JL. J Am Chem Soc 1998;120:4644.
144. Hecht S, Ihre H, Frechet JMJ. J Am Chem Soc 1999;121:9239.
145. Kricheldorf HR, Hachmann-Thiessen H, Schwarz G. Macromolecules 2004;37:6340.
146. Wang J-L, Dong C-M. Polymer 2006;47:3218.
147. Könczöl L, Döll W, Buchholz U, Mülhaupt R, J Appl Polym Sci 1994;84:815.
148. Percec V, Wilson DA, Leowanawat P, Wilson CJ, Hughes AD, Kaucher MS, Hammer DA, Levine DH, Kim AJ, Bates FS, Davis KP, Lodge TP, Klein ML, DeVane RH, Aqad E, Rosen BM, Argintaru AO, Sienkowska MJ, Rissanen K, Nummelin S, Ropponen J, Science 2010;328:1009.
149. Lagunas C, Fernández-Francos X, Ferrando F, Flores M, Serra A, Morancho JM, Salla JM, Ramis X. React Funct Polym 2014;83:132.
150. Leuchtenberger W, Huthmacher K, Drauz K. Appl Microbiol Biotechnol 2005;69:1.

151. Vocus/PRWEB, February 21, 2011. http://www.prweb.com/releases/2011/2/prweb8151116.htm

152. Jacoby M. Chem. Eng. News 2001;5:30.

153. Nathan A, Kohn J. Amino acid derived polymers. In Biomedical Polymers: Design-to-Degrade Systems; Shalaby S.W., Ed.; New York: Hanser publishers; 1994; Chapter 3, p 117.

154. Sun H, Meng F, Dias AA, Hendriks M, Feijen J, Zhong Z. Biomacromolecules 2011;12,:1937.

155. Rodríguez-Galán A, Franco L, Puiggalí J. Polymers 2011;3:65.

156. Rodríguez-Galán A, Franco L, Puiggalí J. Biodegradable Poly(ester amide)s: Synthesis and applications. In Biodegradable Polymers: Processing, Degradation; Felton, G.P., Ed.; USA: NOVA Science Publisher; 2011; Chapter 4, p 207.

157. Bourke SL, Kohn J. Adv. Drug Deliv. Rev 2003;55:447.

158. Katsarava R, Gomurashvili Z. Biodegradable Polymers composed of naturally occurringα-amino acids, In Handbook of Biodegradable Polymers - Isolation, Synthesis, Characterization and Applications; Lendlein, A., Sisson, A., Eds.; Wiley-VCH, Verlag GmbH & Co. KGaA; 2011. Chapter 5, p. 107.

159. Katsarava R, Kharadze D, Japaridze N, Omiadze T, Avalishvili L. Makromol Chem 1985;186:939.

160. Huang SJ, Bansleben DA, Knox JR. J Appl Polym Sci 1979;23:429-437.

161. Yoneyama M, Hashimoto T, Arai K. Polym. Prepr. Jpn. 1994;43:177.

162. Kartvelishvili T, Tsitlanadze G, Edilashvili L, Japaridze N, Katsarava R. Macromol Chem Phys 1997;198:1921.

163. Gomurashvili ZD, Katsarava R, Tugushi D. Poly(ester urea) polymers and methods of use. WO 2007050415. 2007.

164. Katsarava R, Beridze V, Arabuli N, Kharadze D, Chu CC, Won CY. J Polym Sci Part A: Polym Chem 1999;37:391.

165. Guo K, Chu CC. J Polym Sci: Part A: Polym Chem 2005;43:3932.

166. Legashvili I, Nepharidze N, Katsarava R, Sannigrahi B, Khan IM. J Biomater Sci Polymer Edn 2007;18:673.

167. Yamanouchi D, Wu J, Lazar AN, Kent KC, Chu CC, Liu B. Biomaterials 2008;29:3269.

168. Katsarava R, Alavidze Z. Polymer blends as biodegradable matrices for preparing biocomposites. US patent 6703040. 2004.

169. Jikia D, Chkhaidze N, Imedashvili E, Mgaloblishvili I, Tsitlanadze G, Katsarava R, Morris JG, Sulakvelidze A. Clin Exp Dermatol 2005;30:23.

170. Markoishvili K, Tsitlanadze G, Katsarava R, Glenn J, Sulakvelidze A. Int J Dermatol 2002;41:453–458

171. Jokhadze G, Machaidze M, Panosyan H, Chu CC. Katsarava R. J Biomater Sci Polym Ed 2007;18:411.

172. DeFife KM, Grako K, Cruz-Aranda G, Price S, Chantung R, Macpherson K, Khoshabeh R, Gopalan S, Turnell WG. J Biomater Sci 2009;20:1495.

173. Lee SH, Szinai I, Carpenter K, Katsarava R, Jokhadze G, Chu CC, Huang Y, Verbeken E, Bramwell O, de Scheerder I. Coron Artery Dis 2002;13:237.

174. Frykberg RG, Armstrong DG, Giurini J, et al. J Foot Ankle Surg 2000; 39 :S1–S60.

175. Lee SW, Belcher AM. Nano Lett 2004;4:387.

176. Salalha W, Kuhn J, Dror Y, Zussman E. Nanotechnology 2006;17:4675.

177. Tang Z, Huang X, Baxi S, Chambers JR, Sabour PM, Wang Q. Food Res Int 2013;52:460.

178. O'Flaherty S, Ross RP, Flynn J, Meaney WJ, Fitzgerald GF, Coffey A. Lett Appl Microbiol 2005;41:482.

179. Gill JJ, Pacan JC, Carson ME, Leslie KE, Griffiths MW, Sabour PM. Antimicrob Agents Chemother 2006;50: 2912.

180. Hanlon GW, Denyer SP, Olliff CJ, Ibrahim LJ. Appl Environ Microbiol 2001;67:2746.

181. Dini C, Islan GA, De Urraza PJ, Castro GR. Macromol Biosci 2012;12:1200.

182. Bordet J, Ciuca M. Compt Rend Soc Biol 1921;84:745.

183. Twort FW. Lancet 1915;2:1241.

184. d'Herelle F. C.R. Hebd Seances Acad Sci 1917;165:373.

185. Abedon ST. Phage evolution and ecology. Advances in Applied Mircobiology. San Diego, CA: Elsevier Academic Press Inc; 2009. Vol. 67. p. 1.

186. O'Flaherty S, Ross RP, Meaney W, Fitzgerald GF, Elbreki MF, Coffey A. Appl Environ Microbiol 2005;71:1836.

187. Blair JE, Williams REO. Bull World Health Organ 1961;24:771.

188. Ackermann HW. Classification of bacteriophages. R.L. Calendar Ed. The Bacteriophages. New York, NY: Oxford University Press; 2006.

189. Bradley DE. Bacteriol Rev 1967;31:230.

190. Kutter E, Sulakvelidze A. Bacteriophages Biology and Applications. FL: CRC Press, Boca Raton; 2005.

191. Grahn AM, Butcher SJ, Bamford JKH, Bamford DH. PRD1. Dissecting the genome, structure, and entry. R.L. Calendar Ed. The Bacteriophages. New York, NY: Oxford University Press; 2005.

192. Van Duin J, Tsareva N. Single-stranded RNA phages. R.L. Calendar Ed. The Bacteriophages. New York, NY: Oxford University Press; 2005.

193. Fane BA, Brentlinger KL, Burch AD, Chen M, Hafenstein S, Moore DE, Novak CR, Uchiyama A. Cubic and filamentous phages. R.L. Calendar Ed. The Bacteriophages. New York, NY: Oxford University Press: 2005.

194. Mosig G, Eiserling F. T4 and related phages: structure and development R.L. Calendar Ed. The Bacteriophages. New York: Oxford University Press; 2005.

195. Rakonjac J, Bennett NJ, Spagnuolo J, Gagic D, Russel M. Curr Issues Mol Biol 2011;13:51.

196. Ptashne M. A Genetic Switch: Phage Lambda Revisited. New York: Cold Spring Harbor Laboratory Press, Cold Spring Harbor; 2004.



197. Little JW. Lysogeny, prophage induction, and lysogenic conversion M.K.F.D.I.A.S.L. Waldor (Ed.), Phages: Their Role in Bacterial Pathogenesis and Biotechnology. Washington, D.C.: ASM Press: 2005. p. 37.

198. Schommer NN, Gallo RL. Trends Microbiol 2013;660.

199. Bondarenko O, Juganson K, Ivask A, Kasemets K, Mortimer M, Kahru A. Arch Toxicol 2013;87:1181.

200. Kalghatgi S, Spina CS, Costello JC, Liesa M, Morones-Ramirez JR, Slomovic S, Molina A, Shirihai OS, Collins JJ. Sci Transl Med 2013;5:192.

201. Ma Y, Pacan JC, Wang Q, Xu Y, Huang X, Korenevsky A, Sabour PM. Appl Environ Microbiol 2008;74:4799.

202. Stanford K, McAllister TA, Niu YD, Stephens TP, Mazzocco A, Waddell TE, Johnson RP. J Food Prot 2010;73:1304.

203. Ma Y, Pacan JC, Wang Q, Sabour PM, Huang X, Xu Y. Food Hydrocolloids 2012;26:434.

204. Puapermpoonsiri U, Spencer J, van der Walle CF. Eur J Pharm Biopharm 2009;72:26.

205. Alfadhel M, Puapermpoonsiri U, Ford SJ, McInnes FJ, van der Walle CF. Int J Pharm 2011;416:280.

206. Avella M, Errico ME, Rimedio R. J Mater Sci 2004;39:6133.

207. Miranda-Trevino JC, Coles CA. Appl Clay Sci 2003;23:133.

208. Beyer G. Plast Addit Compound 2002;4:22.

209. McNally T, MurphyWR, Lew CY, Turner RJ, Brennan GP. Polymer 2003;44:2761.

210. Solomon MJ, Almusallam AS, Seefeldt KF, Somwangthanaroj A, Varadan P. Macromolecules 2001;34:1864.

211. Alexandre M, Dubois P. Mater Sci Eng R 2000;28:1.

212. Wypych F, Satyanarayana KG. J. Colloid Interface Sci 2005;285:532.

213. Ray SS, Okamoto M. Prog Polym Sci 2003;28:1539.

214. Zanetti M, Lomakin S, Camino G. Macromol Mater Eng 2000;279:1.

215. Kornmann X, Lindberg H, Berglund LA. Polymer 2001;42:1303.

216. Xie W, Gao Z, Liu K, Pan W-P, Vaia R, Hunter D. Thermochim Acta 2001;367/368:339.

217. Stöber W, Fink A, Bohn EJ. Colloid Interface Sci. 1968;26:62.

218. Giesche HJ. Eur. Ceram. Soc. 1994;14:205.

219. Wong S, Kitaev V, Ozin GA. J Am Chem Soc 2003;125:5589.

220. Pileni MP. Nat Mater 2003;2:145.

221. Engin B, Polymer2011;52:5118.

222. Choi M, Kim C, Ok Jeon S, Soo Yook K, Yeob Lee J and Jang J, Chem Commun 2011;47:7092.

223. Yang F, Ou Y and Yu Z, J Appl Polym Sci 1998;69:355.

224. Xu X, Li B, Lu H, Zhang Z and Wang H, J Appl Polym Sci 2008;107:2007.

225. Vassiliou AA, Papageorgiou GZ, Achilias DS and Bikiaris DN, Macromol Chem Phys 2007;208:364.

226. Vassiliou AA, Bikiaris D, Mabrouk K, Kontopoulou M. J Appl Polym Sci 2011;119:2010.

227. Caris CHM, Kuijpers RPM, Vna Herk AM, German AL. Makromol Chem Macromol Symp 1990;35/36:535.

228. Jansenn AWG. Van Herk AM, German AL. ACS Polym Prepr 1993;34:532.

229. Hagi N, Oonaka S. Japan. Patent 05026879 A2.1993

230. Matsui H, Suzuki T. D. E. 3210865 A1. 1982

231. Ray SS, Yamada K, Okamoto M, Ueda K. Macromol Mater Eng 2003;288:203.

232. Singh NK, Purkayastha BD, Roy JK, Banik RM, Yashpal M, Singh G. ACS Appl Mater Interfaces 2010;2:69.

233. Han SI, Lim JS, Kim DK, Kim MN. Im SS. Polym Degrad Stab 2008;93:889.

234. Chouzouri G, Xanthos M. Acta Biomater. 2007;3:745.

235. Lee SR, Park HM, Lim H, Kang T, Li X, Cho WJ, Ha C-S. Polymer 2002;43:2495.

236. Maiti P, Batt CA, Giannelis EP. Biomacromolecules 2007;8:3393.

237. Bikiaris DN, Nianias NP, Karagiannidou EG, Docoslis A. Polym Degrad Stab 2012;97:2077.

238. Chrissafis K, Roumeli E, Paraskevopoulos KM, Nianias N, Bikiaris DN. J Anal Appl Pyrol 2012;96:92.

239. Thesis Doctoral Jingsong Chu. Characterization of the Micro Injection Molding Process and Its Products Department of Chemical Engineering. McGill University, Montreal, Quebec, Canada 2009.

240. Wood RW, Loomis AL. Philos Mag 1927;4:417.

241. Wood RW, Loomis AL. J Am Chem Soc 1927;49:3086.

242. Richards WT. J Am Chem Soc 1929;51:1724–1729.

243. Mark H. J Acoust Soc Am 1945;16:183.

244. Weissler A. J Chem Educ 1948;25:28.

245. Ashokkumar M, Mason TJ, Sonochemistry, in: Kirk-Othmer Encyclopedia of Chemical Technology On-Line, Wiley Interscience; 2007.

246. Mason TJ, Peters D. Practical Sonochemistry: Power Ultrasound Uses and Applications, 2nd ed., Horwood Publishing; 2003.

247. Mason TJ, Lorimer JP. Applied Sonochemistry The Uses of Power Ultrasound in Chemistry and Processing, Wiley-VCH; 2002.

248. Dinari M, Mallakpour S. J Polym Res 2014;21:350.

249. Sacristán M, Plantá X, Morell M, Puiggalí J. Ultrason Sonochem 2014;21:376.

250. Gedanken A. Ultrason Sonochem 2004;11:47–55.

# Chapter 2.

## Objectives

The present Thesis is focused in the development and study of new biodegradable polyesters with potential applications as commodities and specialties. The last mainly concern to the biomedical field and specifically includes the development of scaffolds for tissue engineering and drug delivery systems. The work is mainly focused on the study of new poly(alkylene dicarboxylate)s since they constitute a specific family of polyesters that offer great possibilities especially considering that most of them can be obtained from renewable resources. Thus, the extensive application of such polymers could not only mitigate the negative effect of non-degradable plastics on the environment but also reduce the dependence on fossil resources. The main goals can be grouped in three areas that will be described in the next lines.

1. The first part is addressed to the study of new copoly(alkylene dicarboxylate)s derived from renewable dicarboxylic acids with an odd number of carbon atoms like pimelic and azelaic acids or an even number like succinic acid. Even diols with highly different length such as 1,4-butanediol and 1,9-nonanediol are also considered.

   1.1. Synthesis and characterization of poly(alkylene dicarboxylate)s derived from 1,9-nonanediol and mixtures with different ratios of pimelic acid and azelaic acid. In this chapter the study of thermal properties, crystallization kinetics and the arrangement of comonomer units is carried out.

   1.2. The crystalline structure of poly(nonamethylene pimelate) and poly(nonamethylene azelate) is studied as representative of odd,odd polyesters as well as the random copolymer derived from an equimolar mixture of the two dicarboxylic units. Crystalline morphology appears an interesting point due to the lack of information concerning this series of odd, odd polyesters as well as the implications derived from the incorporation of foreign comonomer units into the crystalline phase. Finally, enzymatic degradation of lamellar crystals is evaluated.

   1.3. Synthesis and characterization of poly(butylene azelate-*co*-butylene succinate) samples with different azelate/succinate ratios. In this case, the series of even,odd polyesters is explored and specifically the effect of incorporating monomers with

highly different length merits attention. The goal is to get insight into the crystallization behavior of copolyesters constituted by highly differentiated units and evaluate the capability to control thermal properties of new copolyesters since other characteristics like biodegradability are strongly influenced by the amorphous phase content.

1.4. The crystalline structure of poly(butylene azelate-*co*-butylene succinate) samples is considered as well as the crystalline morphologies of melt processed samples. Special interest merits the study of the crystallization behavior of these copolyesters constituted by highly differentiated units since the degree of crystallinity is expected to decrease with increasing the minor component content because of crystal lattice incompatibility of the two homopolymers. These features should also have an impact on the enzymatic degradability which will therefore also evaluated. is poly(butylene azelate-*co*-butylene succinate)poly(nonamethylene pimelate) and poly(nona-methylene azelate) is studied as representative of odd,odd polyesters as well as the random copolymer derived from an equimolar mixture of the two dicarboxylic units. Crystalline morphology appears an interesting point due to the lack of information concerning this series of odd,odd polyesters as well as the implications derived from the incorporation of foreign comonomer units into the crystalline phase. Finally, enzymatic degradation of lamellar crystals is evaluated.



2. The second part is focused to the processing of poly(nonamethylene azelate) as a representative polyester by means of ultrasounds micromolding technology. The capability of this new technology to render nanocomposites is also evaluated.

2.1. Ultrasound micro-molding technology is tested as a new method to get polymer/clay nanocomposites. To this end poly(lactide) and poly(nonamethylene azelate) are selected as polymer matrices and neat N757 clay or the organomodified C20A, C25A and N848 organo-modified clays are used as nanoparticles. Structure of

nanocomposite produced by ultrasound micro-moldings is investigated as well as their basic properties and crystallization behavior.

2.2. Nanocomposites based on poly(nonamethylene azelate) and functionalized silica nanoparticles are prepared by means of ultrasound micro-molding technology. Dispersion of particles and properties of the nanocomposites is evaluated giving attention on crystallization kinetics since particles should clearly affect nucleation and crystal growth.

3. The third part is aimed to the study of polyester derivatives that incorporate urea groups, have grafted polyethylene glycol segments and finally have the form of multiarm star structures. These polymers appear interesting for tissue engineering, drug delivery systems and preparation of thermally reworkable materials.

3.1. A poly(ester urea) containing L-leucine, 1,6-hexanediol and carbonic units is considered for preparation of electrospun scaffolds. Good properties and solubility characteristics appears ideal for loading drugs, active enzymes that could accelerate degradation and bacteriophages that could prevent of infection risks.



3.2. Grafting reactions through maleic anhydride functionalization of lactide and trimethylene carbonate copolymers is studied. The derived copolymers having polyethylene glycol lateral chains will be characterized and both degradability and biocompatibility evaluated. Preparation of microspheres for drug delivery is carried out.

3.3. Star polymers based on a commercial poly(ethyleneimine) core and polyester multiarms may provide advantageous technological applications in different fields as for example the development of epoxy coatings. Incorporation of ester labile groups may provide the capability to get thermally rework able materials. Crystallization behavior from solution and the melt state should depend on the length of the arms and also the homogeneity of sizes. These features are evaluated from crystallization kinetics data.

# *Chapter 3.*

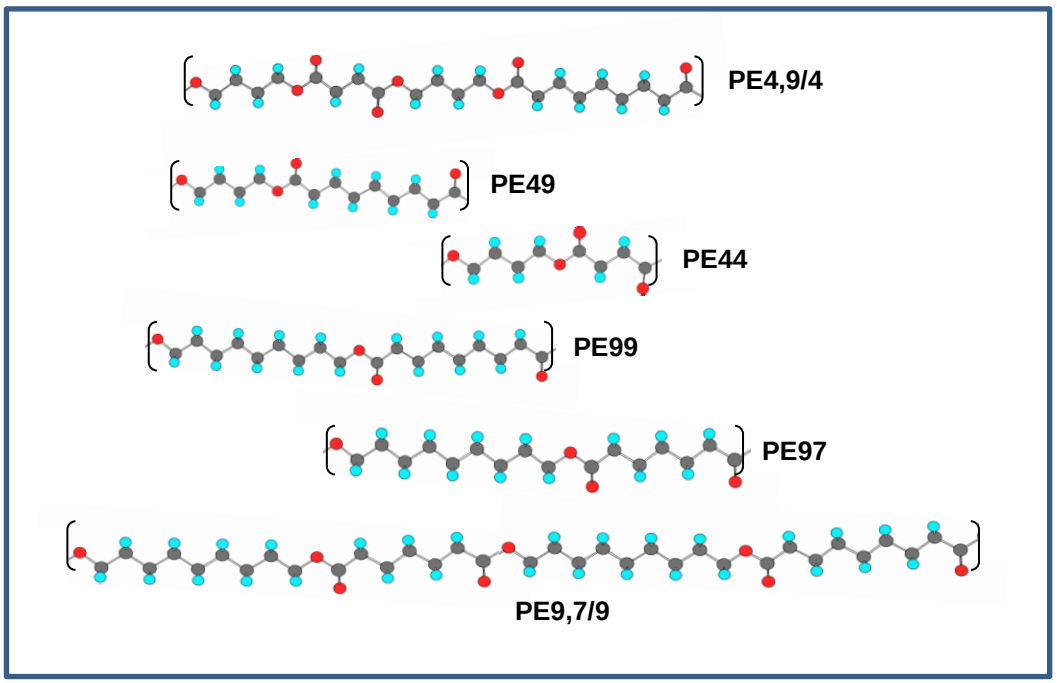

# Chapter 3.1

## *Study on the crystallization of poly(alkylene dicarboxylate)s derived from 1,9-nonanediol and mixtures with different ratios of azelaic acid and pimelic acid units.*

Polyalkylene dicarboxylates derived from 1,9-nonanediol and mixtures with different ratios of pimelic acid and azelaic acid were synthesized by thermal polycondensation. All samples had a high degree of crystallinity although it was found to decrease with the comonomer content.

Crystallization kinetics of the two homopolymers and the copolymer with the eutectic composition was studied by calorimetric and optical microscopy techniques. Similar Avrami parameters were determined for the three samples and a spherulitic growth with heterogeneous nucleation was deduced. Spherulites showed negative birefringence and a fibrillar or ringed texture depending on the sample. Furthermore, clear differences were found in the primary nucleation density, the spherulitic growth rate and even in the secondary nucleation constant deduced from the Lauritzen-Hoffman treatment.

The three studied samples had a similar arrangement of molecular chains, and consequently their WAXD patterns showed the same strong reflections related to the molecular packing. SAXS data revealed that a lamellar insertion mechanism was characteristic for non-isothermal crystallization from the melt. In addition, significant differences were found between the crystal lamellar thicknesses of the homopolymer and copolymer samples. Diffraction and

spectroscopic data suggested that the lamellar crystals of the eutectic copolymer were mainly constituted by azelate units whereas the pimelate units were preferentially located in the amorphous regions including the interlamellar amorphous layer associated with the chain folds.

## I. Introduction

Great efforts are being focused into the development of biodegradable polymers from renewable resources to avoid problems associated with more conventional petrochemical feedstocks such as decreasing availability, increasing price and indeed environmental pollution caused by plastic waste. Vegetable oils are a promising alternative since coming from abundant and economical biological sources can lead to biodegradable materials. Specifically, potential applications and uses of polyols and polyurethanes derived from plant oils are well known. [1-4]

Polyesters also constitute a family of degradable polymers of great and increasing interest since they can cover a wide range of applications as specialities, mainly in the biomedical field, and commodities.[5-11] Poly(alkylene dicarboxylate)s, a specific group within polyesters, are gaining increasing attention because the marketing of polybutylene succinate, which is supplied by Showa High Polymers as Bionolle™ and is characterized by a relatively low production cost, easy processability and good thermal and mechanical properties. [12,13] Several works in the literature deal with the structure and crystallization process of poly(alkylene dicarboxylate)s. [14-23] It was demonstrated that their molecular conformation and packing arrangement depend on the length of the polyalkylene segment and the parity of chemical units involved (*i.e.,* odd or even number of main chain atoms). However, studies have mainly been focused on even-even compounds and little attention has been devoted to the odd-odd series probably because of their expected low thermal properties. This problem can be overcome by using monomers with a high content of methylene groups as the melting point of polyesters generally increases when the ratio between ester and methylene groups in the main chain decreases. [24]

Commodity oils like sunflower can provide high purity fatty acids (*e.g.,* oleic acid), which can be used for chemical synthesis of dicarboxylic acid and diol monomers of poly(alkylene dicarboxylate)s. Thus, azelaic acid and 1,9-nonanediol can be obtained by ozonolysis cleavage of the alkene double bond of oleic acid and subsequent oxidation and reduction. [3]

The main goal of this work is the basic characterization and study of the crystallization process of odd-odd polyesters derived from natural resources, specifically from 1,9-nonanediol, pimelic and azelaic acids. Special attention is paid to copolymers obtained from mixtures of both dicarboxylic acids since melting points, crystallinities and basic morphologies can vary according to their ratio. Note that azelate and pimelate moeities have a highly similar chemical structure and consequently an identical molecular conformation is expected. In this way, comonomer units could be compatible in such a way that they are able to share a crystalline lattice. [25] This could occur in the isomorphic co-crystallization where only one crystalline phase containing both crystalline units is developed and in the isodimorphic crystallization when at least one of the two crystalline phases incorporates the corresponding minor component in its crystalline lattice. Several works have recently addressed the isomorphic crystallization of copoly(alkylene dicarboxylate)s, which were mainly constituted by even units, such as poly(butylene succinate-*co*-ethylene succinate),[26] poly(butylene succinate-co-propylene succinate), [27] poly(hexamethylene succinate-*co*-hexamethylene adipate),[28] poly(hexamethylene sebacate-*co*-hexamethylene adipate),[29,30] poly(hexamethylene sebacate-*co*-hexamethylene suberate)[31] and poly(hexamethylene suberate-co-hexamethylene adipate).[31] Results pointed out that isomorphism was feasible and that a smaller difference between the chemical structure of comonomer units led to less free energy to incorporate foreign units and to a higher extent of comonomer unit inclusion in the host crystalline lattice.[31]



## II. Experimental Section

### 1. Materials

All reagents and solvents were purchased from Sigma-Aldrich and used without further purification.

Poly(nonamethylene pimelate) (PE97), poly(nonamethylene azelate) (PE99), and poly(nonamethylene azelate-*co*-pimelate) (PE9,7/9-*x*) were synthesized by thermal polycondensation of the appropriate mixture of dicarboxylic units with an excess of 1,9-

nonanediol (2.2:1 molar ratio) (Figure 1). In this work, the composition of the reaction medium is defined by the molar ratio between pimelate and azelate units (*x*). Titanium tetrabutoxyde was used as a catalyst and the reaction was first performed in a nitrogen atmosphere at 150 ºC for 4 h and then in vacuum at 180 ºC for 18 h. Polymers were purified by precipitation with ethanol of chloroform solutions (10 wt-%).

**Figure 1.** Synthesis of copoly(alkylene dicarboxylate)s from 1,9-nonanediol and pimelic and azelaic acids.

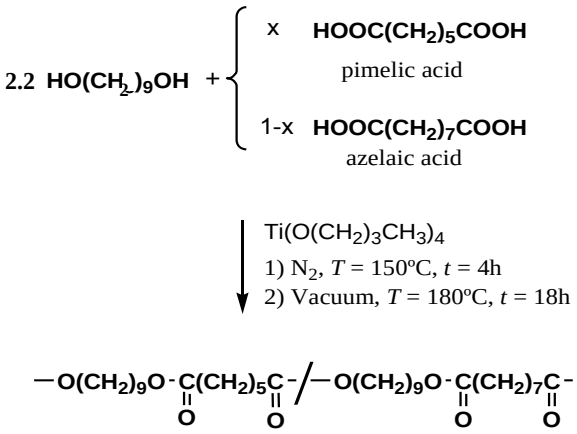


**PE 9,7/9 -x**



## 2. Measurements

Molecular weights were estimated by GPC using a liquid chromatograph (Shimadzu, model LC-8A) equipped with an Empower computer program (Waters) and a refractive index detector. A PL HFIP gel guard precolumn and PL HFIP gel column (Agilent Technologies Deutschland GmbH) were employed. The polymer was dissolved and eluted in 1,1,1,3,3,3-hexafluoroisopropanol at a flow rate of 0.5 mL/min (injected volume 100 µL, sample concentration 1.5 mg/mL). The number and weight average molecular weights were calculated using polymethyl methacrylate standards.

$^{1}$H- and $^{13}$C-NMR spectra were acquired with a Bruker AMX-300 spectrometer operating at 300.1 MHz and 75.7 MHz, respectively. Chemical shifts were calibrated using tetramethylsilane as an internal standard. Deuterated chloroform was used as the solvent.

Infrared absorption spectra were recorded with a Fourier Transform FTIR 4100 Jasco spectrometer in the 4000-600 $cm^{-1}$ range. A Specac model MKII Golden Gate attenuated total reflection (ATR) with a heated Diamond ATR Top-Plate was used.

Calorimetric data were obtained by differential scanning calorimetry with a TA Instruments Q100 series equipped with a refrigerated cooling system (RCS) operating from -90 ºC to 550 ºC. Experiments were conducted under a flow of dry nitrogen with a sample weight of approximately 10 mg while calibration was performed with indium. Heating and cooling runs were performed at rates of 20 ºC/min and 10 ºC/min, respectively.

Spherulites of polyesters were grown from homogeneous melt-crystallized thin films placed between two cover glasses. These films were obtained by evaporation of a dilute solution of the polymer in chloroform. Samples were crystallized isothermally at different temperatures below the melting point using a Linkam temperature control system configured by a THMS 600 heating and freezing stage connected to an LNP 94 liquid nitrogen cooling system. Films with thickness lower than 10 µm were obtained by this experimental procedure. Optical photographs were taken using a Zeiss AxioCam MRC5 digital camera mounted on a Zeiss Axioskop 40 Pol light polarizing microscope. A first-order red tint plate was used to determine the sign of spherulite birefringence under crossed polarizers.



Simultaneous time-resolved SAXS/WAXD experiments were taken at the NCD beamline (BL11) of the Alba synchrotron radiation light facility of Cerdanyola del Valles (Catalunya). The beam was monochromatized to a wavelength of 0.098 nm and the samples were confined between Kapton films. SAXS and WAXD profiles were acquired simultaneously during heating/cooling experiments in time frames of 12 s. Samples were held above fusion for 3 min to erase thermal history before performing the subsequent cooling run. All heating and cooling runs were performed at a rate of 3 ºC/min. Two linear position-sensitive detectors were used: [32] the SAXS detector was calibrated with different orders of diffraction from silver behenate whereas the

WAXD detector was calibrated with diffractions of a standard of an alumina ($Al_2O_3$) sample. The diffraction profiles were normalized to the beam intensity and corrected considering the empty sample background. WAXD peaks were deconvoluted with the PeakFit v4 program by Jandel Scientific Software. The correlation function and corresponding parameters were calculated with the CORFUNC program[33] for Fibre Diffraction / Non-Crystalline Diffraction provided by the Collaborative Computational Project 13.

## III. Results and Discussion

### 1. Synthesis of PE97, PE99 and PE9,7/9-*x* samples

The results summarized in Table 1 indicate that samples could be synthesized with a polydispersity index (PDI) and a molecular weight typical of polycondesation reactions involving two monomers with different functionality (*i.e*. diol and dicarboxylic units). Thus, PDI and $M_n$ ranged from 2.33 to 2.70 and from 7,900 to 13,500 g/mol, respectively. A clear trend for the dependence of molecular weigth with composition was not oberved, although lower molecular sizes were achieved when pimelic acid content in the reaction mixture was higher. In any case, molecular weights were sufficient to ensure film- and fiber-forming properties. Polymerization yields determined after reprecipitation of samples varied in a narrow range (65-78 %); no relationship between yield and monomer feed ratio indicative of a preferred reactivity was observed.



Infrared spectra of all samples synthesized revealed the characteristic absorption bands for methylene (2931-2925 and 2852-2851 $cm^{-1}$), C=O (1731-1729 $cm^{-1}$) and C-O (asymmetric and symmetric stretchings at 1242-1223 and 1171-1167 $cm^{-1}$, respectively). Figure 2a shows a representative spectrum obtained for PE99 homopolymer whereas a detailed summary of absorption bands is given in Table 2 (discussed below).

**Table 1.** Synthesis data of studied polyesters.

| Polymer | Yield (%) | $f_P$ [a] | $M_n$ [b] (g/mol) | $M_w$ [b] (g/mol) | PDI [b,c] |
|---|---|---|---|---|---|
| PE97 | 73 | 1 | 7,900 | 19,600 | 2.47 |
| PE9,7/9-0.85 | 67 | 0.86 | 9,400 | 21,900 | 2.33 |
| PE9,7/9-0.70 | 76 | 0.71 | 9,800 | 23,000 | 2.36 |
| PE9,7/9-0.50 | 78 | 0.53 | 13,500 | 32,300 | 2.40 |
| PE9,7/9-0.30 | 78 | 0.32 | 11,700 | 29,900 | 2.57 |
| PE9,7/9-0.15 | 65 | 0.17 | 12,700 | 31,800 | 2.50 |
| PE99 | 73 | 0 | 13,200 | 40,700 | 3.10 |

[a]Pimelate molar fraction determined from $^{13}$C NMR spectra. [b]From GPC.
[c]Polydispersity index.

**Figure 2.** Characteristic FTIR (a) and $^{1}$H-NMR (b) spectra of PE99.

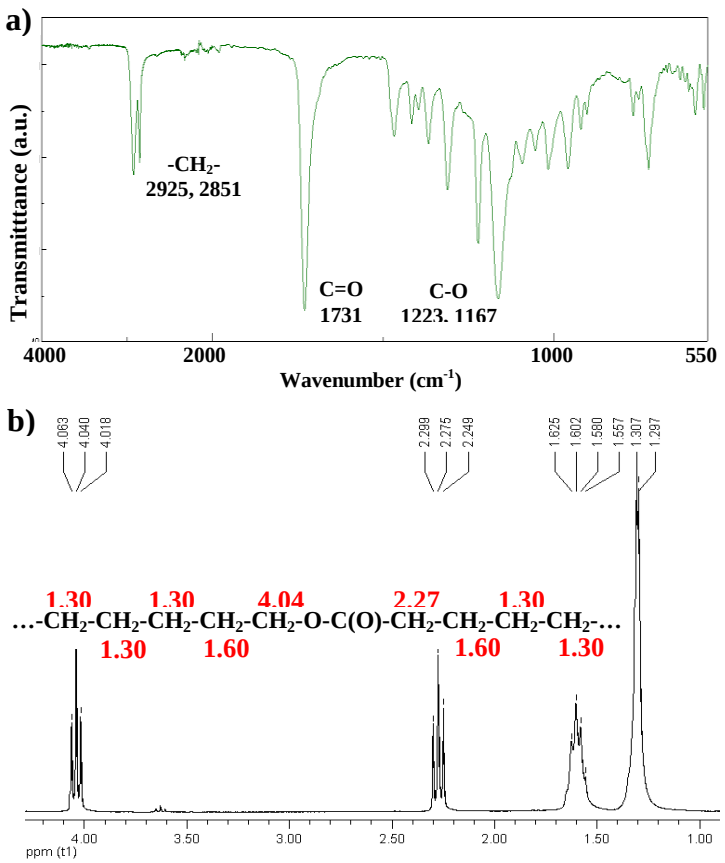

**Table 2.** FTIR transmission bands[a] ($cm^{-1}$) observed in the spectra of PE97, PE99 and PE9,7/9-0.5 taken at temperatures where crystalline (25 ºC) and amorphous (90 ºC) phases were predominant.

| PE97 | | PE99 | | PE9,7/9-0.5 | |
|---|---|---|---|---|---|
| **25 ºC** | **90 ºC** | **25 ºC** | **90 ºC** | **25 ºC** | **90 ºC** |
| 2931 | 2927 | 2925 | 2927 | 2926 | 2928 |
| 2852 | 2856 | 2851 | 2855 | 2851 | 2855 |
| 1729 | 1732 | 1731 | 1732 | 1730 | 1732 |
| 1465 | 1458 | 1466 | 1457 | 1466 | 1458 |
| 1417 | 1412 | 1417 | 1412 | 1417 | 1411 |
| 1398 | **1395** | 1398 | 1395 | 1397 | **1395** |
| **1368** | 1353 | **1363** | **1357** | **1368** | **1353** |
| **1345** | | **1315** | | ***1344, 1312*** | |
| **1242**[b] | **1242**[b] | **1223** | **1240** | ***1242***[b]***, 1224*** | **1240**[b] |
| 1171 | 1167 | 1167 | 1167 | 1169 | 1167 |
| **1091** | **1081** | 1092 | 1089 | 1091 | 1087 |
| | **1065** | 1051 | 1048 | 1051 | |
| **1028** | | **1017** | | ***1024*** | |
| **954** | | **958** | | **956** | |
| **918** | | **921** | | **920** | |
| **838** | | | | **838** | |
| 794 | 790 | | | 798 | 792 |
| 723 | 723 | 722 | 721 | 723 | 723 |

[a]Bold characters indicate the wavenumbers of distinctive bands for crystalline and amorphous phases. Bold and italic characters point out the wavenumbers of interesting bands observed in the crystalline phase of the PE9,7/9-0.5 copolymer.

[b]The band is narrow in the crystalline state whereas appears very broad in the amorphous state.

$^1$H NMR spectra were highly similar for all samples, showing characteristic signals at 4.04 (O-C***H*****$_2$**), 2.27 (C(O)-C***H*****$_2$**), 1.60 (O-C***H*****$_2$**C***H*****$_2$** + C(O)-C***H*****$_2$**C***H*****$_2$**) and 1.30 ppm, as can be seen in Figure 2b for PE99. The relative intensity of the last signal was the only difference between the spectra, as logically deduced from the different number of methylene protons of azelate and pimelate units that contributed to the indicated signal. A small triplet assigned to C***H*****$_2$**OH terminal

groups was the only additional signal detected for PE97, which is the sample with the lowest molecular weight. Note also the good resolution of the $^{1}$H-NMR spectra, as expected for low viscosity media and moderate molecular weight samples. Thus, 4.04 and 2.27 signals always appeared as clear triplets.

$^{13}$C-NMR spectra were more powerful since the vicinal carbons of the dicarboxylate units appeared well differentiated (i.e. 34.29 and 34.10 ppm for azelate and pimelate units, respectively). Figure 3 shows a representative $^{13}$C NMR spectrum with the assignment of the observed signals. The variation in intensity associated with the two kinds of **C**(O)-***C***H$_2$ carbon atoms with copolymer composition is also pointed out. The areas of these two signals were used to determine the pimelate molar fraction:

$$f_P = A_{34.10} / (A_{34.29} + A_{34.10}) \quad (1)$$



**Figure 3.** $^{13}$C-NMR spectra of PE99 showing the assignment of carbon signals. Insets show the signals of the methylene carbons vicinal to the carbonyl group for PE9,7/9-0.15 (up) and PE9,7/9-0.50 (down) copolymers.

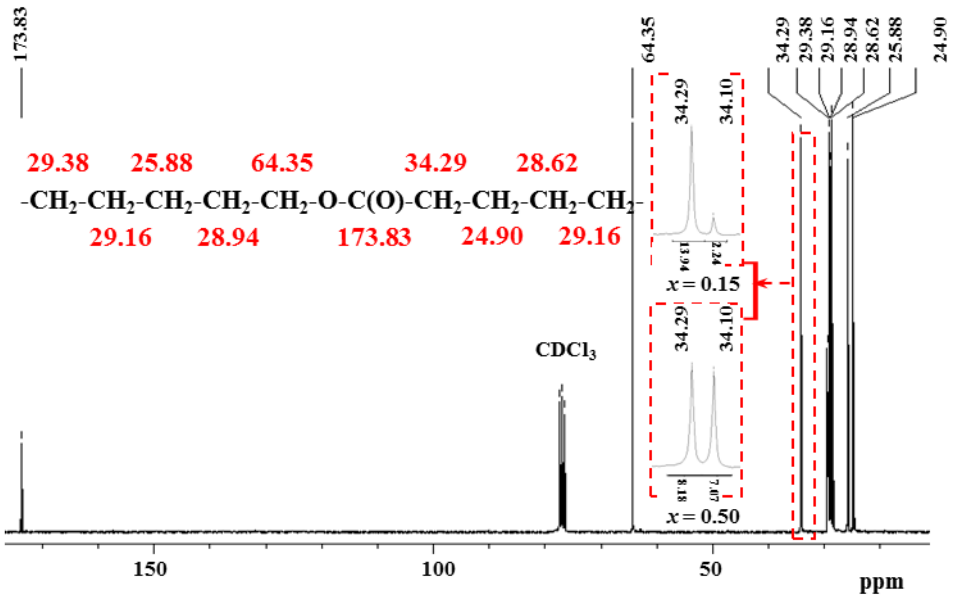

Table 1 show that the experimental composition of all copolymers is in full agreement with the feed monomer ratio.

Unfortunately, both $^{1}H$ and $^{13}C$ NMR spectra were insensitive to triad effects, and consequently no information concerning sequence distribution could be derived. Specifically, the O-C$H_2$ protons were not split in the $^{1}H$ NMR spectra and became insensitive to the two different dicarboxylic units to which the diol could be linked. A triplet was always clearly detected since very few differences were expected due to the large number of aliphatic methylene groups of both azelaic and pimelic units. On the contrary, splitting has been reported when dicarboxylic units of clearly different nature (*i.e.*, aliphatic or aromatic) were used. [34]

## 2. Infrared spectroscopic data of amorphous and crystalline PE97, PE99 and PE9,7/9-0.5 samples



FTIR is highly sensitive to molecular conformation and packing density, hence its usefulness in polymer crystallization studies. Characteristic bands can be correlated to the crystalline and amorphous phases of the bulk, and typically remain distinguishable over the course of crystallization.

FTIR spectra corresponding to semicrystalline and amorphous samples were obtained from the as-synthesized samples at room temperature and at 90 ºC (*i.e.*, about 30 ºC above the melting temperature of each polymer), respectively. Figure 4 compares the characteristic spectra of PE97, PE99 and PE9.7/9-0.5 amorphous and semicrystalline samples, whereas the main absorption bands are summarized in Table 2.

Spectra of amorphous samples were practically identical due to the similar chemical repeat units and also to the similar molecular interactions that should be established in the melt state. Only minor differences were detected in the broad band near 1090-1070 $cm^{-1}$ since it was split in the pimelate rich samples (see asterisk in Figure 4).

Transmission bands generally became broader in the spectra of amorphous samples, and could therefore be distinguished from those associated with crystalline domains, which

appeared at the same wavenumber. This is the case, for example, of the asymmetric stretching bands of the C-O group of PE97, which is observed for both crystalline and amorphous phases at 1242 $cm^{-1}$. On the contrary, a significant wavenumber difference was found for PE99 (*i.e.* 1240 and 1223 $cm^{-1}$). In the amorphous state, this stretching mode appeared at the same wavenumber for both homopolymers whereas a large difference was found in the crystalline state due to a different molecular environment of the ester groups. Bands at 1345-1315, 1028-1017, 954-958 and 921-918 $cm^{-1}$ were also noticeable since appeared in the semicrystalline samples only.

The spectrum of the semicrystalline PE9.7/9-0.5 sample is highly interesting since some bands were split and appeared at the typical wavenumbers of the corresponding homopolymers. Thus, the asymmetric stretching of the C-O group gave rise to two narrow bands at 1242 and 1224 $cm^{-1}$, indicating that two kinds of ester groups exist in the copolymer as a result of different interactions with neighboring chains. Specifically, some ester groups had the same arrangement as the PE97 crystalline structure whereas other groups were arranged according to the PE99 structure. Furthermore, it is qualitatively observed that the intensity of the 1224 $cm^{-1}$ band is clearly greater, and consequently the PE99 arrangement seems to be predominant. The difference on intensities cannot be justified by distinct relative absorption coefficients since both bands appeared with similar intensity in the spectra (not shown) of an equimolar mixture of the two homopolymers.



Similar considerations can be made about the copolymer bands at 1344 and 1312 $cm^{-1}$, which are attributed to deformational $CH_2$ vibrations of polyesters,[35] and are related to those observed at 1345 $cm^{-1}$ and 1315 $cm^{-1}$ in PE97 and PE99 homopolymer spectra, respectively. Again, the higher intensity was found for the band associated with the PE99 structure. Finally, some bands like that at 1024 $cm^{-1}$ and even that at 956 $cm^{-1}$ appeared in the copolymer at an intermediate wavenumber with respect to the homopolymers (i.e. 1028 and 954, and 1017 and 958 $cm^{-1}$ for PE97 and PE99, respectively).

**Figure 4.** Transmitance FTIR spectra (1400-800 $cm^{-1}$) of amorphous (red profiles) and semicrystalline (blue profiles) PE97 (a), PE9,7/9-0.50 (b) and PE99 (c) samples. Boxes highlight characteristic crystalline bands in the spectrum of the copolymer that can be related to each homopolymer (see arrows). Asterisk points to the splitting of the 1090-1070 $cm^{-1}$ amorphous band for the PE97 sample.

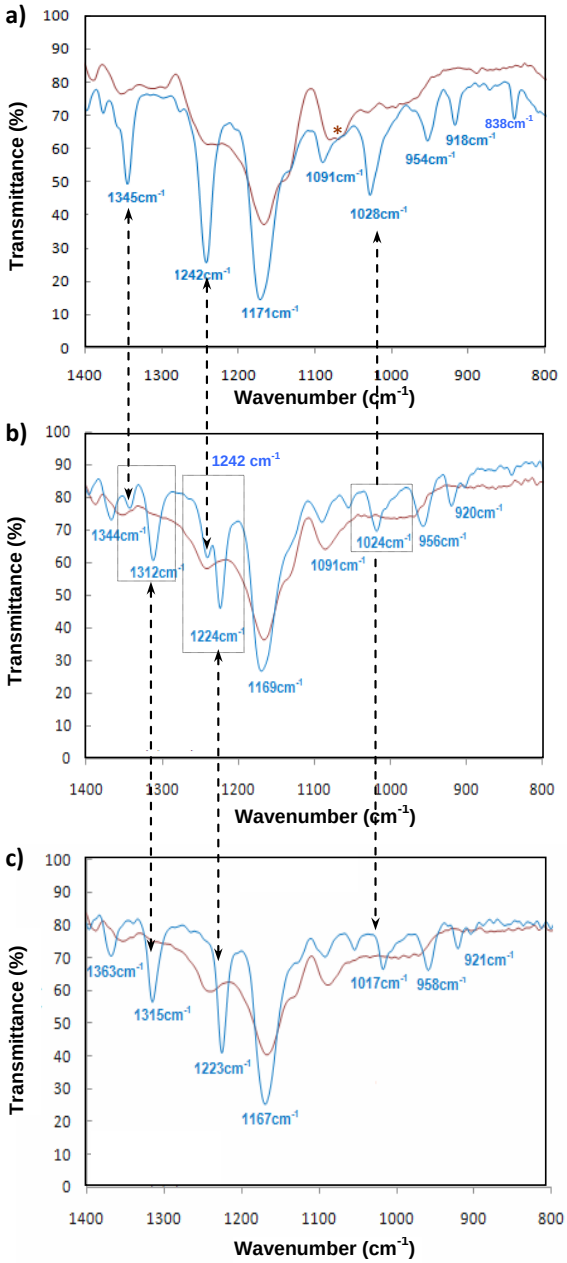

### 3. Calorimetric data of PE97, PE99 and PE9,7/9-*x* samples

Thermal properties of the synthesized sample were determined by the four run protocol depicted in Figure 5 for a representative copolymer. Melt and hot crystallization data, together with glass transition temperatures, are summarized in Table 3 for all samples. Several points merit further discussion:

a) All samples were semicrystalline and showed a single melting peak independent of the crystallization procedure (*i.e.* from solution or from the melt). No multiple melting peaks were observed, and consequently no evidence of distinct crystal populations with different lamellar thicknesses was found.

b) Samples were able to crystallize from the melt state at the maximum rate allowed by the equipment. Thus, no cold crystallization peaks were detected in the heating run of quenched samples, whereas melting peaks were clearly observed (*e.g.* Figure 5d). In addition, these peaks had practically the same enthalpy as those measured at a slow cooling rate for hot crystallized samples (Figure 5b) and even for solution crystallized samples (Figure 5a).



c) The melting temperature of each homopolymer decreased with the comonomer content. The eutectic composition and minimum temperature corresponded to the PE9.7/9-50 sample (Figure 6). In addition, PE99 had a higher melting temperature than PE97, as can be presumed from its higher methylene content.[24]

d) Melting enthalpies of all samples were always high. Thus, azelate and pimelate units were easily incorporated into the PE97 and PE99 crystalline structures, respectively. Despite the small variation, a slight decrease was observed in the melting enthalpy of each homopolymer when comonomer units were incorporated, as shown in Figure 6 for samples crystallized from the melt. The minimum enthalpy was achieved with the PE9,7/9-50 sample and the variation was higher when PE99 was impurified due to its higher enthalpy compared with PE97.

e) Solution crystallized samples always had a higher melting enthalpy than melt crystallized samples. However, a similar dependence of enthalpy upon composition was observed.

f) Non-isothermal crystallization from the melt state required a rather similar degree of supercooling (*e.g.* between 13 and 18 ºC at a cooling rate of 10 ºC/min) for all samples. Thus, the peak crystallization temperature of PE97 was lower than that of PE99 and logically higher than that of copolymers.

g) Glass transition temperatures ranged in a narrow interval (-45 ºC to -60 ºC) for all samples, the lower values corresponding to PE9,7/9-*x* copolymers despite having a higher molecular weight than PE97 homopolymer.

**Figure 5.** DSC traces obtained with the PE9,7/9-0.50 copolymer during the heating run (20 ºC/min) of the as-synthesized sample (a), the cooling run (10 ºC/min) after keeping the sample in the melt state for three minutes (b), the heating run (20 ºC/min) of the hot crystallized sample (c) and the heating run (20 ºC/min) of a sample previously cooled at the maximum rate allowed by the equipment from the melt state (d). The inset shows a magnification where the glass transition is clearly observed.



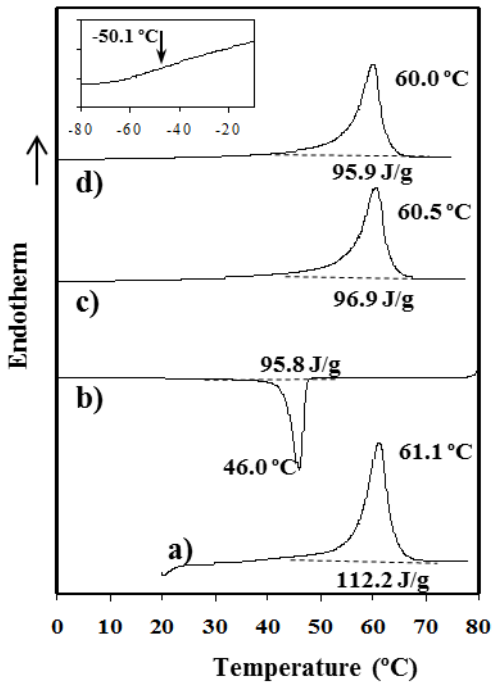

**Table 3.** Calorimetric data of PE9,7/9-*x* samples.

| Sample | 1st Heating scan | | Cooling scan | | 2nd Heating scan | | 3rd Heating scan | | |
|---|---|---|---|---|---|---|---|---|---|
| | $T_f$ (ºC) | $\Delta H_f$ (J/g) | $T_c$ (ºC) | $\Delta H_c$ (J/g) | $T_f$ (ºC) | $\Delta H_f$ (J/g) | $T_g$ (ºC) | $T_f$ (ºC) | $\Delta H_f$ (J/g) |
| PE97 | 65.6 | 121.0 | 50.1 | 106.5 | 64.9 | 107.0 | - 49.6 | 64.9 | 106.1 |
| PE9,7/9-0.85 | 64.4 | 122.6 | 44.9 | 107.0 | 63.5 | 107.5 | - 53.0 | 63.3 | 106.6 |
| PE9,7/9-0.70 | 62.9 | 117.2 | 44.4 | 103.2 | 62.2 | 105.5 | - 60.6 | 61.8 | 103.2 |
| PE9,7/9-0.50 | 61.1 | 112.2 | 45.9 | 95.8 | 60.5 | 96.9 | - 50.1 | 60.0 | 95.9 |
| PE9,7/9-0.30 | 62.4 | 115.7 | 47.8 | 99.0 | 62.5 | 101.5 | - 50.9 | 62.1 | 100.1 |
| PE9,7/9-0.15 | 64.1 | 119.4 | 49.2 | 102.3 | 64.4 | 104.0 | - 54.9 | 64.3 | 102.7 |
| PE99 | 65.7 | 120.2 | 52.6 | 104.4 | 66.6 | 106.0 | - 45.4 | 66.2 | 104.9 |

**Figure 6.** Variation of the melting temperature and enthalpy of poly(nonamethylene azelate-*co*-pimelate)s with the molar percentage of azelate units. Enthalpies are given as kJ/mol considering the molecular weight of the repeat unit determined according to the copolymer composition.



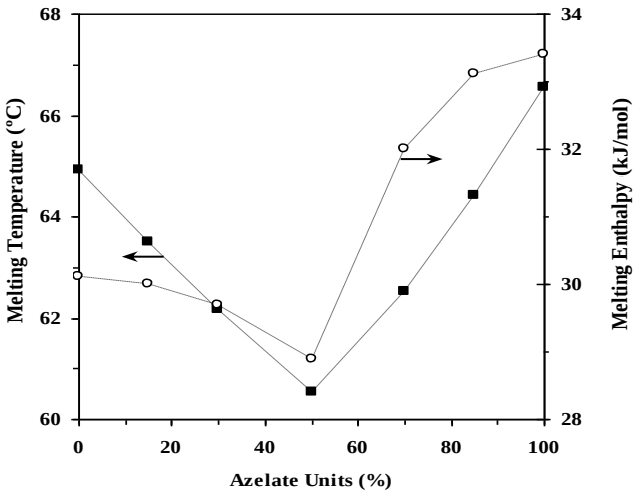

## 4. DSC isothermal crystallization study of PE97, PE99 and PE9,7/9-0.5 samples

Figure 7a shows the DSC exotherms of the PE9,7/9-0.5 sample during crystallization experiments from the melt state at selected temperatures. Peaks logically shifted to higher times and became broader with increasing the crystallization temperature. The time evolution of the relative degree of crystallinity, $\chi(t)$, was determined through the ratio area of the exotherm up to time $t$ divided by the total exotherm area, i.e.:

$$\chi(t) = \int_{t0}^{t} (dH/dt)dt \; / \; \int_{t0}^{\infty} (dH/dt)dt \qquad (2)$$

where d$H$/d$t$ is the heat flow rate and $t_0$ the induction time. A characteristic sigmoidal dependence on time was always found, as plotted in Figure 7a (inset).

Kinetic crystallization data were analyzed assuming the well known Avrami equation[36,37] for primary crystallization:

$$1 - \chi(t) = \exp[-Z\,(t-t_0)^n] \qquad (3)$$

where $Z$ is the temperature-dependent rate constant and $n$ the Avrami exponent whose value varies with the crystallization mechanism. A normalized rate constant, $k = Z^{1/n}$, is usually evaluated for comparison since its dimension (time$^{-1}$) is independent of the value of the Avrami exponent.

Table 4 summarizes the main kinetic parameters of the primary crystallization process of the homopolymers and PE9,7/9-0.5 copolyester, as deduced from the plots of log{-ln[1- $\chi$ ($t$)]} against log ($t$ - $t_0$) (Figure 7b for PE9.7/9-0.5). The values of the Avrami exponent for the hot isothermal crystallizations line in a narrow range, from 2.25 to 2.94, 2.58 being the average value. This suggests a predetermined (heterogeneous) nucleation with spherical growth that occurred under geometric constraints since the theoretical value should be equal to 3. Sporadic

(heterogeneous) and homogeneous nucleation can be clearly discarded as a higher exponent, close to 4, should be derived.

The values of the corresponding reciprocal crystallization half-times ($1/\tau_{1/2}$), calculated as the inverse of the difference between the time at which crystallization begins and the time at which 50% of crystallization is completed, are also summarized in Table 4. This parameter is a direct measure of the crystallization process, and could therefore be used to check the accuracy of the Avrami analysis by comparison with the theoretical kinetic value (i.e., $1/\tau_{1/2} = (Z / \ln 2)^{1/n}$) as reported in Table 4. A similar dependence of $1/\tau_{1/2}$ and the kinetic rate constant on the crystallization temperature for the three polymers can also be inferred from Figure 7c. This Figure also shows that PE99 crystallized faster than PE97 despite having a greater molecular weight and that the lowest overall crystallization rate corresponded to the copolyester, as could be logically expected. It should be pointed out that the three samples required similar supercooling to start crystallization since the melting points of PE99 and the copolyester samples were the highest and the lowest, respectively.



Isothermal crystallizations of the polymers gave rise to samples characterized by a single melting peak which clearly shifted to higher temperatures with increasing crystallization temperature (*e.g.* Figure 8a for the PE9.7/9-0.5 sample). These results clearly reflect the lamellar thickening effect and make it possible to deduce the equilibrium melting temperatures (i.e. those corresponding to an ideal infinite crystal) by the Hoffman-Weeks approach (Figure 8b).[38] Theoretical equilibrium melting temperatures of 79.2 and 74.8 ºC were determined for the PE99 and PE97 homopolymers, respectively. Copolymerization decreased these temperatures according to the comonomer content. Thus, the minimum value corresponded to the PE9,7/9-0.5 sample (*i.e.* 72.8 ºC).

**Figure 7.** (a) Exothermic DSC peaks corresponding to the hot isothermal crystallizations of PE9,7/9-0.50 at temperatures between 54 and 51 ºC. Inset shows the development of relative crystallinity over time for the indicated isothermal crystallizations. (b) Avrami plots corresponding to the isothermal crystallization of PE9,7/9-0.50. (c) Overall crystallization rates (full symbols and solid lines) and the reciprocal of the crystallization half-times (empty symbols and dashed lines) determined at different temperatures for PE99 (○), PE97 (Δ) and PE9,7/9-0.50 (□) samples.

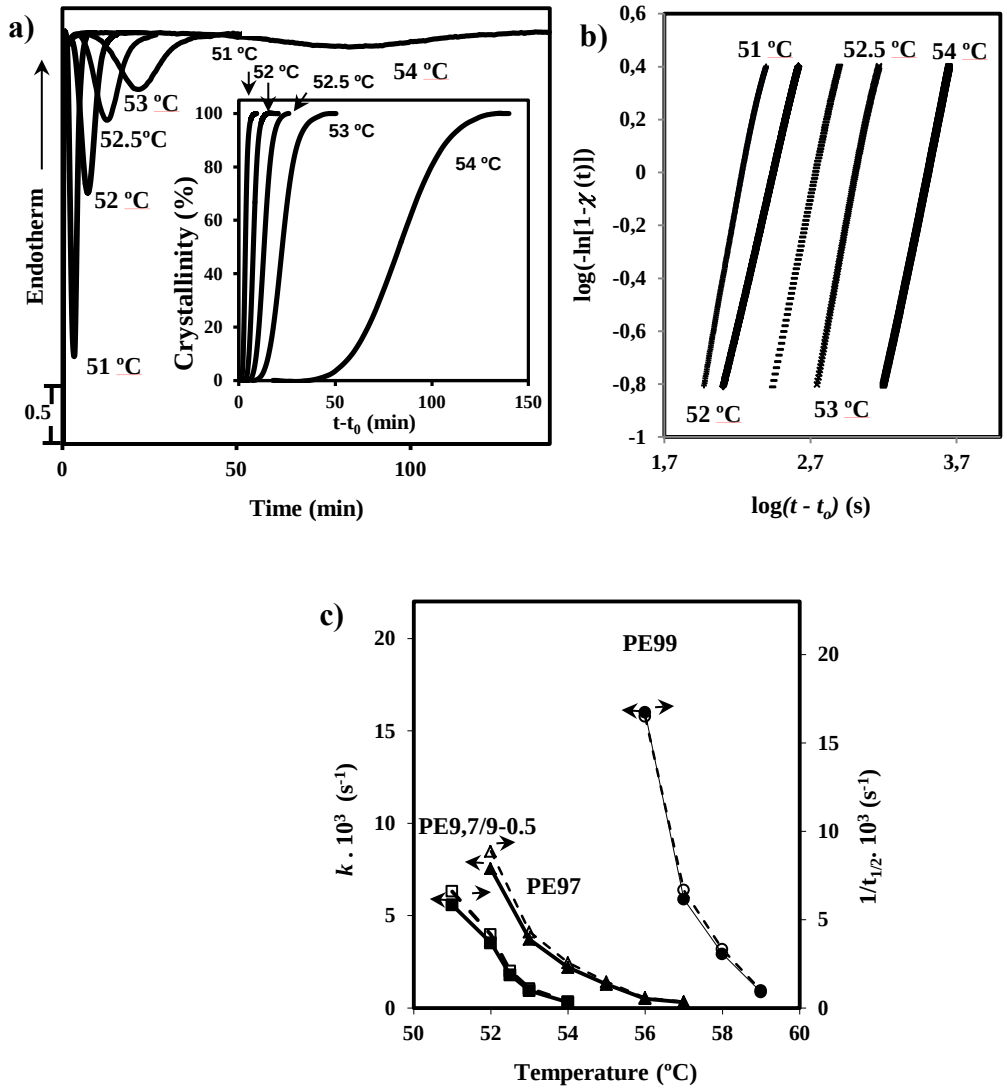

**Table 4.** Main crystallization kinetic parameters determined by DSC for the two homopolymers and the copolymer with the highest comonomer content.

| Sample | $T$ (ºC) | $Z \cdot 10^6$ ($s^{-n}$) | $n$ | $K \cdot 10^3$ ($s^{-1}$) | $1\ \tau_{1/2} \cdot 10^3$ ($s^{-1}$) | $(Z/\ln 2)^{1/n} \cdot 10^3$ ($s^{-1}$) |
|---|---|---|---|---|---|---|
| PE97 | | | | | | |
| | 52 | 8.49 | 2.39 | 7.54 | 8.87 | 8.79 |
| | 53 | 0.34 | 2.66 | 3.71 | 4.30 | 4.26 |
| | 54 | 0.26 | 2.47 | 2.19 | 2.56 | 2.55 |
| | 55 | 0.063 | 2.48 | 1.27 | 1.48 | 1.48 |
| | 56 | $2.21\ 10^{-03}$ | 2.63 | 0.51 | 0.58 | 0.58 |
| | 57 | $8.55\ 10^{-05}$ | 2.88 | 0.32 | 0.35 | 0.35 |
| PE9,7/9-0.50 | | | | | | |
| | 51 | 8.15 | 2.26 | 5.58 | 6.59 | 6.56 |
| | 52 | 2.99 | 2.25 | 3.53 | 4.15 | 4.15 |
| | 52.5 | 0.13 | 2.51 | 1.79 | 2.09 | 2.08 |
| | 53 | 0.025 | 2.51 | 0.94 | 1.10 | 1.09 |
| | 54 | $1.78\ 10^{-04}$ | 2.78 | 0.31 | 0.36 | 0.36 |
| PE99 | | | | | | |
| | 56 | 18.48 | 2.60 | 15.23 | 17.93 | 17.5 |
| | 57 | 0.28 | 2.94 | 5.89 | 6.82 | 6.67 |
| | 58 | 0.077 | 2.81 | 2.92 | 3.31 | 3.32 |
| | 59 | $2.80\ 10^{-03}$ | 2.79 | 0.86 | 0.97 | 0.99 |

**Figure 8.** (a) DSC heating runs (20 ºC/min) of PE9,7/9-0.50 samples isothermally crystallized at temperatures ranging from 54 to 51 ºC. (b) Hoffman-Weeks plot of temperatures corresponding to endothermic melting peaks versus crystallization temperature for several PE9,7/9-*x* samples. For the sake of clarity experimental data of some intermediate compositions are described by dashed lines. Equilibrium melting temperatures are explicitly indicated at the corresponding intersection points.

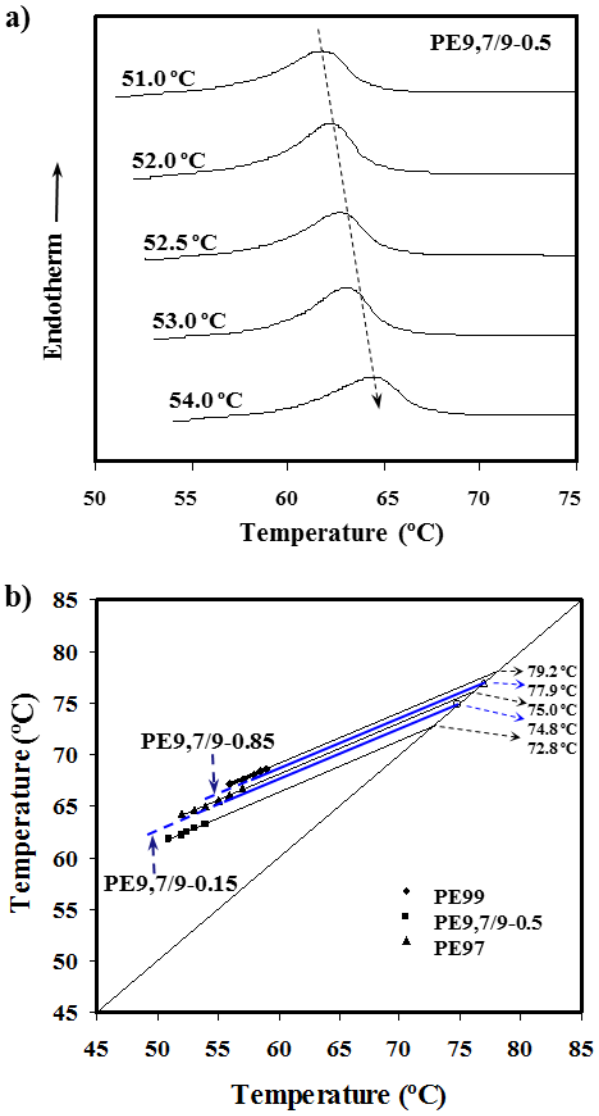

## 5. Optical microscopy crystallization study of PE97, PE99 and PE9,7/9-0.5 samples

All polyester samples crystallized from the melt into spherulites with negative birefringence but different textures (Figures 9a-9c). Ringed spherulites were mainly observed with PE99 over the whole range of tested crystallization temperature whereas fibrillar textures were always observed for PE97. For the sake of completeness, Figure 9d also shows the crystallization of a 50% molar mixture of the two homopolymers, which clearly differentiated from the PE9,7/9-0.5 spherulites depicted in Figure 9b. It should be pointed out that both kinds of spherulites (fibrillar and ringed) were observed in the homopolymer mixture, as expected for an independent crystallization of each polymer. On the contrary, only fibrillar spherulites were observed for the copolymer sample, suggesting that cocrystallization took place, as also deduced from the calorimetric data. It is also worth noting that this copolymer, like PE97, required a high degree of supercooling to crystallize.



Crystallization from the melt of both homopolymers and the representative PE9,7/9-0.5 copolymer was studied by optical microscopy in the range where spherulites with adequate dimensions formed and which varied from 62 ºC to 47 ºC depending on the sample. A larger dimension was obtained at temperatures sufficiently high to have a low nucleation rate compared with the crystal growth rate. This size decreased with the crystallization temperature, the minimum temperature considered for each polymer being that corresponding to a final spherulite radius close to 10 µm.

Spherulite radii grew linearly with time up to impingement within the studied temperature intervals (*e.g.,* Figure 10a for the copolymer) and allowed the calculation of the corresponding growth rates, *G*, displayed in Figure 10b. The maximum *G* values measured were clearly different, the highest corresponding to PE99 (*i.e.* 35 µm/min) and the lowest corresponding to the copolymer (*i.e.* 6 µm/min), as could be presumed.

**Figure 9.** Polarized optical micrographs of spherulites of PE97 (a), PE9,7/9-0.50 (b) and PE99 (c) crystallized at temperatures of 53 ºC, 51 ºC and 59 ºC, respectively. For the sake of completeness, spherulites of a 50% molar mixture of PE97 and PE99 homopolymers and crystallized at 56 ºC are shown in (d).

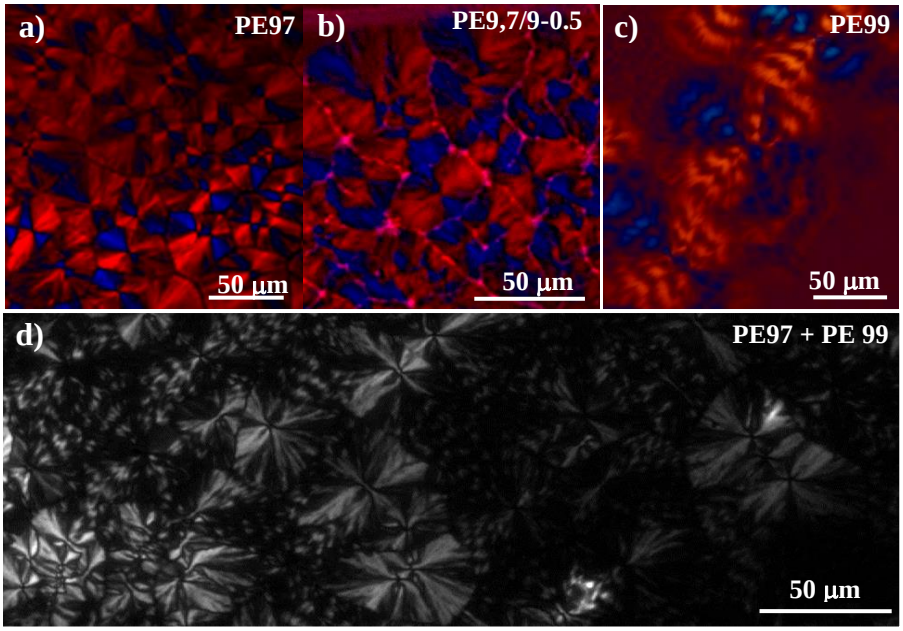




Growth data were then analyzed in terms of crystallization regimes by the mathematical expressions derived from the crystal growth and nucleation model proposed by Lauritzen and Hoffman.[39] It is nevertheless true that the physical meaning of this model may be questioned on account of the new theories based on experimental evidences and different theoretical calculations.[40,41]

The radial growth rate ($G$) of polymer spherulites was thereby calculated by the Hoffman and Lauritzen equation:[39]

$$G = G_0 \exp[-U^*/(R(T_c - T_\infty))] \exp[-K_g/(T_c (\Delta T) f)] \quad (4)$$

where $G_0$ is a constant preexponential factor, $U^*$ represents the activation energy characteristic of the transport of crystallizing segments across the liquid-crystal interface, $T_\infty$ is a hypothetical temperature below which such motion ceases, $T_c$ is the crystallization temperature, $R$ is the gas

constant, $K_g$ is the secondary nucleation parameter, $\Delta T$ is the degree of supercooling measured as $T_m^0$-$T_c$, and $f$ is a correction factor accounting for the variation in the bulk melting enthalpy per unit volume with temperature $(f = 2\ T_c / (T_m^0 + T_c))$.

**Figure 10.** (a) Plots of PE9,7/9-0.50 spherulite radii versus crystallization time for isothermal hot crystallizations performed at temperatures between 50.6 and 53 ºC. (b) Temperature dependence of the crystal growth rate for PE99, PE97 and PE9,7/9-0.50 samples. (c) Change in the nucleation density of PE99, PE97 and PE9,7/9-0.50 samples with isothermal crystallization temperature.

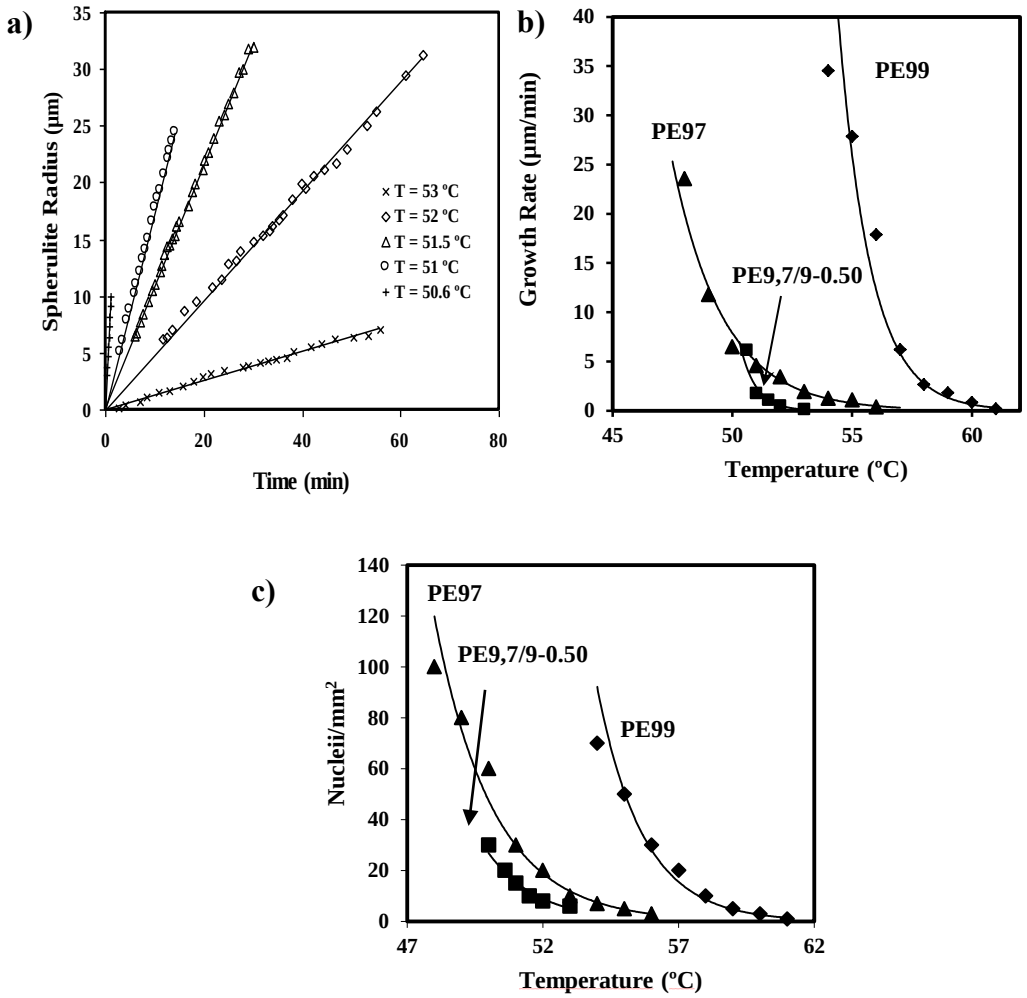

The sets of parameters most commonly used for $U^*$ and $T_\infty$ are those reported by Williams-Landel-Ferry[42] (WLF) ($U^*$ = 4120 cal/mol and $T_\infty = T_g$ - 51.6 K) and Suzuki and Kovacs[43] ($U^*$ = 1500 cal/mol and $T_\infty = T_g$ - 30 K). The plot of ln $G + U^*/R(T_c\text{-}T_\infty)$ versus $1/(T_c\,(\Delta T)\,f)$ for the PE97, PE99 and PE9,7/9-0.5 samples fitted well with a linear regression representative of a single crystallization regime (Figure 11) when the second parameter set was employed. The worst regression coefficient was $r^2$: 0.9934 and the secondary nucleation parameters derived from the slopes of the linear plots of PE97, PE99 and PE9,7/9-0.5 crystallization data 9.29 $10^4$, 1.30 $10^5$, and 2.15 $10^5$ $K^2$, respectively. The highest secondary nucleation constant corresponded to the copolymer, indicating greater difficulty of the lamellar surface in inducing crystallization of incoming polymer chains. Note, also, that the crystal growth rate of PE9,7/9-0.5 became strongly dependent on the crystallization temperature, as shown in the $G$ versus temperature plot (Figure 10b). Nucleation constants were similar for the two homopolymers, although a slightly lower value was deduced for PE97.



**Figure 11.** Plot of ln $G + U^* / R(T_c\text{-}T_\infty)$ versus $1 / T_c\,(\Delta T)\,f$ to determine the $K_g$ nucleation parameter of PE99, PE97 and PE9,7/9-0.50 samples.

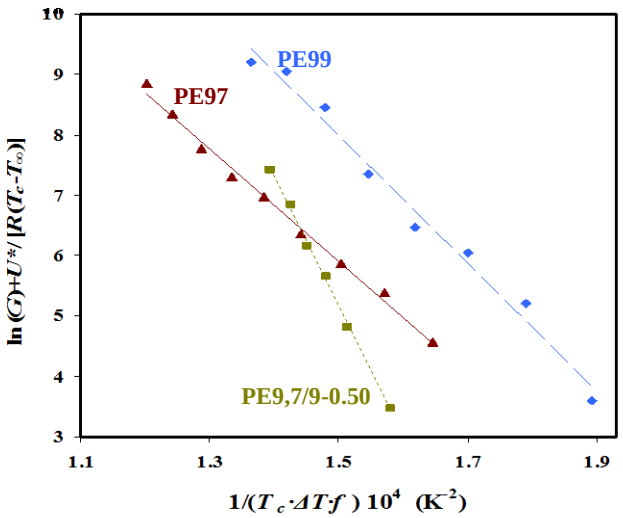

In addition to the crystal growth rate, the overall crystallization of a sample depends on primary nucleation, which may correspond to heterogeneous nuclei or homogeneous nuclei. Primary nucleation is often a rather complex process as it depends on the crystallization temperature, density of heterogeneities and presence/absence of nucleating agents. The number of nuclei slightly increased during crystallization, suggesting a thermal nucleation where all nuclei became progressively active for a given crystallization temperature. A slight degree of heterogeneity in the spherulite size was therefore observed at the end of the crystallization process. Figure 10c shows that the nucleation density increased with decreasing the crystallization temperature for the three samples studied and approached a single exponential dependence, which resulted in more active nuclei (i.e. more favorable thermodynamic conditions for nucleus generation) with progressively decreasing the temperature. The lowest density corresponding to the copolymer, as could be presumed from its lower overall crystallization rate determined from calorimetric data.



## 6. Study on the non-isothermal crystallization of PE97, PE99 and PE9,7/9-0.5 samples by time-resolved SAXS/WAXD experiments

Figure 12 contains time-resolved SAXS and WAXD profiles taken during non-isothermal hot crystallization at a cooling rate of 3 ºC/min for a representative polymer (PE97 homopolymer). In all cases, the SAXS long period peak and crystal diffractions appear simultaneously, as expected for a crystallization process controlled by nucleation and crystal growth.

The SAXS long period peak is clearly seen at a value of the scattering vector, $q = 2\pi\sin\theta / \lambda$, in the 0.28-0.39 $nm^{-1}$ range after subtraction of the empty sample background observed near the beam stop. This peak, which can be attributed to the lamellar structure of the spherulites, appeared at slightly different *q* values depending on the polymer sample and shifted to higher *q* values (*i.e.* lower spacings) during crystallization, showing a more pronounced change in the initial stages.

WAXD profiles showed an amorphous halo ($q$ = 20.3 $nm^{-1}$) whose intensity decreased with crystallization and on which Bragg reflections formed. The most intense appeared at 0.414-0.413 nm ($q$ = 15.18-15.21 $nm^{-1}$) and 0.370 nm ($q$ = 16.98 $nm^{-1}$) and should correspond to the (110) (020) reflections of the typical structure of a polyalkylene dicarboxylate. [20-23] The intensity of the indicated reflections increased sharply at the beginning of crystallization and slowly after a short time interval. This second step corresponds to a secondary crystallization which could also be envisaged from the asymmetric shape of the DSC crystallization peaks (Figure 5b). WAXD profiles of the two homopolymers and the PE9,7/9-0.5 copolymer are compared in Figure 13a. Note that the spacings observed for both homopolymers are practically identical and consequently the similar packing arrangement should enable co-crystallization.

**Figure 12.** Time-resolved SAXS (a) and WAXD (b) three-dimensional profiles of PE97 during non-isothermal hot crystallization at 3 ºC/min.



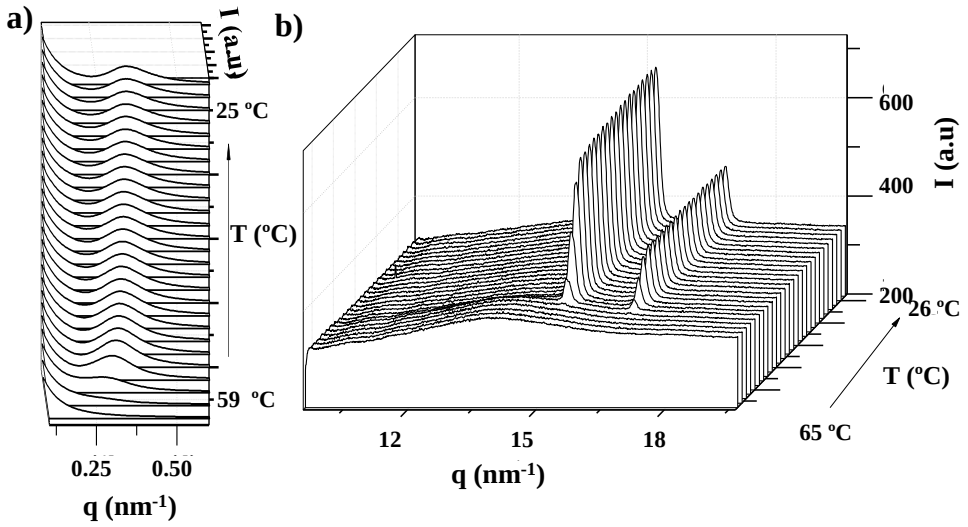

The degree of crystallinity of the three samples could be estimated from the corresponding room temperature profiles by considering the intensity of the amorphous background ($I_B$) and overall intensity ($I_T$):

$$X_c^{WAX} = (I_T - I_B) / I_T \quad (5)$$

WAXD measurements indicated that relative crystallinities ranged between 0.67 and 0.48. The highest and lowest values corresponded to PE99 and the copolymer, respectively, in agreement with DSC calorimetric data and the random disposition of dicarboxylic units. It should also be pointed out that PE97 was slightly less crystalline than PE99 (i.e., 0.68 respect to 0.67) as can be qualitatively deduced from the more intense amorphous halo observed in the WAXD profile (Figure 13a).

SAXS profiles taken at the end of crystallization revealed clear differences between the lamellar thicknesses of the three samples (Figure 13b), the highest and lowest corresponding to PE9,9/7-0.5 and PE97, respectively. SAXS data were analyzed in more detail during crystallization considering the normalized one-dimensional correlation function,[44] $\gamma(r)$, which corresponds to the Fourier transform of the Lorentz-corrected SAXS profile:



$$\gamma(r) = \int_0^\infty q^2 I(q) \cos(qr) dq \; / \; \int_0^\infty q^2 I(q) dq \quad (6)$$

**Figure 13.** WAXD (a) and SAXS (b) profiles of PE99, PE97 and PE9,7/9-0.50 samples taken at room temperature. The amorphous halo obtained by deconvolution is explicitly shown for the copolymer sample.

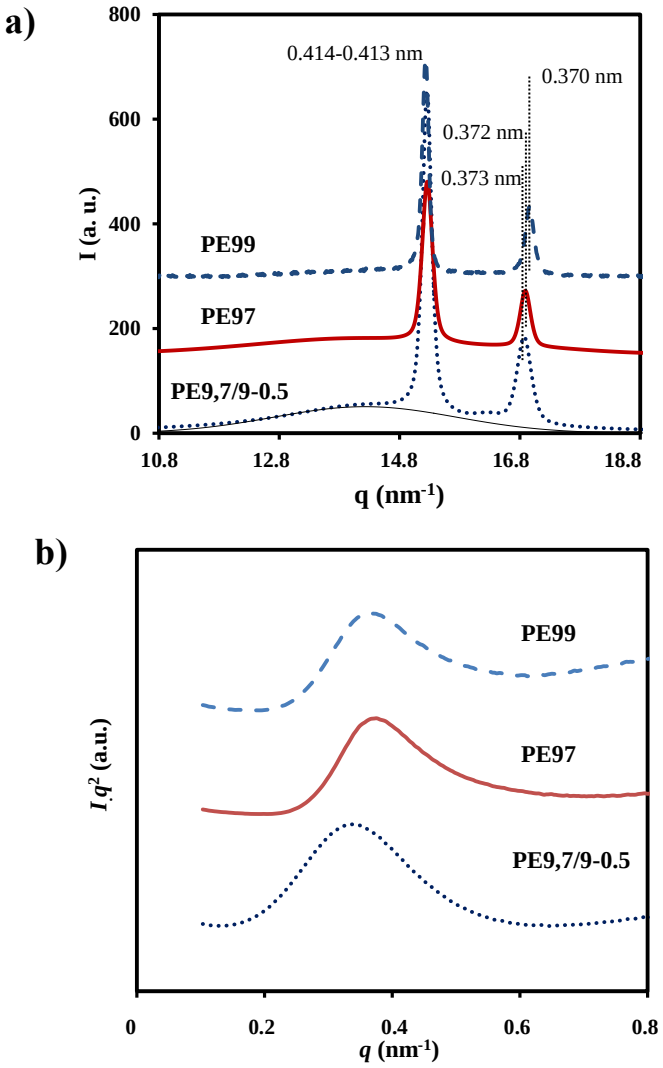


SAXS data were collected within a limited angular range only. That is why extrapolations to low and high *q* values were performed using Vonk's model[45] and Porod's law, respectively.

Figure 14a illustrates the correlation functions calculated for the three samples from SAXS profiles taken at the end of crystallization. In general, their analysis allowed the determination of morphologic parameters like: (1) long period, $L_\gamma$ (i.e. *r* value of the first maximum of the correlation function); (2) amorphous layer thickness, $l_a$, (i.e. *r* value for the intersection of the linear regression in the autocorrelation triangle with the ordinate equal to the first minimum of the correlation function); and (3) crystalline lamellar thickness, $l_c$, (calculated as $L_\gamma$-$l_a$).

The $L_\gamma$ values were in all cases close to the long periods determined from twice the value of the first minimum of the correlation function. Thus, the most probable distance between the centers of gravity of two adjacent crystals appeared to be equal to twice the most probable distance between the centers of gravity of a crystal and its adjacent amorphous layer. This suggests a narrow distribution of the layer widths of the major component, which in this case corresponds to the crystal phase.

Data obtained during the non-isothermal hot crystallization revealed a significant decrease of $L_\gamma$ long spacings at the beginning of the process (i.e. during primary crystallization), although a continuous decrease could still be observed during the secondary crystallization (Figure 14b). These last changes were mainly due to the decrease in the crystalline lamellar thickness, which suggests the occurrence of a lamellar insertion mechanism throughout the crystallization process of the three samples (*i.e.* formation of thinner lamellar crystals between loosely stacked primary lamellae). Note that the amorphous layer thickness remained practically constant during crystallization.



Figure 14b clearly shows that PE99 had the highest and lowest $l_c$ and $l_a$ values, respectively (*i.e.* 11.7 and 4.25 nm). Hence, the highest crystallinity within the lamellar stacks, $X_c^{SAXS}$, (calculated as $l_c$ / $L_\gamma$) was determined for PE99 (*i.e.* 0.74). Crystallinity was clearly lower for PE97 (*i.e.* 0.60), showing a similar trend to that observed from WAXD crystallinities. Both homopolymers have a similar lamellar thickness but clear differences exist between the crystalline lamellar (*i.e.* from 11.7 to 9.36 nm) and amorphous layer (*i.e.* from 4.25 to 6.24 nm) thicknesses. It seems therefore that irregular molecular folds on the lamellar surface should involve larger segments when the polymer is constituted by the slightly more rigid pimelate units.

**Figure 14.** Correlation functions (a) for non-isothermal hot crystallization of PE99, PE97 and PE9,7/9-0.50 samples. (b) Temperature evolution of $L_\gamma$(♦), $l_c$ (▲), and $l_a$ (■) during non-isothermal hot crystallization performed at 3 ºC/min with PE99 (dashed lines), PE97 (solid lines) and PE9,7/9-0.50 (dotted lines) samples.

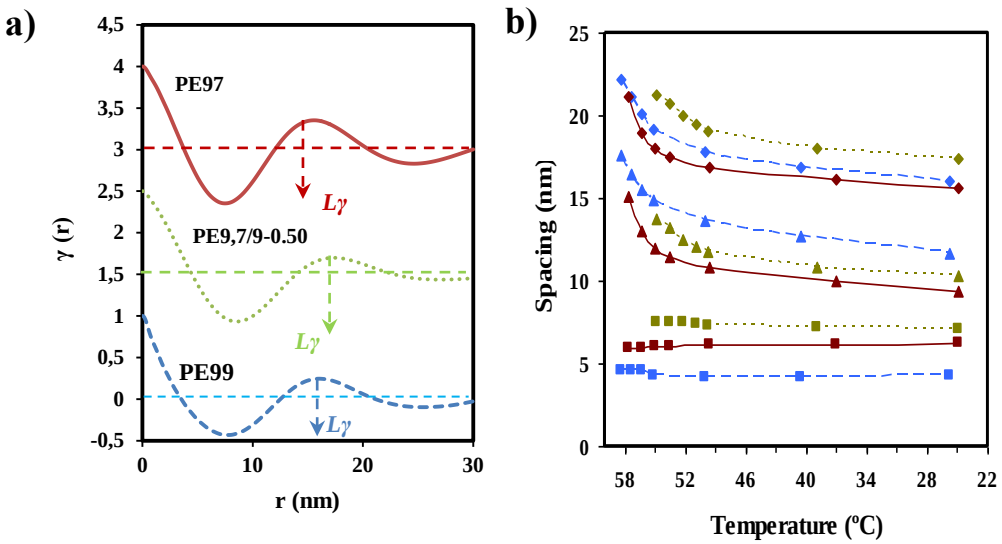




The greatest amorphous layer thickness (*i.e.,* 7.17 nm) was observed for the copolymer, indicating that chain defects caused by the presence of comonomer units could be placed in the amorphous interlamellar regions. $X_c^{SAXS}$ was minimum for the copolymer (*i.e.,* 0.59), although this crystallinity was very similar to that calculated for PE97 due to the lower crystalline lamellar thickness of the homopolymer having pimelate units.

Results point out that crystallization of PE9,7/9-0.5 should start by the arrangement of azelate rich moieties according to the favoured crystallization of PE99 respect to PE97, a feature clearly supported by primary nucleation, crystal growth rate and overall crystallization rate data. Pimelate units seem to be mainly incorporated as defects into the interlamellar amorphous region giving rise to the observed increase in the corresponding spacing. In fact, and as explained above, FTIR spectra revealed also that crystalline bands associated with PE99 were predominant in the copolymer sample.

Combined SAXS and WAXD data were used to verify the assignment of $l_a$ and $l_c$ thicknesses, which could not be distinguished from the analysis of the correlation function.[46-49] Thus, the ratio between $X_c^{WAXD}$ and $X_c^{SAXS}$ is an estimate of the volume-filling fraction of the lamellar stacks, $X_S$, which should be lower than 1 for a correct assignment. For example, ratios of 0.89, 0.96 and 0.82 were determined for PE99, PE97 and PE9,7/9-0.5, respectively, at the end of crystallization.

## VI. Conclusions

Thermal polycondensation using titanium tetrabutoxyde as a catalyst was successfully used to obtain copolyesters constituted by 1,9-nonanediol and different ratios of azelaic and pimelic acid units. Final copolymer compositions were always in good agreement with the feed molar ratio and the attained molecular weights were typical of polycondensation reactions involving monomers with different functionality.



The copolymer with the intermediate composition (i.e. PE9,7/9-0.5) had lowest melting temperature and melting enthalpy. However, the crystallinity of this sample was still high. It seemed possible to incorporate comonomer units into the crystalline structure of each homopolymer.

Homopolymers and copolymers crystallized according to a spherulitic growth and a heterogeneous primary nucleation. Significant differences were found between the spherulitic textures (i.e. fibrilar or ringed) and even on the crystallization kinetics of PE97 and PE99 homopolymers. Specifically, non-isothermal crystallization from the melt was less favourable for the PE97 sample and consequently the PE9,7/9-0.5 copolymer started to crystallize by the arrangement of azelate moieties.

X-ray diffraction data indicated that crystallization always occurred according to a lamellar insertion mechanism. Significant differences were observed between crystal lamellar and amorphous layer thicknesses of homopolymers and the copolymer with intermediate composition. Optical microscopy, DSC, SAXS and FTIR data suggested that this copolymer crystallized, giving

rise to lamellar cores with a predominant PE99 structure, and that pimelate units were mainly located on the amorphous interlamellar regions.

## V. References


1. Lligadas G, Ronda JC, Galià M, Cádiz V. *Biomacromolecules* **2007**;*8*:686.
2. Petrovic ZS. Polym Rev 2008;*48*:109.
3. Hojabri L, Kong X, Narine SS. Biomacromolecules 2010;11:911.
4. Lligadas G, Ronda JC, Galià M, Cádiz V. Biomacromolecules 2010;*11:*2825.
5. Doi Y, Steinbüchel A. Polyesters II – properties and chemical synthesis. New York: Wiley-VCH; 2002.
6. Huang SJ. Encyclopedia of polymer science and engineering. New York: Wiley-Interscience; 1985 pp. 20.
7. Vert M, Li SM, Spenlehauer G, Guerin P. J Mater Sci: Mater Med 1992;3:432.
8. Edlund E, Albertssson A C. J Polym Sci Part A: Polym Chem 1999;37:1877.
9. Kulkarni RK, Moore EG, Hegyeli AF, Leonard F. J Biomed Mater Res 1971;5:169.
10. Kricheldorf HR, Kreiser-Saunders I, Jürgens C, Wolter D. Macromol Symp 1996;103:85.
11. Thombre AG, Cardinal JR. Enciclopedia of Pharmaceutical Technology 2. New York: Marcel Dekker; 1990. pp. 61.
12. Fujimaki T. Polym Degrad Stab 1998;59:209.
13. Lai SM, Huang CK, Shen HF. J Appl Polym Sci 2005;97:257.
14. Fuller CS. J Am Chem Soc 1939;61:2575.
15. Kanamoto T, Tanaka K. J Polym Sci, Part A-2 1971;9:2043.
16. Ueda AS, Chatani Y, Tadokoro H. Polym J 1991;2:387.
17. Aylwin PA, Boyd RH. Polymer 1984;25:323.
18. Liau WB, Boyd RH. Macromolecules 1990;23:1531.
19. Brandrup J, Immergut H. Polymer Handbook. New York: Wiley;1989.
20. Almontassir A, Gestí S, Franco L, Puiggalí J. Macromolecules 2004;37:5300.
21. Gestí S, Almontassir A, Casas MT, Puiggalí J. Polymer 2004;45:8845.
22. Gestí S, Almontassir A, Casas MT, Puiggalí J. Biomacromolecules 2006;7:799.
23. Gestí S, Casas MT, Puiggalí J. Polymer 2007;48:5088–97.
24. Champetier G, Monnerie L. Introduction à la chimie macromoléculaire. Paris: Masson et Cie; 1969.
25. Allegra G, Bassi IW. Adv Polym Sci 1969;6:549.

26. Mochizuki M, Mukai K, Yamada K, Ichise N, Murase S, Iwaya Y. Macromolecules 1997;30:7403.
27. George Z, Papageorgiou, Bikiaris, Dimitrios N. Biomacromolecules 2007;8:2437.
28. Li X, Hong Z, Sun J, Geng Y, Huang Y, An H, et al. J Phys Chem 2009;113:2695.
29. Li X, Sun J, Huang Y, Geng Y, Wang X, Ma Z, et al. Macromolecules 2008;41:3162.
30. Liang Z, Pan P, Zhu B, Dong T, Hua L, Inoue Y. Macromolecules 2010;43:2925.
31. Liang Z, Pan P, Zhu B, Inoue Y. Polymer 2011;52:2667.
32. Rueda DR, García-Gutiérrez MC, Nogales A, Capitán MJ, Ezquerra TA, Labrador A, Fraga E, Beltrán D, Juanhuix J, Herranz JF, Bordas J. Rev Sci Instrum 2006;77.
33. http://www.ccp13.ac.uk/software/program/corfunc/corfunc.htm.
34. Herrera R, Franco L, Rodríguez-Galán A, Puiggalí J. J Polym Sci Part A: Polym Chem 2002;40:4141.
35. Pamula E, Blazewicz M, Paluszkiewicz C, Dobrzynski P. J Mol Struct 2001;596:69.
36. Avrami, M. J Chem Phys 1939;7:1103.
37. Avrami, M. J Chem Phys 1940;8:212.
38. Hoffman JD, Weeks JJ. J Chem Phys 1962;37:1723.
39. Lauritzen JI, Hoffman JD. J Appl Phys 1973;44:4340.
40. Strobl G. Eur Phys J 2000;3:165.
41. Muthukumar M. Eur Phys J 2000;3:199.
42. Williams ML, Landel RF, Ferry JD. J Am Chem Soc 1955;77:3701.
43. Suzuki T, Kovacs A. Polym J 1970;1:82.
44. Vonk CG, Kortleve G Polym 1967;220:19.
45. Vonk CG. J Appl Cryst 1975;8:340.
46. Hsiao BS, Gardner KH, Wu DQ, Chu B. Polymer 1993;34:3986.
47. Ikada Y, Jamshida K, Tsuji H, Hyoan SH. Macromolecules 1987;20:906.
48. Kruger KN, Zachmann HG. Macromolecules 1993;26:5202.
49. Hsiao BS, Wang Z, Yeh F, Yan G, Sheth KC. Polymer 1999;40:3515.

# Chapter 3.2

## *Preferential incorporation of pimelic acid units into the crystalline phase of copoly(alkylene dicarboxylate) derived from 1,9-nonanediol and an equimolar mixture of pimelic and azelaic acids.*

The crystalline structure of two odd, odd polyesters (i.e., poly(nonamethylene pimelate) (PE97) and poly(nonamethylene azelate) (PE99)) has been investigated by means of electron and X-ray diffraction of single crystals and oriented fibers, respectively.

Truncated rhombic crystals were obtained with an aspect ratio that was strongly depended on the supercooling degree. Crystalline lamellae were effectively degraded by lipases, starting the enzymatic attack on the lamellar surfaces. Crystal edges were relatively stable even for annealing processes in the crystallization medium at temperatures close to dissolution. The crystalline structure of both homopolyesters was defined by an orthorhombic $P2_1ab$ space group and a large unit cell containing four molecular segments with an all-trans conformation. Nevertheless, the structure in chain axis projection was equivalent to a simpler cell containing only two segments.

Random copolymers having an equimolar amount of pimelate and azelate units crystallized giving rise to regular lamellae and a molecular arrangement in chain axis projection that was similar to that found for the related homopolymers. The structure of the copolymer was

preferably conditioned by the azelate component but a molecular disorder along the chain axis could also be inferred. The predominant structure of PE99 in the crystalline phase was also corroborated by infrared spectroscopy. Analysis of small angle X-ray scattering pointed out less crystalline lamellae with a higher amorphous thickness for the copolymer respect to the related PE99 homopolymer, probably as a consequence of the preferential incorporation of pimelate comonomer units in the folding surface.

## I. Introduction

Poly(alkylene dicarboxylate)s constitute a family of biodegradable polymers with growing interest since limitations caused by the moderate molecular weight usually attained by conventional thermal polycondensation methods[1] could be overcome by using chain extenders,[2,3] new highly efficient catalysts[4-6] or even ring opening polymerizations.[7,8] Therefore, these polymers are attracting increasing attention to solve "white pollution" concerns caused by traditional non-biodegradable polymers and also for their use as speciality polymers in applications, which mainly involve the biomedical field.[9] Nevertheless, polyesters prepared by ring opening polymerization of lactones (e.g., polyglycolide, polylactide and poly(ε-caprolactone)) are still preferably employed in the last case.

Biodegradable poly(alkylene dicarboxylate)s derived from bio-based monomers have also an additional interest since can reduce the dependence on fossil resources. Typical examples correspond to polyesters having long linear polymethylenic segments and directly prepared from fatty acids coming from plant oils.[10,11] Nevertheless, great efforts are also focused to get bio-based diols and dicarboxilic acids with shorter chain lengths as it is the case of adipic acid, which production could be achieved with engineered yeast strains by α- and/or ω-oxidation of long-chain *n*-alkanes, alcohols or fatty acid substrates.[12] Other well-known examples correspond to pimelic acid that can be obtained by oxidation of ricinoleic acid from castor oil, azelaic acid that can be prepared by ozonolysis cleavage of the alkene double bond of oleic acid and subsequent oxidation and 1,9-nonanediol that can be prepared by reduction of azelaic acid.[13]



Synthesis of copoly(alkylene dicarboxylate)s offers a key opportunity to increase the range of degradable materials and even to get a set of new products with easily tuneable properties. Incorporation of comonomers has a great influence on thermal and mechanical properties, sample crystallinity, and both hydrolitic and enzymatic degradability.[14-16] Noticeable studies refer to random copoly(alkylene dicarboxylate)s constituted by even units, and specifically poly(butylene succinate-*co*-ethylene succinate),[17] poly(hexamethylene succinate-*co*-

hexamethylene adipate),[18] poly(hexamethylene sebacate-*co*-hexamethylene adipate),[19,20] and poly(hexamethylene suberate-*co*-hexamethylene adipate)[21] are representative examples.

Structural studies on poly(alkylene dicarboxylate)s indicate variability on the molecular conformation and also a complex packing arrangement. Kink conformations can be found for example in polymers with a low number of methylene groups (e.g. poly(ethylene succinate)[22] and poly(butylene adipate),[23] whereas an extended conformation is usually postulated for polyesters with long polymethylene sequences.[24,25]

Molecular packing of poly(alkylene dicarboxylate)s may be complex even for those with the simple extended zig-zag conformation. Electron diffraction patterns of such polyesters indicated that the unit cells projected along the chain axis were rectangular and contained only two molecular segments, the parameters being close to $a$ = 0.500–0.504 nm, and $b$ = 0.73–0.75 nm. However, recent works on some 1,4-butanediol[26] and 1,6-hexanediol[27] derivatives have revealed the existence of unit cells where the *b*-axis parameter was doubled. These more complex structures were characterized by the fact that neighbouring molecules along the *b*-axis were only equivalent in chain axis projection. Complex structures were also determined for poly(hexamethylene adipate)[28] and poly(hexamethylne succinate)[29] since the corresponding unit cells contained eight molecular segments. It should be pointed out that most of these structural studies involved diols and dicarboxylic acids with an even number of carbon atoms, whereas few reported data concern to odd-odd polyesters as those involved in the present work.



Degradation of semicrystalline polymers preferably takes place in the amorphous phase but must also occurs in the crystalline phases despite their closely-packed structure. Single lamellar crystals obtained by crystallization from dilute solutions are ideal systems to detect how hydrolytic and/or enzymatic degradation of these crystalline phases takes place. Therefore, extensive studies have been performed with single crystals of different polyesters [30.31] including poly(ethylene succinate),[32] poly(butylene adipate)[33] and poly(octamethylene suberate).[34] In some cases, the enzymatic attack was observed to occur preferentially on determined crystal sectors, suggesting that both molecular packing and the nature of molecular folds play a crucial role in the enzymatic degradation process.[34]

The present work is focused on the study of the crystalline structure of poly(nonamethylene azelate) and poly(nonamethylene pimelate) homopolymers and the related copolymer constituted by an equimolar ratio of the two dicarboxylic units as examples of bio-based odd-odd poly(alkylene dicarboxylate)s. Furthermore, distribution of comonomer units in the crystalline phase of the random copolymer is evaluated as well as the repercussions on the single crystal morphology and the degradation behaviour.

## II. Experimental Section

### 1. Synthesis of poly(alkylene dicarboxylate)s

All reagents and solvents were purchased from Sigma-Aldrich and used without further purification.

Syntheses of poly(nonamethylene pimelate) (PE97), poly(nonamethylene azelate) (PE99), and poly(nonamethylene azelate-*co*-pimelate) (PE9,7/9) were carried out following a typical two-setp polycondensation process (Figure 1). Basically samples were obtained by thermal polycondensation of an excess of 1,9-nonanediol (2.2:1 molar ratio) with azelaic acid, pimelic acid or the equimolar mixture. Titanium tetrabutoxyde was used as a catalyst and the reaction was first performed in a nitrogen atmosphere at 150 ºC for 4 h and then in vacuum at 180 ºC for 18 h. Polymers were purified by precipitation with ethanol of chloroform solutions (10 wt-%). Weight average molecular weights and polydispersity indices determined by GPC and using polymethyl methacrylate standards were 19,600 g/mol and 2.47 for PE97, 40,700 and 3.10 for PE99 and 32,300 and 2.40 for PE9,7/9 and samples.

Composition of the copolymer was corroborated from $^{13}$C-NMR spectra since vicinal carbons of the dicarboxylate units appeared well differentiated (i.e. 34.29 and 34.10 ppm for azelate and pimelate units, respectively). Specifically the molar-% of pimelate units in the copolymer was 53%.

**Figure 1.** Synthesis of PE97 and PE99 homopolyesters and PE9,7/9 copolyester.

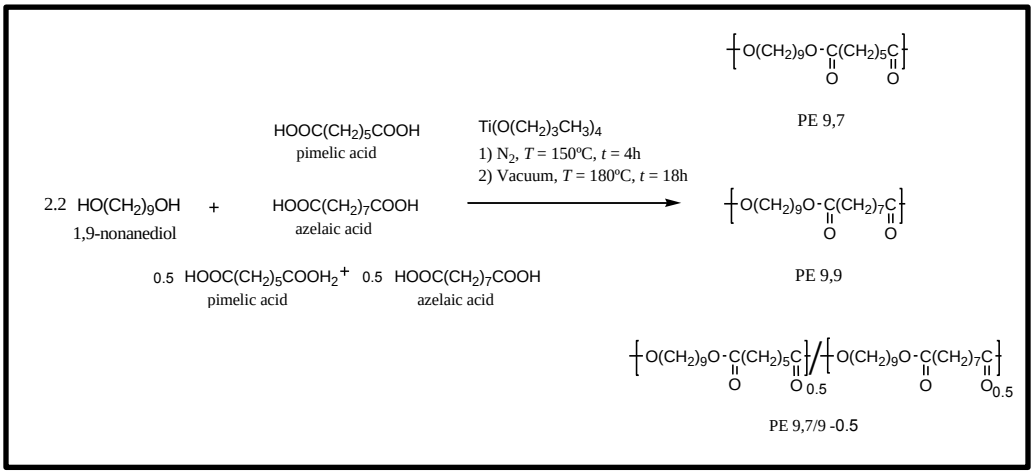


## 2. Measurements Materials



Molecular weights were estimated by GPC using a liquid chromatograph (Shimadzu, model LC-8A) equipped with an Empower computer program (Waters) and a refractive index detector. A PL HFIP gel guard precolumn and PL HFIP gel column (Agilent Technologies Deutschland GmbH) were employed. The polymer was dissolved and eluted in 1,1,1,3,3,3-hexafluoroisopropanol at a flow rate of 0.5 mL/min (injected volume 100 µL, sample concentration 1.5 mg/mL). The number and weight average molecular weights were calculated using polymethyl methacrylate standards.

Infrared absorption spectra were recorded with a Fourier Transform FTIR 4100 Jasco spectrometer in the 4000-600 $cm^{-1}$ range. A Specac model MKII Golden Gate attenuated total reflection (ATR) with a heated Diamond ATR Top-Plate was used. Absorbance measurements were determined from the area of the corresponding peaks after defining the baseline with the software program of the FTIR equipment. In order to avoid overlapping problems, the spectra of

the random copolymer or the mixture of homopolymers were deconvoluted using the PeakFit v4 program by Jandel Scientific Software.

$^{13}$C-NMR spectrum was acquired with a Bruker AMX-300 spectrometer operating at 75.7 MHz. Chemical shifts were calibrated using tetramethylsilane as an internal standard. Deuterated chloroform was used as the solvent.

Calorimetric data were obtained by differential scanning calorimetry with a TA Instruments Q100 series. Experiments were conducted at a heating rate of 20 ºC/min under a flow of dry nitrogen with a sample weight of approximately 10 mg. Calibration was performed with indium.

Lamellar crystals of the studied polyesters were obtained by isothermal crystallization in dilute (0.50–0.25 mg/mL) 1,6-hexanediol solutions at temperatures between 30 and 50 ºC. In all cases, the crystals were recovered from mother liquor by centrifugation, repeatedly washed with *n*-butanol and deposited on carbon-coated grids, which were shadowed with Pt-Carbon at an angle of 15º for bright field observations.



A Philips TECNAI 10 electron microscope was used and operated at 80 and 100 kV for bright field and electron diffraction modes, respectively. Selected area electron diffraction patterns and bright field micrographs were taken with a SIS MegaView digital camera. The diffraction patterns were internally calibrated with gold ($d_{111}$ = 0.235 nm).

X-ray powder diffraction patterns were acquired with a PANalytical X´Pert diffractometer with Cu $K_\alpha$ radiation (λ = 0.1542 nm) and a silicium monocrystal sample holder. Fiber diffraction patterns were collected with Ni-filtered Mo$K_\alpha$ radiation of wavelength 0.0712 nm by a Mar Research 345 image plate detector. Oriented fiber and film samples were obtained by melt drawing.

Experimental fiber densities were calculated by the flotation method using ethanol and carbon tetrachloride as solvents. Values of 1.07, 1.06, and 1.03 g/mL were obtained for PE97, PE99 and PE9,7/9 samples, respectively. Structural simulation was carried out with the diffraction software package of the Cerius2 computer program (Accelrys Inc.).[35]

Polyester single crystals were degraded with lipases from *Rhizopus oryzae* (55.7 units/mg). Grids with deposited lamellar crystals were floated over 30 µL of a pH 7.2 buffered medium of 50 mM Tris-HCl and placed in a humid chamber at 40 ºC for 10 min. Grids were then laid over the degradation medium, which consisted of 30 µL of the above buffered solution containing 2.2 mg/ml of the enzyme, and placed in the chamber under the above conditions for 3h. After digestion, grids were successively washed in a Tris-HCl buffer, distilled water and ethanol. A Pelco pad with 40 concave recesses (diameter of 4.5 mm and depth of 1.5 mm) was used throughout the whole protocol.

SAXS diffraction pattern were taken at the NCD beamline (BL11) of the Alba synchrotron radiation light facility of Cerdanyola del Valles (Catalunya). The beam was monochromatized to a wavelength of 0.098 nm and the samples were confined between Kapton films. Samples were held above fusion for 3 min to erase thermal history before performing a subsequent cooling run at a rate of 3 ºC/min after which SAXS diffraction patterns were taken. The SAXS detector was calibrated with different orders of diffraction from silver behenate. The diffraction profiles were normalized to the beam intensity and corrected considering the empty sample background. The correlation function and corresponding parameters were calculated with the CORFUNC program for Fibre Diffraction / Non-Crystalline Diffraction provided by the Collaborative Computational Project 13.



## III. Results and Discussion

### 1. Morphology of single crystals of PE97, PE99 and PE9,7/9-0.5 samples

Lamellar crystals of both PE97 and PE99 homopolyesters were obtained by isothermal crystallization in dilute diol solutions and a narrow temperature range (i.e., 30-50 ºC). This range was limited due to the relatively low melting point of the considered polyesters (i.e., 65-66ºC) and the degree of supercoiling that was necessary to get feasible nucleation and crystal growth processes. Our best results were specifically attained using 1,6-hexanediol since isolated crystals with large dimensions were predominant in the considered temperature interval for both samples.

Morphology of single crystals was clearly dependent on the crystallization temperature as shown in Figure 2 for PE97. Thus, irregular crystals became predominant at the lowest assayed crystallization temperature (i.e., 30 ºC) as a consequence of a microsectorization derived from the increased instability of the characteristic growth faces (Figure 2a). This feature is typical of high supercoling degrees where the diffusion of molecules to the growth front controls the crystallization process in such a way that lead to the formation of dendrites.[36]

A slight increase of temperature led to highly regular lamellar crystals with a lozenge morphology, being the angle between the most developed growth faces (i.e., the {110} faces as then will be explained) close to 110 º (Figure 2b). In general, slightly truncated multi-layered crystals were observed, being the thickness of each individual layer between 1.0 and 1.3 nm as deduced from the corresponding shadows. Lamellar overgrowths usually emanated from right and left handed helical dislocations, which appeared in a similar ratio as expected from the achiral molecular structure. The face dimension of the basal crystal usually reached a maximum value close to 5 µm. Terrace growths (Figure 2d) were also frequently observed under these experimental conditions, being clearly detected crystallographic coherence between successive layers (i.e., no rotation was observed between crystals that appeared in a crystallographic register).



Isolated and well developed lamellae were frequently found when crystallization temperature was raised to 50 ºC. The lateral habit changed significantly and a close to hexagonal morphology was derived (Figure 2c). Therefore, the length of the truncated faces increased with crystallization temperature although at 50 ºC was still shorter than measured for the {110} faces. Figure 2c shows also that the {110} faces tend to curve (see red arrows) as approached the truncated faces. Nevertheless, an angle close to 122º could be estimated between {110} and the truncated faces if this curvature was neglected.

Crystal growth faces became more irregular and frequent striations appeared on the lamellar surface (Figure 2d) when synthesized polymer samples were non purified by precipitation (i.e., samples contained low molecular weight fractions). Striations highlighted the sectorization of crystals and formed always an angle between 60º and 70º with the {110} growth

faces. The origin of these defects is not clear although they have frequently been reported for different polyesters, deserving explanations based on the aggregation of microcrystals or the existence of different chain-packing states in the crystal.

**Figure 2.** Transmission electron micrographs showing lamellar crystals of PE97 crystallized from 1,6-hexanediol at 30 ºC (a), 40 ºC (b,d) and 50 ºC (c).

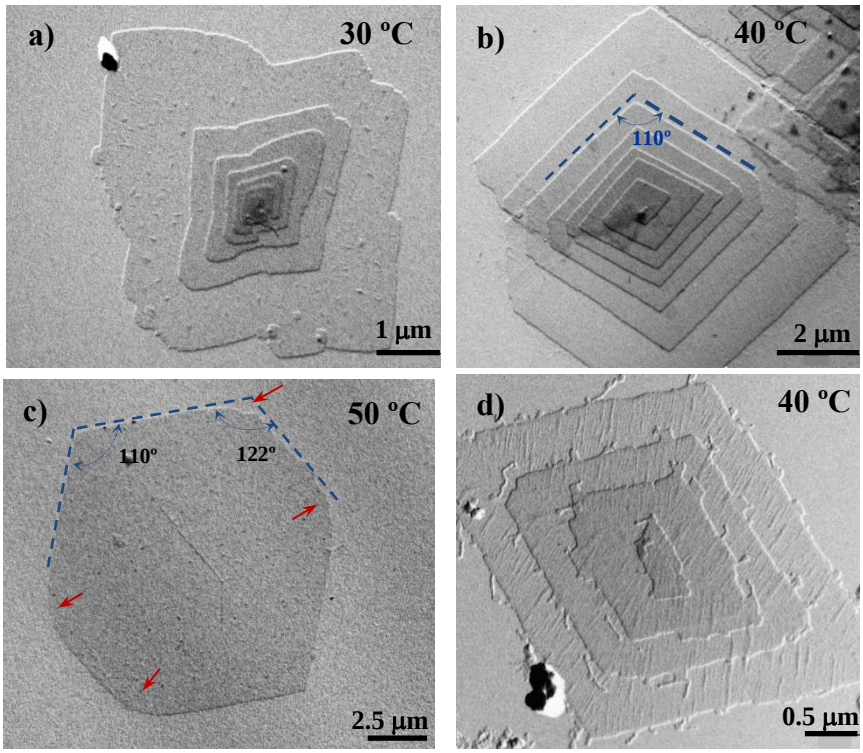




Similar morphologic features were found in the crystallization experiments carried out with PE99 (Figure 3). Angles between the predominant growth faces slightly changed to 112º and 123º as shown in Figure 3a. In general, truncation was favoured for the azelate derivative since the pseudohexagonal morphology was reached at lower temperatures. Note the high similarity between single lamellar crystals obtained at 50 ºC (Figure 2c) and 45 ºC (Figure 3a) with the pimelate and azelate derivatives, respectively. Differences concerning the degree of truncation are clearer when crystals prepared at 40 ºC are compared (Figures 2b and 3b).

Crystals of PE99 showed also typical defects as the presence of striations on the lamellar surface. These according to Figure 3b seems to develop preferentially over the {110} sectors. In addition, the {010} growth faces tend to be serrated when temperature decreased (e.g., down to 35 ºC) contrasting with the more regular growth that can still be detected for the {110} faces. Figure 3c shows the presence of lozenge aggregates (inside the red ellipsoid) with even significantly developed truncated faces. In this case, the serrated morphology was clearly detected (see red arrows) since microsectorization was favoured and the {010} growth face became more instable. Large lamellae with non-well-defined crystalline habit, rounded faces and peculiar edges (e.g., see blue arrows in Figure 3c) were also detected in the different crystallizations.

Results obtained from both homopolymers were in agreement with a decrease on the degree of truncation by decreasing the crystallization temperature (i.e., by increasing the supercooling degree). However, the differences between the single crystal morphology of homopolymers at a given temperature should be caused by a better solvent affinity of poly(nonamethylene azelate) since both homopolymers had a similar melting temperatures (i.e., 65.7 ºC and 65.6 ºC have been determined from DSC experiments for azelate and pimelate derivatives, respectively).



Large single crystals of the random copolyester PE9,7/9 could also be prepared from 1,6-hexanediol dilute solutions despite its high comonomer content (i.e., 47 mol-%). Although melt crystallization of random poly(alkylene dicarboxylate)s have been extensively studied in the last years,[16-22] this is the first time to our knowledge that single crystal morphology of such random copolymers is evaluated. Figure 4a clearly show pseudohexagonal lamellae of PE9,7/9 with identical morphology and dimensions than those crystals corresponding to the two homopolyesters that are shown in Figures 2c and 3a. Note that angles of 110º and 124º could be measured between the characteristic faces of PE9,7/9 single crystals, a slight curvature can be detected in the {010}-{110} face junction (red arrow) and that the ratio between the lengths of these faces (i.e., $d_{\{010\}}$ / $d_{\{110\}}$) was always close to 0.7 as could be also measured for the homopolyesters. It is interesting to note that this morphology was attained for the random

copolymer at a remarkable lower temperature than for the homopolymers (i.e., 37 ºC with respect 45-50 ºC) since it corresponds to a similar supercooling degree. Note that the melting temperature of the copolymer was significantly lower than determined for homopolyesters (i.e., 61.1 ºC with respect 65.6-65.7 ºC). Figure 4b precisely shows that elongated crystals with $d_{\{010\}}$ / $d_{\{110\}}$ equal to 1.6 were typical of PE9,7/9 crystals prepared at 47 ºC, which is in the middle of the temperature range (45-50 ºC) where the above mentioned PE97 and PE99 crystals with $d_{\{010\}}$ / $d_{\{110\}}$ equal to 0.7 were grown (45-50 ºC).

**Figure 3.** Transmission electron micrographs showing lamellar crystals of PE99 crystallized from 1,6-hexanediol at 45 ºC (a), 40 ºC (b) and 35 (d) ºC (c).

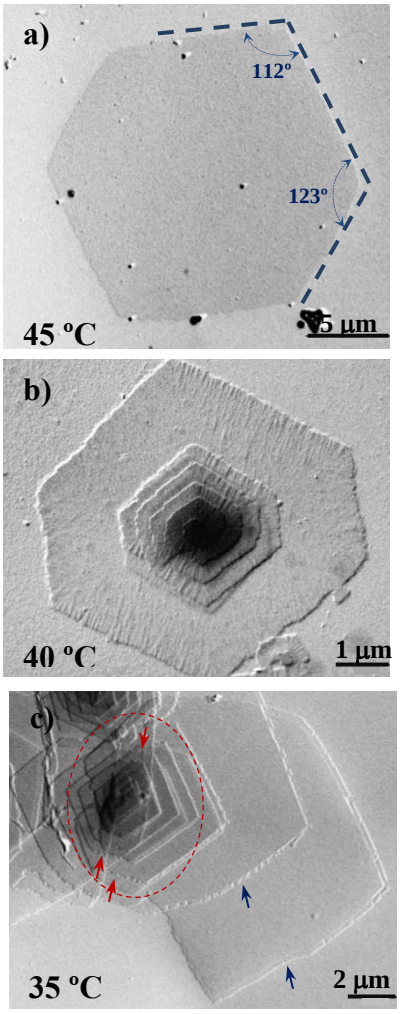

**Figure 4.** Transmission electron micrographs showing lamellar crystals of PE9,7/9 crystallized from 1,6-hexanediol at 37 ºC (a) and 47 ºC (b).

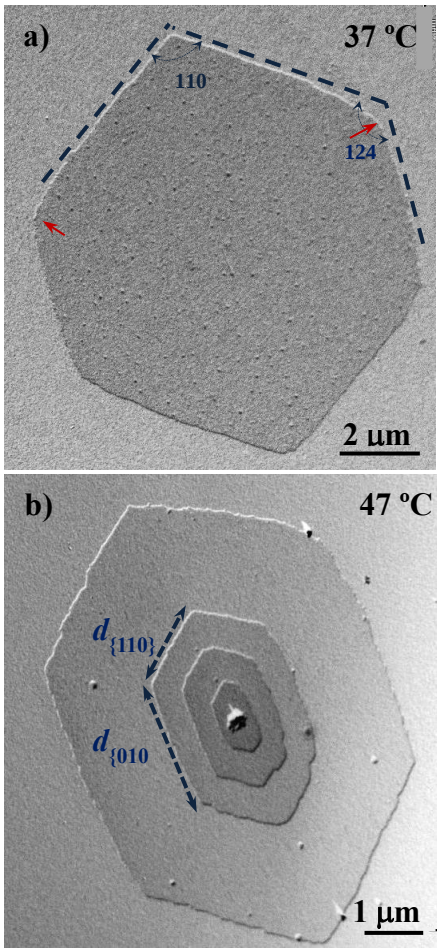




These clear differences between morphologies of copolymer and homopolymer crystals developed at a given temperature support a distinction at a molecular level as expected from random or blocky microstructures. Namely, crystals obtained from PE9,7/9 could not be a simple mixture of PE99 and PE97 crystals since in this case similar morphologies than found with homopolyesters should be observed. On the contrary, PE9,7/9 crystals seem truly derived from a random copolymer and consequently both azelate and pimelate units should be incorporated into lamellae without provoking a significant distortion of crystalline lattice as then will be explained

from diffraction data analysis. Nevertheless, it is possible that azelate and pimelate comonomer units were differently distributed between the lamellar core and the lamellar surface. This observation means that the crystalline part may mainly correspond to one of the two homopolyester structures and therefore the observed regular and well-formed crystals could be better justified. The foreign comonomer units should be in this case preferentially incorporated onto the amorphous lamellar surface despite some proportion could also be found in the dominant crystalline structure.

PE9,7/9 single crystals may also show the typical irregularities previously described for samples of homopolymers as depicted in Figure 5. Note for example that the spiral growth of lamellar crystals shown in the Figure 5a is characterized by the presence of irregular edges and specifically the truncated faces appeared highly serrated as consequence of the above indicated microsectorization. Striations on lamellar surfaces were also frequently observed (Figure 5b). Specifically, they appeared only on the {110} sectors and formed an angle close to 45º with the corresponding growth face. This value differs from the angle detected in PE99 single crystals (Figure 3b), a feature that may suggest a different folding topology. Figure 5b also shows the instability of the {010} growth faces, which appeared again more serrated (blue arrow) or clearly curved (red arrow).



**Figure 5.** Transmission electron micrographs showing lamellar crystals of PE9,7/9 crystallized from 1,6-hexanediol at 37 ºC having highly irregular {010} faces (a) and frequent striations onto the lamellar surface (b).

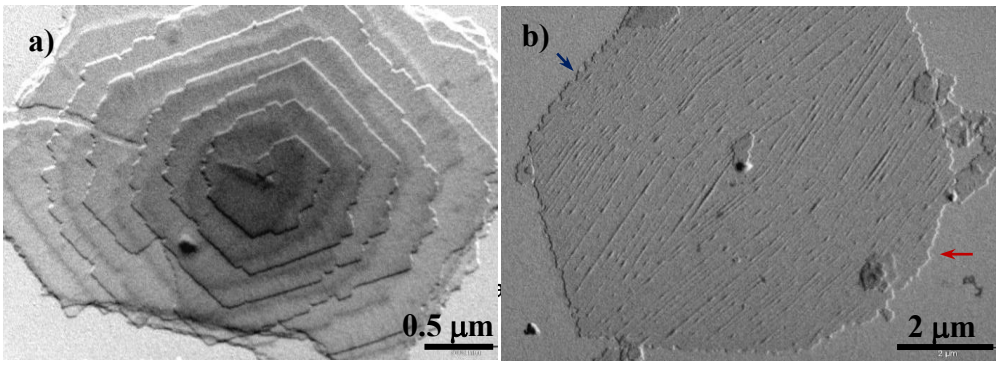

### 2. Electron diffraction data of PE97, PE99 and PE9,7/9-0,5 samples

A single type of electron diffraction (ED) pattern was observed for both homopolyesters and even for the copolyester with similar azelate/pimelate ratio (Figure 6) despite the relatively wide range of assayed crystallization conditions and solvents. Polymorphism must therefore be discarded for the three studied samples. Electron diffraction patterns showed only *hk*0 reflections and pointed out a typical molecular chain orientation perpendicular to the crystal basal plane. Consequently, a molecular folding can be inferred by considering the molecular weight of the samples and the relatively small lamellar thickness deduced from the crystal shadows.

**Figure 6.** *hk*0 electron diffraction pattern of PE97 (a), PE9,7/9 (b) and PE99 (c) lamellar crystals obtained from 1,6-hexanediol solutions at crystallization temperatures of 50 ºC, 37 ºC and 45 ºC for (a), (b) and (c), respectively. Systematic absences are observed for *h*00 and 0*k*0 reflections with odd values for the *h* and *k* indices as shown by the red dashed circles in (a).

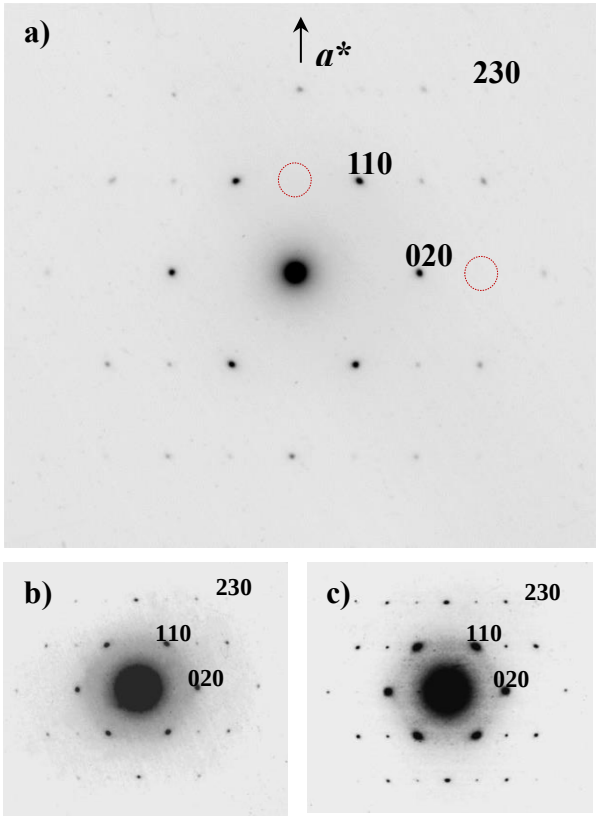

All reflections observed in the ED patterns could always be indexed according to rectangular unit cells (Table 1) with dimensions similar to those of polyethylene and polyesters defined by an all-trans molecular conformation and a unit cell containing only two molecular chains. Thus, *a* and *b* parameters were close to 0.500 and 0.740 nm, respectively. In all cases, the patterns were characterized by systematic *h*00 and 0*k*0 absences for odd *h* and *k* values that indicate the existence of translational symmetry elements.

Correlation of bright field micrographs and selected area electron diffraction patterns indicates that single crystals were bounded by four {110} faces with two truncated {010} faces of variable dimensions, as aforementioned. The {110} growth faces formed angles between 110º and 112º, whereas a value close to 122-124º was measured between the {110} and {010} faces. Both angles are in agreement with those calculated from the dimensions of the planar unit cells (i.e., 112 and 124º).



**Table 1.** Calculated and measured electron diffraction spacings *d* (nm) for PE97, PE99 and PE9,7/9.

| Index[a] | $d_{calc}$ | $d_{measd}$[b] | $d_{measd}$[b] | $d_{measd}$[b] |
|---|---|---|---|---|
| | | **PE 97** | **PE 99** | **PE 9,7/9** |
| 110 | 0.414 | 0.416 vs | 0.413 vs | 0.416 vs |
| 020 | 0.370 | 0.370 vs | 0.370 vs | 0.370 vs |
| 120 | 0.297 | 0.298 w | 0.297 w | 0.298 w |
| 200 | 0.250 | 0.247 m | 0.250 m | 0.247 m |
| 210 | 0.234 | 0.233 vw | 0.237 vw | 0.233 vw |
| 130 | 0.221 | 0.222 m | 0.219 m | 0.222 m |
| 220 | 0.207 | 0.208 w | 0.208 w | 0.208 w |
| 040 | 0.185 | 0.185 w | 0.186 w | 0.185w |
| 230 | 0.176 | 0.176 vw | 0.178 vw | 0.176 vw |
| 310 | 0.163 | 0.162 vw | 0.165 vw | 0.163 vw |

[a] On the basis of rectangular unit cells with parameters: *a* = 0.500 nm and *b* = 0.740 nm.
[b] Abbreviations denote relative intensities: vs, very strong; s, strong; m, medium; w, weak; vw, very weak.

### 3. Annealing and degradation of single crystals

Single crystals of the studied polyesters were obtained at temperatures very close to their dissolution temperature. Thus, solution-grown lamellae suspended in the selected solvent could be annealed in a very restricted temperature range (e.g., 55 ºC for the two homopolyesters and 50 ºC for the copolyester). Figures 7a and 7c show lamellae of PE97, as a representative sample, after being submitted to the indicated annealing process. Interestingly, framed crystals were observed independently of the initial lamellar morphology (i.e., the truncated and pseudohexagonal crystals obtained at 30 ºC and 50 ºC) as a consequence of both a limited thickening that only involved the crystal edges and the complete dissolution of the thinner and inner part of the lamellae. At intermediate annealing times a partial dissolution was produced (Figure 7b) and holes were clearly detected inside the crystals while edges remained logically practically unaltered.

Enzymatic degradation of polymer single crystals can be initiated by a fast attack at the chain folds in the amorphous lamellar surfaces to evolve subsequently at a slower rate when the dense lamellar core is reached. Alternatively or simultaneously, degradation can also be initiated from the crystal edges, leading to a systematic decrease of the crystal size in the lamellar plane. In some cases, lamellar sectors evidenced a different susceptibility to the enzymatic attack, a feature that was related with the existence of distinct chain folds.[34]



Enzymatic degradation of the lamellar crystals was followed in a lipase medium, being observed a similar pattern for the studied copolyester and the two homopolymers. Figure 7c shows the morphology of a representative pseudohexagonal crystal with well-developed {110} and {010} sectors after being exposed for 3 h to the degradation medium. Lamellar edges can be clearly detected despite the crystal was practically fully degraded, a feature that is in agreement with their high stability as was deduced from annealing experiments. Enzymatic attack was therefore initiated in the lamellar surface giving rise the complete dissolution of the inner part of the lamellae at the last stage of degradation. The selected enzyme was able to degrade the close packed crystalline region and furthermore did not show a preferential attack over the {110} or

{010} sectors. In this way, the expected differences in the chain folding on the indicated sectors were not relevant for the studied samples.

**Figure 7.** Transmission electron micrographs showing lamellar crystals of PE97 crystallized from 1,6-hexanediol at 30 ºC (a,b) and 50 ºC (c) after being kept for 3 (a,c) and 2 (b) days in the crystallization media at 55 ºC. Transmission electron micrographs of PE99 lamellar crystals crystallized from 1,6-hexanediol at 45 ºC and exposed for 3 h to the enzymatic degradation medium (d).

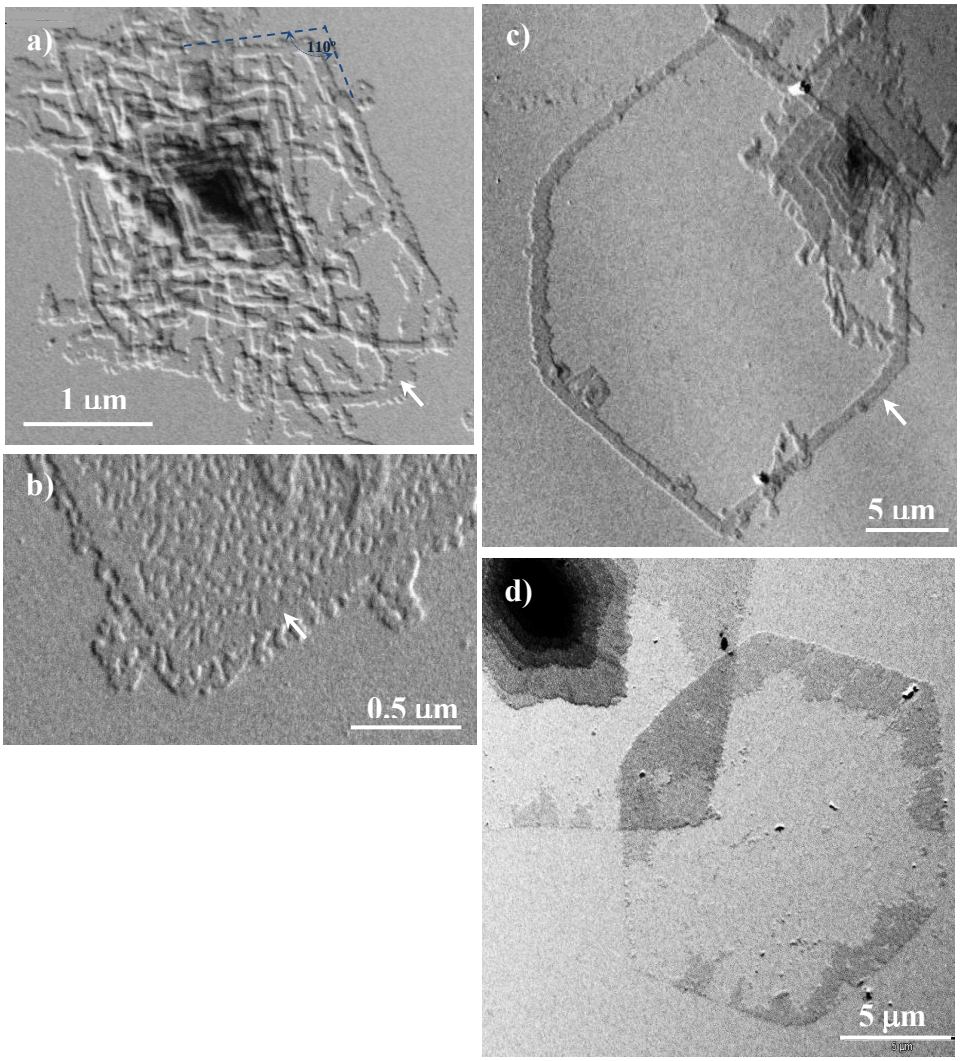

### 4. X-ray fiber diffraction data of PE97, PE99 and PE9,7/9-0.5 samples

X-ray diffraction patterns of annealed fibers of the two homopolymers showed a high degree of orientation (Figure 8). Reflections extended over a considerable number of layer lines and revealed some structural disorder along the chain axis. The weak streaks that can be detected in the different layer lines must be highlighted, although high intense and well defined spots were also characteristic for the 9$^{th}$ and 10$^{th}$ layer lines of PE97 (i.e., (*hk*9) reflections) and PE99 (i.e., (*hk*,10) reflections), respectively. The high intensity of reflections appearing on these layer lines are related to the typical zig-zag nature of polymethylene chains with an extended conformation (i.e., 0.240-0.250 nm should correspond to the layer line spacing). In addition, close to meridional reflections on the 18$^{th}$ and 20$^{th}$ layer lines were also detected with high intensity due to the indicated zig-zag molecular conformation.

Patterns also show also some well-defined meridional reflections that suggest an orthorhombic unit cell. Note the 006 and 008 reflections in the fiber pattern of PE97 (Figure 8a) and the 005 and 007 reflections in the pattern of PE99 (Figure 8b). Spacings of the indicated reflections pointed out chain axis periodicities close to 2.25 and 2.50 nm for the pimelate and azelate derivatives, respectively. These values are in full agreement with an all-trans molecular conformation and a chain axis periodicity that involves only one chemical repeat unit.



Strong *hk*0 equatorial reflections appear at practically the same spacings (Table 2) of those appearing in electron diffraction patterns and consequently conventional polyester orthorhombic unit cells with *a* and *b* parameters close to 0.50 and 0.74 nm, respectively can be postulated. Nevertheless, the streaks and the relatively weak reflections observed in some layer lines (see red circles in Figure 8) suggest a cell with greater dimensions as previously reported for some poly(alkylene dicarboxylate)s.[26-29] Note also that these off meridional reflections can clearly be detected in diffraction patterns recorded from oriented films due to their greater intensity (Figure 9). Specifically, significant reflections that agree with an orthorhombic lattice with a double *b* axis parameter (i.e., 1.48 nm) were detected and consequently the final indexing summarized in Table 2 is based on the larger unit cell. In addition, it should be indicated that

medium-angle equatorial signals with superlattice values have also been reported for other polyester lamellar crystals, being in these cases suggested a rippling nature to the fold surface as a potential explanation.[37,38]

The chain axis projected structures of the two studied odd-odd polyesters are highly similar considering the intensities of hk0 reflections observed in the electron diffraction patterns and in the equator of the X-ray fiber patterns. Note also that the chain axis projection of the smaller (b = 0.74 nm) and the larger unit (b = 1.48 nm) cells should be equivalent.

Reflections detected in the strong 9$^{th}$ and 10$^{th}$ layerlines of PE97 and PE99 showed a remarkable distinctive feature concerning their relative intensities. Thus, (129) and (049) reflections had relatively similar intensities whereas (12,10) reflection was clearly more intense than (04,10) (see arrows in Figure 8).



**Figure 8.** Fiber X-ray diffraction patterns of melt spun PE97 (a) and PE99 (b) fibers.

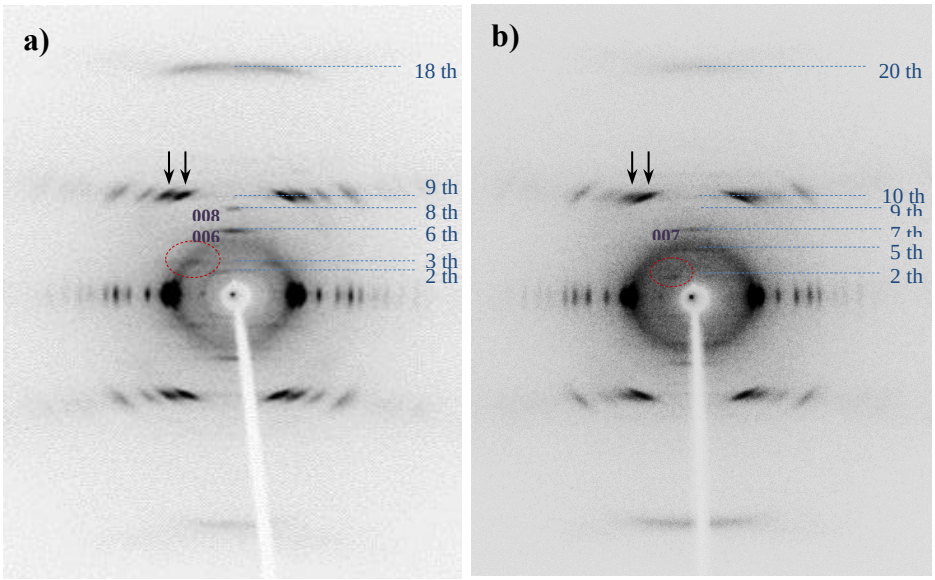

**Table 2.** Calculated and measured fiber X-ray diffraction spacings *d* (nm) for polyesters PE97 and PE99.

| PE97 | | | PE99 | | |
|---|---|---|---|---|---|
| **Index**[a] | $d_{calc}$ | $d_{measd}$[b] | **Index**[c] | $d_{calc}$ | $d_{measd}$[b] |
| 120 | 0.414 | 0.416 vs E | 120 | 0.414 | 0.416 vs |
| 040 | 0.370 | 0.370 vs E | 040 | 0.370 | 0.370 vs |
| 140 | 0.297 | 0.298 w | 140 | 0.297 | 0.298 w |
| 200 | 0.250 | 0.247 m | 200 | 0.250 | 0.247 m |
| 220 | 0.234 | 0.233 vw | 220 | 0.234 | 0.233 vw |
| 160 | 0.221 | 0.222 m | 160 | 0.221 | 0.222 m |
| 240 | 0.207 | 0.208 w | 240 | 0.207 | 0.208 w |
| 080 | 0.185 | 0.185 w | 080 | 0.185 | 0.185w |
| 260 | 0.176 | 0.176 vw | 260 | 0.176 | 0.176 vw |
| 320 | 0.163 | 0.162 vw | 320 | 0.163 | 0.163 vw |
| 006 | 0.375 | 0.373 m | 005 | 0.500 | 0.505 vw |
| 008 | 0.281 | 0.283 w | 007 | 0.357 | 0.357 w |
| 129 | 0.214 | 0.214 s | 12,10 | 0.214 | 0.214 vs |
| 049 | 0.207 | 0.209 s | 04,10 | 0.207 | 0.209 m |
| 149 | 0.191 | 0.192 w | 14,10 | 0.191 | 0.194 vw |
| 229 | 0.172 | 0.170 m | 22,10 | 0.172 | 0.172 m |
| 00,18 | 0.125 | 0.123 m | 00,20 | 0.125 | 0.122 m |

[a]On the basis of rectangular unit cells with parameters: *a* = 0.500 nm, *b* = 1.480 nm and *c* (chain axis) = 2.25 nm.

[b]Abbreviations denote relative intensities and orientations: vs, very strong; s, strong; m, medium; w, weak; vw, very weak; E, equatorial; M, meridional; off M, off meridional.

[c]On the basis of rectangular unit cells with parameters: *a* = 0.500 nm, *b* = 1.480 nm and *c* (chain axis) = 2.50 nm.

**Figure 9.** Fiber X-ray diffraction pattern of an oriented film of PE99 with labelling of significant (01*l*) reflections. The inset corresponds to a low intensity pattern that allows the two strongest equatorial reflections to be distinguished at 0.414 and 0.370 nm.

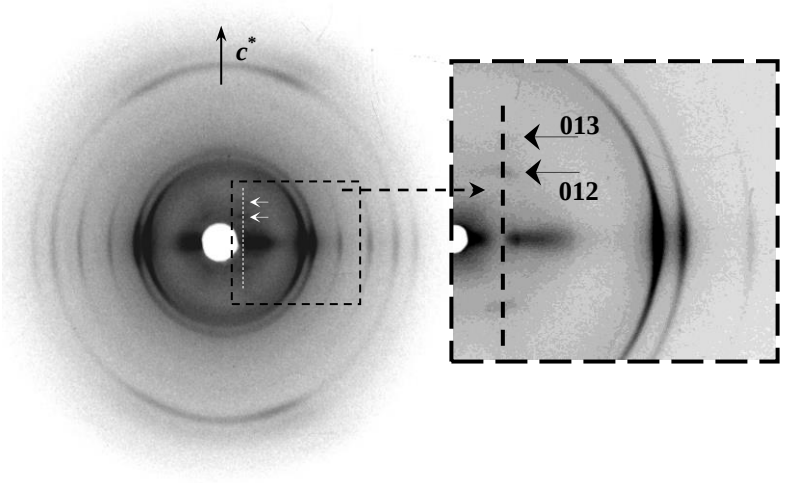




The measured densities of PE97 and PE99 fibers were 1.07 g/mL and 1.06 g/mL, respectively, which were fairly close to the values calculated (1.13 and 1.12 g/mL) from the deduced cell dimensions and a cell content of four chain segments. Nevertheless, some amorphous content logically exists as can be inferred from the lower experimental densities.

Odd-odd polyester molecules displaying an all-trans conformation have a 2*mm* molecular symmetry with binary axes perpendicular to the molecular chain through the middle of diol and dicarboxylic acid units. Only one chemical repeat unit is involved in the chain axis periodicity due to the lack of translational symmetry elements (e.g., $2_1$ screw axis or *c* glide plane). These molecules have all carbonyl groups pointing in the same direction unlike even-even, odd-even and even-odd polyesters. In a rough approximation molecular packing was simulated considering the *hk*0 electron diffraction pattern and the single rectangular unit cell (*b* = 0.74 nm) containing only two molecular segments related by a binary axis and having an all-trans molecular conformation (Figure 10). A relative good agreement between experimental and theoretical intensities was found for a setting angle close to ±50º with respect to the *a* axis.

Fiber diffraction data and the observed systematic absences points out to a large unit cell (*b* = 1.48 nm) and a $P2_1ab$ space group that implies a polar structure and allows to minimize the packing energy by varying the chain axis shift between molecules 1 and 3 (Figure 10a). Note that this feature is not possible with the smaller cell (*b* = 0.74 nm and $P2_1am$ space group) since the indicated chains are not shifted. This restriction also precluded to get a minimum concordance between simulated and experimental diffraction patterns when the small unit cells are considered.

**Figure 10.** (a) Projection along the c-axis of the molecular packing of PE97 defined by a $P2_1ab$ space group. For the sake of completeness the smaller unit cell containing only two molecular segments is also drawn (dotted red lines). Color code: Carbon, grey; oxygen, red; hydrogen, light brown. (b) Simulated *hk*0 electron diffraction pattern for the crystalline structure of PE97 defined by a molecular setting angle of ±50º.

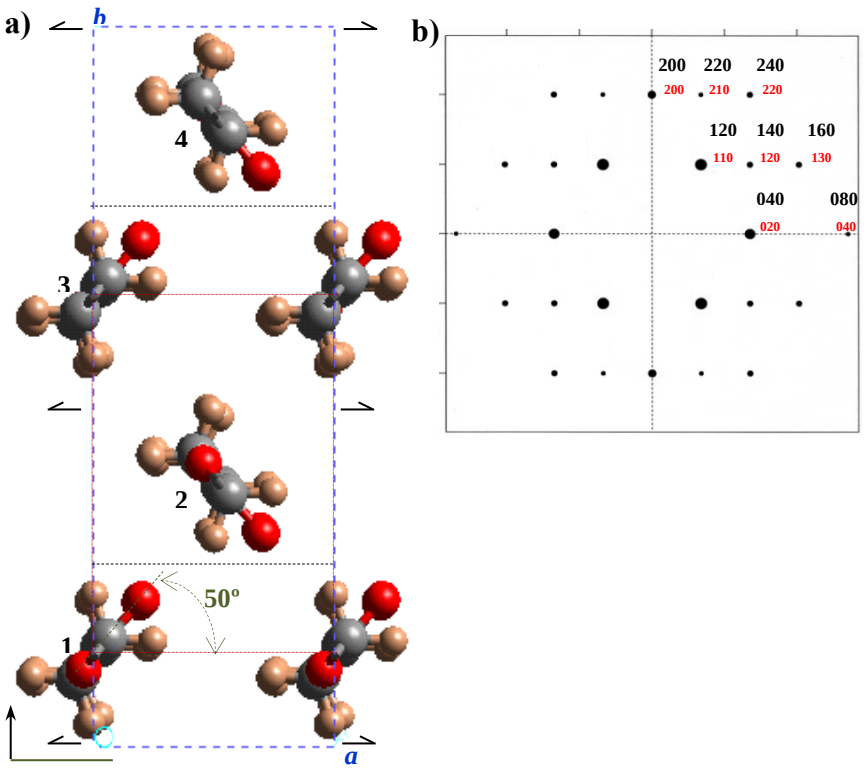

Figure 11 shows the X-ray diffraction pattern of the PE9,7/9 copolymer, being interesting to remark the well-defined *hk*0 reflections that indicate an ordered arrangement in chain axis projection as expected from the regular lamellar crystals and the corresponding electron diffraction patterns. A disorder that concerns the disposition of molecular chains along the *c* axis is also observed since *hk*0 reflections of inner layer lines practically disappeared. Nevertheless, 00*l* weak reflections at spacings of 0.500 nm and 0.375 nm (i.e., at similar values of 005 and 007 reflections of PE99) could be detected suggesting that the copolymer structure was mainly determined by the azelate units. In the same way, the relative intensity between (12*l*) and (04*l*) reflections observed in the $9^{th}$ or $10^{th}$ strongest layerline ($9^{th}$ or $10^{th}$ depending on which was the dominant structure) was closer to that determined for PE99 (i.e., the (04*l*) reflection was much weaker than the (12*l*) reflection).

**Figure 11.** Fiber X-ray diffraction patterns of a melt spun PE9,7/9 fiber.



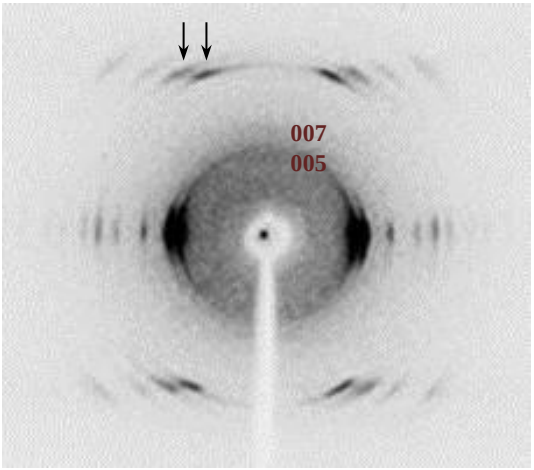


### 5. FTIR spectroscopic data of PE97, PE99 and PE9,7/9 samples

The random copolyester PE9,7/9 easily crystallizes from the melt sate, as revealed by the oriented fiber patterns, and also from dilute solutions giving rise as above explained to highly

regular lamellar crystals. Diffraction data points towards a predominant crystalline structure defined by the azelate units, but results are no fully conclusive. Therefore, FTIR spectra were recorded since well differentiated bands could be associated to the crystalline structure of each homopolyester (Figure 12).

The spectra of all samples was characterized by the very strong stretching band of the C=O group at 1728 $cm^{-1}$ that appeared in both semicrystalline and completely amorphous samples (i.e., in the spectra recorded at a temperature higher than the polymer melting point). However, the spectra of lamellar crystal samples of PE97 and PE99 have some distinctive and isolated bands that are only associated to crystalline domains and appear at different wavenumbers for each homopolymer. Thus, the 1345 and 1240 $cm^{-1}$ bands seem characteristic of the pimelate derivative, whereas 1312 and 1223 $cm^{-1}$ bands are characteristic of the azelate derivative. For example, the asymmetric stretching band of the C-O group seems clearly susceptible to small changes on the intermolecular interactions between neighbouring chains (namely on slight differences between crystalline structure of both polyesters) and specifically varied from 1240 to 1223 $cm^{-1}$. Absorbance ratios between the characteristic crystalline bands and the common band at 1728 $cm^{-1}$ can be taken for further quantitative analyses. Thus, values of 0.15 and 0.30 were found for $A_{1345}/A_{1728}$ and $A_{1240}/A_{1728}$ ratios in the PE97 spectrum, whereas values of 0.21 and 0.24 were determined for $A_{1312}/A_{1728}$ and $A_{1223}/A_{1728}$ ratios in the PE99 spectrum. The indicated four crystalline bands were observed in the spectrum of the copolymer sample but PE99 signals were more intense than expected for a crystalline sample having an equal content of azelate and pimelate units as can be verified by comparison with the experimental spectrum of a mixture having a 50 mol-% of both homopolymers (Figure 12) and also from the values determined for the above indicated absorbance ratios. Thus, ratios involving PE97 and PE99 bands were smaller and greater, respectively than half the corresponding values determined for the homopolyesters. Specifically, $A_{1345}/A_{1728}$ and $A_{1240}/A_{1728}$ ratios were 0.055 and 0.11 (i.e. smaller than 0.15/2 and 0.30/2, respectively) and $A_{1312}/A_{1728}$ and $A_{1223}/A_{1728}$ ratios were 0.14 and 0.17 (i.e. greater than 0.21/2 and 0.24/2, respectively). These observations clearly points out that the lamellar core of the copolymer sample was predominantly constituted

by azelate units (i.e. 65 mol-% instead of the theoretical value of 50 mol-%) and that probably the pimelate units were mainly excluded into the amorphous lamellar surface.

**Figure 12.** Absorbance FTIR spectra (1800-1000 $cm^{-1}$ region) of PE9,7/9. Insets compare the common C=O band at 1728 $cm^{-1}$ (left), the characteristic bands for azelate and pimelate derivatives at 1345 $cm^{-1}$ and 1312 $cm^{-1}$ (medium) and the characteristic bands at 1240 $cm^{-1}$ and 1223 $cm^{-1}$ (right) for pimelate and azelate derivatives. Absorbance scale has been increased in the medium and right insets in order to show more clearly the different peaks. Profiles correspond to PE97 (red), PE99 (green), PE9,7/9 (black) and an equimolar mixture of PE97 and PE99 (blue).

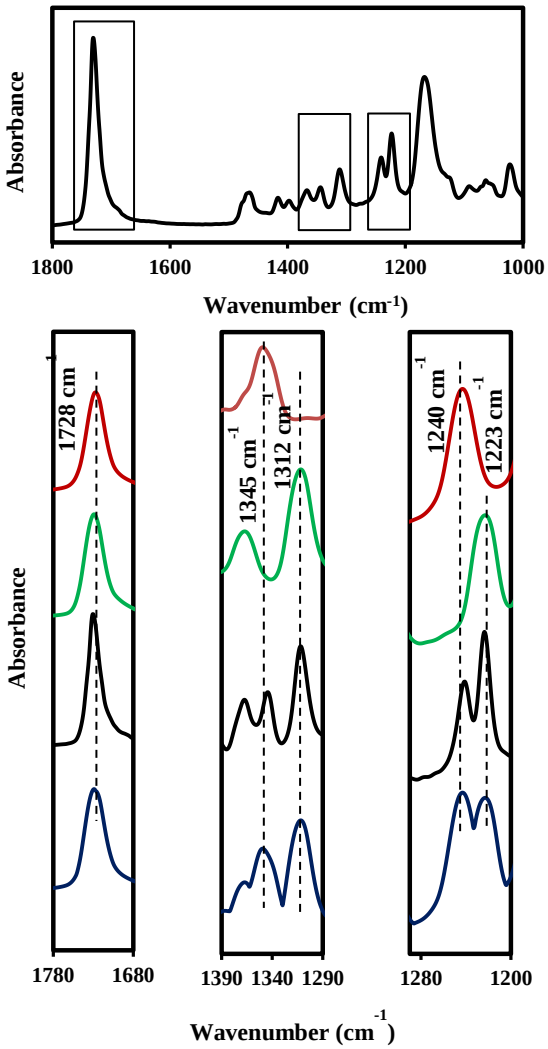

## 6. SAXS data and analysis of correlation function of PE97, PE99 and PE9,7/9 samples crystallized from the melt state

In order to get insight into the lamellar structure SAXS peaks were analysed by means of the correlation function that allowed distinguishing morphologic parameters like: a) long period, $L\gamma$, b) amorphous layer thickness, $l_a$, and c) crystalline lamellar thickness, $l_c$, (calculated as $L\gamma$-$l_a$). Thefore, lamellar structure of polymers non-isothermally crystallized from the melt state at a cooling rate of 3 ºC/min was analysed from the SAXS profiles taken at room temperature (Figure 13a).

The SAXS long period peak is clearly seen at a value of the scattering vector, $q = 2\pi \sin\theta / \lambda$, in the 0.35-0.38 $nm^{-1}$ range after subtraction of the empty sample background observed near the beam stop. This peak, which can be attributed to the lamellar structure of the spherulites, revealed clear differences between the lamellar thicknesses of the three samples, the highest and lowest values corresponding to PE9,9/7 and PE97, respectively.



Normalized one-dimensional correlation function,[41] $\gamma(r)$, was calculated from equation 1 and considering extrapolations to low and high $q$ values by using Vonk's model[42] and Porod's law, respectively.

$$\gamma(r) = \int_0^\infty q^2 I(q)\cos(qr)dq \; / \; \int_0^\infty q^2 I(q)dq \qquad (1)$$

Correlation functions calculated for the three samples from SAXS profiles are shown in Figure 13b. In all cases, the $r$ values of the first maximum, $L\gamma$, were close to twice the value of the first minimum, suggesting a narrow distribution of the layer widths of the major component (i.e., the crystal phase). Clear differences were found in the long period values between the copolymer (17.50 nm) and the two homopolymers (15.95 and 15.60 nm for PE99 and PE97, respectively).

Analyses of correlation function allows also verifying that changes on the amorphous layer thickness were more significant, Specifically, 7.17, 6.24 and 4.25 nm were calculated for PE9,7/9, PE97 and PE99 samples, respectively. Crystallization of PE97 and PE99

homopolymers was also characterized by well differentiated $l_c$ and $l_a$ values despite crystals had similar long periods. In particular, higher and lower $l_c$ and $l_a$ thicknesses were determined for PE99 (i.e., 11.7 and 4.25 nm), which means a considerably higher crystallinity within the lamellar stacks. These crystallinities, $X_c^{SAX}$, can be calculated as $l_c / L\gamma$ and results 0.74 and 0.60 for PE99 and PE97, respectively. It seems therefore that irregular molecular folds on the lamellar surface should involve larger segments when the polymer is constituted by the slightly more rigid pimelate units.

**Figure 13.** SAXS profiles (a) and corresponding correlation functions (b) for non-isothermally crystalized PE97, PE99 and PE9,7/9 samples.

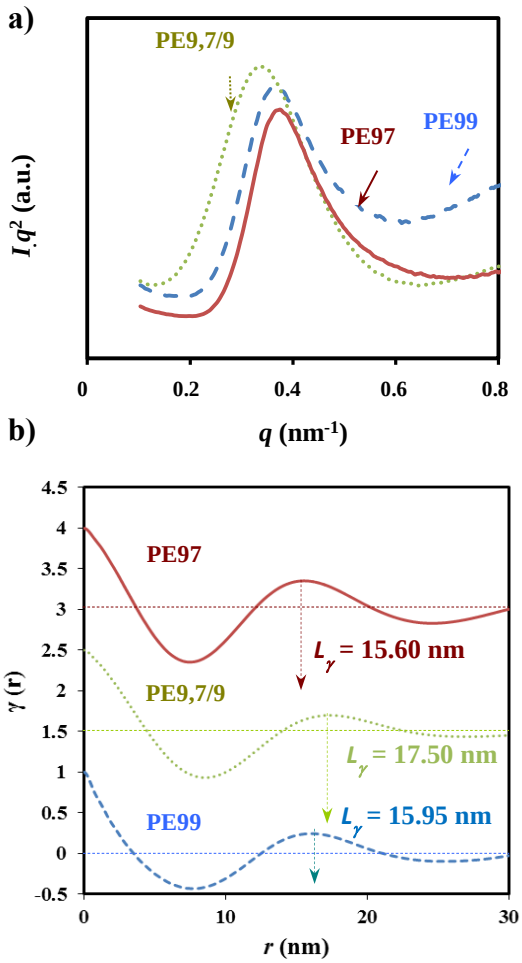

The greatest amorphous layer thickness was observed for the copolymer, indicating that chain defects caused by the presence of comonomer units could be placed in the amorphous interlamellar regions. Similar $X_c^{SAXS}$ values were found for PE97 and PE9,7/9 samples (i.e. 0.60 and 0.59, respectively) since the difference between the amorphous layer thickness was compensated by the lower crystalline lamellar thickness of the homopolymer. Results suggest that crystallization of PE9,7/9 should start by the arrangement of azelate rich moieties and therefore pimelate units seem to be mainly incorporated as defects into the interlamellar amorphous region giving rise to the observed increase in the corresponding spacing. In fact, and as explained above, FTIR spectra revealed also that crystalline bands associated with PE99 were predominant in the copolymer sample.

## VI. Conclusions

Poly(nonamethylene pimelate) and poly(nonamethylene azelate) crystallize according to an orthorhombic $P2_1ab$ space group and unit cells with parameters $a$ = 0.500 nm, $b$ = 1.480 nm and $c$ (chain axis) = 2.25 or 2.50 nm. Molecules adopt an all-trans conformation and the packing is defined by a setting angle respect to the $a$ axis close to ±50º. Morphology of lamellar crystals is variable and specifically the aspect ratio increases as the degree of supercooling decreases.



Copolymers having an equimolar ratio of pimelic and azelaic units are able to crystallize giving rise to well-formed lamellae and a molecular packing similar to that found in the related homopolymers. Nevertheless, a slight disorder along the chain axis can be deduced from the poorer X-ray fiber diffraction patterns. In any case, the crystalline phase of the copolymer is mainly constituted by azelate units as could be deduced from both X-ray diffraction data and FTIR spectroscopy. Pimelate units are on the contrary mainly located in the lamellar folding surface giving rise to an increase of both the lamellar long period and the amorphous layer thickness as well as a significant decrease on the crystallinity of the lamellar stacks.

Single crystals of the three studied samples were easily degraded by enzymes, which initiated the attack on the amorphous lamellar surfaces in such a way that crystals edges remain practically unaltered until the late stages of degradation. Crystal edges are also more stable

during annealing processes performed in the crystallization medium at temperatures close to dissolution. Unusual framed crystals with rhombic and hexagonal morphologies can be obtained by this thermal treatment.

## V. References


1. Shirahama H, Kawaguchi Y, Aludin MS, Yasuda H. J Appl Polym Sci 2001;80:340.
2. Fujimaki T. Polym Degrad Stab 1998;29:209.
3. Tserki V, Matzinos P, Pavlidou E, Panayiotou C. Polym Degrad Stab 2006;91:377.
4. Takasu A, Ishii M, Inai Y, Hirabayashi T, Inomata K. Macromolecules 2003;36:7055.
5. Takasu A, Iio Y, Oishi Y, Narukawa Y, Hirabayashi T. Macromolecules 2005;38:1048.
6. Sokolsky-Papkova M, Langerb R, Domb AJ. Polym Adv Technol 2011;22:502.
7. Sugihara S, Toshima K, Matsumura S. Macromol Rapid Commun 2006;27:203.
8. Habeych DI, Eggink G, Boeriu CG. Biocatal Biotransform 2011;29:299.
9. Díaz A, Katsarava R, Puiggalí J. Int J Mol Sci 2013;15 :7064.
10. Quinzler D, Mecking S. Angew Chem Int Ed 2010;49:4306.
11. Stempfle F, Quinzler D, Heckler I, Mecking S. Macromolecules 2011;44:4159.
12. Yang Y, Lu W, Zhang X, Xie W, Cai M, Gross RA. Biomacromolecules 2010;11:259.
13. Hojabri L, Kong X, Narine SS. Biomacromolecules 2010;11:911.
14. Gan Z, Abe H, Doi Y. Biomacromolecules 2000;1:704.
15. Gan Z, Abe H, Doi Y. Biomacromolecules 2000;1:713–720.
16. Gan Z, Abe H, Doi Y. Biomacromolecules 2001;2:313.
17. Mochizuki M, Mukai K, Yamada K, Ichise N, Murase S, Iwaya Y. Macromolecules 1997;30:7403.
18. Li X, Hong Z, Sun J, Geng Y, Huang Y, An H. J Phys Chem 2009;113:2695.
19. Li X, Sun J, Huang Y, Geng Y, Wang X, Ma Z, Shao CG, An HN, Yan TZ, Li LB. Macromolecules 2008;41:3162.
20. Liang Z, Pan P, Zhu B, Dong T, Hua L, Inoue Y. Macromolecules 2010;43:2925.
21. Lian Z, Pan P, Zhu B, Inoue Y. Polymer 2011;52:2667.
22. Ueda AS, Chatani Y, Tadokoro H. Polym J 1971;2:387.
23. Minke R, Blacwell J. J Macromol Sci Phys1980;B18:233.
24. Aylwin PA, Boyd RH. Polymer 1984;25:323.
25. Kanamoto T, Tanaka K. J Polym Sci A 1971;9:2043.
26. Almontassir A, Gestí S, Franco L, Puiggalí J. Macromolecules 2004;37:5300.
27. Gestí S, Almontassir A, Casas MT, Puiggalí J. Polymer 2004;45:8845.

28. Gestí S, Almontassir A, Casas MT, Puiggalí J. Biomacromolecules 2006;7:799.

29. Gestí S, Casas MT, Puiggalí J. Polymer 2007;48:5088.

30. Iwata T, Doi Y. Polym Int 2002;51:852.

31. Iwata T, Doi Y. Macromolecules 1998;31:2461.

32. Iwata T, Doi Y. Macromolecules 2001;34:7343.

33. Iwata T, Kobatashi S, Tabata K, Yonezawa N, Doi D. Macromol Biosci 2004;4:296.

34. Casas MT, Puiggalí J. Polym Degrad Stab 2009;94:1941.

35. Cerius2Accelrys Inc. Cambridge, UK; 2002.

36. Bassett DC, Keller A. Philos Mag 1962;7:1553.

37. Girolamo M, Keller A, Stejny J. Makromol Chem 1975;176:1489.

38. Furuhashi M, Iwata T, Sikorski P, Atkins E, Doi Y. Macromolecules 2000;33:9423.

41. Vonk CG, Kortleve G. Polym 1967;220:19.

42. Vonk CG. J Appl Cryst 1975;8:340.

# *Chapter 3.3*

## *Study on the crystallization of poly(butylene azelate-co-butylene succinate) copolymer.*

Poly(butylene azelate-*co*-butylene succinate) samples with different azelate/succinate ratios were synthesized and characterized. Calorimetric data indicate a semicrystalline character for all copolyesters studied and a melting point depression that could be interpreted on the basis of complete exclusion of comonomers from well organized lamellae. Crystallization first occurred through the succinate rich segments, which resulted in a peculiar behavior of copolymers having an intermediate composition. In this case, crystallization of azelate segments was paradoxically enhanced when samples were quenched. Equilibrium melting temperatures significantly decreased with increasing comonomer content compared to those of the corresponding homopolymers. Incorporation of comonomers had a distinct effect on the secondary nucleation constant depending on the composition as deduced from Lauritzen and Hoffman analysis. Thus, azelate units clearly increased the nucleation constant of copolymers rich on succinate units, whereas the incorporation of succinate units had a lower influence on the constant of copolyesters having high azelate content.

## I. Introduction

Poly(alkylene dicarboxylate)s are polyesters of great interest due to their easy synthesis and potential applications derived from their biodegradability.[1,2] In general, these polymers are highly crystalline, a feature that may improve some properties but also hinder the degradation process. In order to obtain materials with tuneable properties, efforts are currently focused on forming random copolymers that can be easily synthesized by using mixtures of diols and/or dicarboxylic acids. In this way, hydrophobicity, crystallinity and degradation rate can be controlled.[3,6] Polybutylene succinate (PBS), a polymer supplied by Showa High Polymers as Bionolle,™ is currently the most widely employed poly(alkylene dicarboxylate) due to its relatively low production cost, good thermal and mechanical properties and easy processability.[7,8] Different types of copolymers and blends of PBS have recently been developed to increase biodegradability, decrease costs, increase commercial offer or even modify final properties.[9-14]



Random copolymers constituted by two crystallizable units may show a different crystallization behavior depending on the compatibility of the two components in crystal lattices. Comonomer units can generally be excluded in the organized lamellae and remain only in the amorphous phase or are compatible in such a way that they are able to share a crystalline lattice (Figure 1). Isomorphic co-crystallization is characterized by the formation of only one crystalline phase containing both crystalline units. In this case, these units must meet strict molecular requirements such as having a similar chemical structure and even molecular conformation to allow their incorporation into the resulting crystalline structure with minimum distortion. In contrast, two crystalline phases and pseudo-eutectic behavior are observed when isodimorphism occurs. Increase of minor comonomer concentration in each crystalline phase lowers the melting temperature and crystallinity of copolymers. Obviously, requirements are in this case less strict, and consequently isodimorphism is more frequently observed in random copolymer crystallization than isomorphism. Note, however, that

isodimorphism implies that at least one of the two crystalline phases incorporates the corresponding minor component in its crystalline lattice.

It now seems interesting to get insight into the crystallization behavior of copolyesters constituted by highly differentiated units and evaluate the capability to control thermal properties of new copolyesters since other characteristics like biodegradability are strongly influenced by the amorphous phase content. Azelaic acid has nine carbon atoms while succinic acid has only four, thus appearing as an ideal comonomer for the present study. Furthermore, it can be obtained by ozonolysis cleavage of the alkene double bond of oleic acid and subsequent oxidation andreduction.[15] Hence, all new synthesized copolymers can be derived from renewable sources, just like Bionolle™.

PBS shows polymorphism but a monoclinic structure known as *α*-crystal modification is attained under the most common crystallization conditions. Molecular conformation is defined by the torsional angle sequence ($T_7G\bar{T}G$) where the gauche and minus gauche angles belong to the succinate unit.[16-18] To the best of our knowledge of polybutylene azelate, the crystal lattice parameters have so far not been reported. However, an orthorhombic unit cell (instead of a monoclinic one) should be expected when aliphatic polyesters have an odd number of methylene groups in the diol and/or in the dicarboxylic units.[19,20]



## II. Experimental Section

### 1. Materials

All reagents and solvents were purchased from Sigma-Aldrich and used without further purification. Copolymers were synthesized by two-stage melt polycondensation of the appropriate mixture of dicarboxylic acids with an excess of 1,4-butanediol (1.2:1 molar ratio) (Figure 2). The composition of the reaction medium is defined by the molar ratio of azelate units (*x*), which is also used in the abbreviated copolymer name (*e.g.*, PE4,9/4 0.85 means the polyester (PE) derived from 1,4-butanediol (4) and having 85 and 15 molar-% of azelate (9) and succinate (4) units, respectively). Homopolymers will be named PE44 and PE49.

Titanium tetrabutoxyde was used as a catalyst and the reaction was first performed in a nitrogen atmosphere at 150 ºC for 6 h and then in vacuum (5 Pa) at 180 ºC for 18 h. Polymers were purified by precipitation with ethanol of chloroform solutions (10 wt%).

## 2. Measurements

Molecular weights were estimated by GPC using a liquid chromatograph (Shimadzu, model LC-8A) equipped with an Empower computer program (Waters) and a refractive index detector. A PL HFIP gel guard precolumn and PL HFIP gel column (Agilent Technologies Deutschland GmbH) were employed. The polymer was dissolved and eluted in 1,1,1,3,3,3-hexafluoroisopropanol at a flow rate of 0.5 mL/min (injected volume 100 µL, sample concentration 1.5 mg/mL). The number and weight average molecular weights were calculated using polymethyl methacrylate standards.

$^{1}$H-NMR spectra were acquired with a Bruker AMX-300 spectrometer operating at 300.1 MHz. Chemical shifts were calibrated using tetramethylsilane as an internal standard. Deuterated chloroform was used as the solvent.



Calorimetric data were obtained by differential scanning calorimetry with a TA Instruments Q100 series equipped with a refrigerated cooling system (RCS) operating from -90 ºC to 550 ºC. Experiments were conducted under a flow of dry nitrogen with a sample weight of approximately 5 mg while calibration was performed with indium. Thermal characterization was performed following a four run protocol consisting on a heating run (20 ºC/min) of the as-synthesized sample, a cooling run (10 ºC/min) after keeping the sample in the melt state for three minutes, a subsequent heating run (20 ºC/min) of the non-isothermally crystallized sample and finally a heating run (20 ºC/min) of a sample previously cooled from the melt state at the maximum rate allowed by the equipment.

**Figure 1.** Scheme of the comonomer unit arrangement in lamellae for full exclusion and inclusion models. In the latter case, isomorphic and isodimorphic structures are considered. In the last case, the two crystalline phases are represented with blue and red colours and the comonomer inclusion has been drawn for both phases.

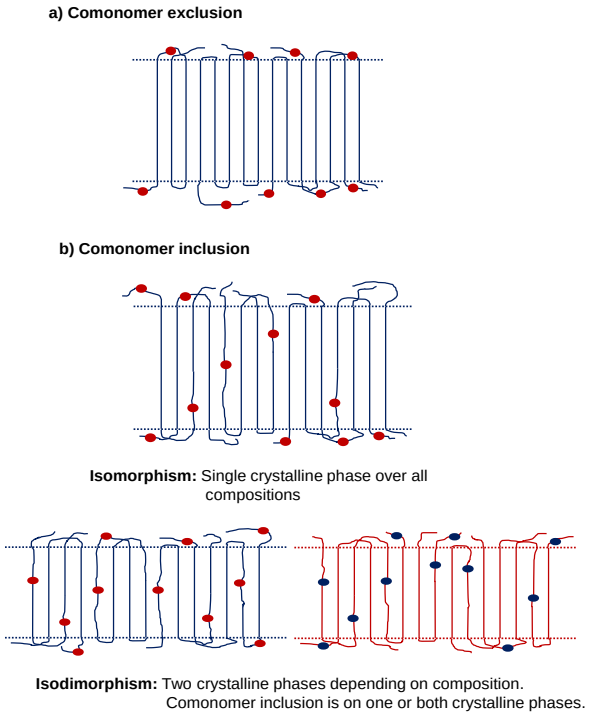




**Figure 2.** Synthesis scheme of all poly(butylene azelate-*co*-butylene succinate) copolymers.

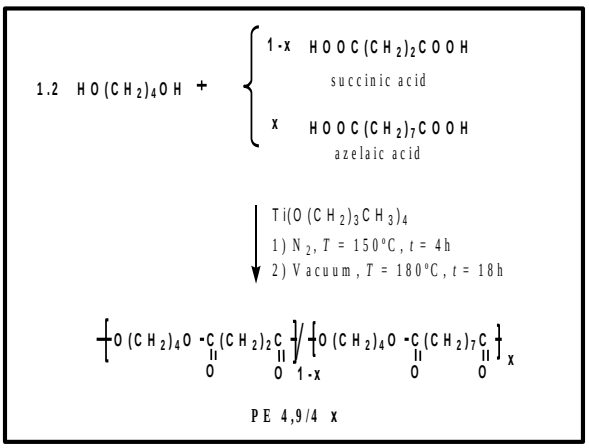

## III. Results and Discussion

### 1. Synthesis of PE4,9/4 x samples

Results in Table 1 indicate that samples could be synthesized with a polydispersity index (PDI) and a molecular weight typical of polycondensation reactions involving two monomers with different functionality (*e.g.*, diol and dicarboxylic units). Thus, PDI and $M_n$ ranged from 1.77 to 2.40 and from 10,900 to 17,400 g/mol, respectively. Polymerization yields determined also after reprecipitation of samples varied in a narrow range (65-78 %); no relationship between yield and monomer feed ratio indicative of a preferred reactivity was observed. Therefore, the slight variations in molecular weight and reaction yields seem a consequence of the lack of complete reproducibility of the synthesis procedure. In any case, final molecular weights were sufficient to ensure film- and fiber-forming properties.



**Table 1.** Synthesis data of PE4,9/4-*x* samples.

| Polymer | Yield (%) | $f_A$[a] | $M_n$[b] (g/mol) | $M_w$[b] (g/mol) | PDI[b,c] |
|---|---|---|---|---|---|
| PE49 | 77 | 1 | 15000 | 27700 | 1.85 |
| PE4,9/4 0.85 | 73 | 0.88 | 12100 | 29000 | 2.40 |
| PE4,9/4 0.65 | 70 | 0.65 | 10900 | 21300 | 1.95 |
| PE4,9/4 0.50 | 68 | 0.48 | 17400 | 30200 | 1.74 |
| PE4,9/4 0.35 | 69 | 0.35 | 14100 | 29500 | 2.09 |
| PE4,9/4 0.20 | 65 | 0.24 | 15600 | 32800 | 2.10 |
| PE44 | 68 | 0 | 14300 | 25300 | 1.77 |

[a]Azelate molar fraction determined from $^1$H NMR spectra.

[b]From GPC.

[c]Polydispersity index.

Infrared spectra of all samples synthesized revealed the characteristic absorption bands for methylene (2946-2928 and 2857-2854 $cm^{-1}$), C=O (1725-1712 $cm^{-1}$) and C-O (asymmetric and symmetric stretchings at 1224-1207 and 1170-1152 $cm^{-1}$, respectively). $^{1}H$ NMR spectra (*e.g.*, Figure 3 for the representative PE4,9/4 0.5 copolymer) were highly similar for all samples and showed characteristic signals associated with the different units, which allowed determining the final copolymer composition. Specifically, the areas of the triplet at 2.29 ppm and the singlet at 2.63 ppm were used to determine the ratio between azelate and succinate units incorporated into the polymer chain (*i.e.*, $f_A = A_{2.29} / (A_{2.29} + A_{2.63})$). These values, summarized in Table 1, show full agreement between the experimental composition and the monomer feed ratio (*i.e.*, $x \approx f_A$) for all synthesized copolymers.

**Figure 3.** Characteristic $^{1}H$-NMR spectra of PE4,9/4 0.5 sample.



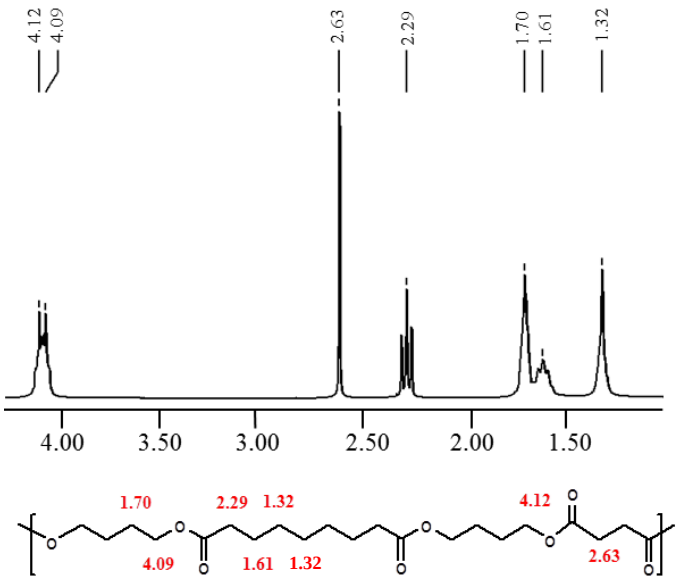


The spectra also showed that the signal associated with the O-C$H_2$ protons was complex due to their sensitivity to the neighboring dicarboxylate unit (*e.g.*, two triplets at 4.12 and 4.09 ppm were detected for the neighboring succinate and azelate units, respectively).

Unfortunately, this signal was insensitive to a triad effect, and therefore no information concerning sequence distribution could be derived. Splitting has been reported when copolyesters are derived from dicarboxylic units of clearly different nature (*e.g.,* aliphatic or aromatic).[21]

Interestingly, no terminal group signals were detected, in agreement with the relatively high molecular weight of the samples.

### 2. Calorimetric data of PE4,9/4 x samples

DSC thermal analysis showed that all samples were semicrystalline, as revealed by the melting endothermic peaks observed for the as-synthesized samples in the DSC scans in Figure 4. In fact, samples with intermediate compositions showed broad or multiple melting peaks. Furthermore, the melting point and total heat of fusion of the predominant peak decreased with the comonomer content compared to those of the corresponding homopolymers. Fusion of PE49 was characterized by a single melting peak whereas PE44 showed a shoulder indicative of a typical process where thinner lamellae melted and recrystallized, giving rise to more perfect crystals with higher melting temperature. These two populations of lamellae are clearly envisaged for the PE4,9/4 0.2 sample but a more complex melting process is observed for the sample containing 50 mol% of comonomer units.



Thermal properties were analyzed in more detail (Table 2) following a four run protocol as shown in Figure 5 for the least crystalline sample (*i.e.*, PE4,9/4 0.5). In this specific case, the highest melting peak I at 65 ºC was not detected in the subsequent heating runs performed with slowly crystallized (10 ºC/min) and quenched samples. As discussed below, two peaks related to the melting of crystals having the PE44 structure (II and III) can always be detected at the higher temperatures (*i.e.*, 39-56 ºC range). It is also worth noting the appearance of a new peak (IV) around 31 ºC, which may be associated with the melting of secondary crystals that may be constituted by PE49 rich phases. Melting peaks were observed in the third run for all samples, indicating that they were able to crystallize even at

the maximum cooling rate allowed by the equipment. Glass transition temperatures could also be determined from the third heating run (not shown) as summarized in Table 2.

**Figure 4.** DSC heating scan (20 ºC/min) of as-synthesized PE44 (a), PE4,9/4 0.20 (b), PE4,9/4 0.5 (c), PE4,9/4 0.85 (d) and PE49 (e) samples.

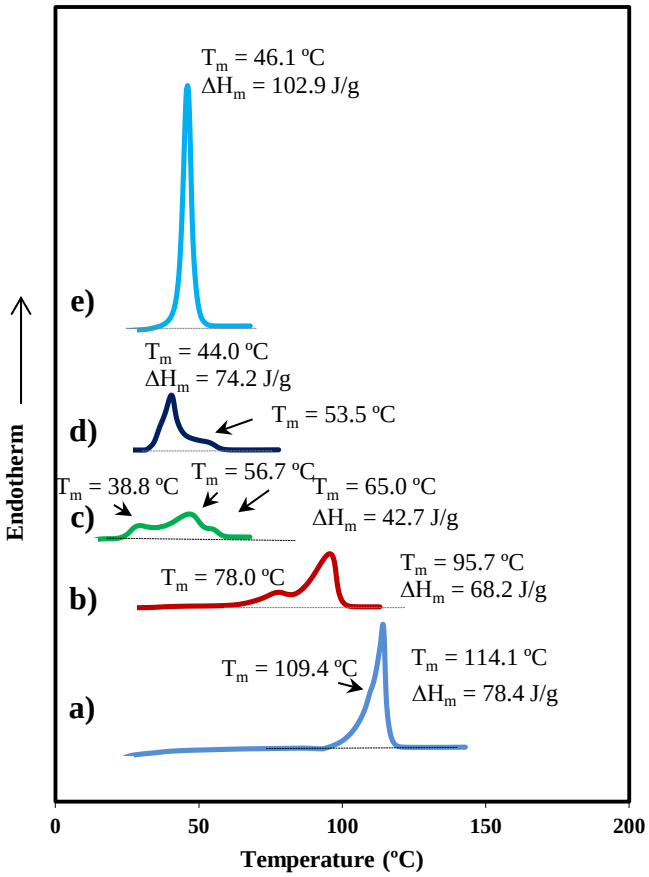

**Table 2.** Calorimetric data of PE4,9/4-*x* samples.[a]

| Sample | 1st Heating scan | | Cooling scan | | 2nd Heating scan | | | 3rd Heating scan | |
|---|---|---|---|---|---|---|---|---|---|
| | $T_f$ (ºC) | $\Delta H_f$ (J/g) | $T_c$ (ºC) | $\Delta H_c$ (J/g) | $T_f$ (ºC) | $\Delta H_f$ (J/g) | $T_g$ (ºC) | $T_f$ (ºC) | $\Delta H_f$ (J/g) |
| PE49 | 46.1 | 102.9 | 27.9 | 68.9 | 43.2 | 70.8 | -62.0 | 42.9 | 68.9 |
| PE4,9/4 0.85 | **44.0**, 53.5 | 74.2 | 20.2 | 55.0 | 39.8 | 56.8 | -59.0 | 39.3 | 54.1 |
| PE4,9/4 0.65 | **40.4**, 68.4, 77.4 | 44.6 | 13.8 | 59.8 | 36.5 | 61.3 | -57.2 | 36.2 | 60.4 |
| PE4,9/4 0.50 | 38.8, **56.7**, 65.0 | 42.7 | 16.5 | 28.1 | 31.5, 47.6, **56.4** | 29.1 | -59.4 | 31.1, 44.6, **55.3** | 39.9 |
| PE4,9/4 0.35 | 68.4, **77.4** | 50.5 | 30.6 | 37.1 | 61.1, 77.4 | 38.5 | -53.7 | 77.0 | 39.2 |
| PE4,9/4 0.20 | 78.0, **95.7** | 68.2 | 49.5 | 45.3 | 95.4 | 46.8 | -46.3 | 95.5 | 52.4 |
| PE44 | 109.4, **114.1** | 78.4 | 76.6 | 58.9 | 113.5 | 59.5 | -37.7 | 113.7 | 59.7 |

[a]When multiple melting peaks are observed the most intense one is indicated in bold numbers.

Figure 6 illustrates the heating scans performed with PE4,9/4 0.5 after being cooled from the melt state at different rates. It is clear that the temperature of peak II remained practically constant and its enthalpy increased compared to that of peak III when the cooling rate increased. On the other hand, the temperature of peak III decreased with increasing the cooling rate (*e.g.*, decreasing the crystallization time). This behavior suggests that peak III may be the so called annealing peak which is associated with defective secondary crystals belonging in this case to the PE44 structure. Note also that the total enthalpy of peaks II and III is practically independent of the previous cooling process, supporting the idea that peaks correspond to a balance between well-formed and defective crystals that depends on the crystallization time. Figure 6 also shows the increase in intensity of peak IV with higher cooling rates suggesting an increase on the ratio of PE49 crystals. The temperature of this peak remained practically constant and lower than the characteristic one for PE49, a feature compatible with crystallization of azelate units when the appropriate supercooling was quickly achieved during cooling. As the temperature of the melting peak of the PE49 polymer is much higher than in the 50% copolymer (46.1 ºC, see Figure 4, vs. 34 ºC in Figure 6), this result suggests that crystallization of segments with composition close to PE44 somehow interfere with the crystallization of segments with composition close to PE49. This interference became more significant at low cooling rates since crystallization of PE49 domains was clearly hindered.



Despite the existence of multiple melting peaks, all samples were able to crystallize from the melt, giving rise to a single exothermic peak whose temperature decreased again compared to that of the corresponding homopolymers (Table 2).

Figure 7 plots the melting temperatures for sample PE4,9/4 of segments having compositions close to PE44 (*e.g.*, those corresponding to peaks II and III) and the predominant one of segments having compositions close to PE49 of the as-synthesized samples as well as those observed in the third heating run (*i.e.*, quenched samples). A clear melting point depression with respect to pure PE44 or pure PE49 occurred with increasing azelate or succinate content, respectively. Again PE4,4/9 0.5 exhibited a complex behavior since the multiple melting peaks may derive from incorporation of comonomers into both PE44 and PE49 phases. In any case, as

explained before, the latter option seems less likely. Representation of the melting enthalpy (Figure 7 for the first heating scan) also showed a eutectic point at the intermediate composition.

**Figure 5.** DSC traces obtained with PE4,9/4 0.50 during the heating run (20 ºC/min) of the as-synthesized sample (a), the cooling run (10 ºC/min) after keeping the sample in the melt state for three minutes (b), the subsequent heating run (20 ºC/min) of the non-isothermally crystallized sample (c) and the heating run (20 ºC/min) of a sample previously cooled from the melt state at the maximum rate allowed by the equipment (d).

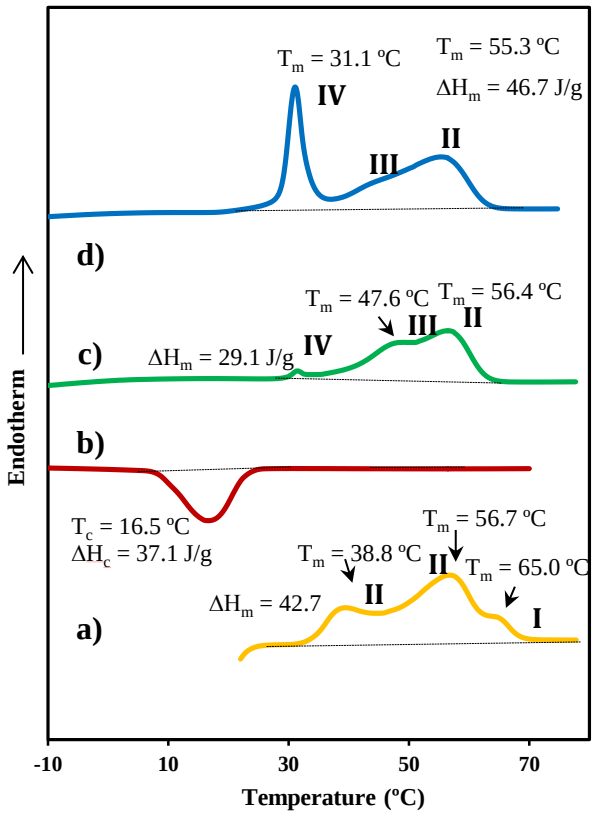


Data in Table 2 indicate the existence of a single glass transition temperature that depended on composition in all cases. Thus, no phase separation between azelate and succinate rich domains took place in the amorphous state. It is well known that for miscible systems the

glass transition temperature as a function of weight fraction can be predicted by various expressions, among which the Fox equation is probably the most commonly used:[22]

$$1/T_g = w_1 / T_{g1} + w_2 / T_{g2} \quad (1)$$

where $w_i$ and $T_{gi}$ represent the weight fraction and the glass transition temperature of each component and homopolymer, respectively.

**Figure 6.** DSC heating scans (20 ºC/min) of PE4,9/4 0.50 after being crystallized from the melt state at the indicated cooling rates.

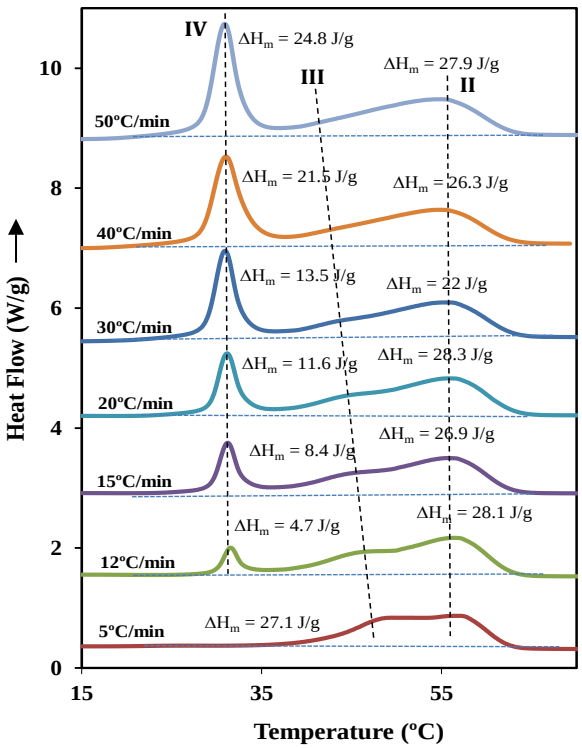


The plot in Figure 8 shows strong disagreement between theoretical and experimental values for azelate weight percentages lower than 72%, and especially for the sample with identical molar ratio of both units (*i.e.*, 58 wt%). It is clear that the observed decrease is a consequence of preferential crystallization of succinate units and enrichment of the amorphous phase with azelate units. Samples with the highest azelate content are in better agreement with

the predicted values although they tend to be even higher (*e.g.* sample with azelate content of 89 wt%), as expected if the amorphous phase was enriched with succinate units.

**Figure 7.** Variation of the melting temperature (♦,◊,●) and enthalpy (□) of PE4,9/4 *x* samples with the molar percentage of azelate units. Blue symbols correspond to the main peaks for compositions close to PE44 (*i.e.*, $x \leq 0.5$) (♦) and the predominant one for compositions close to PE49 (*i.e.*, $x \geq 0.65$) (●) as observed in the first heating run. Red symbols correspond to the main peak observed in the third heating run (*e.g.*, quenched samples).

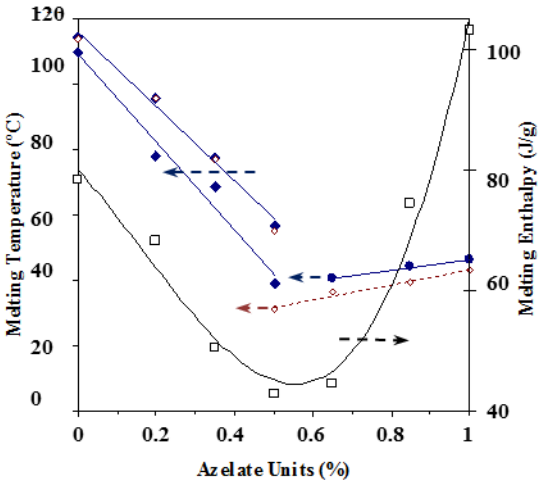


**Figure 8.** Variation of the glass transition temperature with azelate content.

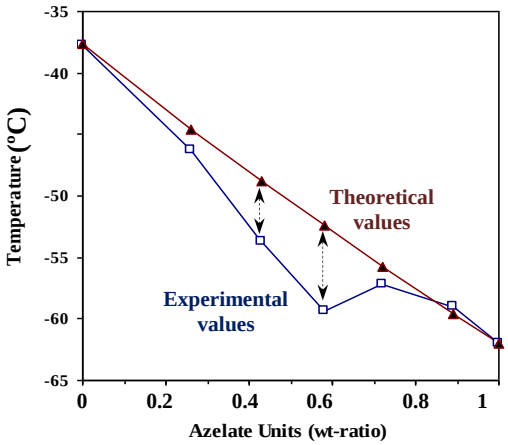

### 3. Determination of equilibrium melting temperatures

Equilibrium melting temperature ($T_m^o$) is a crucial parameter to determine the growth rate of a crystal and specifically the degree of supercooling ($T_m^0 - T_c$). The Hoffman-Weeks extrapolation[23] is a commonly accepted method to estimate the equilibrium melting temperature due to its simplicity and straightforward experimental implementation; although it is subject to criticism[24] and improvements have been proposed [25]. The method is based on equation 2, which was deduced from a combination of the well-known Gibbs-Thomson equation and secondary nucleation theory.[26] The derived equation relates the melting temperature, $T_m$, of a crystal formed at a temperature $T_c$, the equilibrium melting temperature and the thickening coefficient, $\gamma$, defined as the ratio between the thickness of the grown crystal, $l_c$, and the initial thickness of a "virgin lamella", $l_g^*$:

$$T_m = T_m^0 (1 - 1/\gamma) + T_c / \gamma \qquad (2)$$



A straight line is obtained by plotting $T_m$ as a function of $T_c$, with the equilibrium temperature corresponding to the intersection of this line with the $T_m = T_c$ line. The validity of equation 2 implies that lamellar crystals thicken at a specific crystallization temperature, which also influences the thickening parameter.

Figure 9 compares the complex melting behavior of PE4,9/4 0.5 and PE4,9/4 0.35 copolymers crystallized at different temperatures. Both showed the annealing peak III corresponding to the PE44 structure, which shifted at higher temperatures with increasing crystallization temperature. A similar behavior was found for peak II whereas the temperature remained constant for peak I. This behavior is consistent with a recrystallization process where thinner lamellae became thicker and more stable (peak I). Note that the intensity of peak I decreased with increasing crystallization temperature, as expected from a lower recrystallization caused by the more perfect crystals initially formed. It is also interesting that the relative intensity of peak I is lower for copolymers having higher comonomer content (*i.e.*, PE4,9/4 0.5 as opposed

to PE4,9/4 0.35), demonstrating that recrystallization was slower and crystal perfection could not be fully accomplished.

**Figure 9.** DSC heating scans (20 ºC/min) of PE4,9/4 0.50 (a) and PE4,9/4 0.35 (b) samples isothermally crystallized at the indicated temperatures.

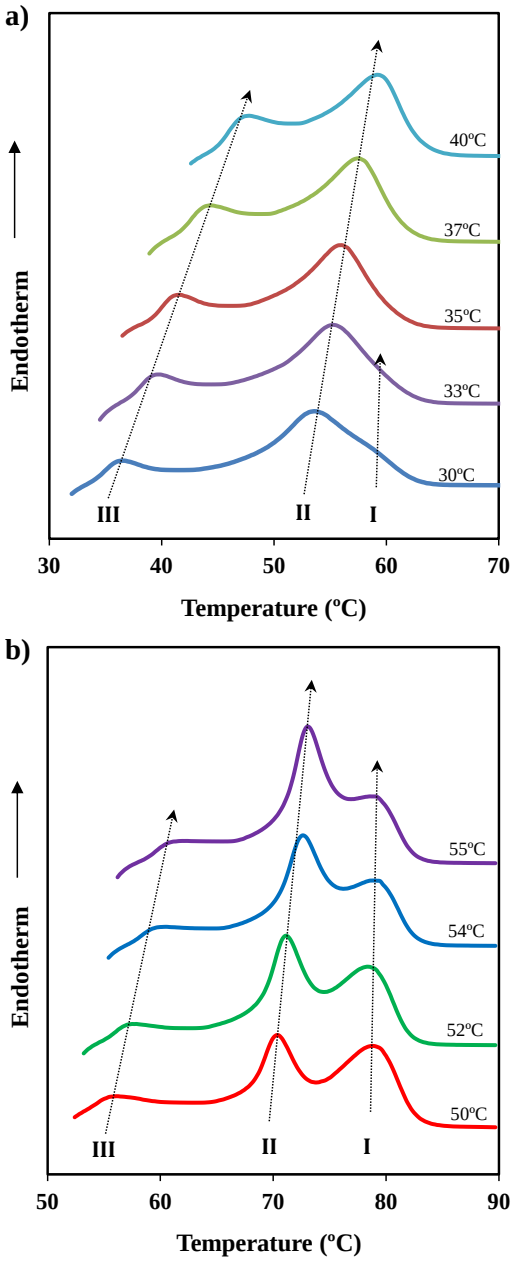

Figure 10 shows the Hoffman-Weeks plots of neat PE49 and the copolymers studied considering the evolution of peak II for samples with azelate content lower than 50 mol-% and the clearly predominant peak observed for the other copolymers. Note that the value determined for PE44 is in close agreement with the 127.5-140 ºC range previously reported for this sample.[27-30] Equilibrium melting temperature of copolymers clearly decreased compared to that of the predominant dicarboxylate homopolymer, especially for higher comonomer contents (*i.e.*, PE4,9/4 0.50 < PE4,9/4 0.35 < PE4,9/4 0.20 < PE 44 and PE4,9/4 0.65 < PE4,9/4 0.85 < PE 49). It is also worth pointing out that the slope of the plots, $1/\gamma$, can be regarded as a measure of the stability of crystals undergoing the melting process and that significant differences are found. Thus, the incorporation of comonomer units clearly decreased the slope, suggesting a greater difference between $l_c$ and $l_g^*$. In the same way, the azelate homopolymer seemed less stable than the succinate one.



**Figure 10.** Hoffman-Weeks plot of temperatures corresponding to endothermic melting peaks versus crystallization temperature for PE4,4/9 *x* samples. Equilibrium melting temperatures are explicitly indicated at the intersection point with the $T_m = T_c$ line.

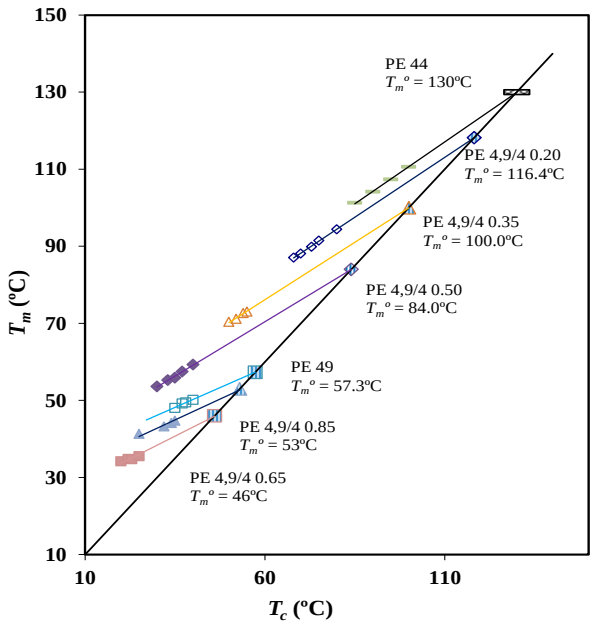

## 4. Melting point depression

Equilibrium aspects of copolymer crystallization are well established for a random distribution of monomer sequences.[30-33] Thus, it has been considered that for a copolymer constituted by two monomers A and B crystallizing in the crystal lattice of A, comonomers B may be excluded from the crystals or included as defects in the lattice.

Melting point depression in thermodynamic equilibrium can be estimated in the case of comonomer exclusion by the Flory equation 3.[31] The melting temperature of crystals built from "infinitely long" homopolymer sequences of units A in the copolymer is calculated, leading to the upper bound of the copolymer melting temperature:

$$1/T_m^0 - 1/T_m = R \ln (1-X_B) / \Delta H_m^0 \quad (3)$$

where $X_B$ is the molar ratio of the minor comonomer (B) in the copolymer, ln (1-$X_B$) is the collective activities of A sequences at the upper bound of the melting temperature, $\Delta H_m^0$ is the homopolymer equilibrium heat of fusion (36 kJ/mol for PE44[32] and 57 kJ/mol for PE49), as determined from the heat of fusion and degree of crystallinity estimated from X-ray diffraction data (not shown) and *R* is the gas constant.



Figure 11 compares the experimental equilibrium melting temperatures of copolymers with those predicted by the Flory equation. It is clear that much disagreement exists between both sets of data because of the drawback of the Flory model (*i.e.*, the hypothesis of a homopolymer sequence of infinite length) which different methodologies try to solve. Specifically, homopolymer sequences of a defined length $\xi$ have been considered to build crystals of lamellar thickness corresponding to that length.[33] Thus, the melting point can be calculated using the model postulated by Baur:

$$1/T_m^0 - 1/T_m = R/\Delta H_m^0 [\ln (1-X_B) - \langle\xi\rangle^{-1}] \quad (4)$$

where $\langle\xi\rangle = [2\ X_B\ (1-X_B)]^{-1}$ is the average length of homopolymer sequences in the melt.

Good agreement was found in this case between experimental and calculated data (Figure 11), allowing inference of comonomer exclusion. Note that inclusion models such as that postulated by Sánchez and Eby[34] use an excess of free energy, which is associated with defects caused by the incorporation of foreign units, leading to equilibrium melting temperatures higher than those predicted by the Flory equation. Combined models[35] based on Sánchez-Eby and Baur equations have also been proposed to simulate experimental data ranging between the regions defined by these two models, which is clearly not the case of the studied copolymers.

**Figure 11.** Variation of the experimental and theoretical equilibrium melting temperature with azelate content.

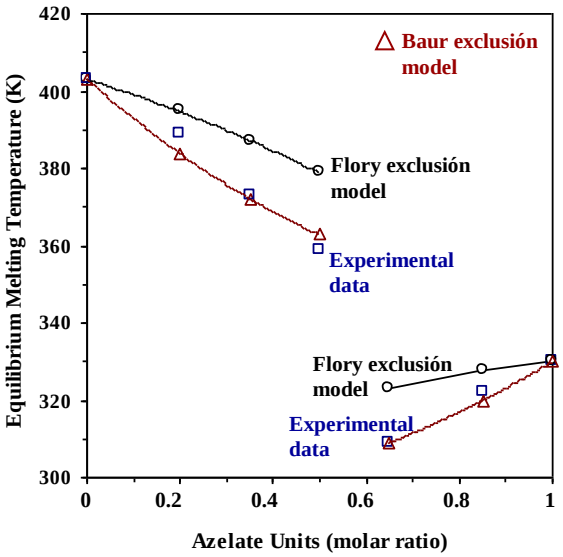




### 5. Kinetic crystallization data of PE4,9/4 samples from calorimetric studies

Figure 12a contains the DSC exotherms of the representative PE49 sample during isothermal crystallization experiments performed at selected temperatures with samples coming from the melt state. In general, the analysis temperature range is highly limited due to the significant increase in primary nucleation as temperature decreased (*e.g.*, the exothermic signal could not be accurately recorded). DSC peaks logically shifted to higher temperatures and

became broader with increasing the crystallization temperature. The time evolution of the relative degree of crystallinity, $\chi(t)$, can be determined through the ratio area of the exotherm up to time $t$ divided by the total exotherm area, *i.e.*:

$$\chi(t) = \int_{t0}^{t} (dH / dt)dt \; / \; \int_{t0}^{\infty} (dH / dt)dt \qquad (5)$$

where d$H$/d$t$ is the heat flow rate and $t_0$ the induction time. A characteristic sigmoidal time dependence was always found, as plotted in Figure 12a (inset).

Kinetic crystallization data were analyzed assuming the well-known Avrami equation[36,37] for primary crystallization:

$$1 - \chi(t\text{-}t_0) = \exp[-Z\,(t\text{-}t_0)^n] \qquad (6)$$

where $Z$ is the temperature-dependent rate constant and $n$ the Avrami exponent whose value varies with the crystallization mechanism. A normalized rate constant, $k = Z^{1/n}$, is usually evaluated for comparison due to the independence of its dimension (time$^{-1}$) from the value of the Avrami exponent.



Table 3 summarizes the main kinetic parameters of the primary crystallization process for all PE4,4/9 $x$ samples at one representative temperature as deduced from the plots of log{-ln[1-$\chi(t\text{-}t_0)$]} against log ($t$ - $t_0$) (*e.g.* Figure 12b for PE49). The values of the Avrami exponent for the isothermal crystallizations lie in a narrow range (between 2.55 and 2.05) with the average value being 2.26. This suggests a predetermined (heterogeneous) nucleation with spherical growth since the theoretical value should be equal to 3. The experimental values may be lower due to a crystallization that occurred under geometric constraints. Sporadic (heterogeneous) and homogeneous nucleation with a three dimensional growth can be clearly discarded as a higher exponent, close to 4, should be derived. Slightly lower values for the Avrami exponent were found for PE4,9/4 0.85 and PE4,9/4 0.65 copolymers, suggesting more confined growth of the major PE49 component since PE44 segments should be arranged first due to their higher crystallization temperature.

The values of the corresponding reciprocal crystallization half-times ($1/\tau_{1/2}$), calculated as the inverse of the difference between crystallization start time and half crystallization time, are also given in Table 3. This parameter is a direct measure of the crystallization process, and could therefore be used to check the accuracy of Avrami analyses, as demonstrated by the agreement with the theoretical kinetic value (*i.e.*, $1/\tau_{1/2} = (Z / \ln 2)^{1/n}$).

**Table 3.** Main crystallization kinetic parameters determined by DSC for the studied samples at representative crystallization temperatures.

| Sample | *T* (ºC) | *Z* ($s^{-n}$) | *n* | *k* ($s^{-1}$) | $1/\tau_{1/2}$ ($s^{-1}$)[a] | $1/\tau_{1/2}$ ($s^{-1}$)[b] | $K_g$ ($K^2$) × $10^5$ |
|---|---|---|---|---|---|---|---|
| PE49 | 39 | $2.07\ 10^{-7}$ | 2.31 | $1.28\ 10^{-3}$ | $1.41\ 10^{-3}$ | $1.50\ 10^{-3}$ | 0.63 |
| PE4,9/4 0.85 | 32 | $3.10\ 10^{-6}$ | 2.05 | $2.05\ 10^{-3}$ | $2.34\ 10^{-3}$ | $2.46\ 10^{-3}$ | 0.81 |
| PE4,9/4 0.65 | 22 | $1.05\ 10^{-5}$ | 1.96 | $2.88\ 10^{-3}$ | $3.41\ 10^{-3}$ | $3.48\ 10^{-3}$ | 0.70 |
| PE4,9/4 0.50 | 33 | $9.97\ 10^{-7}$ | 2.36 | $2.86\ 10^{-3}$ | $3.27\ 10^{-3}$ | $3.35\ 10^{-3}$ | 2.41 |
| PE4,9/4 0.35 | 54 | $2.31\ 10^{-7}$ | 2.38 | $1.63\ 10^{-3}$ | $1.82\ 10^{-3}$ | $1.90\ 10^{-3}$ | 2.20 |
| PE4,9/4 0.20 | 68 | $8.71\ 10^{-7}$ | 2.53 | $4.02\ 10^{-3}$ | $4.72\ 10^{-3}$ | $4.65\ 10^{-3}$ | 1.67 |
| PE44 | 95 | $5.60\ 10^{-8}$ | 2.55 | $1.43\ 10^{-3}$ | $1.73\ 10^{-3}$ | $1.65\ 10^{-3}$ | 1.67 |

[a] Deduced directly from curves of the development of the degree of crystallinity.

[b] Deduced from Avrami analysis.

Figure 13 plots the overall crystallization rates for the samples in function of the degree of supercooling (*i.e.*, the difference between the equilibrium melting temperature and the crystallization temperature), which is low and high for PE49 and PE44, respectively. Note that curves of copolymers appear always shifted to the right respect to related homopolymer curves. In this way, crystallization appears always hindered with increasing comonomer content.

**Figure 12.** (a) Exothermic DSC peaks corresponding to isothermal crystallizations of PE49 at temperatures between 35 and 40 ºC. Inset shows the development of relative crystallinity over time for the indicated isothermal crystallizations. (b) Avrami plots corresponding to isothermal crystallization of PE49.

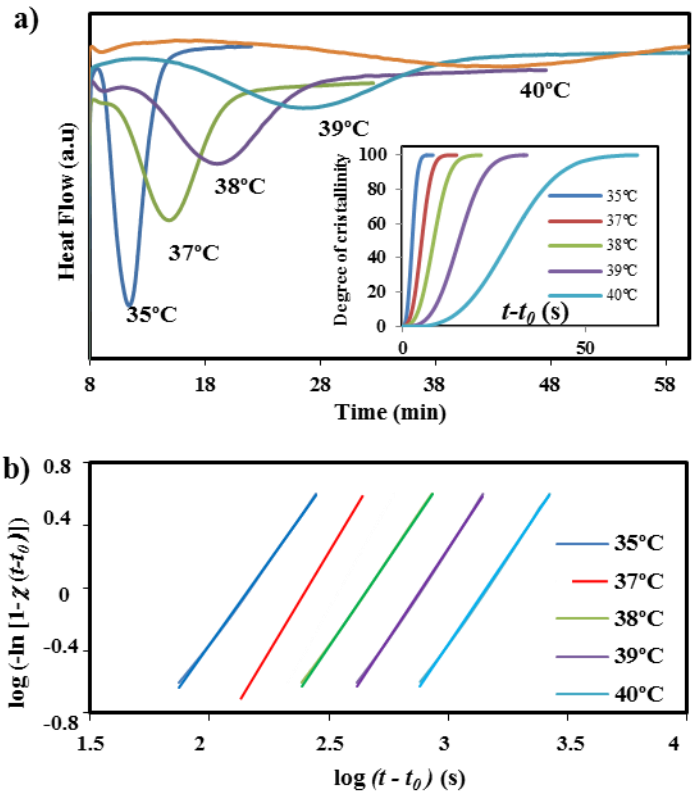


The overall crystallization rate could also be analyzed by the Hoffman-Lauritzen equation,[38] which can be reformulated for dominant heterogeneous nucleation using the reciprocal crystallization half-time[39-41] ($1/\tau_{1/2}$) or the normalized constant[42-45] ($k$) instead of the typical radial growth rate ($G$) determined by hot stage optical microscopy experiments.

We have specifically considered the derived equation for the normalized constant:

$$k = k_0 \exp\left[-U^* / \left(R\left(T_c - T_\infty\right)\right)\right] \times \exp\left[-K_g / \left(T_c\left(\Delta T\right) f\right)\right] \quad (7)$$

where $k_0$ is a constant preexponential factor, $U^*$ represents the activation energy characteristic of the transport of crystallizing segments across the liquid–crystal interface, $T_\infty$ is the temperature below which such motion ceases, $T_c$ is the crystallization temperature, $R$ is the gas constant, $K_g$ is a nucleation parameter, $\Delta T$ is the degree of supercooling measured as $T_m^0 - T_c$, and $f$ is a correction factor accounting for the variation in the bulk melting enthalpy per unit volume with temperature ($f = 2T_c/(T_m^0 + T_c)$).

**Figure 13.** Overall crystallization rates of PE4,9/4 *x* samples as a function of the degree of supercooling.

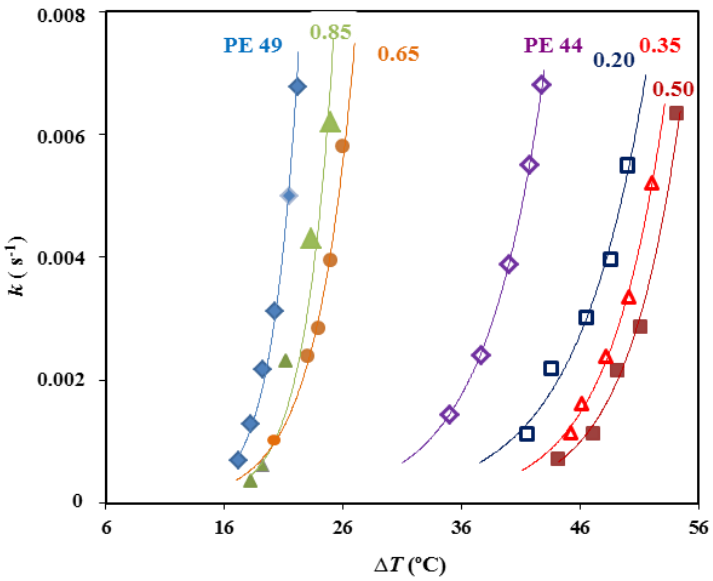


The corresponding Lauritzen and Hoffman plots in Figure 14 show that the data always fitted well with straight lines when the "universal" values reported by Suzuki and Kovacs[46] (*i.e.*, $U^*$ = 1500 cal/mol and $T_\infty = T_g$ -30 K) were employed in the calculations. Kinetic features at low supercoolings are basically governed by the nucleation term, and consequently the crystallization rates could become relatively insensitive to the $U^*$ and $T_\infty$ parameters. Figure 14 also shows that linear fits always had a single slope, which means that all samples crystallized in the small temperature interval according to only one regime. Secondary nucleation constants were deduced from these slopes, as summarized in Table 3. Specifically, a value of $1.67 \times 10^{-5}$ $K^2$ was

determined for PE44, which is in close agreement with reported values[5,29] from conventional analysis based on optical microscopy data. The use of the overall crystallization rate in equation 6 is thus validated. These previous analyses indicate that PE44 crystallized according to two regimes, but regime III with nucleation constants in the 1.51 $\times 10^{-5}$ $K^2$ - 1.85 $\times$ $10^{-5}$ $K^2$ range was characteristic for the crystallization temperature interval considered here.

Table 3 also indicates that the nucleation constant gradually increased (*i.e.*, from 1.67 $\times 10^{-5}$ $K^2$ to 2.41 $\times$ $10^{-5}$ $K^2$) as the azelate content in the copolymer increased from 0 molar-% to 50 molar-%. This point to a clear increase of the energy barrier for the overall crystallization as a consequence of the presence of foreign comonomer units.

**Figure 14.** Plot of ln $k + U^* / R(T_c - T_\infty)$ versus $1 / T_c (\Delta T) f$ to determine the $K_g$ nucleation parameter of the indicated PE4,9/4 *x* samples.

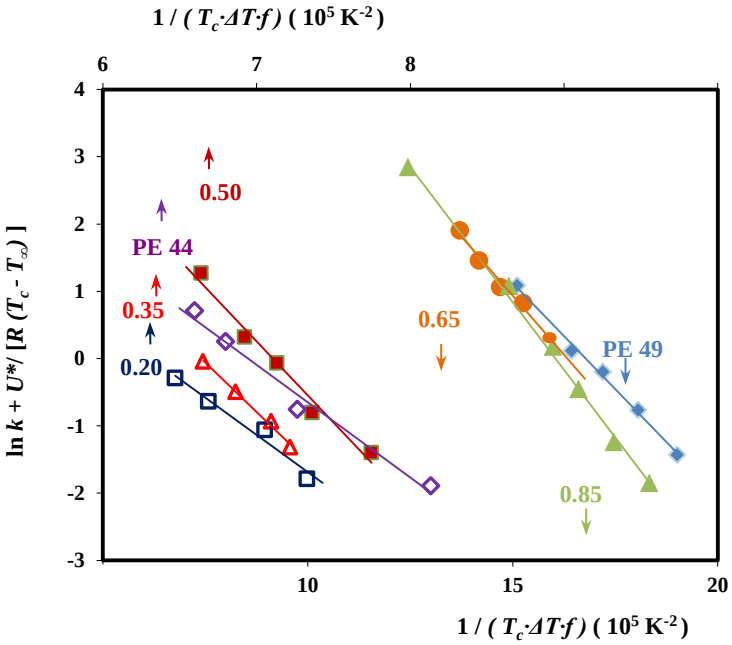


The experimental secondary constant determined for PE49 was considerably lower (*i.e.*, less than half) than for PE44. Thus, a lower surface free energy could be inferred for the PE49 structure assuming crystallization regime III. Note, however, that it is completely impossible to

distinguish between crystallization regimes from the given experimental data since they cover a limited temperature range. Changes on the nucleation constant were lower between samples with low succinate content (*i.e.*, those with $x$ = 0.65, 0.85 and 1), although it seems that copolymers had a slightly higher nucleation constant than the related PE 49 homopolymer. Crystallization of polybutylene azelate segments seems in this case not seriously disfavoured because succinate rich segments with higher crystallization temperature should be the first to be arranged during the crystallization process.

## IV. Conclusions

Thermal polycondensation of mixtures of azelaic and succinic acids with an excess of 1,4-butanediol rendered copolyesters with a variable composition, high yield and relatively high molecular weights. All copolyesters were semicrystalline and had a complex melting behavior due to the presence of crystals with different lamellar thicknesses and even different crystalline phases. Crystallization from the melt first involved the succinate rich segments, resulting in a peculiar behavior for copolymers having an intermediate composition since crystallization of butylene azelate could be enhanced by rapid cooling. No phase separation between azelate and succinate rich domains occurred in the amorphous phases.



Equilibrium melting temperatures, determined by the Hoffman-Weeks plot, were found to decrease compared to those of parent polyesters with increasing the comonomer content. The stability of crystals undergoing the melting process also decreased with the incorporation of comonomer units, the effect being more significant for azelate rich copolymers. A melting point depression which fitted the Baur exclusion model was clearly observed for all copolyesters.

Secondary nucleation constants increased with the comonomer content being the effect less significant when the copolymer was rich on azelate units. Thus, incorporation of succinate units had a slight influence on the energy barrier for overall crystallization of polybutylene azelate, probably as a consequence of the previous arrangement of butylene succinate rich segments.

## V. References


1. Doi Y, Steinbüchel A. Polyesters II – properties and chemical synthesis, Wiley-VCH, New York, 2002.
2. Huang SJ. Encyclopedia of polymer science and engineering, Wiley-Interscience, New York, 1985.
3. Gan Z, Abe H, Doi Y. Biomacromolecules 2000;1:704.
4. Gan Z, Abe H, Kurosawa H, Doi Y. Biomacromolecules 2001;2:313.
5. Papageorgiou GZ, Bikiaris DN. Biomacromolecules 2007;8:2437.
6. Lu X, Zeng JB, Huang CL, Wang YZ. Ind Eng Chem Res 2012;51:8262.
7. Fujimaki T. Polym Degrad Stab 1998;59:209.
8. Lai SM, Huang CK, Shen HF. J Appl Polym Sci 2005;97:257.
9. Li F, Xu X, Hao Q, Yu J, Cao A. J Polym Sci Part B: Polym Phys Ed 2006;44:1635.
10. Qiu Z, Ikehara T, Nishi T. Polymer 2003;44:7519.
11. Qiu Z, Komura M, Ikehara T, Nishi T. Polymer 2003;44:8111.
12. Mochizuki M, Mukai K, Yamada K, Ichise N, Murase S, Iwaya Y. Macromolecules 1997;30:7403.
13. Yang J, Tian W, Li Q, Cao A. Biomacromolecules 2004;5:2258.
14. Li X, Hong Z, Sun J, Geng Y, Huang Y, An H, Ma Z, Zhao B, Shao C, Fang Y, Yang C, Li L. J Phys Chem B 2009;113:2695.
15. Hojabri L, Kong X, Narine SS. Biomacromolecules 2010;11:911.
16. Ihn KJ, Yoo ES, Im SS. Macromolecules 1995;28:2460.
17. Ichikawa Y, Kondo H, Igarashi Y, Noguchi K, Okuyama K, Washiyama. J Polymer 2000;41:4719.
18. Ichikawa Y, Suzuki J, Washiyama J, Moteki Y, Noguchi K, Okuyama K. Polymer 1994; 35:3338.
19. Jourdan N, Deguire S, Brisse F. Macromolecules 1995;28:8086.
20. Gestí S, Casas MT, Puiggalí J. Eur Polym J 2008;44:2295.
21. Herrera R, Franco L, Rodríguez-Galán A, Puiggalí J. J Polym Sci Part A: Polym Chem 2002;40:4141.
22. Fox TG. Bull Am Phys Soc 1956;1:123.
23. Hoffman JD, Weeks JJ. J Res Natl Bur Stand 1962;66:13.

24. Strobl G. Eur Phys J 2000;E3:165.
25. Marand H, Xu J, Srinivas S. Macromolecules 1998;31:8219.
26. Hoffman JD, Davies GT, Lauritzen JI. Treatise in Solid State Chemistry, N.B. Hannay (Ed.), Plenum Press, New York, 1976, Chapter 7.
27. Miyata T, Masuko T. Polymer 1998;39:1399.
28. Yoo ES, Im SS. J Polym Sci Part B: Polym Phys Ed 1999;37:1357.
29. Gan Z, Abe H, Kurokawa H, Doi Y. Biomacromolecules 2001;2:605.
30. Park JW, Kim DK, Im SS. Polym Int 2002;51:239.
31. Flory PJ. Trans Faraday Soc 1955;51:848.
32. Papageorgiou GZ, Bikiaris DN. Polymer 2005;46:1208.
33. Baur VH. Makromol Chem 1966;98:297.
34. Sanchez IC, Eby RK. Macromolecules 1975;8:638.
35. Wendling J, Suter UW. Macromolecules 1998;31:2516.
36. Avrami M. J Chem Phys 1939;7:1103.
37. Avrami M. J Chem Phys 1940;8:212.
38. Lauritzen JI, Hoffman JD. J Appl Phys 1973;44:4340.
39. Philips PJ, Lambert WS. Macromolecules 1990;23:2075.
40. Urbanovici E, Schneider HA, Cantow HJ. J Polym Sci Part B Polym Phys 1997;35:359.
41. Hong PD, Chung WT, Hsu CF. Polymer 2002;43:3335.
42. Chan TW, Isayev AI. Polym Eng Sci 1994;34:461.
43. Fatou JG, Marco C, Mandelkern L. Polymer 1990;31:890.
44. Lu H, Qiao J, Yang Y. Polym Int 2002;51:1304.
45. Kenny JM, Maffezzoli A, Nicolais R. Termochimica Acta 1993;227:83.
46. Suzuki T, Kovacs AJ. Polym J 1970;1:82.

# Chapter 3.4

## *Poly(butylene azelate-co-butylene succinate copolymer: crystalline morphologies and degradation.*

Random copolymers derived from 1,4-butanediol and two dicarboxylic units differing in the parity of the number of methylene groups and length of the polymethylene sequence (*i.e.*, succinic and azelaic acids) were studied in terms of thermal properties, crystalline structure and morphology, crystallization kinetics and biodegradability.

All samples were semicrystalline and their thermal properties varied in a wide temperature range. Copolymers crystallized according to the monoclinic α-form of polybutylene succinate and the orthorhombic structure postulated for polybutylene azelate depending on the predominant dicarboxylate unit. The behavior of the copolymer with an intermediate composition was complex due to strong dependence of the predominant crystalline form on crystallization and processing conditions. Interestingly, crystallization into the azelate structure was favored when samples were rapidly cooled from the melt, resulting in an unexpected increase in the degree of crystallinity. Spherulitic morphologies were clearly different (*i.e.*, ringed spherulites and axialites) depending on the preferential crystalline structure.

Enzymatic degradability of the two homopolyesters was highly different and could be enhanced by incorporation of comonomer units. Preferential enzymatic attack on amorphous regions highlighted the spherulitic morphologies of copolymers having well developed, distinctive ringed structures.

## I. Introduction

Biodegradable polymers attract great interest for both biomedical and ecological applications. Continuous efforts are made to improve performance characteristics of materials for these purposes (*e.g.,* polylactide and poly(ε-caprolactone))[1]. Natural and synthetic aliphatic polyesters are among the most extensively investigated biodegradable polymers. They can be classified into different groups based on the kind of repeat unit: poly(α-hydroxyacid)s, poly(ω-hydroxyacid)s, poly(3-hydroxyalkanoate)s and poly(alkylene dicarboxylate)s.[1-3] The first are usually prepared by ring-opening polymerization while poly(3-hydroxyalkanoate)s are biosynthesized by microorganisms such as *Bacillus megaterium.*

Poly(alkylene dicarboxylate)s are generally produced by direct polycondensation of diol and dicarboxylic acid monomers, which generally leads to polymers with moderate molecular weights. This limitation has recently been overcome by using chain extenders such as diisocyanate[4] and even new catalysts. Polybutylene succinate (PBS), a polymer supplied by Showa High Polymers as Bionolle,™ is currently the best example of renewed interest in poly(alkylene dicarboxylate)s due to its relatively low production cost, good thermal and mechanical properties and easy processability.[5,6] In fact, PBS, together with polylactide and Biopol (*i.e.*, microbial poly((R)-3-hydroxybutyric acid) and its naturally occurring copolymers), are some of the more relevant polyesters used as green polymers. Furthermore, it is significant that PBS derives from succinic acid, which is typically produced in microbes in the metabolic tricarboxylic acid cycle used for energy production. In view of this potential, a great effort is being developed to obtain succinic acid at low cost from renewable resources like starch, glucose or cellulose. This also applies to other C4 derivatives such as 1,4-butanediol, which is the second monomer employed in the synthesis of PBS.

Copolymerization and blending make it possible to easily enrich the family of biodegradable polymers and fulfil several practical requirements. Preparation of new copolyalkylene dicarboxylates offers a key opportunity to increase the range of degradable materials and even to generate a set of products with easily tunable properties. Thus, different types of PBS copolymers and blends have recently been developed to increase biodegradability,

decrease costs, increase commercial offer and even modify final properties.[7-12] An understanding of the relationship between structure, morphology and properties is crucial to design these new materials with enhanced physical and chemical properties. The study of crystallization behavior is also important not only due to its strong correlation with the biodegradation process, but also because of the processability and applicability of materials. Specifically, the processability of PBS is not excellent due to its low crystallization temperature and slow crystallization rate. This problem may be solved by using nucleating agents or alternatively by modifying the chemical structure with, for example, branching agents. Incorporation of comonomers has also a great influence on melting behavior, sample crystallinity, lamellar surface morphology, and consequently enzymatic degradability.[13-15] Several works have recently been addressed to study the crystallization process of random copolyalkylene dicarboxylates. This kind of studies is significant not only because of the processability and applicability of the materials, but also for its strong correlation with the biodegradation process[16]. The studied copolymers are mainly constituted by even units, and specifically poly(butylene succinate-*co*-ethylene succinate),[10] poly(hexamethylene succinate-*co*-hexamethylene adipate)[12], poly(hexamethylene sebacate-*co*-hexamethylene adipate),[17,18] poly(hexamethylene sebacate-*co*-hexamethylene suberate)[19] and poly(hexamethylene suberate-co-hexamethylene adipate)[19] are representative examples.



We are now interested in the crystallization behavior of copolyesters constituted by highly differentiated units since the degree of crystallinity is expected to decrease with increasing the minor component content because of crystal lattice incompatibility of the two homopolymers.[20] Azelaic and succinic acids have significantly different lengths and even different parities of the number of carbon atoms, thus making the former an ideal comonomer for this study. Furthermore, all newly synthesized copolymers can be derived from renewable sources since the azelaic acid component can be obtained by ozonolysis of the alkene double bond of oleic acid, and subsequent oxidation and reduction.[21] In this work, a series of copolymers with progressive variation in composition (*e.g.,* the ratio between azelate and succinate units) is studied and crystallization behavior and enzymatic degradability are evaluated. To our knowledge, this combined analysis has only been performed for poly(butylene-*co*-propylene

succinate) copolymers, which have diol comonomers of very similar length, leading to isodimorphic cocrystallization.[22] The environmentally friendly poly(butylene azelate-*co*-butylene succinate) copolyesters have recently been postulated as highly interesting materials that might find applications from elastomers to high-impact thermoplastics depending on their specific comonomer composition.[23] Storage modulus measured at 20 ºC were found for example to vary between 570 and 110 MPa. Good thermal stability and a complex thermal degradation process were also observed.

**Figure 1.** Synthesis scheme and chemical structure of poly(butylene azelate-co-butylene succinate) copolymers.

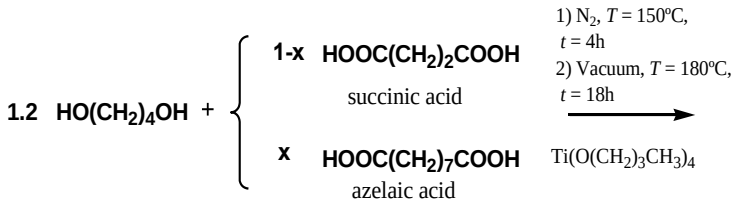


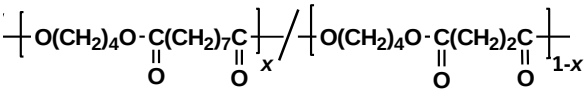


**PE4,9/4 *x***



## II. Experimental Section

### 1. Materials Materials

Copolymers were previously synthesized by two-stage melt polycondensation of the appropriate mixture of dicarboxylic acids with an excess of 1,4-butanediol (1.2:1 molar ratio), as shown in Figure 1.[24] Number and weight average molecular weights ranged between 10,900-17,400 and 21,300-32,800 g/mol (Table 1), respectively, and compositions were gradually varied by controlling the azelaic acid / succinic acid monomer feed ratio. Specifically, samples were

prepared using a molar ratio of azelaic acid units referred to the dicarboxylic acid content of 1.0, 0.85, 0.65, 0.50, 0.35, 0.20 and 0.0. Samples will be named in an abbreviated form indicating the molar ratio, *x*, and the number of carbon atoms in the diol and the dicarboxylic acid unit. Thus, PE4,9/4 0.85 refers to the polyester (PE) derived from 1,4-butanediol (4) and having 0.85 and 0.15 M ratios of azelate (9) and succinate (4) units, respectively, whereas PE49 refers to poly(butylene azelate).

## 2. Measurements

$^{13}$C-NMR spectra were acquired with a Bruker AMX-300 spectrometer operating at 75.5 MHz. Chemical shifts was calibrated using tetramethylsilane as an internal standard. Deuterated chloroform was used as the solvent.

Infrared absorption spectra were recorded with a Fourier Transform FTIR 4100 Jasco spectrometer in the 4000-600 $cm^{-1}$ range. A Specac model MKII Golden Gate attenuated total reflection (ATR) cell with a heated Diamond ATR Top-Plate was used.



Calorimetric data were obtained by differential scanning calorimetry with a TA Instruments Q100 series equipped with a refrigerated cooling system (RCS). Experiments were conducted under a flow of dry nitrogen with a sample weight of approximately 5 mg while calibration was performed with indium.

The spherulitic morphologies was studied by optical microscopy using a Zeiss Axioskop 40 Pol light polarizing microscope equipped with a Linkam temperature control system configured by a THMS 600 heating and freezing stage connected to a LNP 94 liquid nitrogen cooling system. Spherulites were grown from homogeneous thin films prepared from evaporation of dilute solutions of the polymer in 1,1,1,3,3,3-hexafluoroisopropanol (0.5 mg/mL). Next, small sections of these films were pressed or smeared between two cover slides and inserted into the hot stage. Thicknesses of all squeezed samples were close to 10 μm. Samples were kept at approximately 20 ºC above their melting point for 5 min to eliminate sample history effects. Samples were then quickly cooled to the selected crystallization temperature. Micrographs were taken with a Zeiss

AxiosCam MRC5 digital camera. A first-order red tint plate was employed to determine the sign of spherulite birefringence under crossed polarizers.

For AFM studies, thin films deposited on cover slides were cold and hot crystallized at selected temperatures. Height and amplitude images of spherulites were obtained with a Molecular Imaging PicoSPM using a NanoScope IV controller in ambient conditions and a scan window size of 10 x 10 $\mu m^2$. The tapping mode AFM was operated at constant deflections (*i.e.*, vertical constant force with triangular gold-coated silicon nitride). The row scanning frequency was set to 1 Hz and the physical tip-sample motion speed was 10 μm/s.

X-ray powder diffraction patterns were acquired with a PANalytical X´Pert diffractometer with $CuK_\alpha$ radiation (λ = 0.1542 nm) and a silicium monocrystal sample holder. Fiber diffraction patterns were collected with Ni-filtered $MoK_\alpha$ radiation of wavelength 0.0712 nm by a Mar Research 345 image plate detector. Oriented fiber samples were obtained by melt drawing.

Degradation study samples were cut from regular films of 1 × 1 $cm^2$ and 200 μm in thickness prepared by melt pressing 300 mg of the appropriate polymer at a temperature of 10 °C above the melting peak temperature.



Enzymatic degradation was conducted at 25 and 37 °C by using a *Rhizopus oryzae* lipase (55.7units/mg). The enzymatic medium, 1 mL, consisted of a pH 7.4 sodium phosphate buffer containing sodium azide (0.03 wt%) and 1 mg of the appropriate enzyme. All enzymatic solutions were renewed every 48 h because of enzymatic activity loss. After immersion, samples were rinsed with water, dried to constant weight under vacuum and stored over $P_4O_{10}$ before analysis. Weight retention was then evaluated. Degradation studies were performed in quadruplicate, with given data corresponding to the average values.

Inspection of the morphology of degraded films was conducted by scanning electron microscopy using a Focus Ion Beam Zeiss Neon 40 instrument (Carl Zeiss, Germany). Carbon coating was performed using a Mitec K950 Sputter Coater fitted with a film thickness monitor *k*150x. Samples were visualized at an accelerating voltage of 5 kV.

## III. Results and Discussion

### 1. Study of crystallization of PE4,9/4 x samples from DSC and FTIR analyses

Copolymer microstructure (*e.g.*, blocky or random monomer distribution) determines the crystallization behavior and ultimate properties of samples with a given composition. The synthesis procedure for preparing the new copolyesters makes it possible to assume a practically random distribution for similar reactivities of the two carboxylic groups. $^{1}$H-NMR spectra were useful to determine the final content of azelaic acid (A) and succinic acid (S) units (Table 1) by considering the triplet areas at 2.29 ppm and the singlet at 2.63 ppm associated with the $CH_2$-CO protons (Figure 2) of the respective dicarboxylate unit. On the other hand, they failed to give sequence information, unlike $^{13}$C-NMR spectra. In this case, the $CH_2$-O carbon of the 1,4-butanediol unit (B) gave rise to four signals depending on neighboring dicarboxylate units, as shown in Figure 1 for the representative PE4,9/4 0.5 sample. The relative areas allowed deducing the percentage of ABS, SBS, ABA and SBA sequences which became very close to theoretical values determined for a random distribution. Hence, it is interesting to note that copolymerization was effective, as deduced from the significant percentage of ABS and SBA heterosequences.



Thermal properties of new copolymers are summarized in Table 1, whereas Figure 3 shows the melting behavior of samples previously submitted to the same hot crystallization process (*i.e.,* slow cooling at 10 ºC/min after keeping the sample in the melt state for 3 min). A clear melting point depression with respect to pure homopolymers occurred with increasing comonomer content. Furthermore, the melting enthalpy showed an eutectic behavior with a minimum value for the intermediate composition (*i.e.*, PE4,9/4 0.5 copolymer), which is consistent with an exclusion model where comonomer units cannot be incorporated into organized lamellae and remain in the amorphous phase. All polymers met goals concerning availability of samples with a gradual, highly variable degree of crystallinity and melting points within a wide temperature range (*i.e.,* from 40 ºC to 140 ºC).

**Figure 2.** $^{13}$C-NMR (a) and $^{1}$H- (b) spectra (region) showing distinctive -$CH_2O$- signals (a) for the four ABS, SBS, ABA and SBA chemical sequences and the -$CH_2CO$- signals (b) of the two dicarboxylate units for representative PE4,9/4 0.35 and PE4,9/4 0.50 samples.

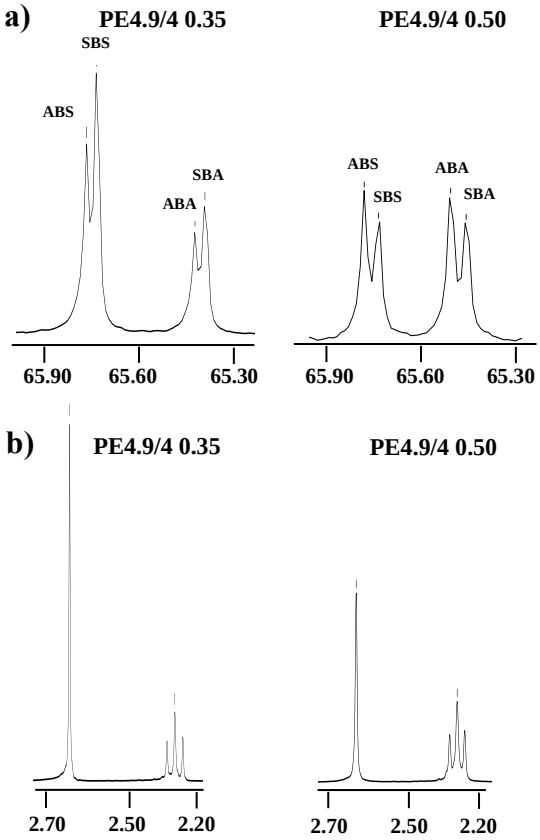




The melting behavior was especially complex for the sample with the intermediate composition as at least three melting peaks could be detected. Peaks I and II can be associated with PE44 lamellar crystals of different thicknesses whereas peak III, which appeared at the lowest temperature, corresponds to a PE49 crystalline domain. Surprisingly, it was possible to enhance this peak (and also the total fusion enthalpy) by previously crystallizing samples at increasing cooling rates (Figure 4a). Thus, the degree of crystallinity can be enhanced by rapid crystallization such as quenching at 50 ºC/min. FTIR spectra (Figure 4b) of the 1400-800 $cm^{-1}$ region showed that the relative intensity of bands associated with PE44 (1330 and 1045 $cm^{-1}$)

and PE49 (*e.g.*, 1308, 1223 and 1064 $cm^{-1}$) crystalline phases decreased and increased, respectively, when samples crystallized at increasing cooling rates. It seems that the development of the PE49 crystalline phase was more favored when the temperature associated with the formation of its primary nuclei was reached fast enough to avoid termination of previous PE44 crystallization. Probably, crystallization of PE49 was hindered in a confined system derived for a complete PE44 crystallization. Combined DSC and FTIR techniques demonstrated a peculiar behavior for these copolymers having an intermediate composition since crystallization of butylene azelate rich fragments could be enhanced by rapid cooling.

**Figure 3.** DSC heating scans (20 ºC/min) of PE44 (a), PE4,9/4 0.20 (b), PE4,9/4 0.5 (c), PE4,9/4 0.85 (d) and PE49 (e) samples after being cooled (10 ºC/min) from the melt state to room temperature.

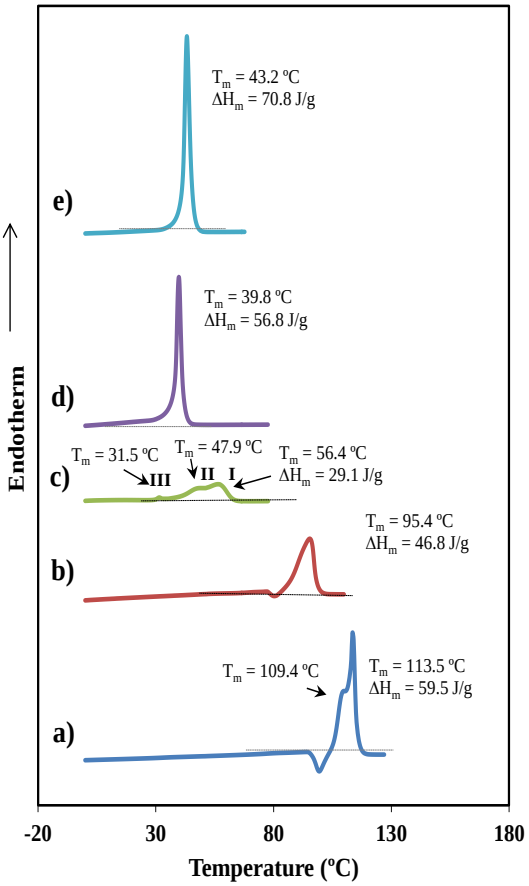

**Table 1.** Basic characterization data of PE4,9/4 *x* samples.[a]

| Polymer | $f_A$[a] | $M_n$[b] (g/mol) | $M_w$[b] (g/mol) | $T_c$[c] (ºC) | $\Delta H_c$[c] (J/g) | $T_f$[d] (ºC) | $\Delta H_f$[d] (J/g) | $T_m^0$[e] (ºC) |
|---|---|---|---|---|---|---|---|---|
| PE49 | 1 | 15,000 | 27,700 | 27.9 | 68.9 | 43.2 | 70.8 | 57 |
| PE4,9/4 0.85 | 0.88 | 12,100 | 29,000 | 20.2 | 55.0 | 39.8 | 56.8 | 53 |
| PE4,9/4 0.65 | 0.65 | 10,900 | 21,300 | 13.8 | 59.8 | 36.5 | 61.3 | 46 |
| PE4,9/4 0.50 | 0.48 | 17,400 | 30,200 | 16.5 | 28.1 | 31.5, 47.9, **56.4**[f] | 29.1 | 84 |
| PE4,9/4 0.35 | 0.35 | 14,100 | 29,500 | 30.6 | 37.1 | 61.1, 77.4 | 38.5 | 100 |
| PE4,9/4 0.20 | 0.24 | 15,600 | 32,800 | 49.5 | 45.3 | 95.4 | 46.8 | 116 |
| PE44 | 0 | 14,300 | 25,300 | 76.6 | 58.9 | 109.4, 113.5 | 59.5 | 130 |

[a]Azelate molar fraction determined from $^1$H NMR spectra.[19]

[b]From GPC.[19]

[c]From the cooling scan (10 ºC/min) of a molten sample.

[d]From the heating scan (20 ºC/min) of melt crystallized sample.

[e]Equilibrium melting temperature determined from calorimetric studies.[19]

[f]Bold characters correspond to the most intense peak.



Neighboring compositions (*e.g.*, PE4,4/9 0.65 and PE4,4/9 0.35 copolymers) also exhibited a complex melting behavior that depended on the previous crystallization process. However, all peaks were only associated with the crystalline phase of the predominant component (*e.g.*, PE49 for $x$ = 0.65 and PE44 for $x$ = 0.35). Figure 5a shows how PE4,9/4 0.65 has a typical recrystallization process where thinner lamellae thicken during the heating process, giving rise to crystals with a higher melting peak. This process is enhanced for badly crystallized samples (*e.g.*, at a high cooling rate) but all the crystalline domains correspond to the PE49 phase, as revealed by the unchanging FTIR spectra (Figure 5b). In Figure 6, it can be seen how the crystallization of PE4,9/4 0.35, which was performed at the highest rate, did not favor the formation of PE 49 domains (*e.g.*, no new melting peak at low temperature was enhanced), as is characteristic of the PE4,9/4 0.50 sample.

**Figure 4.** DSC heating scans (20 ºC/min) (a) and FTIR spectra (b) of PE4,9/4 0.50 samples after crystallizing from the melt at the indicated cooling rates. Spectra of homopolymers are also given for comparison purposes. Characteristic bands associated to crystalline structures of PE 44 (*i.e.*, 1330 and 1045 $cm^{-1}$) and PE 49 (*i.e.*,1308, 1223 and 1064 $cm^{-1}$) are labelled.

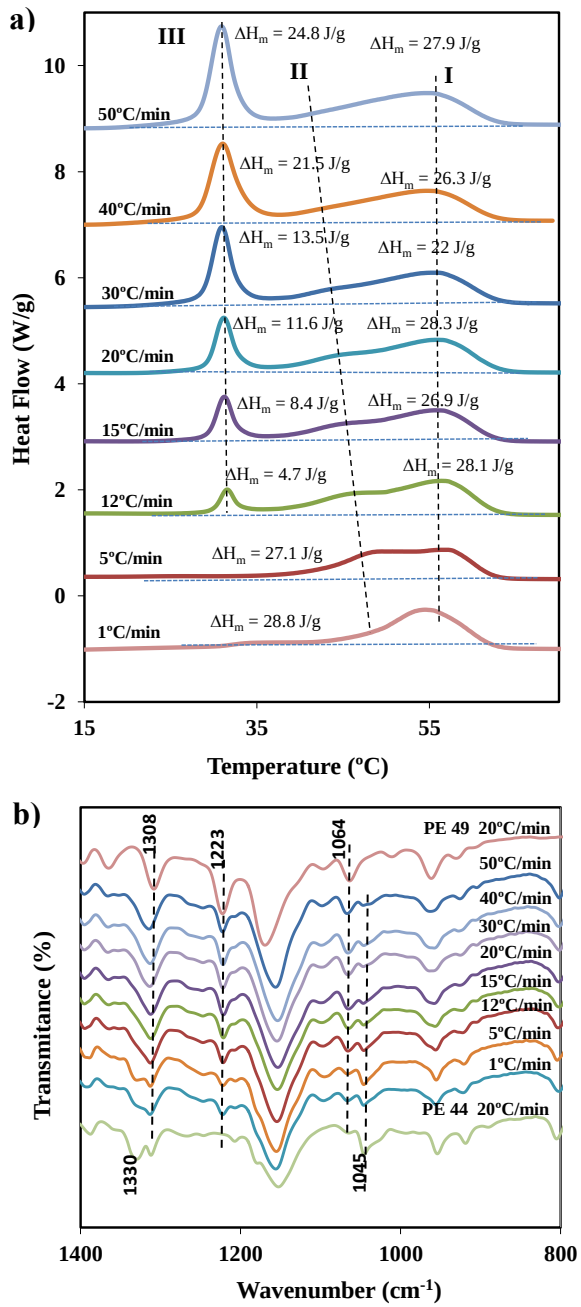

**Figure 5.** DSC heating scans (20 ºC/min) (a) and FTIR spectra (b) of PE4,9/4 0.65 samples after crystallizing from the melt at the indicated cooling rates.

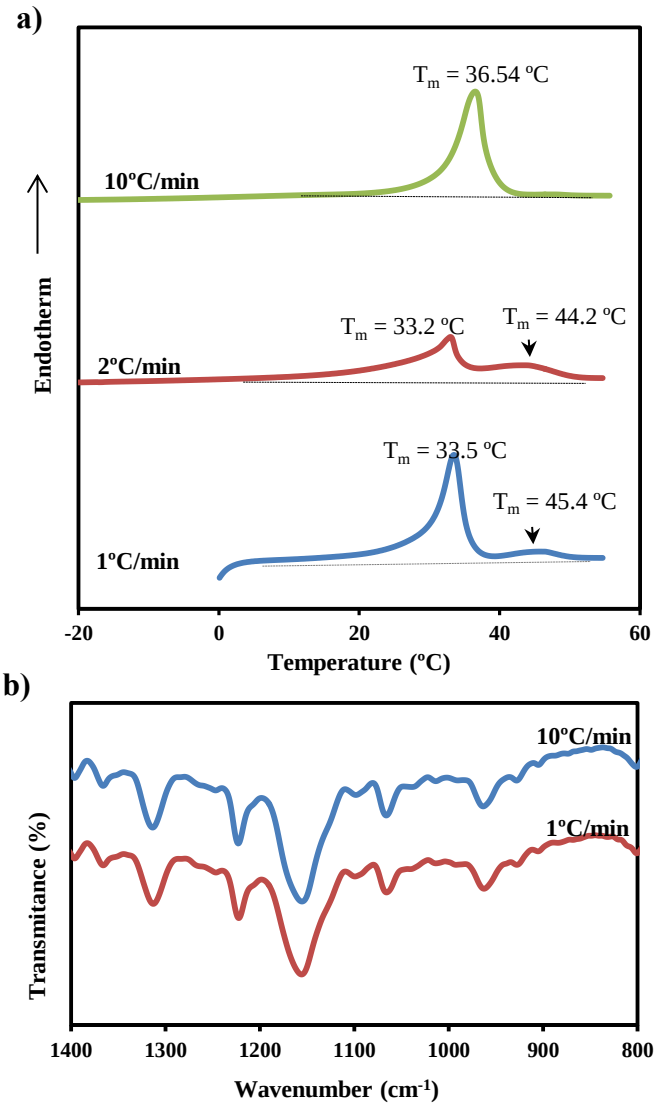




Despite their complex melting behavior, all samples crystallized from the melt, giving rise to a single exothermic peak (Figure 7) at a supercooling close to 40 ºC with respect to the melting temperature. DSC scans made it possible to determine the appropriate conditions for performing further cold crystallization experiments.

**Figure 6.** DSC heating scans (20 ºC/min) of PE4,9/4 0.35 samples after crystallizing from the melt at the indicated cooling rates.

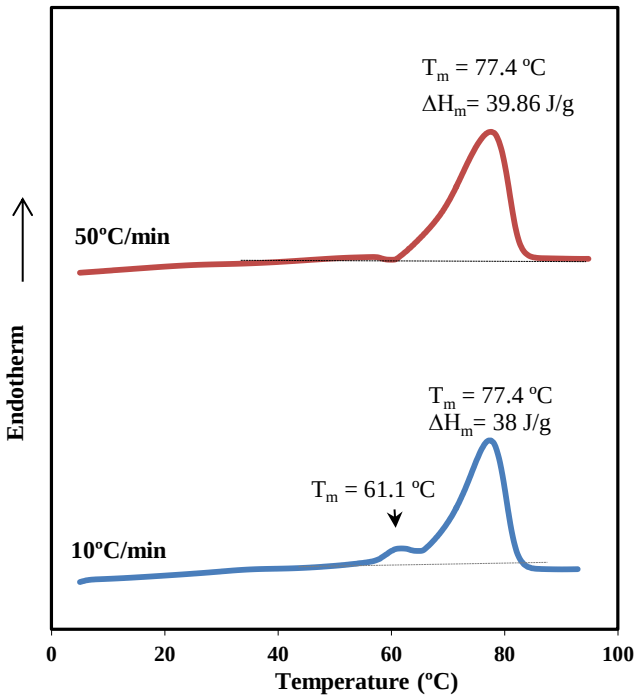




### 2. Crystalline structures of PE4,9/4 x samples

Figures 8 and 9 show X-ray diffraction profiles of as-synthesized powder samples and fiber diffraction patterns of melt drawn samples, respectively. PE44 data correspond to the *α*-crystal modification, which usually occurs under the most common crystallization conditions. This structure is defined by a $P12_1/n1$ monoclinic space group with unit cell dimensions *a* = 0.523 nm, *b* = 0.912-0.908 nm, *c* (chain axis) = 1.079-1.090 nm, and β = 123.9º .[25-27] Molecular conformation corresponds to the $T_7G\overline{T}\overline{G}$ torsional angle sequence where the gauche and minus gauche angles belong to the succinate unit. The most intense reflections observed in powder and fiber diffraction patterns appear at 0.452, 0.408 and 0.393 nm, and are indexed as the (020), (021) and (110) planes.

**Figure 7.** DSC cooling scans (10 ºC/min) of melted PE4,9/4 *x* samples.

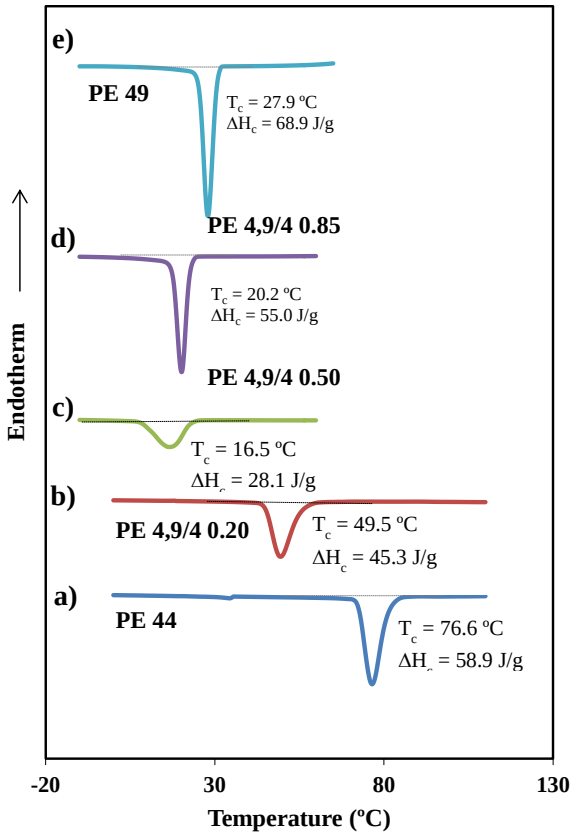




The crystalline structure of PE49 has not been reported yet, but an orthorhombic unit cell with *a* = 0.496 nm, *b* = 0.746 nm, *c* (chain axis) = 3.65 nm can be deduced from the experimental patterns (Table 2). Thus, 00*l* reflections appear with clear meridional orientation and allow estimating a chain repeat identical to the value expected for an all-trans conformation (*i.e.*, ca. 3.65 nm for two chemical repeat units). Systematic absences are observed for odd 00*l* reflections since chain periodicity corresponds to two repeat units related to a two-fold screw axis. The other two unit cell parameters are close to values reported for aliphatic polyesters having a planar *zig-zag* conformation.[28] The observed reflections point to a $P2_12_12_1$ space group since a higher symmetry can be discarded as no systematic absences related to *h*0*l*, 0*kl* and *hk*0 reflections were observed. The powder diffraction profile showed practically only two strong

peaks that corresponded to the (110) and (020) reflections at 0.415 nm and 0.377 nm. These can be clearly distinguished from those characteristic of the PE44 crystalline structure even if the second polymorphic form,[26] the so named β form with unit cell parameters $a$ = 0.584 nm, $b$ = 0.832 nm, $c$ (chain axis) = 1.186 nm, and β = 131.6º, is considered.

**Table 2.** Measured and calculated diffraction spacings (nm) for PE49.

| *hkl*[a] | $d_{calc}$ (nm) | $d_{measd}$[b] (nm) |
|---|---|---|
| 110 | 0.413 | 0.413 vs E |
| 020 | 0.373 | 0.373 s E |
| 120 | 0.298 | 0.301 w E |
| 200 | 0.248 | 0.249 w E |
| 130 | 0.222 | 0.221 vw E |
| 220 | 0.207 | 0.205 w E |
| 013 | 0.636 | 0.638 vw off M |
| 004 | 0.912 | 0.912 w M |
| 006 | 0.608 | 0.607 vw M |
| 008 | 0.456 | 0.453 mM |
| 00,10 | 0.365 | 0.365 m M |
| 01,15 | 0.231 | 0.227 w off M |
| 02,14 | 0.214 | 0.212 m off M |
| 02,15 | 0.204 | 0.202 m off M |

[a]Indexed according to an orthorhombic unit cell with $a$ = 0.496 nm, $b$ = 0.746 nm and $c$ = 3.65 nm. [b]From a fiber diffraction pattern. Abbreviations denote relative intensities and orientations: vs, very strong; s, strong; m, medium; w, weak; vw, very weak; E, equatorial; M, meridional; off M, off meridional.

Powder diffraction patterns of copolymers showed their crystallization according to the PE44 structure for azelate unit ratios equal to or lower than 0.5 whereas the PE49 structure was characteristic of samples with higher azelate unit content (Figure 8). Nevertheless, a small percentage of the PE44 structure was detected in the profile of PE4,9/4 0.35. Fiber diffraction patterns in Figure 9 show similar trends, although in this case the most relevant features

observed for the sample with the intermediate composition (*i.e., x* = 0.5) were associated with the PE49 structure (*e.g.,* see blue arrows for equatorial and 15$^{th}$ layer line reflections). This structure can be clearly favored by the melt-drawing process, and even by rapid cooling of fibers, as previously deduced from DSC analysis. The pattern was complex since spots corresponding to the PE44 structure were also detected (*e.g.*, see red arrow pointing to the strong (020) reflection).

X-ray profiles also show a gradual variation of spacings associated with the main reflections with copolymer composition. Thus, the *d*-spacing values of the strong (110) and (020) reflections associated with the PE49 structure increased and decreased, respectively, up to 0.421 nm and 0.374 nm with increasing comonomer content. This means that, in essence, packing density remained practically constant as the increase of the *a* parameter was compensated by the decrease of the *b* parameter. By contrast, the *d*-spacing values of the stronger PE44 reflections increased with comonomer content (*e.g.,* from 0.452 nm to 0.460 nm, from 0.393 nm to 0.398 nm and from 0.408 nm to 0.414 nm for (020), (110) and (021) planes, respectively), suggesting a decrease in packing density caused by the presence of foreign units. Note that crystallization temperature decreased with comonomer content, and therefore a small contraction of the unit cell was expected instead of the observed expansion if only a temperature effect was considered. It should also be pointed out the increase in azelate unit content resulted in the splitting of the (020) reflection. This is relevant in the profile of the PE4,4/9 0.50 sample, where a clear peak at 0.454 nm can be observed.



Diffraction data demonstrated that despite the random distribution of comonomer units and the great differences between succinic acid and azelaic acid units (short and long dicarboxylic units constituted by an even and an odd number of main chain atoms), all studied copolymers are semicrystalline. Minimum distortion of the predominant structure seems to occur with increasing comonomer content due to exclusion of foreign units from the crystalline phase.

**Figure 8.** X-ray powder profiles of as-synthesized PE4,9/4 *x* samples with labelling (spacing in nanometers) of main diffraction peaks.

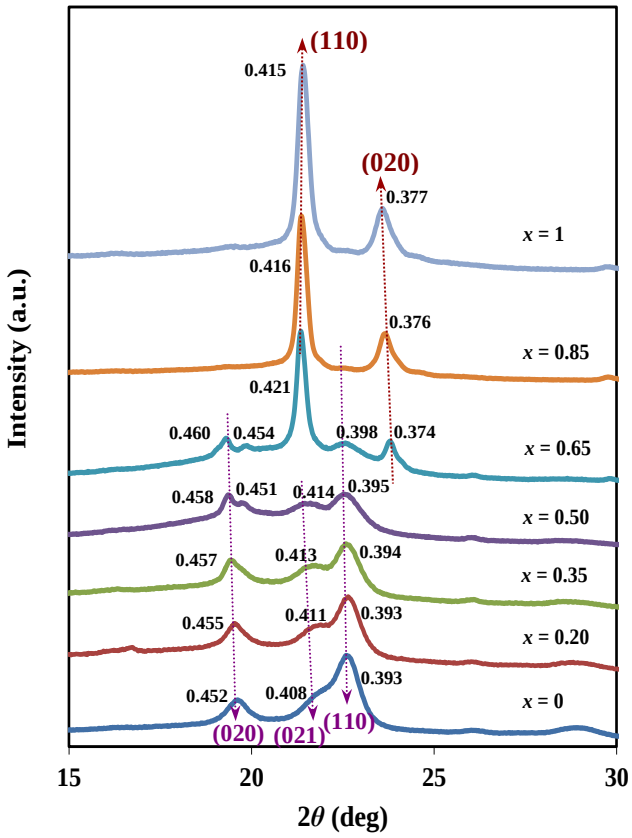

**Figure 9.** X-ray fiber patterns of melt drawn PE44 (a) PE4,9/4 0.5 (b), PE49 (c), PE4,9/4 0.20 (d), PE4,9/4 0.35 (e) and PE4,9/4 0.85 (f) samples. Insets show equatorial reflections at low exposure.

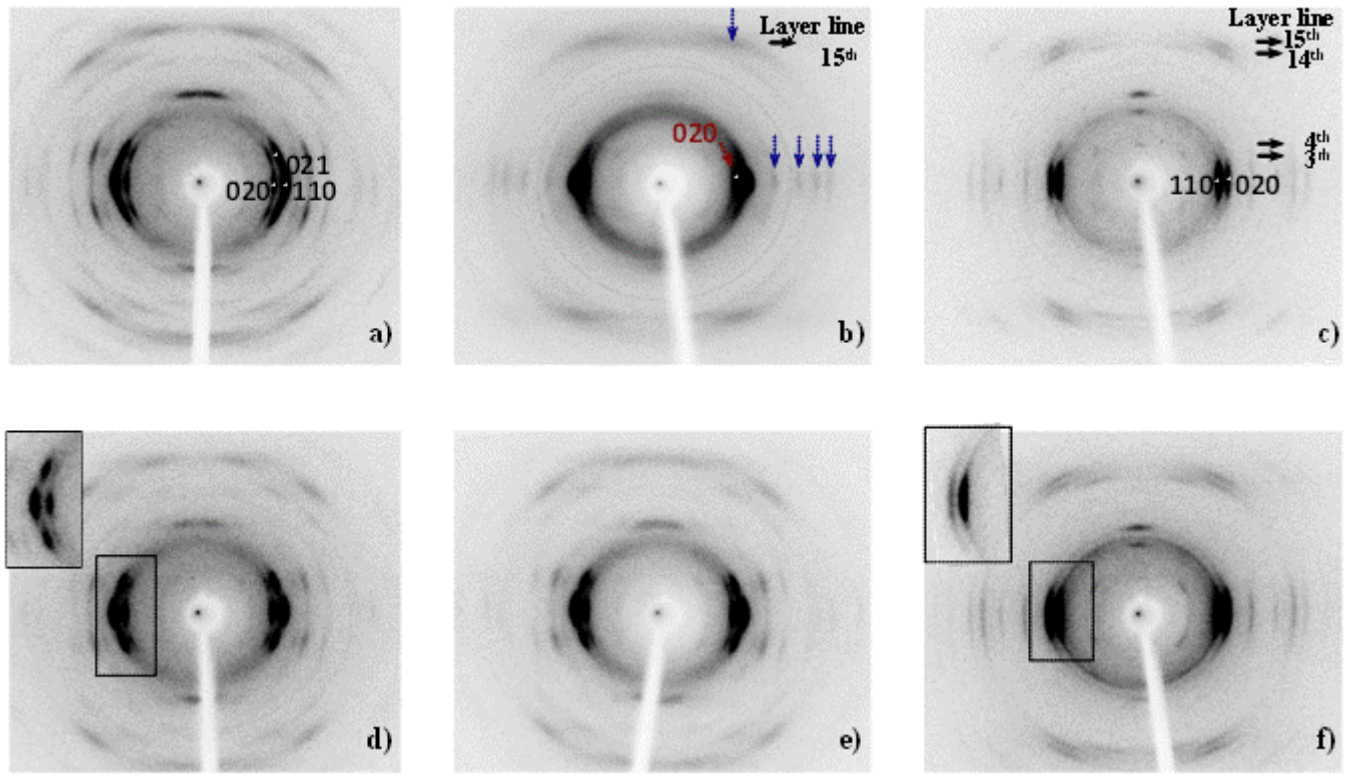

### 3. Spherulitic morphologies of PE4,9/4 x samples

Copolymers crystallized according to two types of spherulitic morphologies depending on which structure mainly developed (*e.g.*, PE44 or PE49). Banded spherulites with concentric extinction rings were characteristic of samples with $x \leq 0.5$, whereas a negatively birefringent, axialitic morphology was characteristic of PE49 and copolymers with $x > 0.5$ (Figure 10). It is well known that poly(butylene succinate) grows in banded spherulites in a wide temperature window with a unclearly delineated high temperature threshold.[29,30] Band periodicity comprises two bands of zero birefringence that suggest cooperative and in phase lamellar twisting with extinction rings corresponding to regions where lamellae have a nearly flat-on arrangement.[31-33]

**Figure 10.** Polarized optical micrographs of PE49 (a), PE4,9/4 0.85 (b), PE4,9/4 0.5 (c) and PE4,9/4 0.20 (d) spherulites prepared by isothermal crystallization at 39, 33, 37 and 57 ºC, respectively.



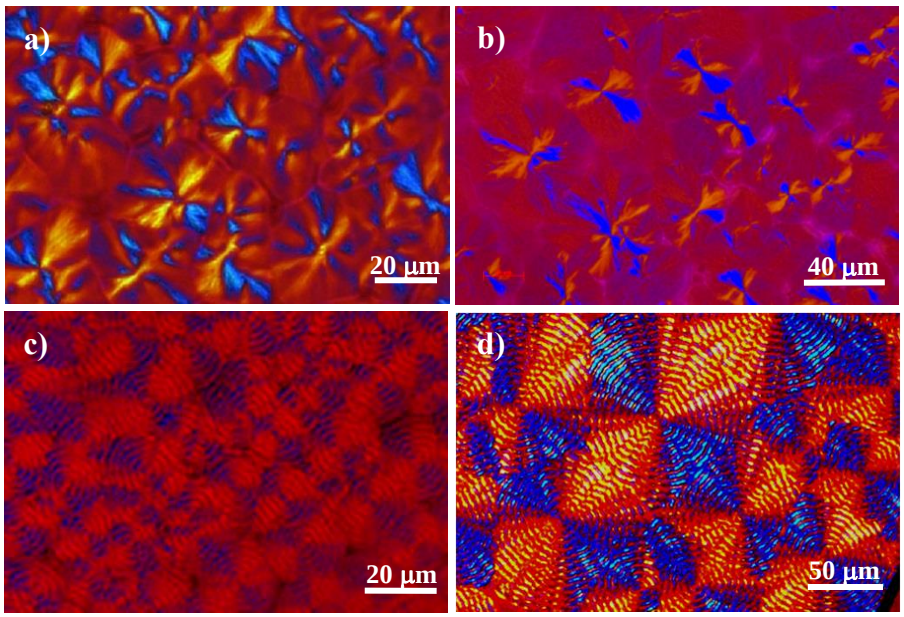

AFM micrographs (Figure 11a) of copolymers with a high succinate content revealed the presence of alternative ridges and valleys along the radial direction which consisted of edge-on and flat-on lamellae, respectively. This morphology was less clear when the succinate content decreased up to 50% due to the reduced size of spherulites and the presence of numerous globular aggregates inside of them (Figure 11b) that can be related to azelate-rich fractions. Nevertheless, the spherulite nuclei and crystals forming the limits of banding can still be envisaged. Figure 11c illustrates the typical axialitic morphology of PE49, which was even observed for copolymers with high azelate content. Axialites were constituted by aligned, edge-on lamellae that developed from the nucleus and flat-on lamellae that developed outward and had a regular thickness (*e.g.,* 9-10 nm for PE49 crystallized at 39 ºC), as revealed by AFM height profiles (not shown). Note also that polarizing optical micrographs of these samples (*e.g*., Figure 10b) revealed the presence of zero birefringence domains (red color) that correspond to flat-on lamellae grown in the outer regions of axialites.



### 4. Enzymatic degradation of PE4,9/4 x samples

The weight loss of neat polyesters and copolymers during enzymatic degradation in the lipase medium is plotted in Figure 12. Studies were performed at 25 ºC due to low melting temperature of some copolymers and obviously to obtain comparable data for all samples at a common temperature. The study of the enzymatic degradability of the considered series of polyalkylene dicarboxylates has never been performed until now despite this family of biobased polyesters show highly promising applications.[23]

The difference in susceptibility towards enzymatic attack of the two homopolyesters (*i.e.*, weight losses were greater than 80% after 28 days of exposure and lower than 5% after 48 days for the azelate and succinate derivatives, respectively) is worth noting. In fact, it has been previously reported that enzymatic degradability of polyesters derived from 1,4-butanediol and aliphatic and linear dicarboxylic acids with a number of methylene groups ranging from 2 to 8 (*i.e.*, from succinic acid to sebacic acid) is highly variable.[34] Specifically,

the azelate derivative degraded faster in lipase media (*e.g.,* from *Pseudomonas fragi* and *Rhizopus delemar*) than the succinate derivative, with differences depending on the selected enzyme. Specificity of enzymes to the polymer substrate and physical properties of polymers should be considered to justify these observations.

**Figure 11.** Atomic force microscopy amplitude images of PE4,9/4 0.20 (a), PE4,9/4 0.50 (b), and PE49 (c) spherulites crystallized at 57, 37, and 39 ºC.

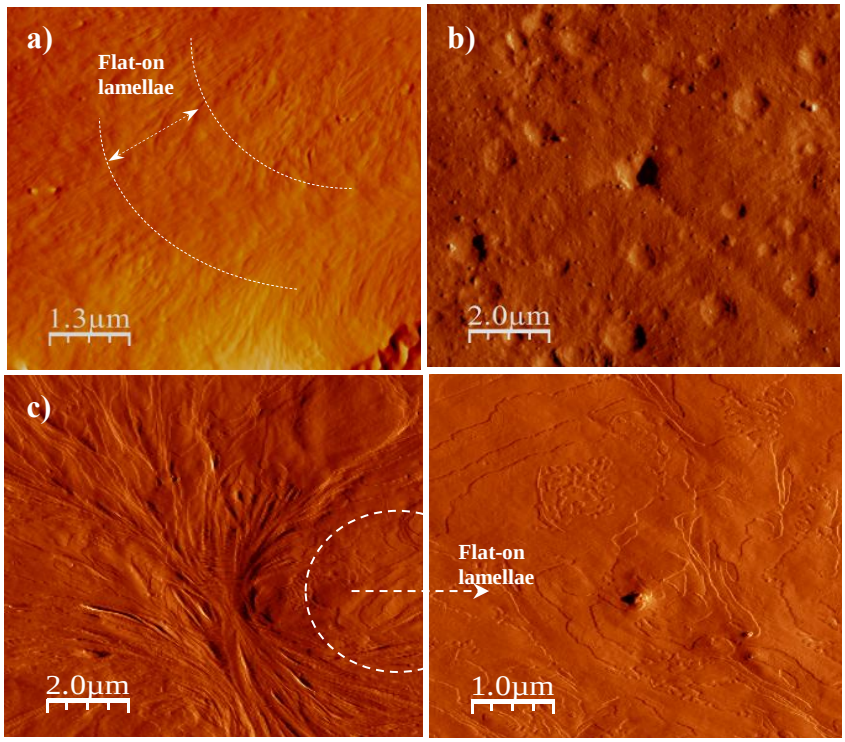




Molecular weights of the polyester were similar, and consequently differences in degradation behavior should be explained in terms of degree of crystallinity,[35] size of crystalline domains,[36] crystalline structure,[37] lamellar surface structure[38] and molecular mobility.[39] Moreover, lipases are endo-type enzymes that degrade ester groups of molecular chains randomly, and therefore biodegradability should not be significantly affected by variations in the molecular weight. Physical characterization of PE49 demonstrated that

crystallization rendered smaller spherulites than those developed from PE44. Furthermore, chain mobility was higher for PE49, as can be deduced from the lower melting and glass transition temperatures (*i.e.*, -62 and -38 ºC for PE49 and PE44, respectively[14]). In addition, PE49 has a more hydrophobic surface which upon binding can induce a conformational change of the lipase enzyme that can make its active site fully accessible.[40,41]

**Figure 12.** Weight loss of PE4,9/4 *x* samples during exposure to the lipase medium at 25 ºC. For comparative purposes, degradation data of PE4,9/4 0.35 sample exposed at 37 ºC are also plotted.

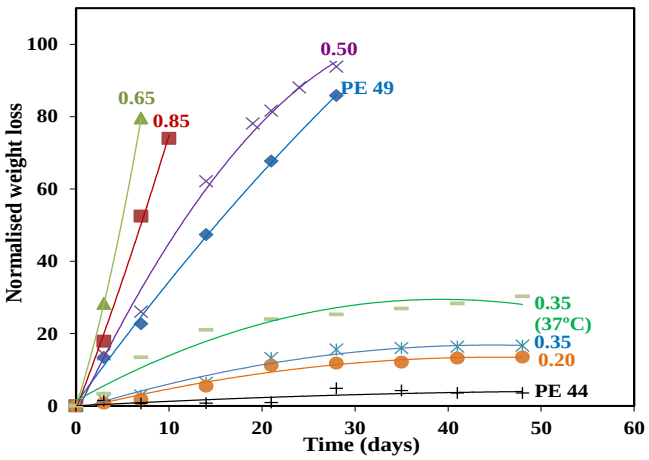




Copolymers were found to degrade faster than the homopolymer corresponding to the predominant crystalline structure (*i.e.*, PE44 for $x \leq 0.5$ and PE49 for $x > 0.5$). In this case, it is clear that the degree of crystallinity and spherulite size decreased with comonomer content. Both crystalline and amorphous phases of copolymers became less ordered or more accessible compared to the corresponding phases of parent homopolymers. Also, crystalline and chemical structure played a fundamental role since no maximum of degradation was found for the intermediate composition ($x = 0.5$), as expected if the increase of the amorphous content is the main factor causing biodegradability.

Figure 12 also shows the enhancement of degradability with increasing temperature. Specifically, results obtained at 25 ºC and the physiological temperature of 37 ºC are compared for the PE4,4/9 0.35 sample, which still has a sufficiently high melting temperature.

Degradation was also evaluated by morphological observation of exposed samples. Homopolymers and copolymers evolved differently, as can be seen in Figures 13 and 14, respectively. Thus, enzymatic attack on the surface of polyester films resulted in pores with degradation products inside that were progressively released into the medium. These pores were abundant in the PE49 sample and more scarce in PE44 despite its longer exposure time (Figure 13). However, a change respect to the surface of unexposed samples was evident even for low weight losses.

Abundant surface cracking and flaking off were usually observed in exposed copolymer samples (Figure 14). In this case, enzymatic attack occurred more easily, probably because of the more abundant amorphous domains and smaller crystalline spherulites. This made it possible for degradation to also occur in the inner parts of films after initiation of enzymatic attack on their surface (see Figure 15 for representative copolymers).



Figure 16 is especially interesting since spherulitic morphologies became progressively highlighted during the degradation process of PE4,4/9 0.20, which is the copolymer that forms largest spherulites. In a first step, the amorphous regions started to degrade and spherulites gradually appeared. Subsequently, degradation took place inside the spherulites and revealed a ringed structure. Edge-on and flat-on lamellae should had different susceptibility to the enzymatic attack and consequently it was possible to detect peculiar morphologies derived from the previously described ringed spherulites (Figure 17). Results point out the capability of enzymes to degrade crystalline regions in a way that depends on morphology (*e.g.*, flat-on or edge-on crystals) and the supramolecular arrangement. Several studies have been performed about degradation of single crystals of different degradable polyesters being found that enzymatic attack may proceed in a different way depending on the crystal morphology, the exposed surface and even the specific folding sectors existing on the lamellar surface.[42,43]

**Figure 13.** Scanning electron micrographs of PE44 (a,b) and PE49 (c) samples before (a) and after exposure to the lipase medium at 25 ºC for 41 days (b), and 28 days (c).

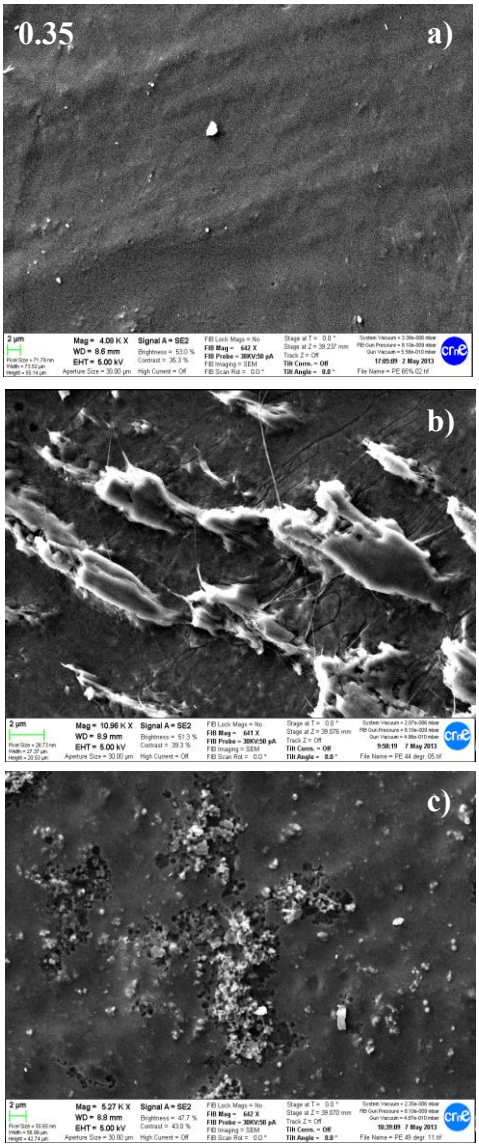

**Figure 14.** Scanning electron micrographs of PE4,9/4 0.85 (a), PE4,9/4 0.65 (b), PE4,9/4 0.50 (c), PE4,9/4 0.35 (d) and PE4,9/4 0.20 (e) samples after exposure to the lipase medium at 25 ºC for 14, 7, 21, 41 and 41 days, respectively. White arrow shows the formation of spherulites after degradation of the surface material.

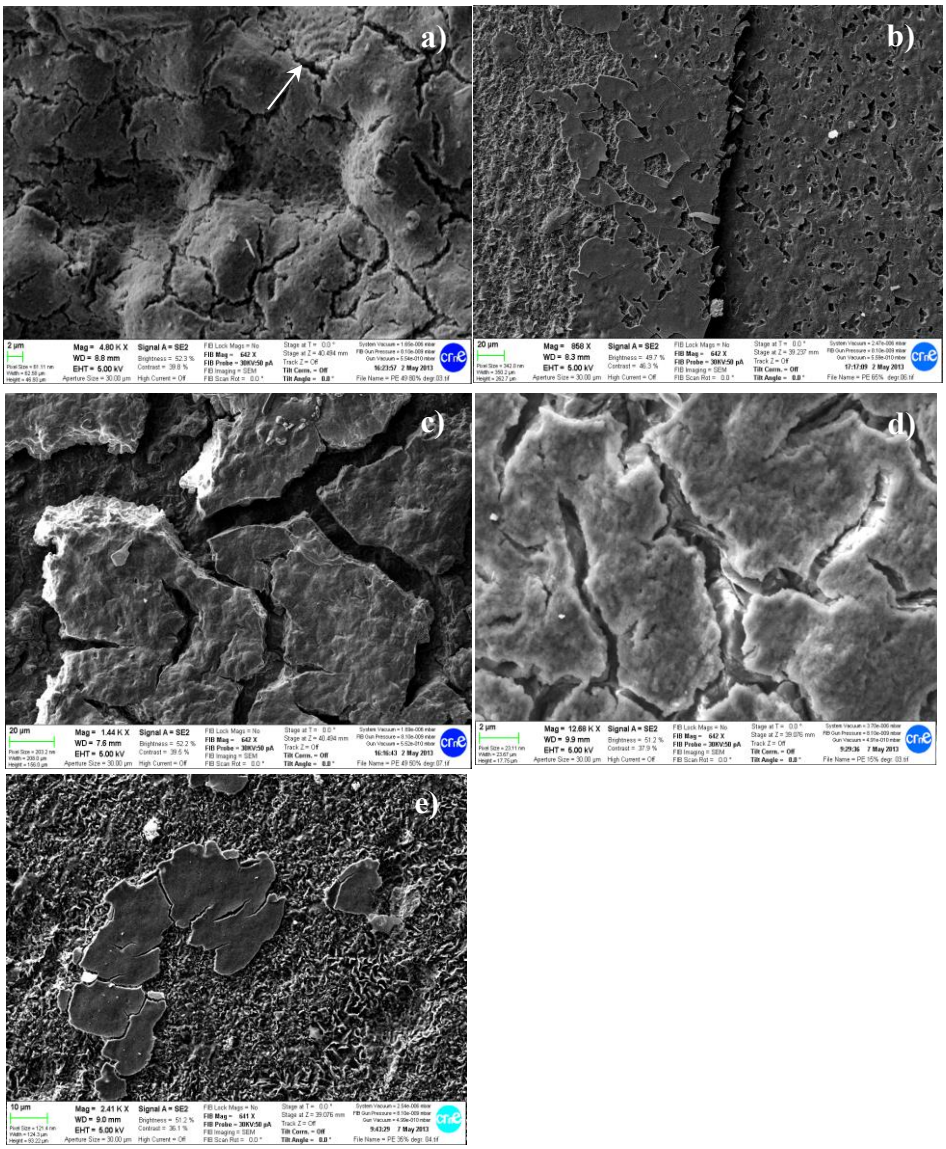

**Figure 15.** Scanning electron micrographs of lateral surfaces of PE4,9/4 0.85 (a), PE4,9/4 0.65 (b), and PE4,9/4 0.35 (e) samples after exposure to the lipase medium at 25 ºC for 14, 7 and 41 days, respectively. Inset shows a detail of the film surface.

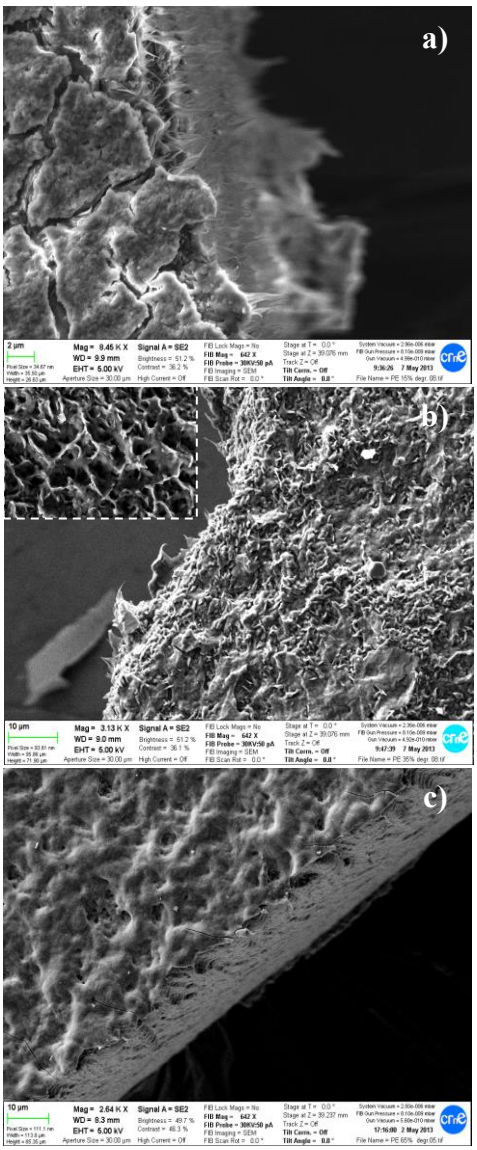

**Figure 16.** a) Scanning electron micrographs of PE4,9/4 0.20 samples after exposure to the lipase medium at 25 ºC for 3 (a), 7 (b), 14 (c) and 21 days (d). White arrows point out spherulitic morphologies that are progressively highlighted.

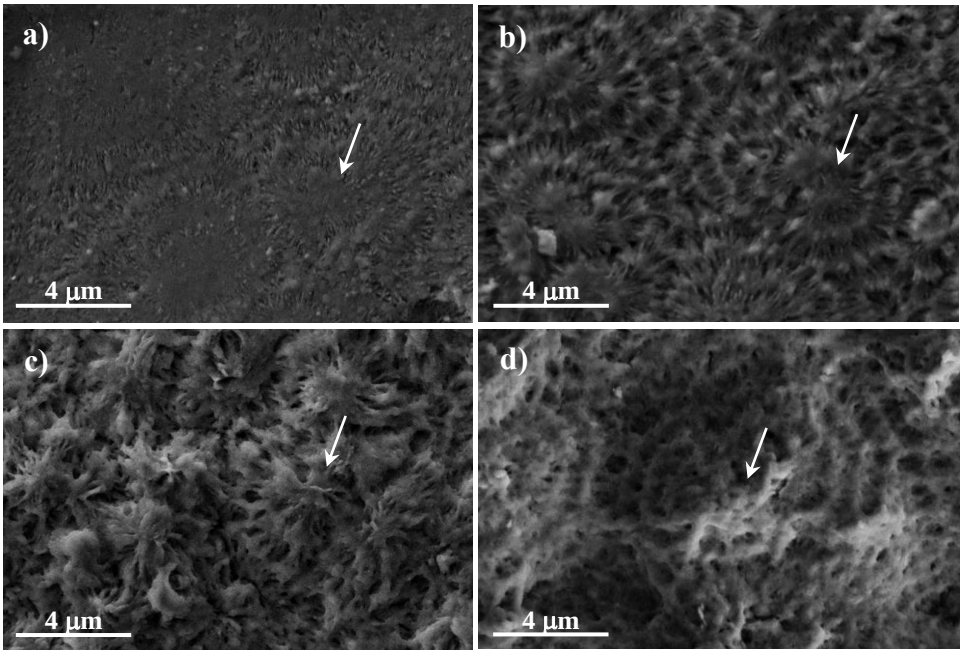




**Figure 17.** a) Scanning electron micrograph of the spherulitic morphology of a PE4,9/4 0.20 sample after exposure to the lipase medium at 25 ºC for 41 days. b) Optical micrograph given for comparative purposes of the ringed structure of a PE4,9/4 0.20 sample isothermally crystallized at 65 ºC.

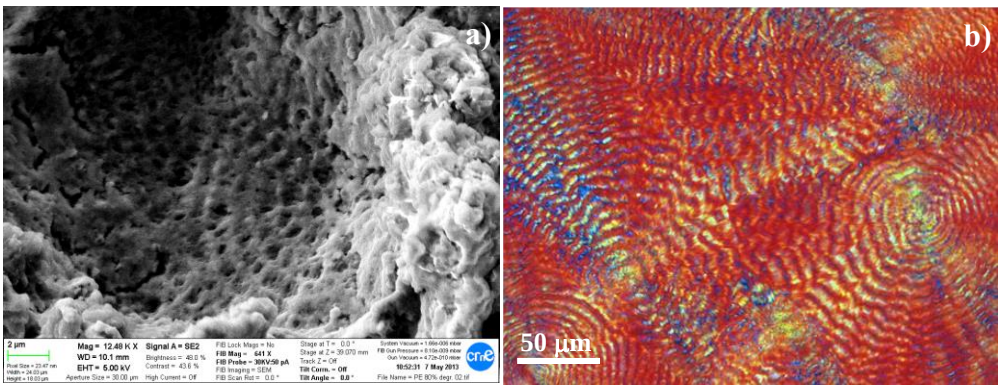

## VI. Conclusions

The outcome of the present study can be summarized as follows:

a) Thermal polycondensation of 1,4-butanediol and mixtures of azelaic and succinic acids is an effective way to prepare copolymers with a random distribution and melting points within a wide temperature range (*i.e.*, 36 ºC-113 ºC).

b) Despite their random distribution, all studied copolymers are semicrystalline and crystallize according to the well differentiated structures of PE44 and PE49 homopolymers depending on whether azelate or succinate is the predominant dicarboxylate unit. Minimum distortion of the unit cell occurs with increasing comonomer content due to exclusion of foreign units from the crystalline phase.

c) The sample with the intermediate composition has the lowest melting enthalpy and a complex crystallization behavior where both PE44 and PE49 structures can be favored depending on crystallization and processing conditions. Interestingly, the PE49 structure, which is characterized by a more extended molecular conformation, is favored by melt drawing, even when the sample is rapidly cooled from the melt.



d) Crystalline morphologies of copolymers are highly different depending on the predominant structure: small negatively birefringent axialitic morphologies for PE49 and large banded spherulites with concentric extinction rings for PE44.

e) Enzymatic degradability of polyesters constituted by azelate or succinate units differs considerably. Thus, samples having distinctive, controlled biodegradability can be easily generated by copolymerization. Copolymers have significant amorphous domains that facilitate enzymatic attack and lead to post-exposure surface textures that are clearly different from those developed in the more crystalline homopolyester samples. Constituent spherulites can become highlighted during degradation if they have the appropriate size and are surrounded by significant amorphous zones.

## V. References


1. Yoshito I, Hideto T. Macromol Rapid Commun 2000;21:117.
2. Doi Y, Steinbüchel A. Polyesters II – properties and chemical synthesis. New York: Wiley-VCH; 2002.
3. Huang SJ, editor Encyclopedia of polymer science and engineering. Vol. 2 New York: Wiley-Interscience; 1985. p. 20.
4. Yasushi I, Tatsuya M. Adv Polym Sci 2012;245: 285.
5. Fujimaki T. Polym Degrad Stab 1998;59:209.
6. Lai SM, Huang CK; Shen HF. J Appl Polym Sci 2005;97:257.
7. Li F, Xu X, Hao Q, Yu J, Cao A. J Polym Sci Part B: Polym Phys Ed 2006;44:1635.
8. Qiu Z, Ikehara T, Nishi T. Polymer 2003;44:7519.
9. Qiu Z, Komura M, Ikehara T, Nishi T. Polymer 2003;44:8111.
10. Mochizuki M, Mukai K, Yamada K, Ichise N, Murase S, Iwaya Y. Macromolecules 1997;30:7403.
11. Yang J, Tian W, Li Q, Cao A. Biomacromolecules 2004;5:2258.
12. Li X, Hong Z, Sun J, Geng Y, Huang Y, An H, et al. J Phys Chem 2009;113:2695.
13. Gan Z, Abe H, Doi Y. Biomacromolecules 2000;1:704.
14. Gan Z, Abe H, Doi Y. Biomacromolecules 2000;1:713.
15. Gan Z, Abe H, Doi Y. Biomacromolecules 2001;2:313.
16. Iwata T, Doi Y. Macromol Chem Phys 1999;200:2429.
17. Li X, Sun J, Huang Y, Geng Y, Wang X, Ma Z, Shao CG, An HN, Yan TZ, Li LB. Macromolecules 2008;41:3162.
18. Liang Z, Pan P, Zhu B, Dong T, Hua L, Inoue Y. Macromolecules 2010;43:2925.
19. Liang Z, Pan P, Zhu B, Inoue Y. Polymer 2011;52:2667.
20. Lee JH, Jeong YG, Lee SC, Min BG, Jo WH. Polymer 2002;43:5263.
21. Hojabri L, Kong X, Narine SS. Biomacromolecules 2010;11:911.
22. Papageorgiou GZ, Bikiaris DN. Biomacromolecules 2007;8:2437.
23. Mincheva R, Delangre A, Jean-Marie Raquez JM, Narayan R, and Dubois P. Biomacromolecules 2013;14:890.
24. Díaz, A., Franco, L., Puiggalí, J. Thermochimica Acta 2014;575:45.
25. Ihn, KJ, Yoo ES, Im SS. Macromoleculess 1995;28:2460.

26. Ichikawa Y, Kondo H, Igarashi Y, Noguchi K, Okuyama K, Washiyama J. Polymer 2000;41:4719.
27. Ichikawa Y, Suzuki J, Washiyama J, Moteki Y, Noguchi K, Okuyama K. Polym 1994;35:3338.
28. Brandrup J, Immergut EH, Grulke EA, Editors. “Polymer Handbook,” 4th ed., chap. 6. New York: Interscience Publishers 1999.
29. Ikehara T, Kurihara H, Kataoka T. J Polym Sci Part B: Polym Phys Ed 2009;47:539.
30. Wang T, Wang H, Li H, Gan Z, Yan S. Phys Chem Chem Phys 2009;11(10):1619.
31. Keith HD, Padden FJ. J Polym Sci 1959;39(101):123.
32. Keller A. J Polym Sci 1959;39:151.
33. Lotz B, ChengSZD. Polymer 2005;46:577.
34. Shirahama H, Kawaguchi Y, Aludin MS, Yasuda H. J Appl Polym Sci 2001;80:340.
35. Yuan M, Wang Y, Li X, Xiong C, Deng X. Macromolecules 2000;33:1613.
36. Rizzarelli P, Puglisi C, Montaudo G. Polym Degrad Stab 2004;85:855.
37. Gan Z, Kuwabara K, Abe H, Iwata T, Doi Y. Polym Degrad Stab 2005;87:191.
38. Casas MT, Puiggalí J. Polym Degrad Stab 2009;94:1941.
39. Marten E, Müller R.J, Deckwer W.D. Polym Degrad Stab 2005;88:371.
40. Jaeger KE, Ransac S, Dijkstra BW, Colson C, van Heuvel M, Misset O. FEMS Microbiol Rev 1994;15:29.
41. Derewenda U, Brzozowski AM, Lawson DM, Derewenda ZS. Biochemistry 1992;31:1532.
42. Iwata T, Doi Y. Polym Int 2002;51:852.
43. Casas MT, Puiggalí J. Polym Degrad Stab 2009;94:1941.

# Chapter 4.

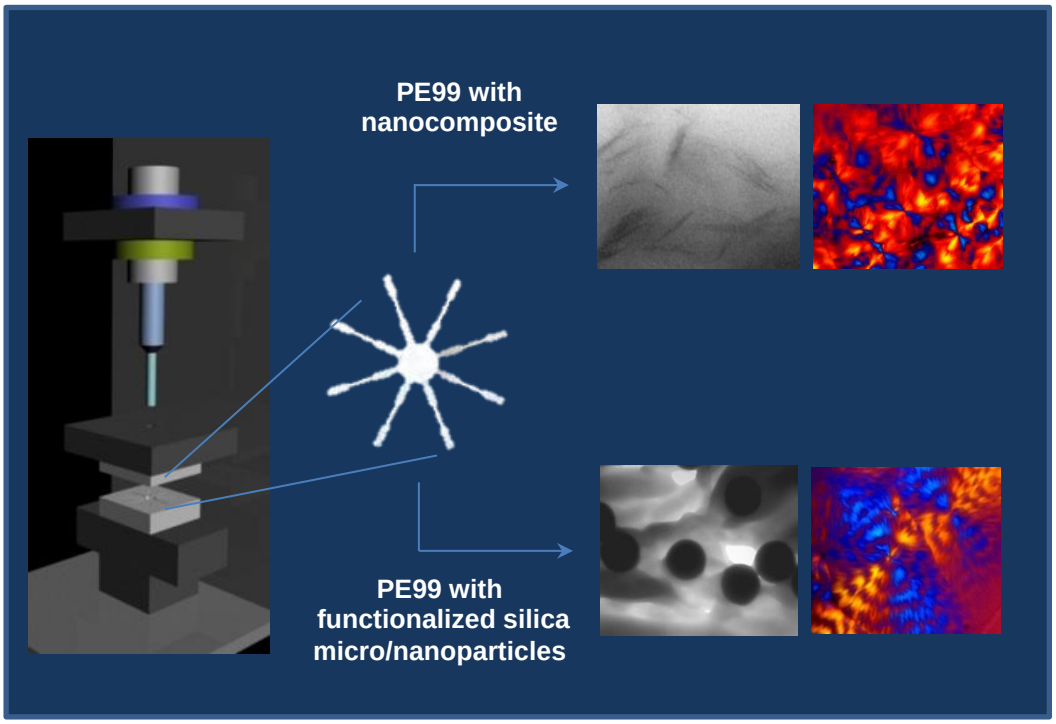
PE99 with
nanocomposite
PE99 with
functionalized silica
micro/nanoparticles

# Chapter 4.1

## *Preparation of micro-molded exfoliated clay nanocomposites by means of ultrasonic technology.*

Ultrasound micro-molding technology has been tested as a new method to get polymer/clay nanocomposites. Biodegradable polylactide (PLA) and poly(nona-methylene azelate) (PE99) have been used as polymer matrices, whereas different silicate clays have been assayed. The new technology is able to get specimens without evidences of degradation during processing. Only the use of organo-modified clays could give rise to a slight molecular weight decrease when the poly(alkylene dicarboxylate) sample was considered. Ultrasonic micro-molding has revealed effective to get directly nanocomposites with the final form required for a selected application, a homogeneous clay distribution up to a load of 6 wt-% and more interestingly exfoliated structures without being necessary the use of a compatibilizer agent between the organic polymer and the inorganic silicate clay. Transmission electron micrographs and X-ray diffraction profiles revealed exfoliated structure when N757, C20A, C25A, and N848 clays were employed.

Crystallization behavior of exfoliated PLA nanocomposites was highly peculiar since clay particles had an antinucleating effect that decreased the overall crystallization rate respect to the neat polymer. In addition, the incorporation of layers into growing spherulites increased the crystal growth rate. A typical crystallization effect was on the contrary observed for nanocomposites derived from the poly(alkylene dicarboxylate) sample.

## I. Introduction

Polymer nanocomposites refer to multiphase materials where at least one of the constituent phases has one dimension in the nanoscale range (<100nm). Nanofillers in polymers give access to polymer composites with enhanced mechanical, optical, thermal or magnetic properties.[1] Nanocomposite materials usually have improved characteristics as compared with their individual components and often show an excellent balance between strength and toughness.[2] Nanocomposites have also great expectatives in the biomedical field due the wide range of applications and the vastly different functional requirements.[3] Potential of nanocomposites are being progressively exploited to make radically new materials while mechanisms responsible for macroscopic properties become clarified.

Nanofillers can be made from a wide range of materials, the most common are clay silicates (aluminosilicate-based nanofillers), carbon nanotubes, metal-oxide ceramics, and metal nonoxide ceramics. Different routes are described to obtain clay nanocomposites such as, *in situ* polymerization, solution method, melt mixing and template synthesis.[4] The *in situ* polymerization represents the best procedure of preparing highly exfoliated nanocomposites with a truly delaminated structure that leads to a significant enhancement of mechanical and physical properties. However, a fully exfoliation of nanosheets is difficult and a mixture between intercalated and exfoliated structures is usually attained independently of the applied methodology. One additional problem concerns the charged and highly hydrophilic nature of clays that make them incompatible with a wide range of polymers. Until now, a necessary prerequisite for successful formation of polymer-clay nanocomposites is the modification of the clay by ion exchange with an organic cation such as an alkylammonium that leads to an organophilic clay. Nevertheless efforts focused to prepare completely exfoliated polymer-clay nanocomposites without being necessary a chemical modification appear nowadays highly interesting and even necessary.

Ultrasonic waves are an energy source for melting and welding polymer samples that has been applied as an assembly procedure for over 40 years. This source has also been applied for the preparation of nanocomposites.[5] Recently, the possibility of using ultrasonic energy for

micro-molding applications has also been studied with highly promising results. Specifically, it has been demonstrated that polylactide (PLA) can be well processed by this technology without an appreciable degradation.[6] It seems also that the ultrasonic energy may make feasible the delamination of a silicate structure and therefore may favor the attainment of an exfoliated structure when a polymer/clay powder mixture is processed. This feature is highly important since nanocomposites can therefore be obtained directly in a single step with the micro-molded form required for a final application as for example micropieces used for biomedical devices.

Biodegradable polymers and particularly polyesters as the indicated PLA have nowadays great interest for biomedical applications due to its attractive mechanical properties, renewability and relatively low cost. They are widely employed for many applications such as sutures, materials for tissue regeneration, orthopedics, scaffolds and systems for controlled release of drugs in medicine.[7-12] The great interest in PLA based bionanocomposites is directly supported by the significant increase in the number of derived scientific publications,[13] which clearly demonstrates an improvement of biodegradation rate and mechanical, thermomechanical and gas barrier properties.[14,15] Poly(alkylene dicarboxylate)s constitute another family of polyesters that offer great possibilities especially considering that most of them can be obtained from renewable resource and reduce the dependence on fossil fuels[16]. Poly(nonamethylene azelate) (PE99) is a clear example since both azelaic acid and 1,9-nonanediol monomers can be obtained by ozonolysis cleavage of the alkene double bond of oleic acid and subsequent oxidation and reduction.[16,17] The effect of the organoclay in biodegradation is complex since the attack of microorganisms depends on the nature of the clay and the chemical structure of added surfactants.[18-21] Thus, the appropriate selection of organoclays may give a method to tune the biodegradation rate.



The main goal of the present study is the evaluation of the capability of ultrasonic energy as a new processing method to get exfoliated nanocomposites. PLA and PE99 have been selected as the polymer matrix since are representative of two families of biodegradable polyesters with extensive or potential biomedical applications. The achievement of exfoliated structures will be evaluated by X-ray diffraction, TEM observations and the study of isothermal

crystallization. The last is significant since it has been reported a peculiar crystallization behavior for PLA/clay exfoliated nanocomposites as it will be later discussed.[22]

## II. Experimental Section

### 1. Materials

The polylactide (PLA) used in this work was a commercial sample (EcoreneR NW 30) from Nature Works (USA) with high crystallinity and a low molecular weight. Poly(nonamethylene azelate) (PE99) was synthesized by thermal polycondensation of azelaic acid with an excess of 1,9-nonanediol (2.2:1 molar ratio). Titanium tetrabutoxyde was used as a catalyst and the reaction was first performed in a nitrogen atmosphere at 150 ºC for 6 h and then in vacuum at 180 ºC for 18 h. Polymer was purified by precipitation with ethanol of a chloroform solutions (10 wt-%). Number average molecular weight and polydispersity index determined by GPC and using poly(methyl methacrylate) standards were 13,200 g/mol and 3.10, respectively.



Four different phyllosilicates were investigated and used as received: pristine sodium montmorillonite (Nanofil 757), organoclay octadecyl ammonium montmorillonite (Nanofil 848, Süd Chemie, ODA), dimethyl dihydrogenated-tallow ammonium montmorillonite (Cloisite 20A, Southern Clay Products, 2MH2HT) and dimethyl hydrogenated-tallow 2-ethylhexyl ammonium montmorillonite (Cloisite 25A, Southern Clay Products, 2MHTEX).

Nanocomposites will be named indicating the abbreviations of polymer and clay and wt-% of added clay (*e.g.*, PLA/N757 6 and PE99/N757 6 indicate the nanocomposites having a 6 wt-% of Nanofil 757 prepared from PLA and PE99, respectively).

### 2. PLA and PE99 clay nanocomposites preparation

Clay nanocomposites were obtained by ultrasonic micro-molding of the appropriate powder mixtures of clays and polymers. 300 mg of polymer and 9.3 or 19.1 mg of clay were ground in a mortar to get well mixed samples with a clay content of 3 and 6 wt-%, respectively.

Mixtures were subsequently loaded in the plasticing chamber of the micro-molding machine and processed by applying the selected force, amplitude and time parameters to get specimens with the geometry indicated below.

### 3. Micro-molding equipment

A prototype Ultrasound Molding Machine (Sonorus®, fabricated by Ultrasion S.L.) was used. The apparatus was composed of a controller (1000 W - 30 kHz digital ultrasound generator from Mecasonic fitted with a 3010 DG digital system), a converter (Mecasonic), an acoustic unit, an electric servomotor control (Berneker and Rainer) with software from Ultrasion S.L. and a thermally controlled mold. Molds (Ascamm) were designed to prepare eight test specimens of small dimensions (1.5 × 0.1 × 0.1 $cm^3$ under IRAM-IAS-U500-102/3 standards).

### 4. Measurements



Molecular weight was estimated by gel permeation chromatography (GPC) using a liquid chromatograph (Shimadzu, model LC-8A) equipped with an Empower computer program (Waters). A PL HFIP gel column (Polymer Lab) and a refractive index detector (Shimadzu RID-10A) were employed. The polymer was dissolved and eluted in 1,1,1,3,3,3-hexafluoroisopropanol containing $CF_3COONa$ (0.05 M) at a flow rate of 0.5 mL/min (injected volume 100 µL, sample concentration 2 mg/mL). The number and weight average molecular weights and molar-mass dispersities were calculated using polymethyl methacrylate standards.

Interlayer spacing of clay nanocomposites was studied by wide angle X-ray scattering (WAXD) using a Bruker D8 Advance model with $CuK_\alpha$ radiation ($\lambda$=0.1542 nm) and geometry of Bragg-Brentano, theta-2theta. One dimensional Lynx Eye detector was employed. Samples were run at 40 kV and 40 mA, with a 2-theta range of 2º-40º, measurement steps of 0.02º, and time/step of 2 to 8 seconds. Deconvolution of WAXD peaks was performed with the PeakFit v4 program by Jandel Scientific Software.

The distribution of the clay in the nanocomposite was also evaluated by morphologic observations using a Philips TECNAI 10 electron microscope at an accelerated voltage of 100 kV. Specimens were prepared by embedding the nanocomposite films in a low viscosity modified Spurr epoxy resin, and after cured were cut in a small sections at room temperature using a Sorvall Porter-Blum microtome equipped with a diamond knife. These sections were collected in a trough filled with water and lifted onto carbon coated copper grids. Bright field micrographs were taken with a SIS MegaView digital camera.

Polarized light microscopy and differential scanning calorimetry techniques were employed to investigate the radial spherulite growth rate and bulk crystallization kinetics, respectively.

The spherulite growth rate was determined by optical microscopy using a Zeiss Axioscop 40 Pol light polarizing microscope equipped with a Linkam temperature control system configured by a THMS 600 heating and freezing stage connected to a LNP 94 liquid nitrogen system. Spherulites were isothermally crystallized from homogeneous thin films obtained by melting 1 mg of PLA based sample between microscope slides or by solvent casting of dilute chloroform solutions of PE99 based samples. The preparation method was modified in the second case in order to reduce the thickness of the film and avoid experimental problems derived from the high nucleation of PE99. Next, small sections of these films were pressed between two cover slides and inserted into the hot stage. Samples were kept at 190 ºC or 90 ºC for 5 minutes for PLA and PE 99 respectively, to wipe out sample history effects and then quickly cooled at the desired temperatures. The radius of the growing spherulites was measured from the photographs taken at different times using a Zeiss AxiosCam MRC5 digital camera. Nucleation was evaluated by counting the number of active nuclei that appeared at constant crystallization temperature, assuming that each spherulite grew from one single active heterogeneous nucleus.



Calorimetric data were obtained by differential scanning calorimetry using a TA instrument Q100 series with $T_{zero}$ technology and equipped with a refrigerated cooling system (RCS) operating at temperatures between -90 and 550ºC. Experiments were conducted under a flow of dry nitrogen with a sample weight around 5 mg, while calibration was performed with

indium. $T_{zero}$ technology requieres a calibration based in two experiments: the first was performed without samples while sapphire disks were used in the second.

Thermal degradation was studied at a heating rate of 10 ºC/min with around 5 mg samples in a Q50 thermogravimetric analyzer of TA Instruments and under a flow of dry nitrogen. Test temperatures ranged from 50 to 600 ºC.

## III. Results and Discussion

### 1. Micro-molding of PLA and PE99

The ability of ultrasounds to plasticize polymers arises from the heating caused by inner and outer frictional losses produced under cyclic deformation. A dissipation of energy results from the rearrangement of the long chain molecules as they tend to accommodate the imposed stress, leading to the melting of all the material.



Samples were processed using a micro-molding equipment which main parts are depicted in Figure 1. Basically this equipment consists of a generator, a converter, a booster, a sonotrode, a plasticizing chamber and a mold. The high frequency (30 kHz) signal produced in the generator is sent to the converter, where piezoelectric crystals expand and contract mechanically at the same rate as the electrical oscillation. The booster amplifies or reduces the amplitude (0-137.5 µm) of the mechanical vibration and then this vibration is transferred under pressure (*i.e.*, by applying a force between 100 and 500 N) by the sonotrode to the polymer sample placed in a plasticizing chamber. A controller regulates the main processing parameters: sonotrode oscillation time (from 0.5 to 10 seg), force and amplitude of the ultrasonic wave. The molten polymer fills the mold trough the feeding channels and then is cooled while pressure is still applied. Finally, the mold is opened to extract the specimens by using the corresponding ejectors.

High intensity ultrasonic waves may cause adverse effects on the polymeric chains as a result of cavitation and the high temperature that can be reached inside the plasticizing chamber.[23-26] Thus, processing conditions (*i.e.*, molding force, amplitude and irradiation time) must be carefully chosen according to the chemical nature of each polymer in order to minimize

degradation effects. Degradation logically increases with irradiation time but a minimum period is necessary to guarantee complete injection into the mold. Effect of amplitude and molding force parameters is more complicated to evaluate but in general it could be stated that the amount of vibration energy depends on the amplitude level. Nevertheless, severe degradation can also occur at low ultrasonic amplitude and high molding force due to chain scissions caused by mechanical shear stress. Note that this stress is essential to make feasible the polymer melt flow and the filling of the mold cavity.

**Figure 1**. Scheme showing the main parts of the ultrasound micro-molding machine.

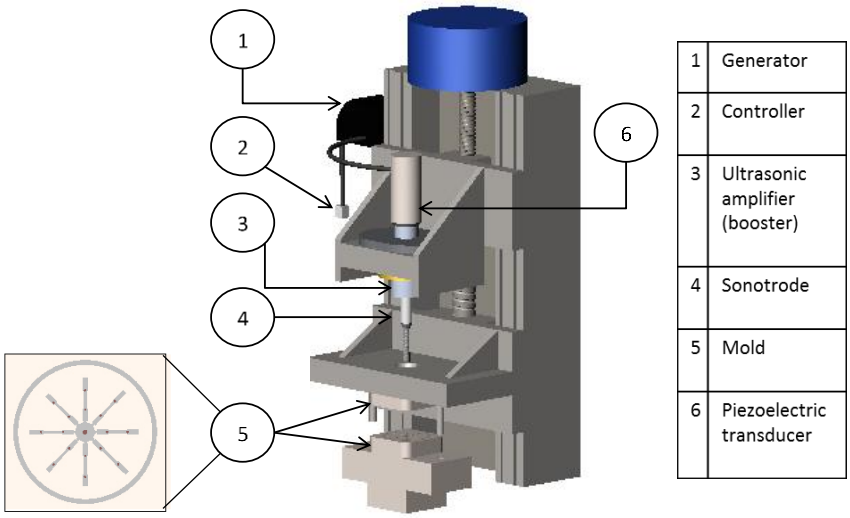




The moderate molecular weight of PLA and PE99 samples and the fact that they were supplied or synthesized in the powder form allowed to perform the micro-molding process under not highly severe conditions. Thus, a minimum irradion time of 1.2 s was sufficient to guarantee a correct mold filling and a minimum amplitude of 24 μm was sufficient to provide the energy necessary to ensure a complete fusion of polymers. In the same way, a moderate molding force (*i.e.*, 300 N) was found in all cases appropriate to get a 100% molding efficiency. Figure 2 shows micrographs of a representative micro-molded PLA under the optimized conditions and its

longitudinal section. It is clear that highly homogeneous specimens without the presence of significant cavities that could affect final properties can be easily obtained. Only some minor pores, as a consequence of processing, can be detected.

**Figure 2**. Homogeneous PLA specimen obtained by ultrasound micro-molding (a) and SEM micrographs showing details of a longitudinal section (b).

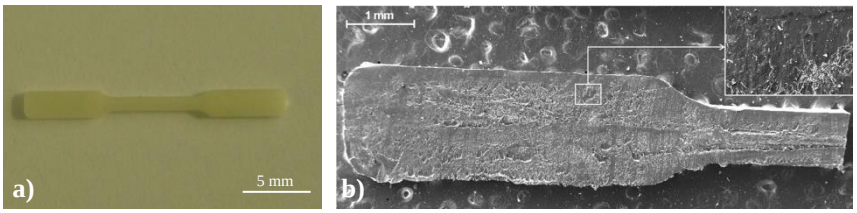


Molecular weights of raw materials and those processed under the indicated conditions are summarized in Table 1. Figure 3 also compares the GPC traces of raw and processed PE99 samples. It is clear that not significant statistical differences were found between samples before and after processing and consequently the new technology is fully adequate to get micropieces of PLA and PE99 with a negligible degradation.



## 2. Micro-molding of PLA and PE99 clay nanocomposites

Clay nanocomposites were obtained by ultrasonic micro-molding of the appropriate powder mixtures of clays and polymers. Clay content was varied from 0 to 6 wt-% being not necessary to modify the processing parameters to get specimens with a good clay dispersion as below discussed. PLA and PE99 nanocomposites were obtained without degradation for all assayed clays as summarized in Table 1 for samples containing up to a 3 wt-% of clay. However, a slight degradation was detected at a higher clay content when PE99 and organomodified clays (*i.e.*, C20A, C25A and N848) were employed as matrix and filler, respectively. This effect was greater for the PE99/N848 nanocomposite but even so it cannot be considered highly relevant. Thus, GPC traces shown in Figure 3 reveals a minimum shift to lower molecular weights for the

nanocomposite sample. Degradation can be well stated considering the number average molecular weight since it changed from 13,200 to 8,700 g/mol (determined for the raw and nanocomposite samples, respectively). Formation of small polymer fragments has a great influence on this averaged molecular weight but a minimum repercusion when the $M_w$ values are considered (*i.e.*, 40,700 and 38,700 g/mol). The given results point out a degradation that may be caused by the presence of the organo-modifier compound and specifically when the PE99 poly(alkylene dicarboxylate) matrix was employed.

### 3. Thermal stability of PE99 clay nanocomposites

Thermogravimetric analysis gave information about the percentage of clay incorporated into the polymer matrix and also about the effect of the added clays on thermal stability. In all cases, a constant char yield was attained at high temperature as shown in Figure 4a for the representative PE99/N757 nanocomposite. Furthermore, the remaining weight percentage was always in full agreement with the expected clay content. The result is meaningful since demonstrated that the clay was not retained in the sprue. Clay was drawed by the molten polymer through the feeding channels giving rise to well dispersed specimens. A great resemblance between TGA traces of the raw PE99 sample and the PE99/N757 nanocomposites can also be detected during first stages of degradation. Even the added clay seems to slightly stabilize the sample, suggesting a certain alteration of the chemical behavior of confined polymer chains.[27] Differences were noticeable at the end of the degradation process as revealed by the shoulders detected in the DTGA plots (Figure 4a). It has been reported that clay particles had a remarkable influence on the last stages of degradation since layered silicates may act as a transport barrier towards degradation products ablation.[28,29]



Figure 4b shows as thermal degradation of PE99 became clearly enhanced when organo-modified clays were added probably as a consequence of their lower stability. Thus, a low temperature peak/shoulder was detected in DTGA traces, being the effect noticeable according to the clay content (not shown) and the type of the clay (*i.e.*, N848 > C25A > C20A). The result is

important since can explain the highest degradation observed for the micro-molded PE99/N848 6 sample.

**Table 1.** Molecular weights of PLA and PE99 nanocomposites prepared from powder mixtures having 3 wt-% of clay and processed under optimal micro-molding conditions (Time: 1.2 s, amplitude: 24.0 $\mu$m and force: 300 N).

| Sample | $M_n$ (g/mol) | $M_w$ (g/mol) | $M_w/M_n$ |
|---|---|---|---|
| PLA[a] | 22,200 ± 2,000 | 70,800 ± 6,000 | 3.2 |
| PLA | 21,800 ± 2,000 | 68,700 ± 6,000 | 3.2 |
| PLA/N757 | 22,300 ± 2,500 | 69,900 ± 6,500 | 3.1 |
| PLA/N848 | 21,500 ± 2,000 | 67,400 ± 6,000 | 3.3 |
| PLA/C20A | 22,000 ± 2,000 | 69,900 ± 6,300 | 3.2 |
| PLA/C25A | 22,500 ± 2,000 | 74,400 ± 6,500 | 3.3 |
| PE99[b] | 13,200 ± 2,000 | 40,700 ± 4,500 | 3.1 |
| PE99 | 14,700 ± 2,000 | 37,200 ± 3,000 | 2.5 |
| PE99/N757 | 14,300 ± 2,000 | 39,900 ± 4,500 | 2.5 |
| PE99/N848 | 8,700 ± 1,000 | 38,700 ± 4,500 | 3.5 |
| PE99/C20A | 14,000 ± 2,000 | 40,600 ± 4,000 | 2.9 |
| PE99/C25A | 10,700 ± 1,500 | 36,500 ± 3,000 | 2.8 |

[a]Raw materials.

**Figure 3**. GPC molecular weight distribution curves determined for the synthesized PE99 powder sample and that processed under optimized conditions. Curves for processed PE99/N757 6 and PE99/N848 3 nanocomposites are also drawn for comparative purposes.

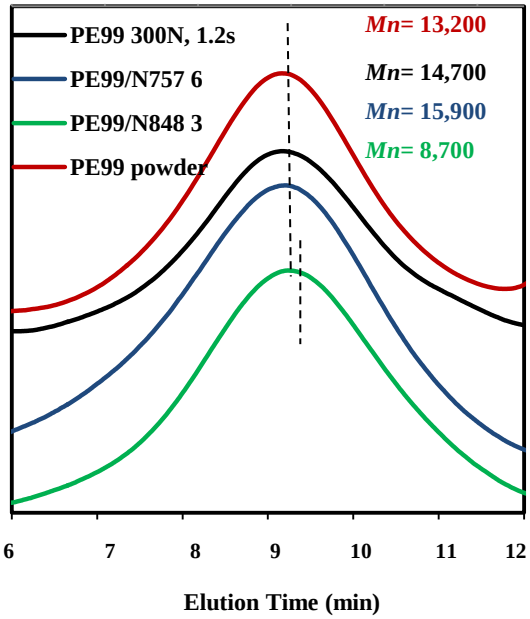




Thermal stability of PLA specimens was not influenced by addition of nanoclays since TGA curves of nanocomposites were overlapped with that of raw PLA (not shown). Results are in full agreement with GPC measurements of processed PLA nanocomposites that demonstrates in this case the lack of degradation during ultrasonic micro-molding.

## 4. Structure of PLA and PE99 clay nanocomposites obtained by means of ultrasonic waves

The achievement of aggregates, intercalated or exfoliated structures was firstly evaluated by means of X-ray diffraction of specimens directly obtained by the micro-molding process. Specifically, attention was paid to the $2\theta$ range of diffraction patterns between 2 and 10º ($\theta$ is the scattering angle) where the characteristic 001 silicate diffraction peak may appear. In

fact, observation of this peak at the same or at lower diffraction angle than the neat clay is an indication of an unaltered structure (aggregate) or an increase of the interlayer spacing as a consequence of intercalation of polymer chains into the silicate galleries. On the contrary, this peak should disappear for an exfoliated structure with well separated layers or even for a structure with a variable interlayer spacing.

Diffraction profiles of PLA nanocomposites loaded with the maximum assayed amount of clay (*i.e.*, 6 wt-%) are compared in Figure 5 with those corresponding to the neat PLA homopolymer and the neat clays. The characteristic (001) interlayer clay spacing (1.07, 1.80, 1.94 and 2.38 nm for N757, N848, C25A and C20A, respectively) disappeared in the spectra of all nanocomposites as expected for the achievement of exfoliated structures. On the contrary, (*hk*0) intralayer clay reflections were always detected as an evidence of the effective incorporation of the clay. Diffraction profiles showed also broad halos which indicate a predominant amorphous phase for PLA specimens processed by the micro-molding process. Only small Bragg reflections at 0.542 and 0.472 nm and associated to (200)+(110) and (203) reflections of the α-form ($10_7$ helical conformation) of polylactide[30,31] could be detected with a variable intensity depending on the nanocomposite. Results are logical since it is well known the difficulty of PLA to be crystallized from the melt state by a fast cooling and that PLA usually crystallizes in the α-form when stress or epitaxial effects are not involved.[32]



Nanocomposites based on PE99 were highly crystalline since Bragg peaks associated to the polymer matrix became predominant in their diffraction pattern (Figure 6). These peaks appeared at 0.413-0.412 and 0.370 nm and were consistent with the molecular packing usually observed in non-substituted poly(alkylene dicarboxylates).[33,34] Chain axis projection of the reported crystalline structures is usually defined by a rectangular unit cell with parameters close to 0.500 nm and 0.740 nm, which is compatible with the observed spacings. In this case, the indicated reflections should correspond to (110) and (020) planes of a typical structure where *c* is the chain axis direction. Clay interlayer (001) reflections were again not observed despite intense (*hk*0) intralayer reflections were evident. Only nanocomposites prepared with the C20A organo-modified clay revealed in some particular cases a small low angle reflection indicative that

dispersion was not completely effective and that some aggregates were still present in the processed sample.

**Figure 4**. Thermogravimetric and derivative thermogravimetric curves of PE99 and its nanocomposites with different percentages of Nanofil 757 (a) and PE99 nanocomposites with 3 wt-% of Nanofil 848, Cloisite 20A and Cloisite 25A (b).

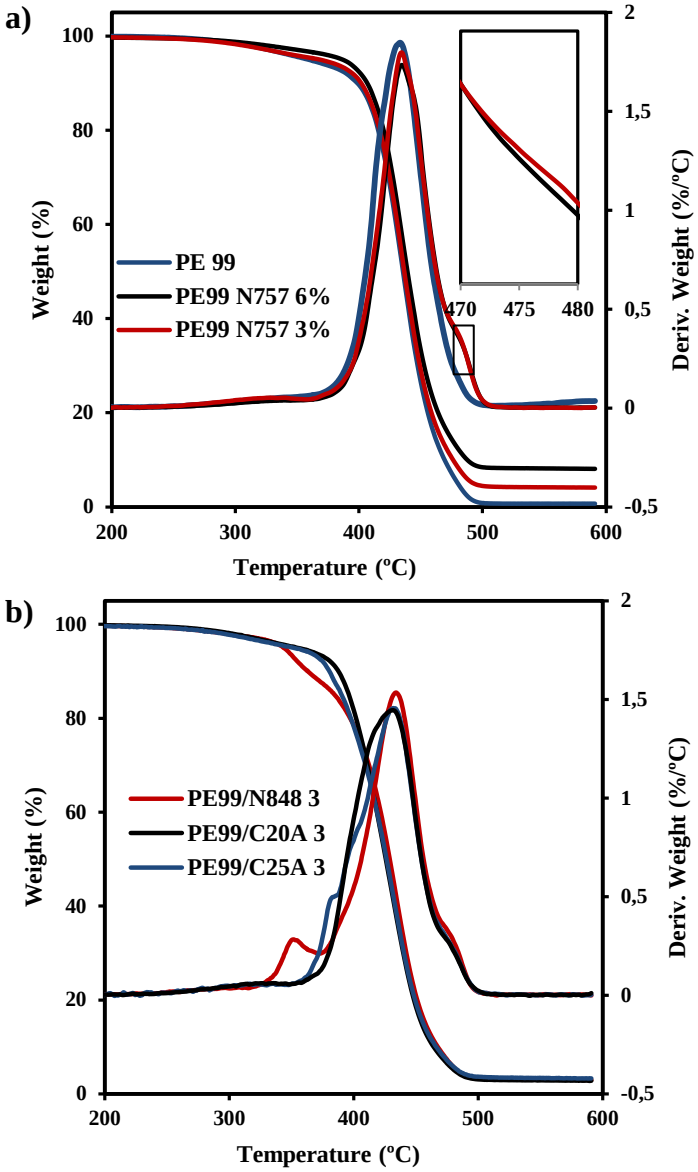

**Figure 5.** X-ray diffraction profiles of PLA nanocomposites with 6 wt-% of C25A, C20A, N848 and N757 clays. For the sake of completeness, the profiles of the PLA polymer matrix and the four clays are also represented.

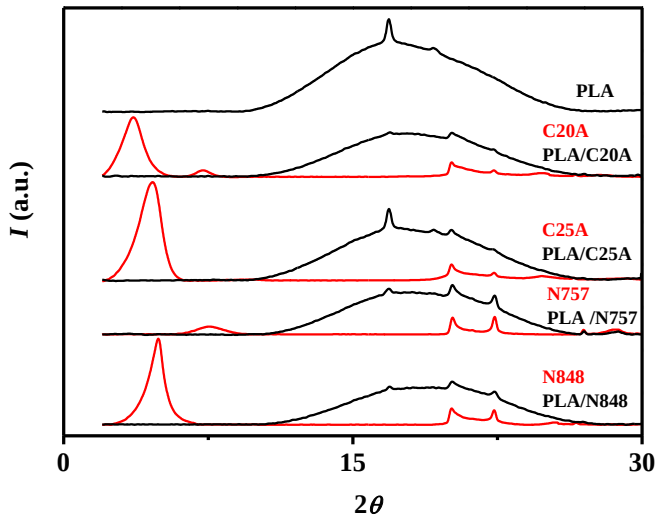




**Figure 6.** X-ray diffraction profiles of PE99 nanocomposites with 3 wt-% of C25A, C20A, N848 and N757 clays. For the sake of completeness, the profiles of the PE99 polymer matrix and the four clays are also represented.

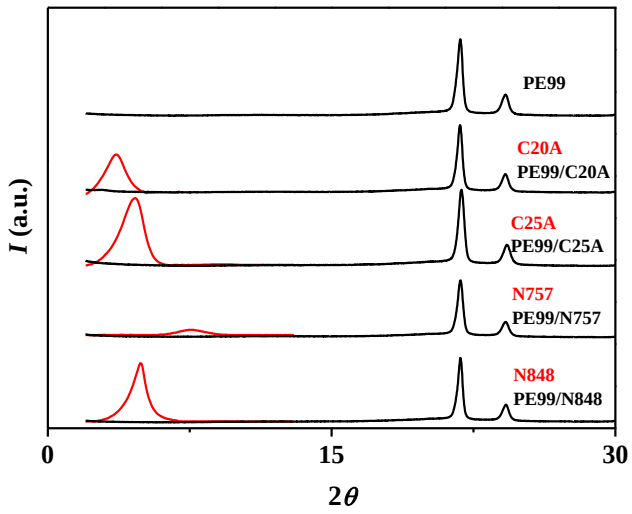

Analysis of clay dispersion in the processed nanocomposites was also carried out by direct observation of the morphology and phase distribution of ultrathin sections of micro-molded specimens by transmission electron microscopy. Flawless ultrasections were obtained more easily from the rigid PLA samples and consequently images were clearer. A good dispersion of silicate layers were always observed for these PLA nanocomposites as shown in the low magnification images given in Figure 7 for representative samples derived from the neat N757 clay and the C25A organo-modified clay. Similar features were deduced from images of nanocomposites based on PE99. Specifically, Figure 8 shows representative high magnification images of the different studied PE99 nanocomposites. A large number of exfoliated silicate sheets resulting from extensive penetration of PE99 molecular chains between silicate layers was observed, together with some intercalated nanostructures homogeneously dispersed in the polymer matrix. This arrangement usually involved a limited number of sheets (between 2 and 5) with variable interlayer spacing, although a more regular structure could be detected in some minority cases (see blue dashed circle for the C20A nanocomposite). Probably, interactions between layers depend on the type of cation (*e.g.,* $Na^+$ and alkylammonium for neat and modified clays, respectively) giving rise to a perfect exfoliation or to the presence of some minor layered structures. Indeed, it is highly interesting that the full exfoliated structure was obtained when the neat clay was employed. Orientation of sheet nanostructures in the direction of the melt flow was always clearly observed independently of the polymer matrix and the clay used.



**Figure 7**. Transmission electron micrographs of the micro-molded PLA/C25A 3 (a) and PLA/N757 3 (b) nanocomposite samples. Circles point out clearly exfoliated layers.

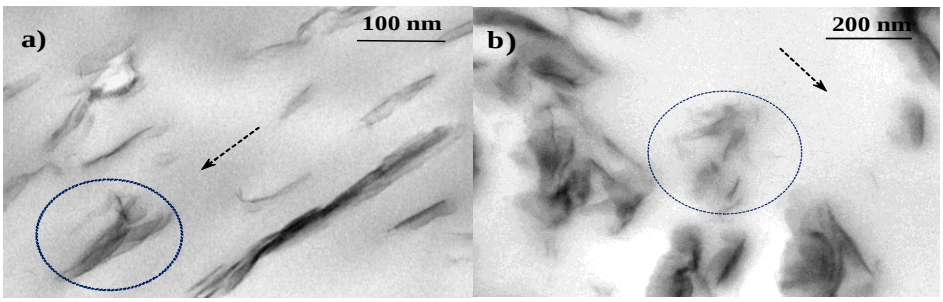

**Figure 8**. Transmission electron micrographs of the micro-molded PE99/N757 3 (a), PE99/C25A 3 (b), PE99/C20A 3 (c) and PE99/Nanofil 848 3 (d) nanocomposite samples.

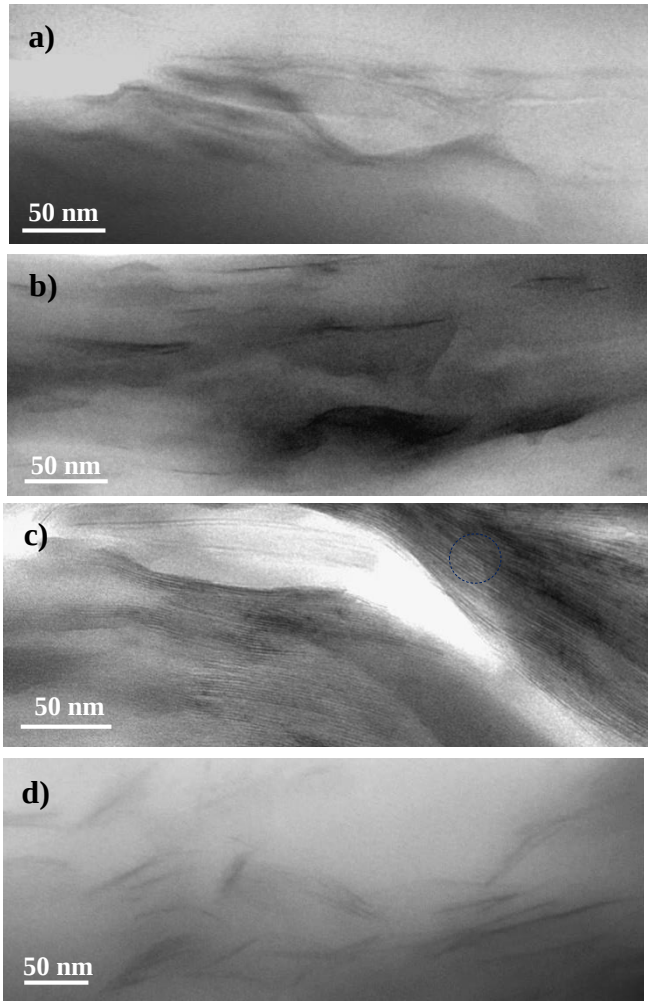




Structural observations demonstrate that micropieces of nanocomposites with exfoliated structures can be obtained by means of the energy provided by ultrasound waves, being completely unnecessary the use of organo-modifier compounds to improve polymer-clay interactions. This point is fundamental since polymer degradation during processing can be suppressed and even thermal stability improved when a neat clay (*e.g.,* N757) is employed.

Capability to get exfoliated structures from different organo-modified clays is also interesting since they can influence the biodegradability of the resultant nanocomposite.[18-21]

## 5. Crystallization kinetics of PLA/C25A nanocomposites

Incorporation of fillers into a polymer matrix may influence on the crystallization kinetics, crystalline morphology and degree of crystallinity, being the effect more significant when interactions between filler and matrix are enhanced. This is the case of the hybrid composites derived from inorganic nanosilicates and organic polymers that are evaluated. Multiple studies have been performed to clarify how nucleation, crystal growth rate and overall crystallization rate can be affected by the presence of nanoparticles, but a unique behavior has not been found. Polylactide derivatives have a peculiar behavior depending on the final nanocomposite structure. Thus, intercalated nanocomposites showed an enhanced nucleation and a higher overall crystallization rate than neat PLA since particles acted as effective nucleating agents.[23] Hovewer, results obtained with the highly miscible C30B organo-modified clay indicated a lower nucleation respect to the neat polymer and an unusual enhanced crystal growth rate.[23]



It seems interesting to take advantage of the facility of ultrasounds to render exfoliated structures and thereby to study the crystallization behavior of the new PLA/C25A nanocomposites.

Figure 9a shows the crystal growth rates determined for PLA and the micro-molded nanocomposites having 3 wt-% and 6 wt-% of C25A at different crystallization temperatures. Data were obtained by measuring the radius of spherulites during crystallization, being observed in all cases a linear increase with time (not shown) that was indicative of the absence of a molecular transport hindering effect. Thus, clay silicate layers seem not excluded from the growing spherulites.

Average growth rates were determined in the 120-140 ºC temperature range where a typical bell shaped curve defined their temperature dependence. Specifically, the maximum rate was found for all samples at a crystallization temperature close to 130 ºC. Data given in Figure 9a clearly demonstrate that growth rates increased as larger amounts of clay particles were added.

**Figure 9**. (a) Spherulite growth rate (*G*) as a function of the crystallization temperature ($T_c$) for neat PLA (+, solid line), PLA/C25A 3 (x, dotted line) and PLA/C25A 6 (▲, dashed line) samples. (b) Change in the nucleation density with isothermal crystallization temperature for neat PLA (+, solid line), PLA/C25A 3 (x, dotted line) and PLA/C25A 6 (▲, dashed line) samples.

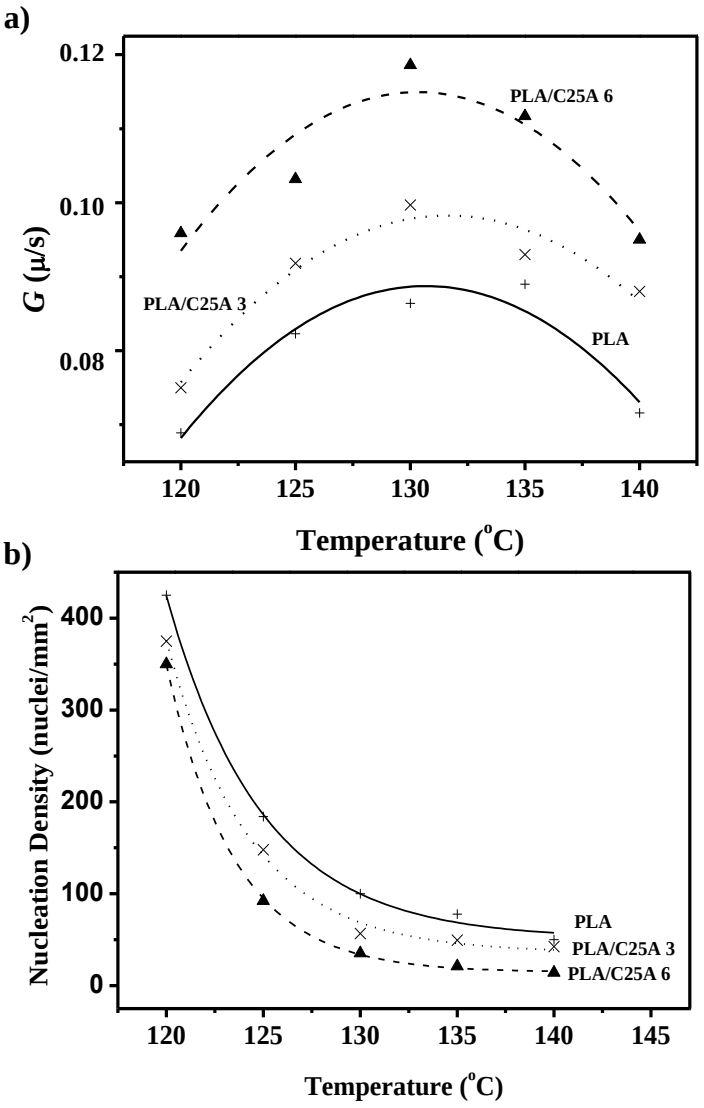




Molecular diffusion should be slow down by the presence of exfoliated layers and consequently crystal growth rate is expected to decrease, which is just opposite to present

observations and also to previously reported experimental data.[22] Well dispersed clays should be incorporated inside growing spherulites, being possible that the new and not completely favorable polymer-clay interactions facilitated the deposition of PLA chains onto the surface of the growing crystal. In this way, the secondary nucleation constant and the crystal growth rate should decrease and increase, respectively, with increasing content of silicate layers. The peculiar behavior cannot be justified supposing that the enhanced crystallization rate was a consequence of a decrease of molecular weight for the nanocomposite sample. In fact, a plausible hypothesis is that degradation during the crystallization process was favoured by the presence of exfoliated silicate layers. GPC chromatograms displayed in Figure 10 allow to discard a degradation effect since identical molecular weight distributions for melt crystallized PLA/C25A 6 nanocomposite and micro-molded specimens of both the neat PLA and the PLA/C25A 6 nanocomposite were found.

**Figure 10.** GPC molecular weight distribution curves determined for ultrasound micro-molded PLA and PLA/C25A 6 samples and the melt crystallized PLA/C25A 6 nanocomposite previously prepared by ultrasound micro-molding.



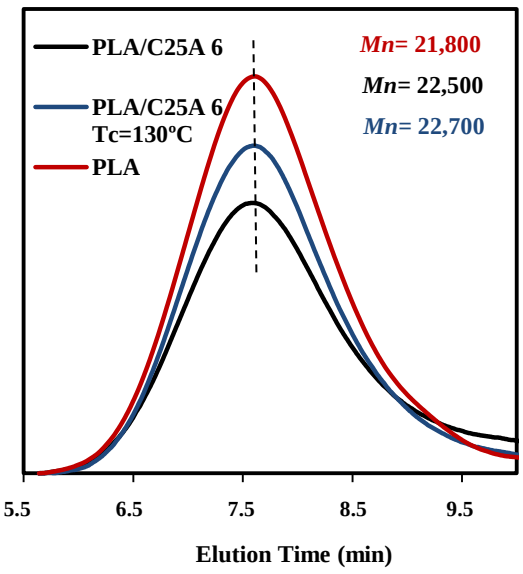

Spherulites had always a negative birefringence as demonstrated by the position of the blue and yellow arms in the optical micrograps (Figure 11) and rendered fibrilar textures. Diameters attained after impingement clearly increased when the clay was incorporated. Figure 9b shows the logical increase of primary nucleation when crystallization temperature was decreased but more interestingly this nucleation decreased by the incorporation of exfoliated clays giving rise to an anti-nucleating effect even at a relatively low clay content (*i.e.,* 3 wt-%). The number of nuclei per area reached a maximum value of 400 nuclei/mm$^2$ for PLA at 120ºC and a minimum value of 25 nuclei/mm$^2$ for PLA/C25A 3 at 140ºC. The observed anti-nucleating effect is peculiar and may be justified considering that active heterogeneities present on the neat polylactide could migrate to the vicinity of clay nanoparticles and became non longer active.

**Figure 11.** Optical micrographs of PLA (a), PLA/C25A 6 (b), PE99 (c) and PE99/N757 6 (d) grown at 125 ºC (a,b) and 59 ºC (c,d).



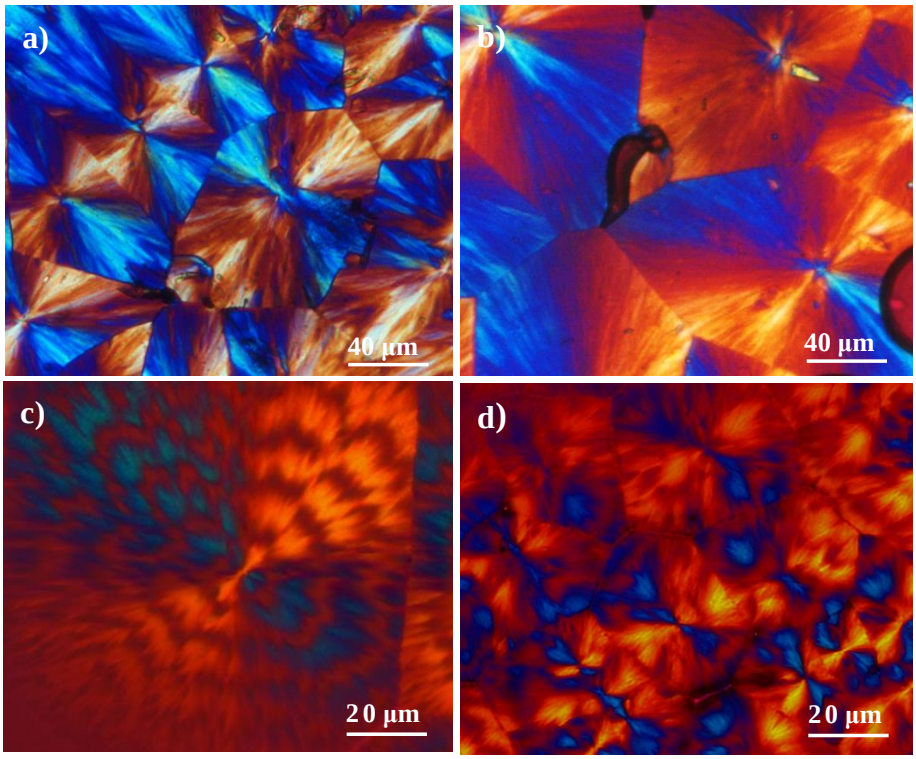

Isothermal crystallization experiments performed by DSC (Figure 12) showed how the overall crystallization rate was influenced by the presence of nanoparticles. This rate includes both primary nucleation and crystal growth kinetic components which as explained before where oppositely affected by the presence of exfoliated layers. DSC peaks became broader with increasing crystallization temperature and shifted to higher crystallization times with increasing clay content as expected if the overall rate was predominantly affected by the change on the primary nucleation. In any case, results clearly demonstrated the high impact of nanoparticles on the crystallization kinetics of PLA, a feature that is easily evidenced due the well-known difficulty of PLA to crystallize and the corresponding low crystal growth rates that facilitate to get experimental measurements over a relatively large temperature range.

**Figure 12**. DSC exothermic peaks of neat PLA (red solid line), PLA/C25A 3 (blue dotted line) and PLA/C25A 6 (black dashed line) samples for crystallization experiments performed at representative temperatures of 120 and 130 ºC.



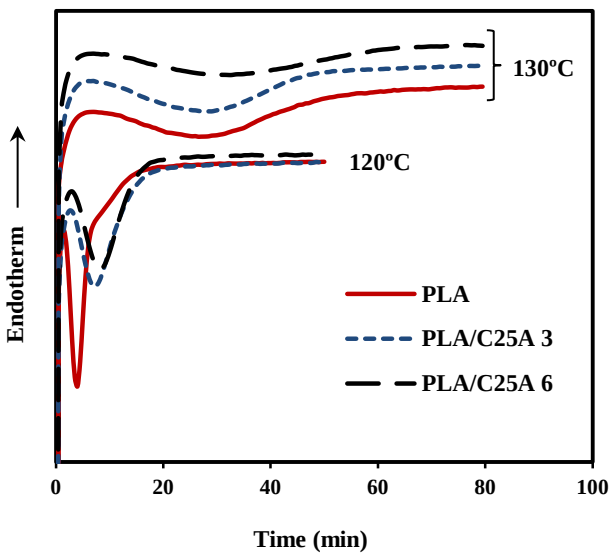

## 6. Crystallization kinetics of PE99/N757 nanocomposites

The influence of exfoliated clays on the crystallization kinetics was also evaluated for the PE99 matrix. In this case the pristine N757 clay was used since degradation caused by ultrasounds was minimized when the organo modifier compound was avoided. Figure 13a shows as the spherulite radius increases linearly with crystallization time for the different assayed isothermal temperatures and the micro-molded specimens of the neat polymer and the nanocomposite loaded with 6 wt-% of the clay. Again silicate layers seems that were not excluded from spherulites but their influence on the growth rate was in disagreement with previous results obtained with PLA compounds. Thus, a typical behavior where exfoliated layers hindered the transport of molecular chains to the surface of growing crystals was determined (Figure 13b). Note that growth rates of PE99 spherulites were high and consequently experimental data could only be performed at a restricted temperature range that corresponded to a low degree of supercoiling. In disagreement with PLA experiments the maximum of a typical bell curve could not be determined.



All PE99 based samples crystallized from the melt into spherulites with negative birefringence and a ringed texture (Figures 11c and 11d) but diameters attained after impingement were clearly different for the neat polyester and its nanocomposite. This feature is also depicted in Figure 13c where is evident the lower size of nanocomposite spherulites and that accurate growth rate measurement could not be performed at temperatures lower than 58 ºC. Exfoliated clay nanocomposites of PE99 had consequently the characteristic behaviour where silicate layers acted as nucleating agents, a result that emphasizes the peculiar antinucleating effect observed for PLA nanocomposites. Figure 13b shows as the density of primary nuclei increases with decreasing the crystallization temperature and reveals a significant difference that is found even at a low supercooling. Thus, PE99 and PE99/N757 6 samples crystallized had nucleation densities of 30 nuclei/$mm^2$ and 80 nuclei/$mm^2$, respectively

**Figure 13**. (a) Variation of PE99 and PE99/N757 spherulitic radii with time for isothermal crystallizations performed at the indicated temperatures. (b) Crystal growth rates of PE99 and PE99/N77 6 samples at the indicated crystallization temperatures. (c) Change in the nucleation density with isothermal crystallization temperature for neat PE99 and PE99/N757 6 samples.

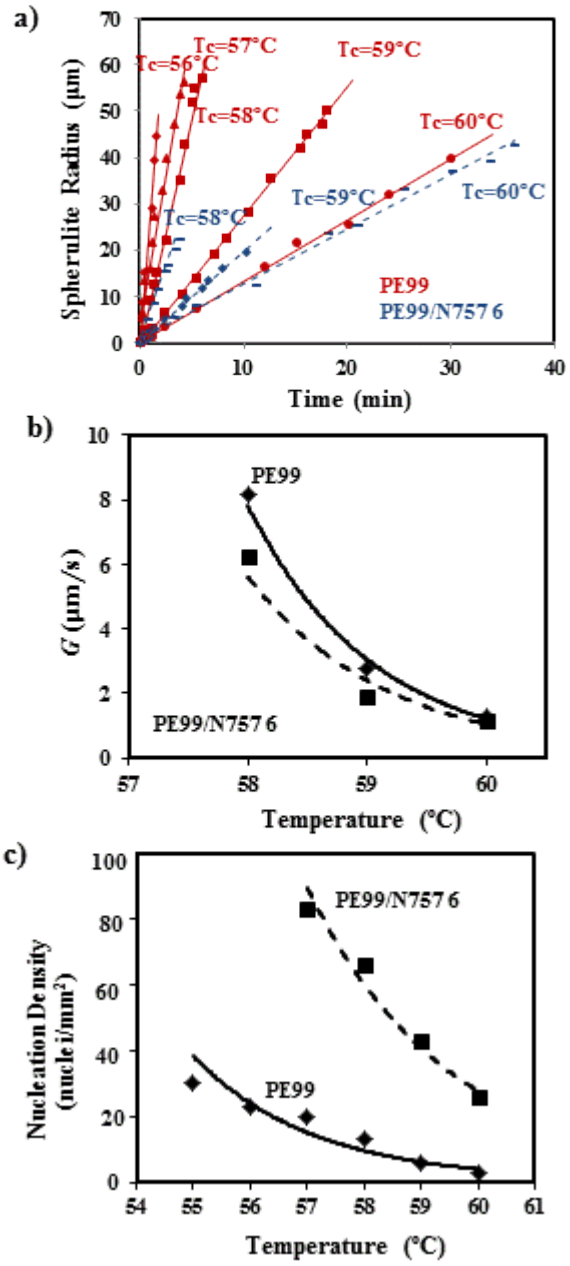

The effect of exfoliated clays on the overall crystallization rate was not clear since they play contrary effects on crystal growth rate and primary nucleation. Thus, DSC crystallization exotherms obtained at different temperatures showed slight differences between the neat polyester and its nanocomposite with 6 wt-% of the N757 clay (Figure 14). Nevertheless, the exotherm of the nanocomposite appeared at a higher time than that observed for the neat polyester when crystallization was performed at the highest temperature (*i.e.,* 60 ºC). In this case nucleation differences were less important and the crystal growth rate was the predominant factor. On the contrary, the exotherm of the nanocomposite appeared at a slightly lower time respect to the neat polyester exotherm when crystallization was performed at the lowest assayed temperature (*i.e.,* 58 ºC) where nucleation differences were more significant. It should be pointed out that optical microscopy measurements were performed with very thin films where primary nucleation was lower that bulk samples used in DSC experiments and consequently with a greater impact of nucleation differences between samples.



**Figure 14**. DSC exothermic peaks of neat PE99 (red solid lines) and PE99/N757 6 (blue dotted lines) samples for crystallization experiments performed at representative temperatures of 58, 59 and 60 ºC.

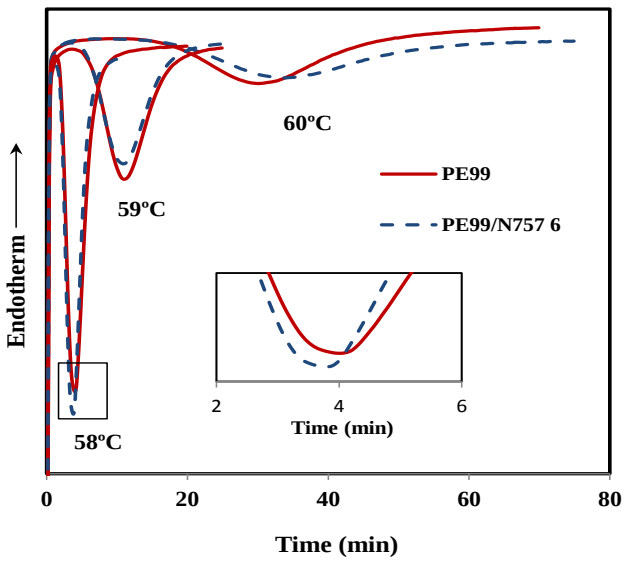

## IV. Conclusions

Ultrasonic micro-molding has been probed as a new and effective method to get nanocomposites with good clay dispersion and exfoliated structures. Two biodegradable polymer matrices coming from renewable resources as well as both neat and organo-modified clays were considered and gave always rise to positive results. Control of processing parameters allowed getting samples with a minimum degradation being best results attained when compatibilizer compounds were not employed. Nevertheless, polylactide nanocomposites with unaltered molecular weights could always be prepared independently of the selected clay. Ultrasonic technology appears as a promising method to get directly molded nanocomposite specimens without modifying the clay or performing a subsequent processing as in the case of nanocomposites prepared by solvent casting, melt mixing or in situ polymerization.

Exfoliated C25A clays had a peculiar influence on the crystallization of polylactide as also previously reported for PLA/C30B nanocomposites. Thus, the exfoliated clay displayed an antinucleating effect but at the same time enhanced the crystal growth rate. The influence of exfoliated clays on the crystallization of poly(nonamethylene azelate) was on the contrary in agreement with a typical behavior where the silicate layers favoured the primary nucleation and hindered molecular transport. In this way, the effect of the clay on the overall crystallization rate was dependent on the crystallization temperature since the two indicated effects point to opposite behaviors.

## V. References


1. Kumar AP, Depan D, Torner S, Singh RP. Prog Polym Sci 2009;34:479.
2. Tjong SC. Mater Sci Eng R 2006;53:73.
3. Fukushima K, Rasyida A, Yang MC. J Polym Res 2013;20:302.
4. Okamoto M. J Ind Eng Chem 2004;10:1156.
5. Dinari M, Mallakpour S. J Polym Res 2014;21:350.
6. Sacristán M, Plantá X, Morell M, Puiggalí J. Ultrason Sonochem 2014;21:376.
7. Gupta AP, Kumar V. Eur Polym J 2007;43:4053.
8. Park J, Lee I. J Polym Research 2011;18:1287.
9. Del Valle LJ, Roa M, Díaz A, Casas MT, Puiggalí J, Rodríguez-Galán A. J Polym Research 2012;19:9792.
10. Chansuna M, Pimpha N, Soongnern V. J Polym Research 2014;21:452.
11. Llorens E, Del Valle LJ, Ferrán R, Rodríguez-Galán A, Puiggalí J. J Polym Research 2014;21:360.
12. Del Valle LJ, Camps R, Díaz A, Franco L, Rodríguez-Galán A, Puiggalí J. J Polym Research 2011;18:1903.
13. Ray SS. Acc Chem Res 2012;45:1710.
14. Sinha Ray S, Yamada K, Ogami A, Okamoto M, Ueda K. Macrmol Rapid Commun 2002;23:943.
15. Nam JY, Sinha Ray S, Okamoto M. Macromolecules 2003;36:7126.
16. Sharma V, Kundu PP. Prog Polym Sci 2008;33:1199.
17. Hojabri L, Kong X, Narine SS. Biomacromolecules 2010;11: 911.
18. Fukushima K, Abbate C, Tabuani D, Gennari M, Camino G. Polym Degrad Stab 2009;94:1646.
19. Zhou Q, Xanthos M. Polym Eng Sci 2010;51:320.
20. Ray SS, Yamada K, Okamoto M, Ueda K. Macromol Mater Eng 2003;288:203.
21. Singh NK, Purkayastha BD, Roy JK, Banik RM, Yashpal M, Singh G. ACS Appl Mater Interf 2010;2:69.
22. Krikorian V, Pocha DJ. Macromolecules 2004;37:6480.
23. Seo Y-S, Park K. Microsyst Technol 2012;18:2053.
24. Chen J, Chen Y, Li H, Lai SY, Jow J. Ultrason Sonochem 2010;17:66.

25. Chen G, Guo S, Li H. J Appl Polym Sci 2002;84:2451.
26. Kang J, Chen J, Cao Y, Li H. Polymer 2010;51:249.
27. Ichikawa Y, Suzuki J, Washiyama J, Moteki Y, Noguchi K, Okuyama K. Polymer 1994;35:3338.
28. Jang BN, Wilkie CA. Polymer 2005;46:2933.
29. Yuan X, Li C, Guan G, Xiao Y, Zhang D. Poly Degrad Stab 2008;93:466.
30. De Santis P, Kovacs AJ. Biopolymers 1968;6:299.
31. Hoogsteen W, Postema AR, Pennings AJ, Ten Brinke G, Zugenmaier P. Macromolecules 1990;23:634.
32. Cartier L, Okihara T, Ikada Y, Tsuji H, Puiggalí J, Lotz B. Polymer 2000;51:8909.
33. Almontassir A, Gestí S, Franco L, Puiggalí J. Macromolecules 2004;37:5300.
34. Gestí S, Casas MT, Puiggalí J. Eur Polym J 2008;44:2295.

# Chapter 4.2

## *Dispersion of functionalized silica micro and nanoparticles into poly(nonamethylene azelate) by ultrasonic micro-molding.*

Ultrasound micro-molding technology has been proved useful to process biodegradable polymers with a minimum material loss. Therefore, this technology appears highly interesting for the production of biomedical micro-devices. It has also been demonstrated that ultrasound energy is able to exfoliate natural clays and provide nanocomposites with improved properties. The use of silica ($SiO_2$) nanoparticles is also interesting due to advantages like low cost and enhancement of final properties. The possibility of using the ultrasound micro-molding technology to get materials with an homogeneous dispersion of particles is explored in this work considering both micro and nano-sized silica particles and a biodegradable polyester derived from 1,9-nonanodiol and azelaic acid as a matrix. Results demonstrated that composites could be obtained up to a 6 wt-% of silica and that degradation was not detected even if particles were functionalized with a compatibilizer agent like (3-aminopropyl) triethoxysilane.

Incorporation of nanoparticles should have a great influence on properties and specifically the effect on the crystallization behavior was evaluated by calorimetric and optical microscopy analyses. The overall crystallization rate was clearly enhanced when functionalized silica microspheres were added, even at a low percentage of 3 wt-%. This increase was mainly a consequence of the capability of nanoparticles to act as heterogeneous nucleii during crystallization but also the enhancement of the secondary nucleation process played a significant rule as was demonstrated by Lauritzen and Hoffmann analysis.

## I. Introduction

Ultrasonic waves are an energy source that has been employed for over 40 years as a plastic welding procedure because it is clean, energy efficient and fast. In fact, absorption of vibration energy leads to the generation of a polymer friction, which may result in a local melting of the sample. First descriptions about the potential use of ultrasonic waves to the molding of plastic powders were given by Fairbanks[1] and Crawford *et al*.,[2] since then different efforts have been carried out to develop the great potential of this technology. Thus, ultrasonic hot embossing appears as a new interesting process for fast and low-cost production of micro systems from polymeric materials.[3-5] The feasibility of this process has been proven by fabricating a variety of micro systems such as flow sensors, micro mixers, heat exchangers, RFID-antennas, thin-film key pads, and micro whistles.

Plasticization of polymers by an ultrasonic source together with direct injection of molten material have also been proposed,[6-8] providing a new micro-molding technology that can be a serious alternative to conventional micro-injection techniques. Basically, a micro-molding equipment (Figure 1) is composed of a plastizincing chamber, a controller, a mold, an ultrasonic generator that produces high frequency (30 kHz) from line voltage and a resonance stack or acoustic unit that is connected to the generator. This unit consists of: a) a converter (piezoelectric transducer) where high frequency signals given by the generator are transmitted through piezoelectric crystals that expand and contract at the same rate that the electrical oscillation; b) a booster that amplifies or reduces the mechanical oscillation (from 0 to 137.5 mm) and c) a sonotrode that transfers this oscillation to the polymer sample placed in the plasticizing chamber by applying a force (from 100 to 500 N).

The heat build-up caused by the resulting friction heat melts the polymer, which flows into the mold cavities through their feeding channels under the sonotrode pressure. A controller regulates the main processing parameters: oscillation time (*e.g.,* from 0.5 to 10 s), molding force and amplitude of the ultrasonic wave.

**Figure 1.** a) Scheme showing the main parts of the ultrasound micro-molding machine. b) Image of a processed PE99 specimen. c) SEM micrograph showing details of a PE99-M 3 micro-molded-specimen. Microparticles can be observed in the inset.

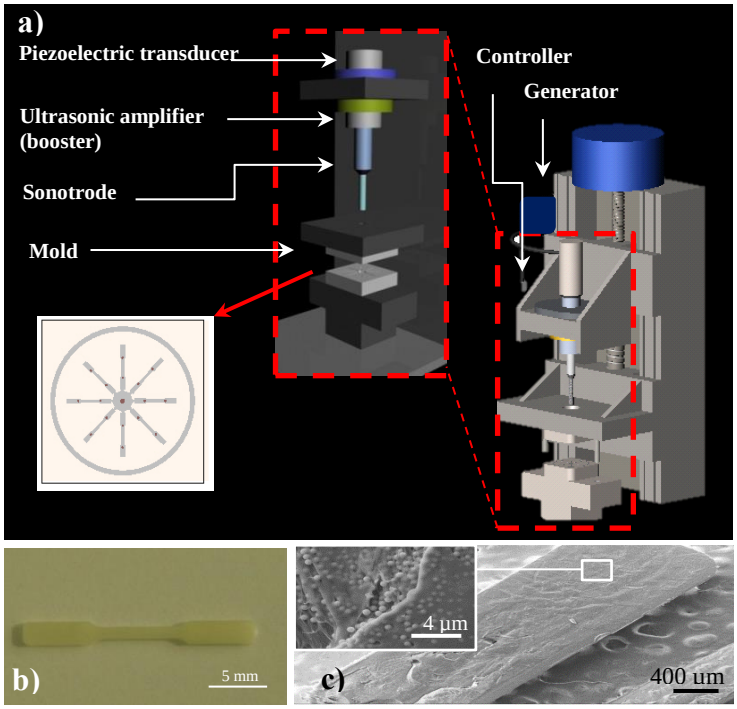




Despite the potential advantages of the use of high intensity ultrasonic waves as an energy source, it should be pointed out that these waves have not only physical effects on the melt rheology of the polymer but also chemical effects on the polymer chain as a result of cavitation and the high temperature that could be achieved inside the plasticizing chamber.[9-12] Therefore, optimization of processing parameters to get minimally-degraded samples is an essential step to apply the new micro-molding technology. In this sense, we have recently found that appropriate conditions can be found for biodegradable polymers that could be interesting for the production of biomedical devices such as polylactide (PLA),[13] poly(butylene succinate) (PBS)[14] and poly(nonamethylene azelate) (PE99).[15] Degradation logically increases with the increase of both irradiation time and amplitude, but a minimum period is necessary to guarantee

complete injection into the mold as well as a minimum amount of vibration energy. Severe degradation can also occur at low ultrasonic amplitude if a high molding force is applied due to chain scissions caused by mechanical shear stress. Nevertheless, a minimum force should be applied to make feasible the polymer melt flow and the filling of the mold cavity.

The capability to provide good dispersions is another interesting point to evaluate the potential of micro-molding technology. This point could involve the incorporation of compounds with and added value (*e.g.,* drugs with a pharmacologic activity) or even the addition of nanoparticles that lead to a large surface area to volume ratio and enhanced physical, chemical, and mechanical properties compared to conventionally filled composites.[16-18]

Ultrasonic micro-molding has recently revealed effective to get directly nanocomposites with the final form required for a selected application, a homogeneous clay distribution up to a load of 6 wt-% and more interestingly exfoliated structures without being necessary the use of a compatibilizer agent between the organic polymer and the inorganic silicate clay.[17,18] Furthermore, polymer degradation was minimized by employing the pristine clay. These promising results were achieved by employing PLA, PBS and PE99 as biodegradable matrices and montmorillonites like the neat N757 and the C20A, C25A and N848 organo-modified clays. Incorporation of nanoparticles had also a remarkable influence on the crystallization kinetics of the polymer matrix being found interesting differences depending on the selected polymer (*e.g.,* PLA or PE99) despite similar exfoliated structures were achieved.[18]



The use of silica ($SiO_2$) nanoparticles is also highly interesting to provide materials with enhanced properties due to their intrinsic advantages (low cost, nontoxicity, high modulus and capability to modify the chemical surface characteristics).[19,20] Therefore, a considerable improvement of properties could be attained when particles with an appropriate surface functionalization to improve interfacial interactions are well dispersed in the polymer matrix.[21-23] Silica particles with sizes suitable for biomedical applications can be easily prepared from base-catalyzed sol–gel processes.[24] These utilize organosilane precursors (*e.g.,* tetraethoxysilane), which, by means of hydrolysis and condensation reactions, lead to the formation of a new phase

(sol). The small colloidal particles within the sol then condense into the gel phase. The ease of introducing various organic functional groups provides high level of versatility to the mesoporous silica materials. The covalent attachment of functional groups usually involves introducing organic structures in the form of silanes, which can be attached using co-condensation or post-synthetic grafting methods.

The present work is focused to evaluate the applicability of ultrasound micro-molding technology to prepare a good dispersion of both silica micro and nanoparticles in a biodegradable polymer matrix that has recently be considered for preparation of clay nanocomposites (*i.e*., PE99). The effect of the incorporation of silica nanoparticles on crystallization kinetics will be also evaluated since they should affect nucleation and crystal growth as it has recently been determined for nanocomposites based on poly(ethylene oxide).[25]

## II. Experimental Section



### 1. Materials

Poly(nonamethylene azelate) (PE99) was synthesized by thermal polycondensation of azelaic acid with an excess of 1,9-nonanediol (2.2:1 molar ratio) as shown in Figure 2a. Titanium tetrabutoxyde was used as a catalyst and the reaction was first performed in a nitrogen atmosphere at 150 ºC for 6 h and then in vacuum at 180 ºC for 18 h. Polymer was purified by precipitation with ethanol of a chloroform solutions(10 wt-%). Number average molecular weight and polydispersity index determined by GPC and using poly(methyl methacrylate) standards were 13,200 g/mol and 3.1 respectively.

Preparation of silica micro/nanoparticles (Figure 2b): In a 250 mL flask, 1.5 mL of deionized water and 3 mL of a 28% ammonium hydroxide solution (Aldrich) were added to 120 mL of absolute ethanol and stirred vigorously for 30 min at room temperature using a magnetic bar. 3mL of tetraethoxysilane (TEOS, Geleste) was added via pipette as quickly as possible. The resultant solution was then purged with dry nitrogen and stirred for 12 h. Spheres with a homogeneous diameter close to 600 nm range were obtained after filtration. The same protocol

but increasing only the stirring speed to 250-1000 rpm was employed to get nanoparticles with diameters close to 25 nm range.

**Figure 2.** Synthesis schemes for PE99 (a), silica spheres (b) and functionalization process (c).

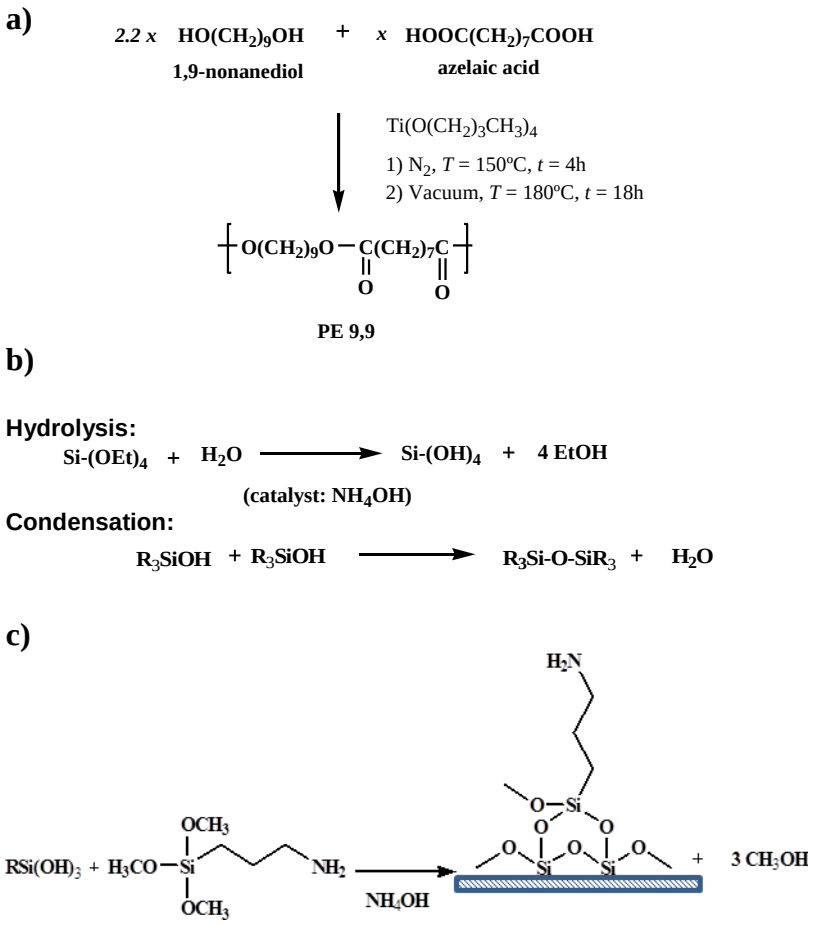


Functionalization of silica micro/nanoparticles (Figure 2c): 1 g of micro/nanospheres, previously dried under vacuum, was introduced into a vessel together 66 µL of pure ethanol. The mixture was sonicated for 15 minutes to enhance dispersion and subsequently 66 µL of ammonium hydroxide were added under stirring for 15 min. Finally, 297 µL of (3-aminopropyl) triethoxysilane (AMPS) were quickly added and reaction was allowed to progress under stirring

during 24 hours at room temperature. The resulting solid was centrifuged, repeatedly washed with ethanol and vacuum dried.

Nanocomposites will be named indicating the abbreviations of polymer, the size (micro or nano) and wt-% of added silica (*e.g.,* PE99-M 6 and PE99-N 6 indicate the composites having a 6 wt-% of micro and nanospheres, respectively ).

### 2. Micro-molding equipment

A prototype Ultrasound Molding Machine (Sonorus®, fabricated by Ultrasion S.L.) was used. The apparatus was composed of a controller (1000 W - 30 kHz digital ultrasound generator from Mecasonic fitted with a 3010 DG digital system), a converter (Mecasonic), an acoustic unit, an electric servomotor control (Berneker and Rainer) with software from Ultrasion S.L. and a thermally controlled mold. Molds (Ascamm) were designed to prepare eight test specimens of small dimensions (1.5 × 0.1 × 0.1 $cm^3$ under IRAM-IAS-U500-102/3 standards).



### 3. Measurements

Molecular weight was estimated by gel permeation chromatography (GPC) using a liquid chromatograph (Shimadzu, model LC-8A) equipped with an Empower computer program (Waters). A PL HFIP gel column (Polymer Lab) and a refractive index detector (Shimadzu RID-10A) were employed. The polymer was dissolved and eluted in 1,1,1,3,3,3-hexafluoroisopropanol containing $CF_3COONa$ (0.05 M) at a flow rate of 0.5 mL/min (injected volume 100 µL, sample concentration 2 mg/mL). The number and weight average molecular weights and molar-mass dispersities were calculated using polymethyl methacrylate standards.

SEM micrographs of micro-molded specimens were taken using a Focused Ion Beam Zeiss Neon40 microscope operating at 5 kV. Carbon coating was accomplished with a Mitec K950 Sputter Coater (fitted with a film thickness monitor *k*150x). Samples were viewed at an accelerating voltage of 5 kV.

FTIR spectra were recorded on a FTIR 4100 Jasco spectrophotometer. The samples were placed in an attenuated total reflectance accessory with thermal control and a diamond crystal (Specac MKII Golden Gate Heated Single Reflection Diamond ATR).

XPS analyses were performed in a SPECS system equipped with a high-intensity twin-anode X-ray source XR50 of Mg/Al (1253 eV/1487 eV) operating at 150 W, placed perpendicular to the analyzer axis, and using a Phoibos 150 MCD-9 XP detector. The X-ray spot size was 650 μm. The pass energy was set to 25 and 0.1 eV for the survey and the narrow scans, respectively. Charge compensation was achieved with a combination of electron and argon ion flood guns. The energy and emission current of the electrons were 4 eV and 0.35 mA, respectively. For the argon gun, the energy and the emission current were 0 eV and 0.1 mA, respectively. The spectra were recorded with pass energy of 25 eV in 0.1 eV steps at a pressure below 6 × 10−9 mbar. These standard conditions of charge compensation resulted in a negative but perfectly uniform static charge. Surface composition was determined through the N1s and Si2p peaks at binding energies of 399.2 and 103.2 eV, respectively, and using the manufacturer's sensitivity factors.



The distribution of the micro/nanoparticles in the composites was evaluated by morphologic observations using the Philips TECNAI 10 electron microscope at an accelerated voltage of 80 kV. Specimens were prepared by embedding the nanocomposite specimens in a low viscosity modified Spurr epoxy resin, and after cured were cut in a small sections at room temperature using a Sorvall Porter-Blum microtome equipped with a diamond knife. These sections were collected in a trough filled with water and lifted onto carbon coated copper grids.

Thermal degradation was studied at a heating rate of 10 ºC/min with around 5 mg samples in a Q50 thermogravimetric analyzer of TA Instruments and under a flow of dry nitrogen. Test temperatures ranged from 50 to 600 ºC.

The spherulite growth rate was determined by optical microscopy using a Zeiss Axioscop 40 Pol light polarizing microscope equipped with a Linkam temperature control system configured by a THMS 600 heating and freezing stage connected to a LNP 94 liquid nitrogen system. Spherulites were isothermally crystallized from homogeneous melt thin films obtained by melting 1 mg of the polymer between microscope slides. Next, small sections of these films were

pressed between two cover slides and inserted into the hot stage. Samples were kept at 90 ºC for 5 minutes to wipe out sample history effects and then quickly cooled at the desired temperatures. The radius of the growing spherulites was measured from the photographs taken at different times using a Zeiss AxiosCam MRC5 digital camera. Nucleation was evaluated by counting the number of active nuclei that appeared at constant crystallization temperature, assuming that each spherulite grew from one single active heterogeneous nucleus. A first-order red tint plate was employed to determine the sign of spherulite birefringence under crossed polarizers.

Crystallization kinetics was also studied by differential scanning calorimetry using a TA instrument Q100 series with $T_{zero}$ technology and equipped with a refrigerated cooling system (RCS). Experiments were conducted under a flow of dry nitrogen with a sample weight around 5 mg, while calibration was performed with indium. Samples were always previously heated (20 ºC/min) up to 25 ºC above their melting temperature, subsequently held for 5 min at this temperature and finally cooled to the selected temperature at a rate of 50 ºC/min. Samples were kept at the isothermal temperature until baseline was attained. A heating run (20 ºC) was also subsequently performed in order to determine the equilibrium melting temperature of the samples.



## III. Results and Discussion

### 1. Characterization of functionalized silica particles

Silica particles were effectively prepared using TEOS as a precursor. TEM micrographs clearly revealed a highly regular spherical form (Figure 3a) for silica particles obtained under a low stirring speed. These particles showed a highly homogeneous diameter that varied in a narrow range (*i.e.*, between 570 and 650 nm). Particles were slightly more irregular in form (Figure 3b) when were prepared under a higher stirring speed. Diameter size was considerably reduced but a homogeneous distribution could still be observed (*i.e.*, values were always within the 20-30 nm interval). The two kinds of silicate preparations will be designed as micro (M) and nano (N) sized particles.

**Figure 3.** TEM micrographs showing functionalized silica microspheres (a) and nanospheres (b).

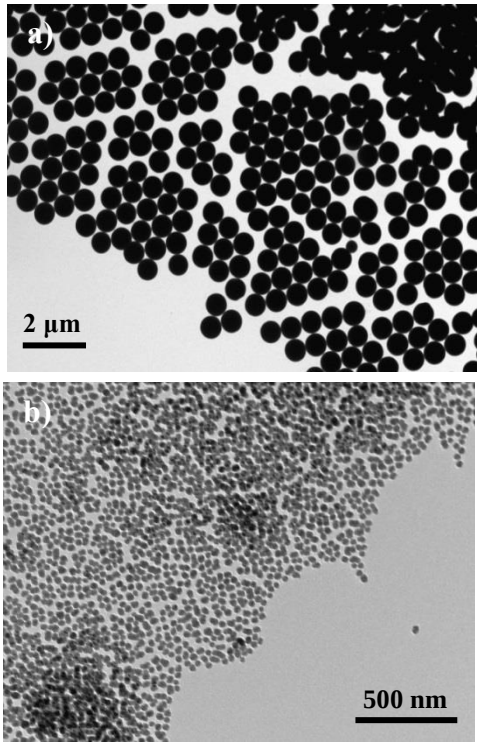




Surface functionalization by reaction with (3-aminopropyl) triethoxysilane was verified from the analysis of XPS spectra (Figure 4) that allowed determining a ratio between N and Si atoms close to 8% (*i.e.*, 8.8% and 7.3% for the micro and nanoparticles, respectively).

Thermogravimetric analyses (Figure 5) demonstrated also a higher weight loss when silica particles were functionalized due to the decomposition of the grafted AMPS groups that took place around 500 ºC. This decomposition step corresponded approximately to a weight loss of 9 % and logically was not detected with non-functionalized particles. A gradual weight loss, which led to a value of only 8-9 % at 590 ºC, was detected for all particles. Thus, at this temperature the total loss was 17% and 8% for functionalized and non-functionalized particles, respectively. Practically no differences were observed in the TGA and DTGA curves of micro and nanoparticles.

**Figure 4.** Silicon (a) and nitrogen (b) XPS signals detected in the functionalized silica nanoparticles.

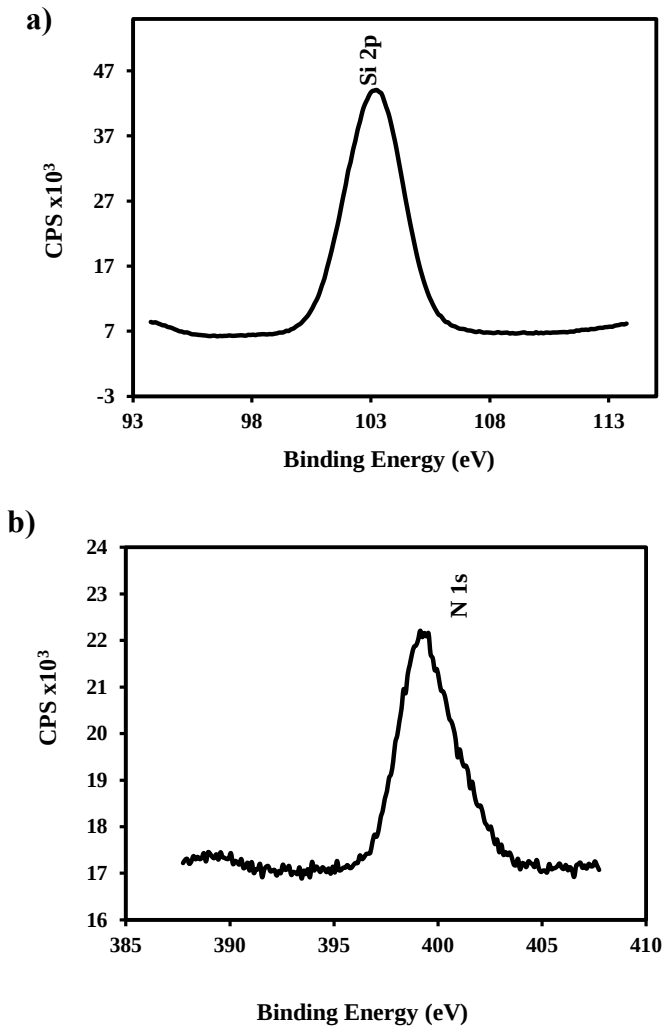

**Figure 5.** TGA (a) and DTGA (b) curves of silica nanospheres, functionalized silica nanospheres and micro-molded PE99, PE99-N 3 and PE99-M 6 specimens.

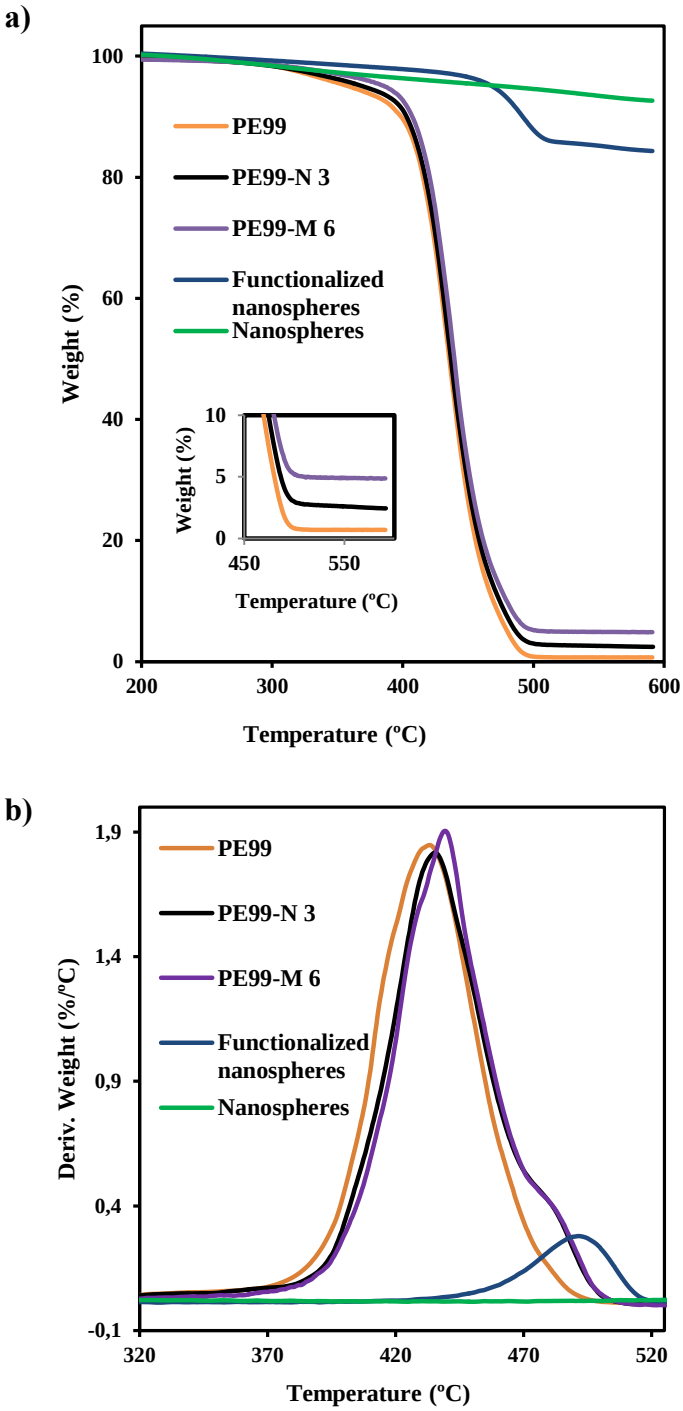

### *2.* Dispersion of functionalized silica micro and nanoparticles by ultrasound micro-molding technology

Processing conditions (amplitude, force and time) were previously optimized for the micro-molding of PE99 samples by the ultrasound technology.[15] These samples were supplied in the powder form, had a moderate molecular weight and could be processed under not highly severe conditions. Thus, a minimum irradiation time of 1.2 s was sufficient to guarantee a correct mold filling, a minimum amplitude of 24 mm was sufficient to provide the energy necessary to ensure a complete fusion of polymers and a moderate molding force (*i.e.*, 300 N) was appropriate to get a 100% molding efficiency. Experimental conditions could be maintained for processing mixtures with functionalized micro and nanospheres up to the maximum studied load of 6 wt-%. Molecular weights of raw PE99 and specimens processed under the indicated optimized conditions are summarized in Table 1, whereas Figure 6 compares GPC traces of PE99, PE99-N 3 and PE99-M 6 specimens. It is clear that not significant statistical differences were found between samples before and after processing and also when functionalized nanospheres were added. Only a slight but not highly significant decrease was detected for samples loaded with the maximum percentage (6 wt-%) of microspheres. New technology appears fully adequate to get micropieces with a negligible degradation of composites constituted by PE99 and functionalized silica micro/nanoparticles.



Figures 1b-1c show optical and SEM images of a representative silicate loaded specimen where a regular texture could be detected in the longitudinal section micrographs. Specimens were highly homogeneous without the presence of cavities that could affect the final properties of the material.

FTIR spectra were also useful to verify the uniform incorporation of silica particles into the micro-molded specimens and to discard that they were concentrated in the sprue. Thus, the typical Si-O stretching band at 1075cm$^{-1}$ was observed in the different parts of all loaded specimens. Hence, spectra taken from specimen zones close (proximal part) and distant (distal part) to the feeding channel showed a similar ratio between the intensity of the band associated

to the C=O stretching band of the polyester and the band associated to the silica particles (Figure 7 for representative samples containing micro and nanoparticles).

**Table 1.** Molecular weights of processed PE 99 and their mixtures with functionalized micro and nanoparticles.[a]

| **Sample** | ***Mn*** **(g/mol)** | ***Mw*** **(g/mol)** | ***Mw/Mn*** |
|---|---|---|---|
| PE99 (raw) | 13,200 | 40,700 | 3.1 |
| PE99 | 14,700 | 37,200 | 2.5 |
| PE99-M 3 | 14,800 | 36,800 | 2.5 |
| PE99-M 6 | 12,600 | 33,800 | 2.7 |
| PE99-N 3 | 15,800 | 39,200 | 2.5 |
| PE99-N 6 | 14,200 | 37,900 | 2.7 |

[a]Micro-molding conditions: Time (s), amplitude ($\mu$m) and force (N): 1.2, 10 and 300.



Analysis of particle dispersion in the processed composites was also carried out by observation of ultrathin sections of micro-molded specimens by transmission electron microscopy. Flawless ultrasections could be obtained, being possible to detect a good dispersion of both micro and nanoparticles in the images given in Figure 8 for representative samples.

**Figure 6**. GPC molecular weight distribution curves determined for micro-molded PE99, PE-N 3 and PE99-M 6 specimens.

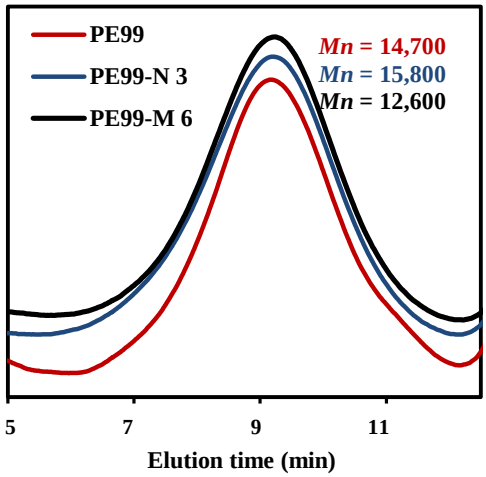


Thermogravimetric analysis gave also information about the percentage of silica particles incorporated into the polymer matrix and about their effect on thermal stability. In all cases, a constant char yield was attained at high temperature as shown in Figure 5a for representative PE99-N 3 and PE99-M 6 specimens. Furthermore, the remaining weight percentage was always in full agreement with the expected silica content (*i.e.,* close to 3 and 6 wt-%). The result is meaningful since demonstrated again that particles were not mainly retained in the sprue. Silica was effectively led by the molten polymer through the feeding channels giving rise to well dispersed specimens. A great resemblance between TGA and DTGA traces of the micro-molded PE99 sample and the silica loaded composites can also be detected during first stages of degradation. Even the added particles seem to slightly stabilize the sample (Table 2 and Figure 5). In any case functionalization of silica particles had not a negative impact on the ultrasound micro-molding process as was also observed from GPC measurements. Differences were only noticeable at the end of the degradation process as revealed by the shoulders detected around 483 ºC in the DTGA plots (Figure 5b) that were attributable to decomposition of the grafted AMPS groups.

**Figure 7.** FTIR spectra showing the characteristic C=O and Si-O stretching bands of PE-N 3 (a) and PE-M 3 (b) micro-molded specimens

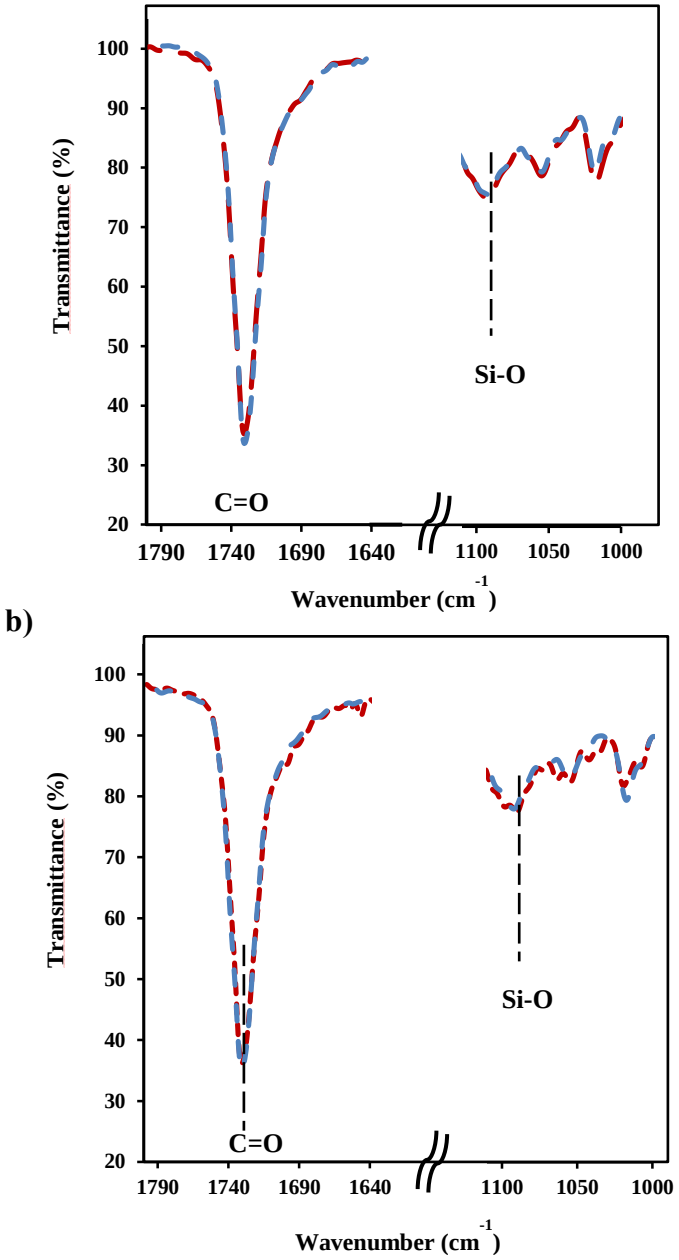

**Figure 8.** TEM micrographs showing the dispersion of functionalized silica microspheres (a,b) and nanospheres (c,d) into the micro-molded PE99-M 3 and PE99-N 3 specimens.

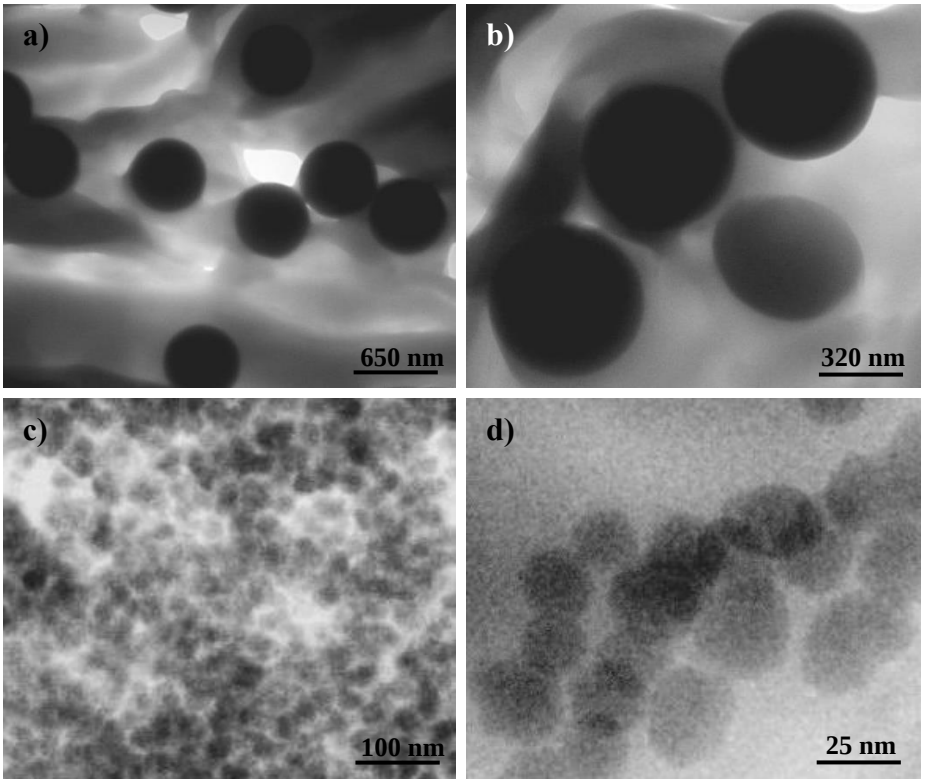




**Table 2.** Characteristic TGA temperatures and remaining weight percentages for the decomposition of the studied micro-molded specimens.

| Polymer | $T_{onset}$ (ºC) | $T_{10\%}$ (ºC) | $T_{20\%}$ (ºC) | $T_{40\%}$ (ºC) | $T_{max}$ (ºC) | Remaining weight (%) |
|---|---|---|---|---|---|---|
| PE 99 | 367 | 397 | 411 | 426 | 433 | 0 |
| PE 99-N 3 | 377 | 405 | 415 | 431 | 436 | 2.7 |
| PE 99-N 6 | 377 | 405 | 415 | 432 | 438 | 5.7 |
| PE 99-M 3 | 377 | 405 | 417 | 431 | 437 | 2.9 |
| PE 99-M 6 | 377 | 404 | 419 | 432 | 439 | 5.8 |

### 3. Calorimetric studies on the influence of functionalized silica nanoparticles on the isothermal crystallization of poly(nonamethylene azelate)

Kinetic analysis was only performed for melt crystallization processes because of the impossibility to obtain amorphous samples by cooling the melted nanocomposite at the maximum rate allowed by the equipment.

Crystallization experiments were therefore carried out in a narrow temperature interval (i.e. between 56 and 59 ºC) due to experimental limitations. The time evolution of the relative degree of crystallinity, *c(t)*, was determined from crystallization exotherms (Figure 9a) from the neat polyester and the PE99-N 3 nanocomposite through the ratio area of the exotherm up to time *t* divided by the total exotherm area:

$$c(t) = \int_{t0}^{t} (dH/dt)dt \; / \; \int_{t0}^{\infty} (dH/dt)dt \qquad (1)$$



where d*H*/d*t* is the heat flow rate and $t_0$ the induction time. The development of crystallinity always showed a characteristic sigmoidal dependence on time for the five melt crystallization experiments performed for the different samples (Figure 9b). These data were analyzed assuming the well-known Avrami equation[26,27] for primary crystallization:

$$1 - c(t-t_0) = \exp[-Z\,(t-t_0)^n] \qquad (2)$$

where *Z* is the temperature-dependent rate constant and *n* the Avrami exponent whose value varies according to the crystallization mechanism. A normalized rate constant, $k = Z^{1/n}$, is usually evaluated for comparison purposes since its dimension ($time^{-1}$) is independent of the value of the Avrami exponent.

**Figure 9.** (a) Exothermic DSC peaks corresponding to isothermal crystallizations of PE99 (garnet) and PE99-N 3 (blue) samples at temperatures between 56 and 59 ºC. (b) Development of the relative degree of crystallinity of PE99 (garnet) and PE99-N 3 (blue) samples at different crystallization temperatures.

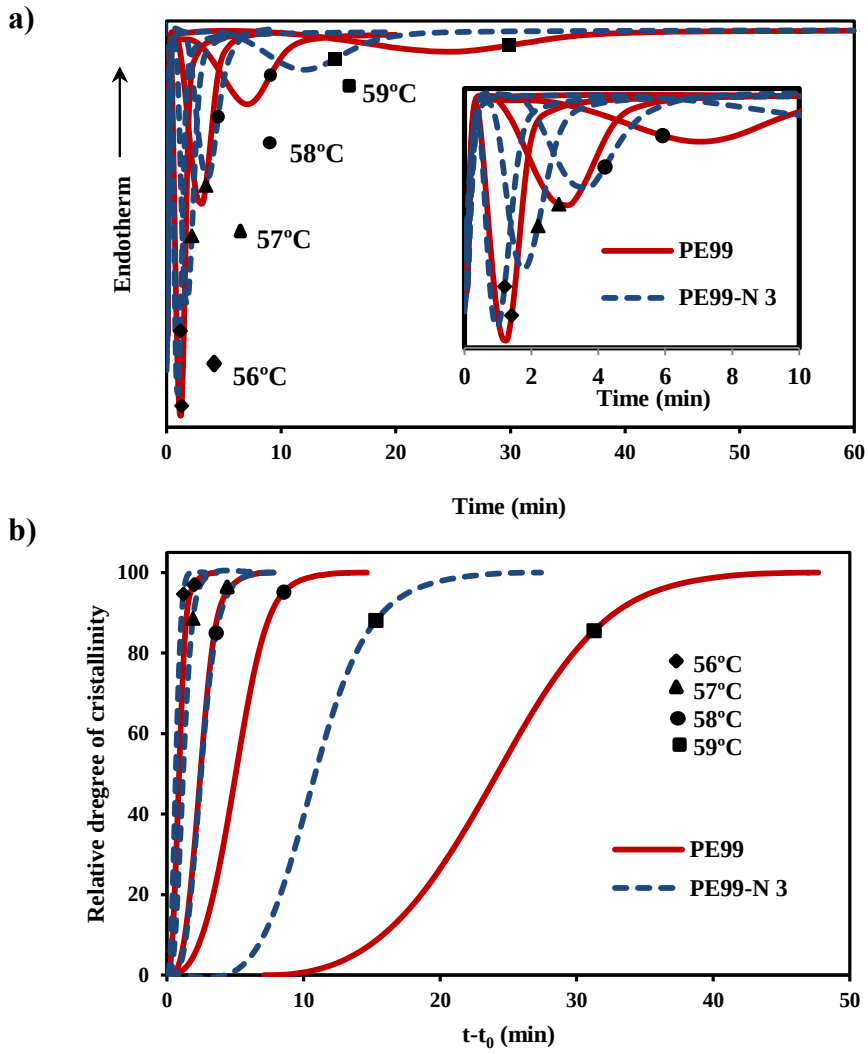




Table 3 summarizes the main kinetic parameters of the primary crystallization process, as deduced from the plots of log{-ln[1-*c* (*t*- $t_0$)]} against log (*t* - $t_0$) (Figure 10). The values of the Avrami exponent for the neat polyester remained in a narrow range, from 2.60 to 2.94, 2.78 being

the average value. This suggests the occurrence of predetermined (heterogeneous) nucleation with spherical growth under high geometric constraints since the theoretical value should be equal to 3. Both sporadic (heterogeneous) and homogeneous nucleation can be clearly discarded as a higher exponent, close to 4, should be derived. Furthermore, homogeneous nucleation usually requires high undercooling, which is not the case. The exponent slightly decreased for the nanocomposite (*i.e.,* 2.54-2.14, being 2.33 the average value), suggesting an increase of geometrical constrains as a consequence of the incorporation of the well dispersed nanospheres. Exponents determined for both samples were found to vary without a well-defined trend within the selected and narrow temperature interval.

**Table 3.** Main crystallization kinetic parameters determined by DSC for the neat polyester and its nanocomposite with 3 wt-% of functionalized silica nanospheres.

| Sample | $T$ (ºC) | $Z \times 10^6$ ($s^{-n}$) | $n$ | $k \times 10^3$ ($s^{-1}$) | $1/\tau_{1/2} \times 10^3$ ($s^{-1}$) | $(Z/\ln 2)^{1/n} \times 10^3$ ($s^{-1}$) |
|---|---|---|---|---|---|---|
| PE99 | | | | | | |
| | 56 | 18.48 | 2.60 | 15.23 | 17.93 | 17.5 |
| | 57 | 0.28 | 2.94 | 5.89 | 6.82 | 6.67 |
| | 58 | $7.70.10^{-2}$ | 2.81 | 2.92 | 3.31 | 3.32 |
| | 59 | $2.80 .10^{-3}$ | 2.79 | 0.86 | 0.97 | 0.99 |
| PE99-N 3 | | | | | | |
| | 56 | 98.56 | 2.42 | 21.98 | 25.97 | 25.58 |
| | 57 | 42.03 | 2.31 | 12.84 | 15.12 | 15.05 |
| | 58 | 2.69 | 2.54 | 6.37 | 7.62 | 7.36 |
| | 59 | 1.89 | 2.14 | 2.12 | 2.54 | 2.52 |



The values corresponding to reciprocal crystallization half-times ($1/t_{1/2}$), calculated as the inverse of the difference between crystallization start time and half-crystallization time, are also given in Table 3. This parameter is a direct measure from the DSC crystallization isotherm, and can therefore be used to check the accuracy of Avrami analysis by comparison with the theoretical kinetic value (*i.e.,* $1/t_{1/2} = (Z / \ln 2)^{1/n}$). Values reported in Table 3 showed a good agreement between the $1/t_{1/2}$ reciprocal times deduced from both methods. Summarized data allows also evaluating the variation of the overall rate constant with temperature for the neat polymer and its nanocomposite with the silica nanospheres. Logically, this rate increased for

each sample by lowering the crystallization temperature. Thus, the rate for the nanocomposite increased from 2.12 × $10^{-3}$ $s^{-1}$ to 21.98 × $10^{-3}$ $s^{-1}$ when crystallization temperature decreased from 59 ºC to 56 ºC. More interestingly, the nanocomposite showed a remarkable higher crystallization rate than the neat polyester at each studied crystallization temperature (*e.g.*, 21.98 × $10^{-3}$ $s^{-1}$ and 15.23 × $10^{-3}$ $s^{-1}$ were determined at 56 ºC for PE99-N 3 and PE99, respectively). Therefore, incorporation of functionalized silica nanoparticles had a drastic influence on the crystallization process and logically on final material properties. It should be pointed out that the ratio between the two kinetic constants decreased (*i.e.*, between 2.5 and 1.4) as crystallization temperature decreased, a feature that deserves further studies on nucleation and crystal growth processes.

**Figure 10.** Avrami plots corresponding to isothermal crystallization of PE99 (a) and PE99-N 3 (b) at the indicated temperatures.

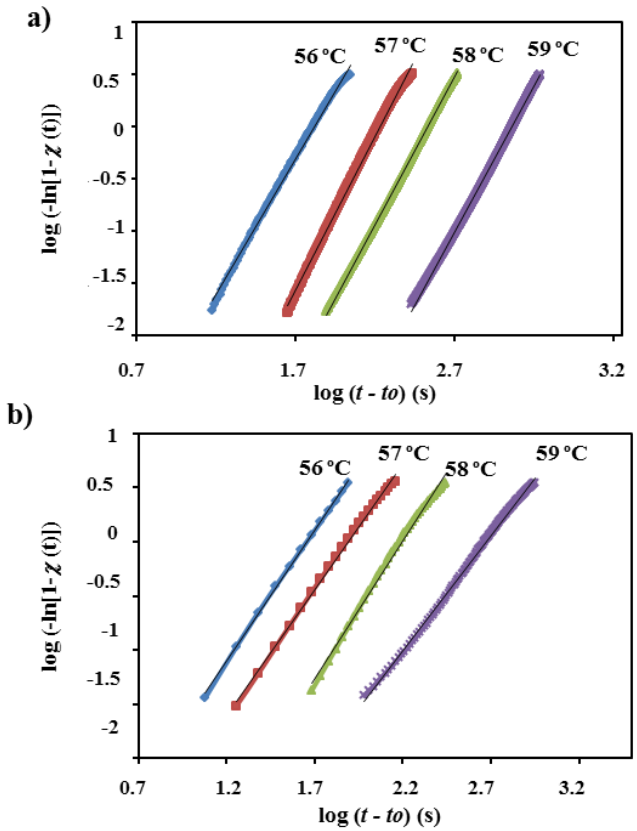

## 4. Optical microscopy studies on the influence of functionalized silica nanoparticles on the isothermal crystallization of poly(nonamethylene azelate)

Crystallization kinetics from the melt state was also studied for micro-molded samples with and without functionalized silica nanospheres by optical microscopy. Spherulite radii grew linearly in both cases with time until impingement, as shown in Figure 11a. Crystal growth rates were clearly higher for the nanocomposite when crystallization temperature was high, being difference minima when this temperature decreased. The relatively high growth rate allowed collecting only experimental data over a narrow temperature range where crystallization was mainly governed by secondary nucleation (*i.e.,* the typical bell curve of crystal growth rate versus temperature could not be attained). The increase on the crystal growth rate for the nanocomposite is peculiar and suggests a favoured deposition of molecules onto the existing crystal surfaces as then will be discussed. At lower temperatures, this effect seems to be counterbalanced by the reduction of chain mobility in presence of silica nanoparticles and the spatial constraints imposed by confinement.[28,29]



Both the pristine polyester and the nanocomposite developed spherulites with similar morphologic features (Figure 12). Thus, both samples crystallized from the melt into ringed spherulites with negative birefringence. The spacing between rings significantly decreased with decreasing crystallization temperatures (*i.e.,* 13 μm at 60 ºC and 5 μm at 56 ºC) and slightly diminished when nanospheres were incorporated (i.e., 5 μm with respect to 4 μm for crystallizations performed at 56 ºC). A more confusing texture was detected for both samples at an intermediate temperature (*i.e.,* 59 ºC) since rings appeared less defined. Note that spherulites of both pristine polyester and the nanocomposite fill all field of view and had a relatively uniform size, which suggest an athermal nucleation (*i.e*., the number of nuclei remains constant during crystallization). More interestingly, this result indicates a good dispersion of silicate nanoparticles in the polyester matrix. In fact, adsorption of PE99 molecules onto the functionalized surface of silica nanoparticles may hinder particle-particle agglomeration and enhance a colloidal stability.

**Figure 11. (**a) Variation of PE99 (garnet) and PE99-N 3 (blue) spherulitic radii with time for isothermal crystallizations performed at the indicated temperatures. (b) Change in the nucleation density with isothermal crystallization temperature for PE99 (garnet) and PE99-N 3 (blue) samples.

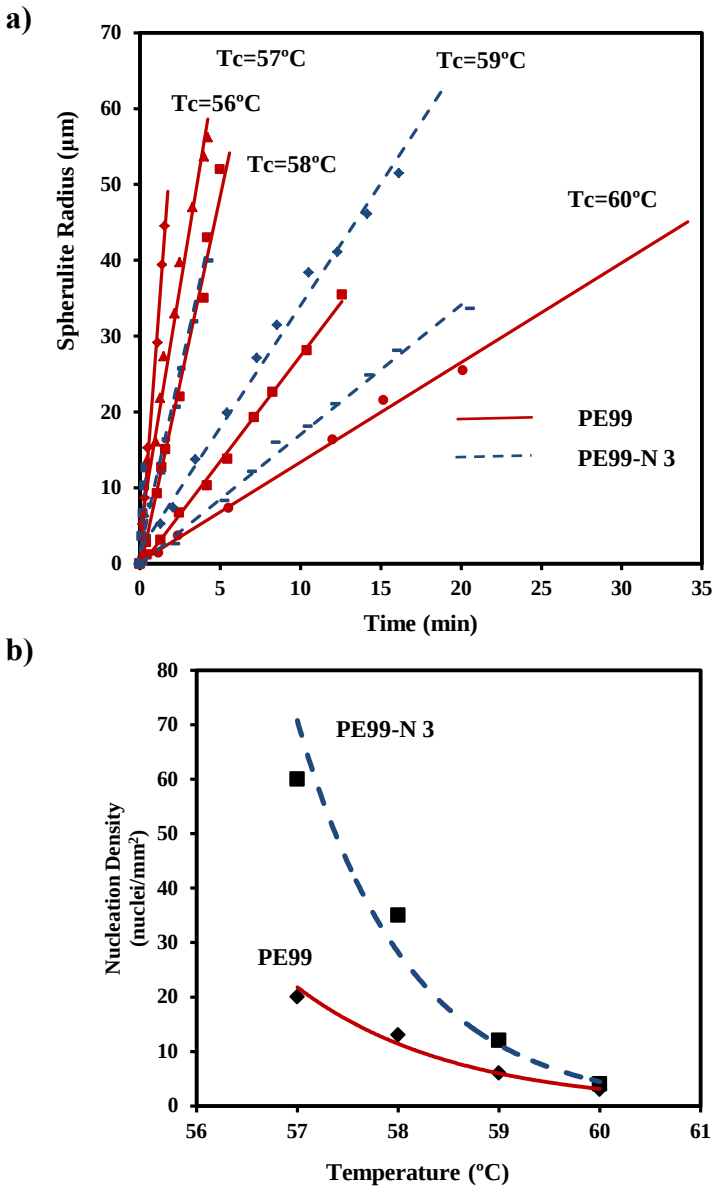

Despite the morphological similarities, great differences were detected in the primary nucleation (Figure 11b). These differences were more remarkable as the crystallization temperature decreased and for example nucleii densities of 60 and 20 nucleii/mm$^2$ were determined from the optical micrographs taken at 57 ºC. Note that crystal growth rates were similar at this temperature and consequently the differences determined for the overall crystallization rate (*e.g.,* 0.01284 and 0.00589 s$^{-1}$ for PE99 and PE99-N 3 at 57 ºC, respectively) could be mainly attributed to a nucleation effect. On the contrary, nucleation densities were similar at high temperature, while crystal growth rates were clearly different. Therefore, the incorporation of nanoparticles had a high impact on the overall crystallization rate due to differences on crystal growth rate and primary nucleation densities, which became more significant at high and low crystallization temperatures, respectively. Figure 11b shows also that the nucleation density increased in an exponential way for the two studied samples as the crystallization temperatures decreased. These changes on nucleation logically affected the final spherulitic size, being observed a diameter decrease from 120 µm to 35 µm and from 80 µm to 15 µm for PE99 and PE99-N 3 samples, respectively, when temperature decreased only from 60 ºC to 56 ºC.



The radial growth rate ($G$) of polymer crystals is usually described by the Lauritzen and Hoffman equation,[30] which is based on the Turnbull–Fisher expression[31] suitable for the crystallization process of homopolymers. The Lauritzen and Hoffman equation is formulated as:

$$G = G_0 \exp[-U^*/(R(T_c - T_\infty))]\exp[-K_g/(T_c(\Delta T)f)] \quad (3)$$

where $G_0$ is a constant preexponential factor, $U^*$ represents the activation energy characteristic of the transport of the crystallizing segments across the liquid–crystal interface, $T_\infty$ is the temperature below which such motion ceases, $T_c$ is the crystallization temperature, $R$ is the gas constant, $K_g$ is the secondary nucleation constant, $\Delta T$ is the degree of supercooling measured as $T_m^0 - T_c$, and $f$ is a correction factor accounting for the variation in the bulk melting enthalpy per unit volume with temperature ($f = 2T_c/(T_m^0 + T_c)$).

It is advisable to rearrange Eq. (3) in a logarithmic form:

$$\ln G + U^*/R(T_c - T_\infty) = \ln G_0 - K_g/[T_c(\Delta T)f] \quad (4)$$

and plot the left-hand side of the equation versus 1/ [$T_c$ ($\Delta T$) $f$ ]. Straight lines with slopes equal to -$K_g$ should be obtained.

**Figure 12.** Optical micrographs of PE99 (a, c, e) and PE99-N 3 (b, d, f) spherulites isothermally grown at 60 ºC (a,b), first step at 59 ºC and a second step at 54 ºC (c,d) and 56 ºC (e,f). Well-defined rings with a interspacing between 3 and 2 mm were detected (see arrows) in the outer part of spherulites grown at 54 ºC.

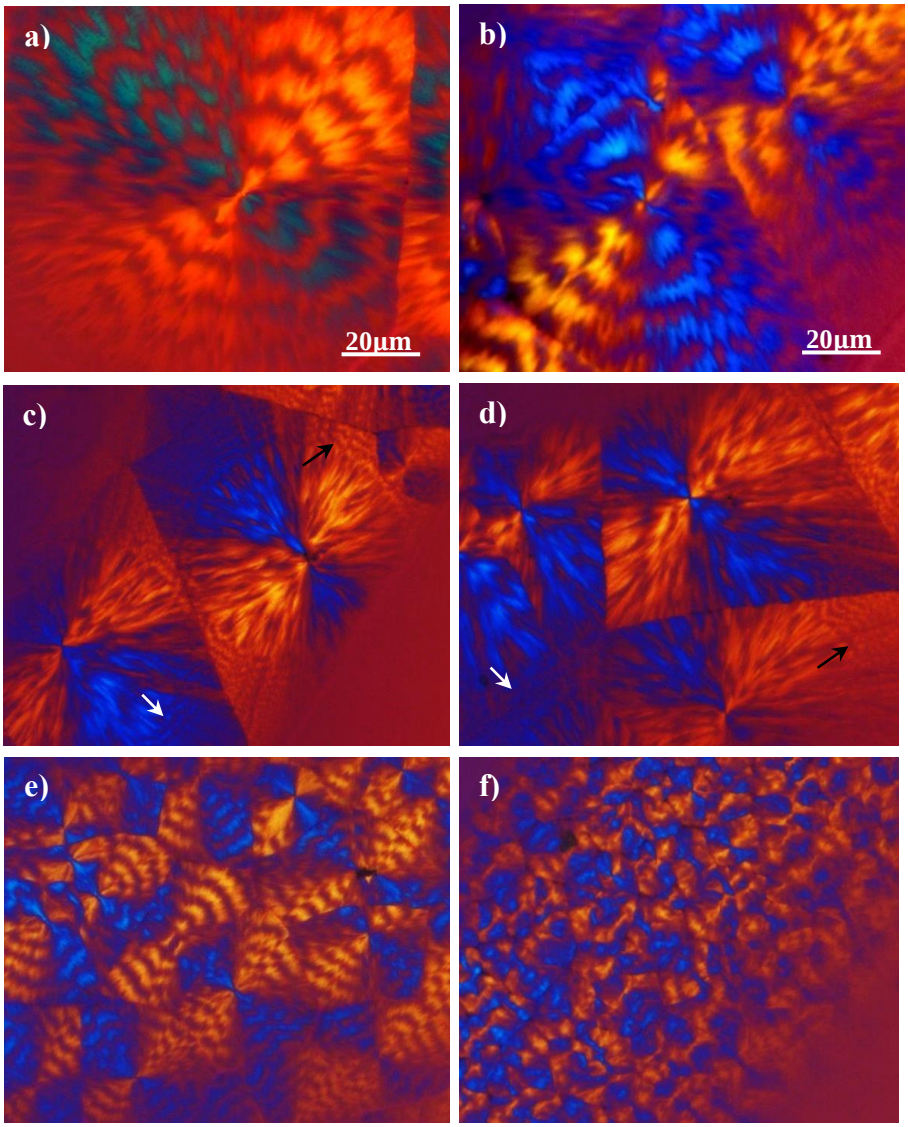

The Lauritzen-Hoffman plot was fitted for both PE99 and PE99-N 3 micro-molded samples with straight lines ($r^2$ > 0.97) when the "universal" values reported by Suzuki and Kovacs[32] (*i.e.*, $U^*$ = 1500 cal/mol and $T_\infty = T_g$ - 30 K) and the experimental glass transition temperature of PE99 (*i.e.*, -45 ºC) were used in the calculation (Figure 13). Kinetic features at low supercoolings are basically governed by the nucleation term, and consequently crystallization rates could become relatively insensitive to the $U^*$ and $T_\infty$ parameters. Therefore, determination of equilibrium melting temperature was important since it influenced on the degree of supercooling and consequently in the nucleation term. Typical Hoffman-Weeks plots[33] where performed with samples crystallized at different temperatures (not shown). Extrapolations of the melting temperatures observed in a subsequent heating run led to equilibrium temperatures of 79.2 ºC and 76.4 ºC for PE99 and PE99-N 3 samples, respectively. The slight change suggests low degree of perfection of lamellae when the functionalized silica nanoparticles were added. The Lauritzen-Hoffman plot allowed estimating secondary nucleation constants of 1.30 × $10^5$ and 1.18 × $10^5$ $K^2$ for PE99 and PE99-N 3 samples, respectively. These values indicate clearly indicate that the presence of functionalized nanoparticles favored the crystallization process. Thus, the enhanced PE99/$SiO_2$ interfacial interaction may decrease the work to fold the polyester chains and promote their deposition on the existing crystal surfaces during the secondary nucleation process.[34,25]



**Figure 13.** Plot of ln $G + U^* / R(T_c-T_\infty)$ versus 1 / $T_c(DT)$ $f$ to determine the $K_g$ secondary nucleation parameter of PE99 (garnet) and PE99-N 3 (blue) samples.

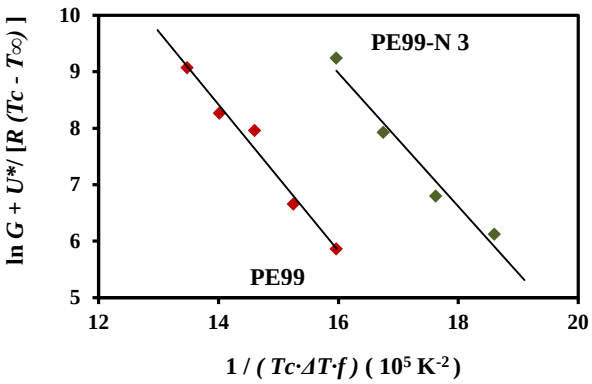

## IV. Conclusions

Poly(nonamethylene azelate) and its mixtures with functionalized silica micro/nanoparticles can be micro-molded by means of ultrasonic energy and using similar time, amplitude and force processing parameters. Minimum polymer degradation was detected in the molded specimens as well as a good dispersion of the added particles. In addition, thermal stability was slightly improved by the addition of silica particles. The decomposition of grafted functional groups was only detected at the end of the thermal degradation process.

Silica nanoparticles had a significant influence on the crystallization process even at the low content of 3 wt-%. Avrami exponents slightly decreased with respect to the neat polymer as a probe of the geometrical constrains caused by the incorporation of the well dispersed nanospheres. The overall crystallization rate of nanocomposites was always greater than that determined for the neat polymer being the ratio of the respective constants between 1.4 and 2.5. Negative and ringed spherulites were obtained at the different assayed temperatures following an athermal nucleation. Furthermore, agglomeration of silicate particles can be discarded from morphological observations. Primary nucleation was significantly enhanced when silica nanoparticles were added, being expected that the functionalized surface of silica nanoparticles favoured the adsorption of polyester molecules. In addition, the enhanced PE99/$SiO_2$ interfacial interaction favours molecular deposition on the existing crystal surfaces causing a decrease on the secondary nucleation constant and an increase on the crystal growth rate.

## V. References


1. Fairbanks HV. Ultrasonics 1974;12:22.
2. Paul DW, Crawford RJ. Ultrasonics 1981;19:23.
3. Schomburg WK, Burlage K, Gerhardy C. Micromachines 2011;2:157.
4. Khuntontong P, Blaser T, Maas D, Schomburg WK. "Fabrication of a polymer micro mixer by ultrasonic hot embossing", Proc. 19th Micro-Mechanics Europe Workshop, MME 2008, 28. - 30. ISBN 978-3-00-025529-8.
5. Khuntontong P, Blaser T, Schomburg WK. Manufacturing 2009;32:152.
6. Michaeli W, Spennemann A, Gartner R. Microsyst Technol 2002;8:55.
7. Michaeli W, Starke C. Polym Test 2005;24:205.
8. Michaeli W, Kamps T, Hopmann C. Microsyst Technol 2011;17:243.
9. Chen J, Chen Y, Li H, Lai SY, Jow J. Ultrason Sonochem 2010;17:66.
10. Chen G, Guo S, Li H. J Appl Polym Sci 2002;84:2451.
11. Kang J, Chen J, Cao Y, Li H. Polymer 2010;51:249.
12. Cao Y, Li H. Polym Eng Sci 2002;42:1534.
13. Sacristán M, Plantá X, Morell M, Puiggalí J. Ultrason Sonochem 2014;21:376.
14. Planellas M, Sacristán M, Rey L, Olmo C, Aymamí J, Casa, MT, Del Valle LJ, Franco L, Puiggalí J. Ultrason Sonochem 2014;21:1557.
15. Díaz A, Casas MT, del Valle LJ, Aymamí J, Olmo C, Puiggalí J. J Polym Res 2014;21:584.
16. Usuki A, Kojima Y, Kawasumi M, Okada A, Fukushima Y, Kurauchi T, Kamigaito O. J Mater Res 1993;8:1185.
17. Kojima, Y.; Usuki, A.; Kawasumi, M.; Okada, A.; Kurauchi, T.; Kamigaito, O. J Polym Sci, Part A: Polym Chem 1993, 31, 983.
18. Kojima Y, Usuki A, Kawasumi M, Okada A, Kurauchi T, Kamigaito O. J Polym Sci, Part A: Polym Chem 1993;31:1755.
19. Engin B. Polymer 2011;52:5118.
20. Choi M, Kim C, Ok Jeon S, Soo Yook K, Yeob Lee J, Jang J. Chem Commun 2011;47:7092.
21. Yang F, Ou Y, Yu Z. J Appl Polym Sci 1998;69:355.
22. Xu X, Li B, Lu H, Zhang Z, Wang H, J Appl Polym Sci 2008;107:2007.

23. Vassiliou AA, Papageorgiou GZ, Achilias DS, Bikiaris DN. Macromol Chem Phys 2007;208:364.
24. Busbee JD, Juhl AT, Natarajan LV, Tongdilia VP, Bunning TJ, Vaia RA, Braun PV. Adv Mater 2009;21:3659.
25. Lee E, Hong J-Y, Ungar G, Jang J. Polym Int 2013;62:1112.
26. Avrami M. J Chem Phys 1939;7:1103.
27. Avrami M. J Chem Phys 1940;8:212.
28. Kennedy M, Turturro G, Brown G, Rand St, Pierre LE. Nature 1980;287:316.
29. Nitta K, Asuka K, Liu B, Terano M, Polymer 2006;47:6457.
30. Lauritzen JI, Hoffman JD. J Appl Phys 1973;44:4340.
31. Turnbull D, Fisher JC. J Chem Phys 1949;17:71.
32. Suzuki T, Kovacs AJ. Polym J 1970;1:82.
33. Hoffman JD, Weeks JJ. J Res Natl Bur Stand 1962;66:13.
34. Wang K, Wu J, Zeng H. Eur Polym J 2003;39:1647.

# *Chapter 5.*

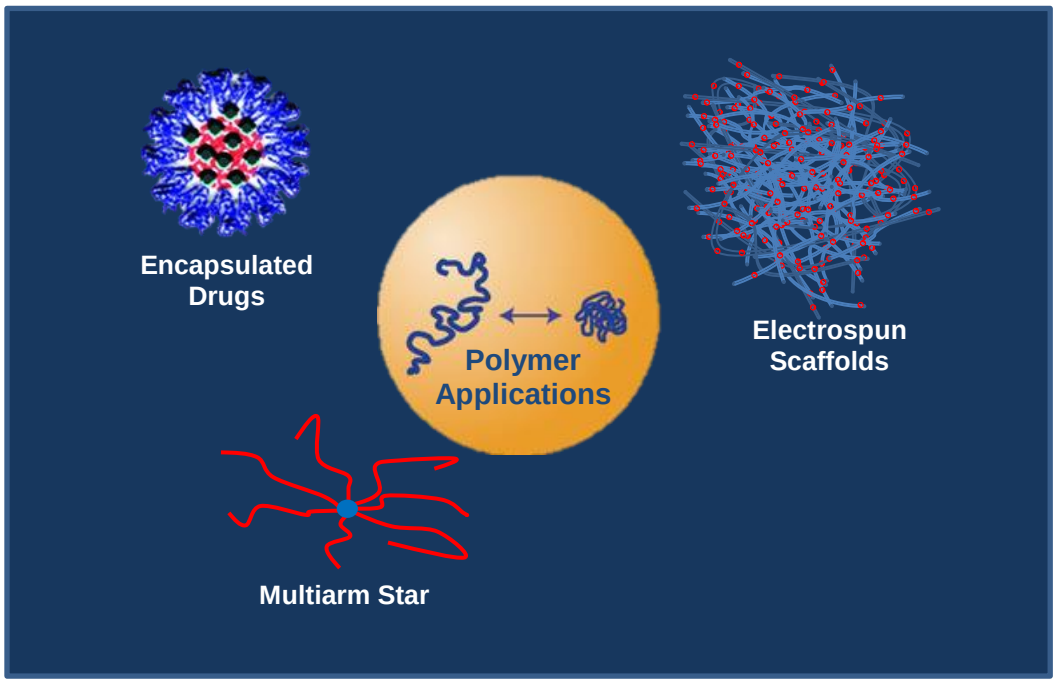
Encapsulated
Drugs
Polymer
Applications
Electrospun
Scaffolds
Multiarm Star

# Chapter 5.1

## *New poly(ester urea) derived from L-leucine: Electrospun scaffolds loaded with antibacterial drugs and enzymes.*

Electrospun scaffolds from an amino acid containing poly(ester urea) (PEU) were developed as promising materials in the biomedical field and specifically in tissue engineering applications. The selected poly(ester urea) was obtained with a high yield and molecular weight by reaction of phosgene with a bis(α-aminoacyl)-α,ω-diol-diester monomer. The polymer having L-leucine, 1,6-hexanediol and carbonic acid units had a semicrystalline character and relatively high glass transition and melting temperatures. Furthermore it was highly soluble in most organic solvents, an interesting feature that facilitated the electrospinning process and the effective incorporation of drugs with bactericide activity (e.g. biguanide derivatives such as clorhexidine and polyhexamethylenebiguanide) and enzymes (e.g. α -chymotrypsin) that accelerated the degradation process. Continuous micro/nanofibers were obtained under a wide range of processing conditions, being diameters of electrospun fibers dependent on the drug and solvent used.

Poly(ester urea) samples were degradable in media containing lipases and proteinases but the degradation rate was highly dependent on the surface area, being specifically greater for scaffolds with respect to films. The high hydrophobicity of new scaffolds had repercussions on enzymatic degradability since different weight loss rates were found depending on how samples were exposed to the medium (e.g. forced or non-forced immersion). New scaffolds were biocompatible, as demonstrated by adhesion and proliferation assays performed with fibroblast and epithelial cells.

## I. Introduction

Poly(ester urea)s (PEUs) have been proposed as a new class of α-amino acid-based polymers with bioabsorbable properties. These polymers can be easily prepared from bis(α-amino acid)-alkylene diester monomers, which can undergo either nonspecific (chemical) or specific (enzymatic) hydrolysis due to the presence of two ester linkages per elemental unit in the molecule. First syntheses were reported in the late 1970s by Huang *et al.*[1] and yielded low molecular weight powdery samples ($M_n$ close to 2,000 g/mol). Later, Yoneyama *et al.* synthesized high molecular weight PEUs by condensing the above diester-diamine monomers with non-physiological diisocyanates.[2] In order to avoid the use of diisocyanates, other syntheses based on polycondesation processes through active carbonates (*e.g.,* di-*p*-nitrophenyl carbonate) were investigated.[3] However, intramolecular cyclization led to low molecular weight polymers, which in turn led to hydantoin formation, and therefore, chain scission.

Problems were solved when an acid chloride of carbonic acid (phosgene, diphosgene, triphosgene) was entered into the polycondensation reaction with a di-*p*-toluenesulfonic acid salt of a bis(α-amino acid)-alkylene diester (Figure 1a).[4] In the interfacial polycondensation reaction, the nucleophilic amino group was readily revealed by addition of an inorganic base, such as NaOH, $NaHCO_3$ and $Na_2CO_3$. This method provides high-yield, high-molecular weight PEUs potentially useful for biomedical applications because of their advantageous mechanical, chemical and biodegradation properties over well-known, chemically similar poly(ester amide)s also derived from α-amino acids.[5] For example, the PEU derived from carbonic acid, L-leucine, and 1,6-hexanediol (named 1L6, as indicated in Figure 1a) has tensile strength at yield, elongation at break and Young's modulus of 21 MPa, 114% and 622 MPa, respectively.[4] Its melting temperature is 114 ºC and its glass transition temperature 47 ºC. New PEUs were proposed to be useful as implantable surgical devices such as vascular stents and hard tissue replacement implants, and also for delivery of a variety of pharmaceutical and biologically active agents to humans and other mammals.

**Figure 1.** (a) Synthesis scheme for the poly(ester urea) derived from L-leucine, 1,6-hexanediol and carbonic acid. (b) Chemical structures of selected antibacterial drugs: chlorhexidine (CHX) and polyhexamethylenebiguanide hydrochloride (PHMB).

**a)**

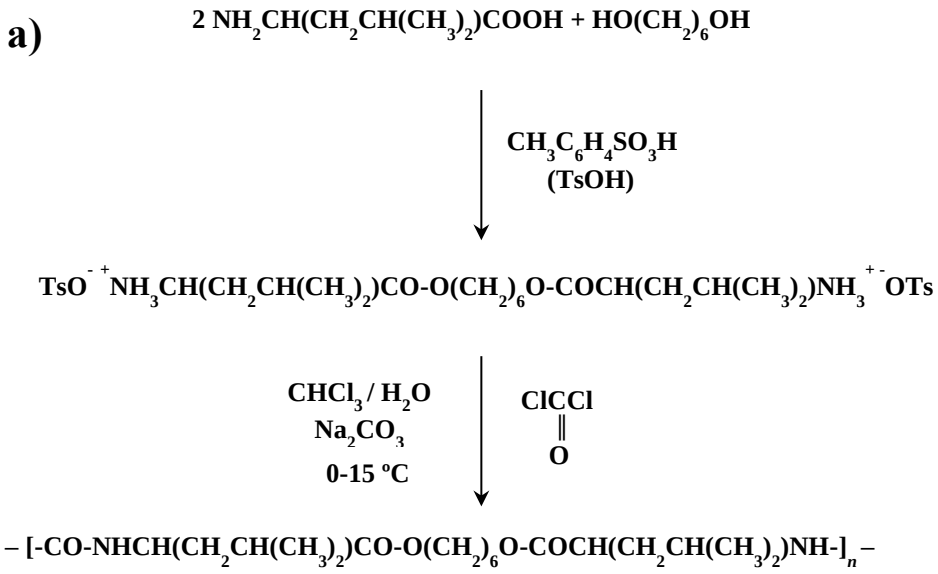


**1L6:** PEU derived from carbonic acid (**1**), L-Leucine (**L**) and 1,6-hexanediol (**6**)

**b)**

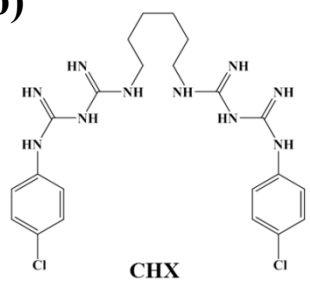

**CHX**

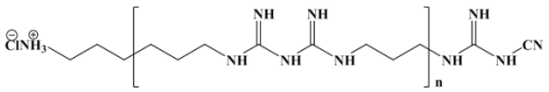

**PHMB**

Micro/nanofiber nonwoven scaffolds produced by electrospinning have shown great potential for tissue engineering applications because of their typically high surface area and

porosity. Electrospinning is a well-known electrostatic technique that uses a high voltage field to charge the surface of a polymer solution droplet at the end of a capillary tube and induce the ejection of a liquid jet towards a grounded target (collector).[6-9] Morphology of fibers obtained in the collector depends on the solution properties (e.g. viscosity, dielectric constant, volatility and concentration) and operational parameters (*e.g.,* strength of the applied electric field, deposition distance and flow rate), which should be conveniently addressed.[10,11]

The unique properties of electrospun fibers have triggered a wide range of other potential applications,[12] including composites,[13,14] sensors,[15] protective clothing,[16] filtration membranes,[17-20] magneto-responsive fibers and superhydrophobic membranes.[21] In addition, the electrospinning process provides a simple way to encapsulate drugs within a micro/nanofiber matrix that can lead to a controlled and sustained release. Several natural and synthetic biodegradable polymers have been successfully electrospun (*e.g.*, polyglycolide,[22] polylactide,[22,23] polycaprolactone,[24] collagen[25,26] and chitosan[26,27]).

The main goal of the present work is to explore the possibilities of PEUs, and specifically of the 1L6 sample, for preparing electrospun scaffolds. Furthermore, loading with anti-bactericidal agents having biguanide groups is explored, as well as the possibility of incorporating degrading agents such as a proteolytic enzyme like α-chymotrypsin. To the best of our knowledge, this is the first time that a poly(ester urea) has been assayed as an electrospinnable polymer, which is in itself an interesting topic because it adds to the range of materials useful for tissue engineering applications. Furthermore, development of antibacterial nanofibers through electrospinning is nowadays a relevant topic for wound dressing applications as has recently been reviewed by Gao *et al.*[28] Different systems have been considered taking into account the substrate polymer (*e.g.*, polylactide and polycaprolactone), the antibacterial agent (*e.g.*, antibiotic, bactericide, silver and metal oxide nanoparticles and chitosan) and the applied procedure (incorporation of the agent in the electrospinning solution, coaxial electrospinning, previous encapsulation of the antibacterial agent, conversion of a precursor to its active form by a post-treatment and attachment of the active agent onto the fiber surface). Specific systems based on the use of bactericide agents are summarized in Table 1,[28] which also reveals the relevance of the use of biguanide derivatives.

**Table 1.** Electrospun scaffolds loaded with bactericide agents.[a]

| Electrospun Polymer | Solvent | Concentration | Antibacterial Agent | Reference |
|---|---|---|---|---|
| PCL/PLA | CF/acetone 3:1 v/v | 10% w/v | Triclosan | 29 |
| PLA | CF/DMF 9:1 v/v | 8% w/v | Triclosan | 30 |
| CA | DMF | 3 wt% | **Chlorhexidine** | 31 |
| PAN | DMSO | 15 wt% | QACs | 32 |
| CA/PEU | DMF/THF 50:50 v/v | 20/10 wt% | **PHMB** | 33 |
| PAN | DMF | 10% w/v | **PHMB** | 34 |
| PAN | DMF | 10 wt % | N-Halamine | 35 |
| PEO/Chitosan | $H_2O$/Acetic acid | 3-4 wt% | K5N8Q | 36 |
| PDLLA, PEO | DMF | 20–24 wt% | Antibacterial peptides | 37 |
| PADAS | HFIP | 10 wt% | **Chlorhexidine** | 38 |
| PLA/PCL | CF-acetone 2:1 v/v | 10-2.5 wt% | Triclosan | 39 |
| PLA/PEG | DCM/DMF 70:30 v/v | 7-35 wt% | Triclosan | 40 |
| PHB/PEO | DMF/CF 80:20 v/v | 10% w/w | **Chlorhexidine** | 41 |



[a] PCL (polycaprolactone), PLA (polylactide), PDLLA (poly(D,L-lactide)), PEG (poly(ethylene glycol)), CA (cellulose acetate), PAN (polyacrylonitrile), PEU (poly (ester urea)), PEO (poly(ethylene oxide)), PADAS (poly(ester amide) derived from alanine, 1,12-dodecanediol and sebacic acid units), QACs (N,N-didecyl-N,N-dimethylammonium chloride and bis-(3-aminopropyl)-dodecylamine), PHMB (polyhexamethylenebiguanide hydrochloride), K5N8Q (potassium 5-nitro-8-quinolinolate), DMF (N,N-dimethylformamide), DMSO (dimethyl sulfoxide), THF (tetrahydrifuran), HFIP (hexafluoroisopropanol), PHB (poly(hydroxybutyrate)), CF (Chloroform), DCM (dichloromethane).

Biguanide (Figure 1b), commonly known as chlorhexidine (1,1′-hexamethylene- bis-5-(4-chlorophenyl) biguanide, CHX), is a widely employed antimicrobial agent.[42] Specifically, CHX is an important antiseptic, disinfectant, pharmaceutical and cosmetic preservative and antiplaque

agent. Its high activity against microorganisms is provided by the presence of secondary amines that can be protonated, and therefore positively charged under normal pH conditions.[43] Immobilization of antimicrobial agents may reduce patient exposure to active agents and potentially increase the duration of antimicrobial efficacy.[44,45] One way to achieve immobilization is by loading micro/nanofibers of electrospun scaffolds with the desired drug.

Other chemical compounds bearing biguanide groups have been developed.[46,47] For example, polyhexamethylenebiguanide hydrochloride (PHMB) is a cationic oligomer having an average of 7-11 biguanide groups spaced by flexible hexamethylene segments (Figure 1b). PHMB has chemical stability, low toxicity, high effectiveness against microorganisms and reasonable cost.[48-50] Gilbert *et al.* demonstrated that activity increased with the number of biguanide groups and that maximum biocidal efficiency was obtained when the hexamethylene group was employed as spacer.[51]

## II. Experimental Section



### 1. Materials

The poly(ester urea) 1L6 was synthesized with an 91-93% yield, as shown in the scheme in Figure 1, following the procedure previously reported by Gomurashvili *et al.*[4]

All solvents, clorhexidine (CHX ≥ 98% (HPLC)), 3-(4,5-dimethylthiazol-2-yl)-2,5-diphenyl-2H-tetrazolium bromide (MTT), enzymes (lipase, proteinase K and α-chymotrypsin) and cell culture labware were purchased from Sigma-Aldrich (Spain). Cosmocil® (polyhexamethylenebiguanide hydrochloride, PHMB) (Batch No 10GR140505) was purchased from Arch UK Biocides (20% aqueous solution), then lyophilized and provided by B. Braun Surgical, S.A. The microbial culture was prepared with reagents and labware from Scharlab (Spain).

*Escherichia coli* CECT 101 and *Micrococcus luteus* CECT 245 bacterial strains were obtained from Spanish Collection of Type Culture (Valencia, Spain). African green monkey kidney fibroblast (COS-7) and epithelial (Vero) cells were purchased from ATCC (USA).

### 2. Molecular weight characterization of the poly(ester urea) 1L6

Weight and number average molecular weights determined by GPC were 74,100 and 51,100 g/mol, respectively. The GPC (Waters Associates, Inc., Milford, United States) was equipped with a high-pressure liquid chromatography pump (Waters 1525 binary HPLC), styragel columns (HR4, HR3 and HR0.5) (7.8 mm × 300 mm) and a refractive index detector (Waters 2414). The polymer was dissolved and eluted in a solution of LiBr (0.1 M) in dimethylformamide at a flow rate of 1.0 mL/min (injected volume 100 µL, sample concentration 2.0 mg/mL). The columns were calibrated with polyethylene glycol standards.

### 3. Electrospinning

Electrospun fibers were collected on a target placed at different distances (10-25 cm) from the needle tip (inside diameter of 0.84 mm). The voltage was varied between 10 and 30 kV and applied to the target using a high-voltage supply (Gamma High Voltage Research, ES30-5W). Polymer solutions were delivered via a KDS100 infusion syringe pump (KD Scientific, USA) to control the mass-flow rate (from 0.5 to 10 mL/h). All electrospinning experiments were carried out at room temperature. Unloaded and α-chymotrypsin, CHX and PHMB loaded electrospun fibers were prepared using optimized parameters (*i.e.,* needle tip-collector distance, voltage and flow rate) and solvent conditions (*i.e.,* solvent ratio, and polymer and drug concentration). Amounts of CHX, PHMB and α-chymotrypsin in the electrospinning solution were selected to render 1L6 scaffolds loaded with 2.8, 0.85 and 10 wt-% of the respective compounds.



### 4. Morphology and properties of electrospun scaffolds

Optical microscopy studies were performed with a Zeiss Axioskop 40 microscope. Micrographs were taken with a Zeiss AxiosCam MRC5 digital camera.

Detailed inspection of texture and morphology of electrospun samples was conducted by scanning electron microscopy using a Focus Ion Beam Zeiss Neon 40 instrument (Carl Zeiss, Germany). Carbon coating was accomplished using a Mitec K950 Sputter Coater fitted with a film

thickness monitor *k*150x. Samples were visualized at an accelerating voltage of 5 kV. Diameter of electrospun fibers was measured with the SmartTiff software from Carl Zeiss SMT Ltd.

Contact angles (CA) were measured at room temperature with sessile drops using an OCA-15 plus Contact Angle Microscope (Dataphysics, USA) and SCA20 software. Values of the right and left sides of distilled water drops were measured 10 s after the drop (5 mL) was deposited on the sample surface. All CA data were an average of six measurements on different surface locations.

### 5. Degradation studies

Degradation study samples were cut from regular films of 1 × 1 $cm^2$ and 200 µm in thickness prepared by melt pressing 300 mg of the appropriate polymer at a temperature of 10 °C above the melting peak temperature or from the mat with an approximate thickness of 60 µm recovered from the electrospinning process.

Enzymatic degradation was conducted at 37 °C using *Rhizopus oryzae* lipase (56-60 units/mg), proteinase K (1 unit/mL) and α-chymotrypsin (40 units/mg). The enzymatic medium, 1 mL, consisted of a pH 7.4 sodium phosphate buffer containing sodium azide (0.03 wt-%) and 1, 0.1 and 1 mg of lipase, proteinase K, and α-chymotrypsin, respectively. All enzymatic solutions were renewed every 48 h because of enzymatic activity loss. After immersion, samples were rinsed with water, dried to constant weight under vacuum and stored over $P_4O_{10}$ before analysis. Weight retention was then evaluated. Degradation studies were performed in quadruplicate, with given data corresponding to the average values.

Morphology of degraded films was inspected by scanning electron microscopy using a Focus Ion Beam Zeiss Neon 40 instrument (Carl Zeiss, Germany). Carbon coating was performed using a Mitec K950 Sputter Coater fitted with a film thickness monitor *k*150x. Samples were visualized at an accelerating voltage of 5 kV.

### 6. Release experiments

Controlled release measurements were made with square pieces (weighing approximately 200 mg) of the electrospun scaffolds. These pieces were weighed and incubated at 37 ºC in an orbital shaker at 200 rpm in tubes of 50 mL for 1 week. PBS buffer (hydrophilic medium) and, alternatively, its mixture with ethanol (*i.e.,* 3:7 *v/v* ratio) as a more hydrophobic component, were used as release media. Drug concentration was evaluated by UV spectroscopy using a Shimadzu 3600 spectrometer. Calibration curves were obtained by plotting absorbance measured at 252 and 234 nm versus CHX and PHMB concentration, respectively, in the hydrophilic medium, whereas 261 (for CHX) and 236 nm (for PHMB) were considered when ethanol was added. Samples were withdrawn from the release medium at predetermined time intervals. The volume was kept constant by addition of fresh medium. All drug release tests were carried out using three replicates and the results were averaged.

Absorbance measurements (282 nm) were also performed to detect the enzyme released in PBS medium from α-chymotrysin loaded scaffolds.



### 7. Antimicrobial test

*Escherichia coli* (*E. coli*) and *Micrococcus luteus* (*M. luteus*) bacteria were selected to evaluate the antimicrobial effect of CHX and PHMB loaded electrospun fibers. The bacteria had previously been grown aerobically to exponential phase in broth culture (5 g/L beef extract, 5 g/L NaCl, 10 g/L peptone, pH 7.2).

Growth experiments were performed on a 24-well culture plate. Square pieces (0.5×0.5×0.1 $mm^3$) of the electrospun scaffolds were placed into each well. Then, 1 mL of broth culture containing $10^3$ CFU was seeded on the electrospun fiber mats. The cultures were incubated at 37 ºC and agitated at 200 rpm. Aliquots of 50 µl were taken at predetermined time intervals for absorbance measurements at 650 nm in a plate reader. Thus, turbidity was directly related to bacterial growth.

Bacterial adhesion onto scaffolds was also determined. The culture media were aspirated after incubation and the material washed once with distilled water. Then, 0.5 mL of sterile 0.01M sodium thiosulfate was added to each well. After addition of 4 mL of broth culture, the plate was incubated at 37 ºC and agitated at 200 rpm for 24 h. The bacterial number was determined as above indicated. All assays were conducted in triplicate and the results averaged.

Scaffolds were fixed with 2.5% *w/v* formaldehyde at 4 ºC overnight. Then, they were washed three times with distilled water and Gram stained for observation by light microscopy.

### 8. Cell adhesion and proliferation assays

Cos-7 and Vero cells were cultured in Dulbecco's modified Eagle medium (DMEM) as previously reported.[52]

Square pieces (0.5×0.5×0.1 $mm^3$) of the electrospun scaffolds were placed and fixed in each well of a multiwell culture plate with a small drop of silicone (Silbione® MED ADH 4300 RTV, Bluestar Silicones France SAS, Lyon, France). They were then sterilized by UV-radiation in a laminar flux cabinet for 15 min. For the cell adhesion and proliferation assays, aliquots of 50-100 µL containing $5x10^4$ cells were seeded onto the electrospun samples in each well and incubated for 24 h (adhesion assay) or 4 days (proliferation assay).



Samples were evaluated by the standard adhesion and proliferation method[52] using three replicates and the results averaged. Samples with adhered and grown cells on the mats were fixed with 2.5% *w/v* formaldehyde at 4 ºC overnight. They were subsequently dehydrated and processed for observation by scanning electronic microscopy.

## III. Results and Discussion

### 1. Electrospinning of poly(ester urea) 1L6

In order to select the most appropriate conditions to obtain continuous 1L6 microfibers, several solvents and binary mixtures were tested at different voltages, flow rates, polymer concentrations and needle tip-collector distances. Selection of the appropriate solvent is

fundamental for continuous microfiber production,[53,54] with a relatively high polymer concentration being generally required to avoid the formation of droplets and electrospun beads, especially when a good solvent is chosen.[55]

1L6 has good solubility in most organic solvents (e.g. chloroform, ethanol and dimethylformamide), but the best results were attained using a $CHCl_3$:EtOH 10:1 v/*v* mixture and even when methanol was employed instead of ethanol. Polymer concentration in the ethanol mixtures had to be higher than 18 wt-%. The high molecular weight of the poly(ester urea) facilitated the electrospinning process and, in fact, continuous microfibers were obtained under a wide range of processing conditions (*i.e.,* needle tip-collector distance, flow rate and voltage). Figure 2 is an example of the optimization process as followed by optical microscopy which shows that good fibers could be attained in most test conditions.

**Figure 2.** Optical micrographs showing the optimization Sequence for the electrospinning parameters and typical morphologies attained in the electrospinning of 1L6 from a $CHCl_3$:EtOH 10:1 *v*/*v* mixture and a polymer concentration of 18 wt-%.



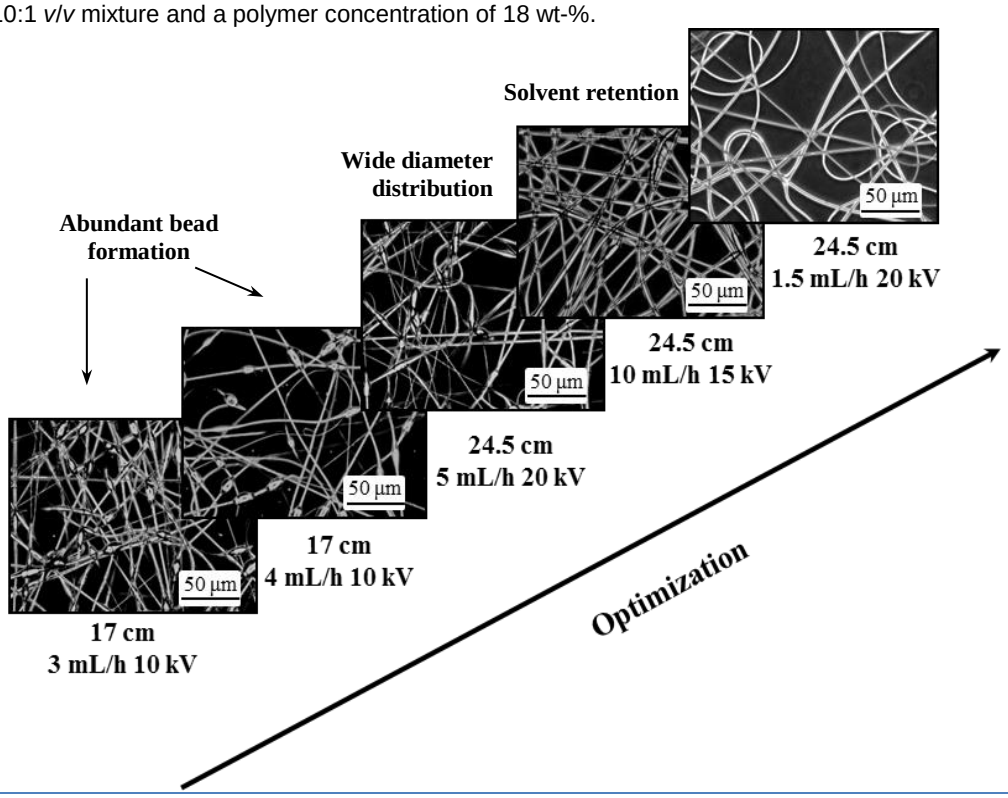

Representative SEM micrographs showing different morphologies are given in Figure 3. Polymer concentration was varied to illustrate the formation of droplets and very thin nanofibers (Figure 3a) at concentrations lower than the above value. At higher values, microfibers were quite similar despite significant differences in conditions (Figures 3b and 3c). Long microfibers with a cylindrical morphology and randomly distributed in the fibrous mats were generally formed. Under optimal process conditions, fibers had a dense but porous structure, a relatively narrow monomodal distribution and an average diameter size of 2.70 µm (Figure 4, Table 2). They were also characterized by a porous surface texture, as shown in high magnification images (Figure 4b).

**Table 2.** Optimal electrospinning conditions for 1L6-CHX, 1L6-PHMB and 1L6-α-Chymotrypsin samples and average diameter size.

| Sample | Voltage (kV) | Rate (mL/h) | Distance (cm) | Diameter (µm) |
|---|---|---|---|---|
| 1L6[a] | 20 | 1.5 | 24.5 | 2.70 ± 0.11 |
| 1L6-CHX[a] | 20 | 1.5 | 24.5 | 2.64 ± 0.14 |
| 1L6-PHMB[a] | 20 | 1.5 | 24.5 | 1.20 ± 0.05 |
| 1L6-α-Chymotrypsin[b] | 25 | 0.5 | 24.5 | 0.458 ± 0.15 |

[a]From solutions contaning 18 wt-% of 1L6.

[b]From solutions contaning 13 wt-% of 1L6.

Electrospinning could also be performed without changing the operational parameters upon incorporation of CHX and PHMB into the polymer solution. CHX loaded electrospun fibers were highly similar to the unloaded samples while incorporation of PHMB resulted in significantly smaller fiber diameters (*i.e.,* from 2.70 to 1.20 µm) (Figures 5a and 5b, Table 1). This indicated a drastic change in the physicochemical characteristic of the electrospinable solution caused by the

presence of polymeric biguanide. No significant changes were found in the fiber surface since a porous texture was detected in both kinds of drug loaded samples.

**Figure 3.** SEM micrographs showing electrospun microfibers obtained from $CHCl_3$:EtOH 10:1 v/*v* mixtures using different voltage, collecting distance, polymer concentration and flow conditions: 25 kV, 24.5 cm, 15 wt-% and 4mL/h (a); 20 kV, 24.5 cm, 18 wt-%, and 1.5 mL/h (b); 25 kV, 24.5 cm, 20 wt-% and 5 mL/h (c). Insets show high magnification images (scale bar 4 μm) to appreciate fiber surface details.

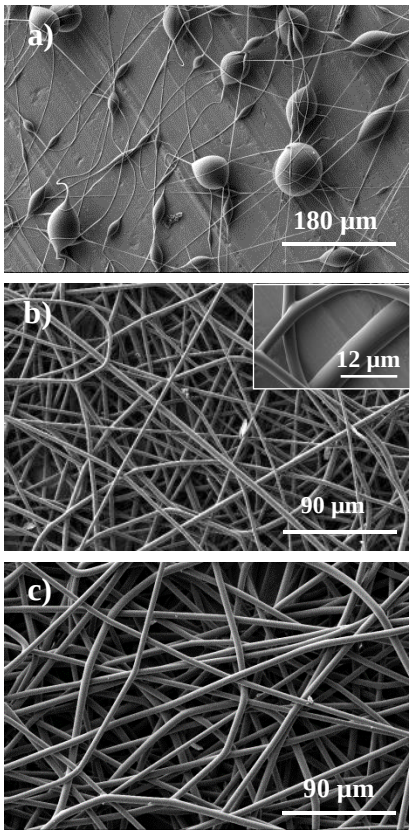

**Figure 4**. SEM micrographs showing electrospun 1L6 microfibers under optimized conditions (a,b) and diameter distribution (c).

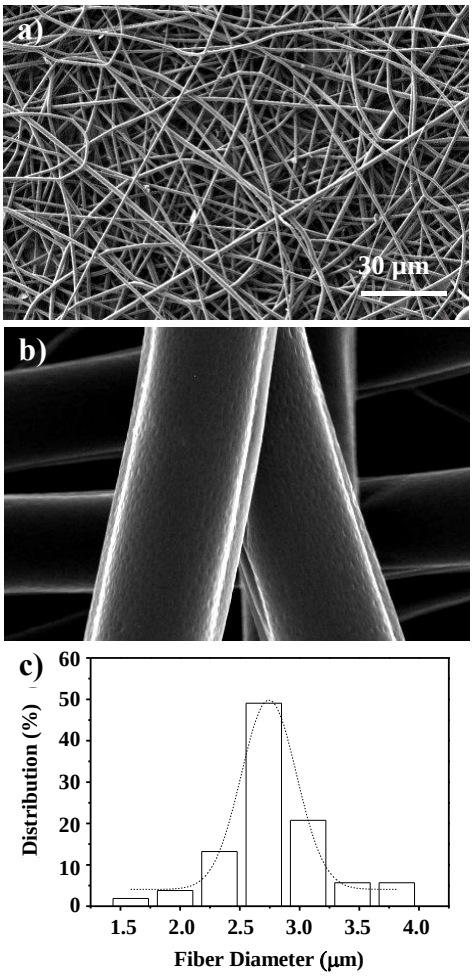

**Figure 5.** SEM micrographs showing electrospun 1L6 scaffolds loaded with 2.8 wt-% of CHX (a), 0.85 wt-% of PHMB (b) and 10 wt-% of α-chymotrypsin. Diameter distributions are shown in each case in the right

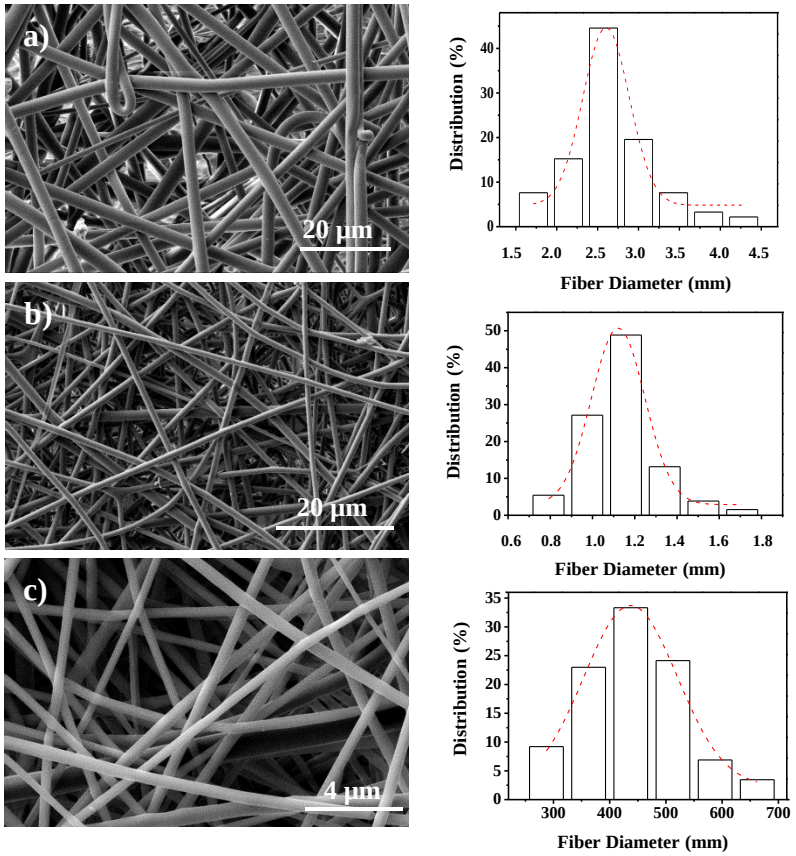




### 2. Hydrophobicity of 1L6 samples

Although wettability of materials depends mostly on both surface energy and roughness, the latter is the key factor after selecting their components. Therefore, hydrophobicity may vary significantly with the form (melt processed film or electrospun scaffold) of the material, and even

be affected by incorporation of a drug. Figure 6 shows the water contact angles values of 1L6 films and scaffolds, as well as CHX and PHMB loaded scaffolds.

The contact angle of the 1L6 microfiber scaffold increased drastically compared to that of the film (*i.e.,* from 89 ± 4º to 127º) since deposition of microfibers led to a much greater surface roughness than expected for a film sample.

The impact of roughness on the contact angle is given by the Wenzel equation:[56]

$$\cos \theta_W = r \cos \theta_Y \quad (1)$$

Which relates the contact angle of a rough surface, $\theta_W$, with the roughness ratio of the surface, $r$, and the contact angle of a smooth surface, $\theta_Y$.

The Wenzel equation shows that contact angles on hydrophobic surfaces increase with surface roughness for a water droplet because the ratio between the true surface area of a rough surface and that of a comparably sized smooth surface is always greater than one. The measured value for the smooth 1L6 film was close to 90º which is strictly the lower limit value for a hydrophobic substance.



The high increase of the contact angle seems however difficult to be justified by the typical Wenzel equation and consequently microfiber scaffolds seem to benefit from air pocket formation. Therefore, Cassie-Baxter equation[57] should also be considered:

$$\cos \theta_w = f_1 \cos \theta_1 + f_2 \cos \theta_2 \quad (2)$$

where $f_i$ represents the fraction of each component (polymer and air) and $\theta_i$ the corresponding contact angles. When $f_2$ represents the area fraction of trapped air, equation 2 can be modified according to simple equation 3:

$$\cos \theta_w = f \cos \theta_Y + (1- f) \cos 180º = f \cos \theta_Y + f - 1 \quad (3)$$

where $f$ is an area fraction of the solid-liquid interface and (1- $f$) is that of the air-liquid interface which contact can be considered to be 180 °.

The contact angles of antibacterial drug loaded scaffolds and the unloaded 1L6 scaffold were highly similar. Thus, the small change in roughness/porosity caused by the lower fiber diameter

(e.g. for PHMB loaded samples) or the hydrophilic character of loaded drugs had a minimum impact.

**Figure 6.** Contact angles for 1L6 film and 1L6 scaffolds unloaded and loaded with CHX, PHMB and α-chymotrypsin.

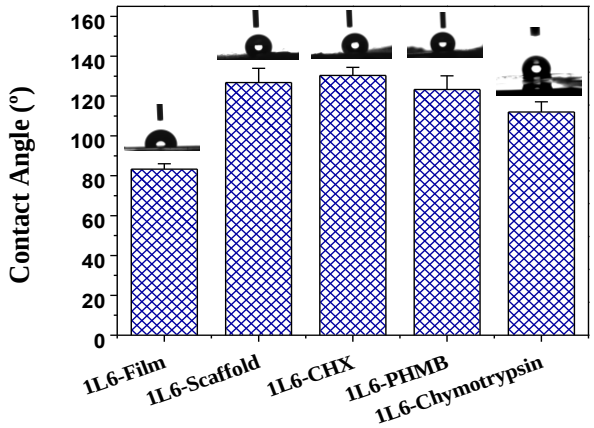




### 3. Degradation of poly(ester urea) 1L6 films and scaffolds

Weight loss in the three media (*i.e.,* lipase, proteinase K and Chymotrypsin) during enzymatic degradation is plotted in Figure 7 for melt-processed films of the studied poly(ester urea). As can be seen, all values are higher than 50% after only 15 days of exposure to the media, demonstrating the susceptibility of the 1L6 sample to enzymatic attack. However, a significant delay in the last stages of degradation was observed in the lipase medium. In fact, degradation was still similar after 21 days of exposure to both α-chymotrypsin and proteinase K media. Weight loss reached a value close to 80% before films became completely brittle. Note also that weight loss was practically linearly dependent on the exposure time to both media. On the contrary, linearity was progressively lost after an initial period, and the maximum level of degradation (80%) was reached after 31 days in the lipase medium. These results suggest the ability of proteinase K and α-chymotrypsin to degrade ester groups as well as CO-NH linkages of

the urea group. By contrast, lipase was only effective with the ester linkages, causing a slightly delayed degradation that became more evident at the end of the process where more resistant urea enriched fragments should be predominant. Degradation was also evaluated in PBS control solution because in this case only hydrolytic attack was expected. Results (not shown) indicate a weight loss of less than 5% after 31 days of exposure.

**Figure 7.** Plots of weight loss versus exposure time for 1L6 films exposed to proteinase K (■), α-chymotrypsin (▲) and lipase (♦) media.

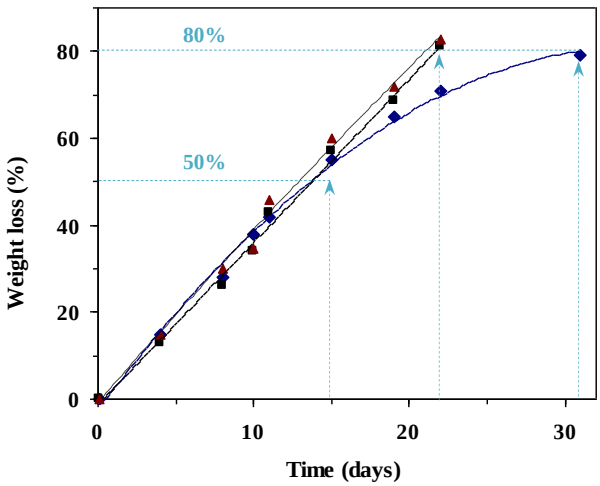


SEM micrographs taken after exposure of film samples to the degradation media show that degradation progressed steadily on their surface, with abundant formation of deep cracks (*e.g.*, Figure 8b). This contrasts with the practically unaltered surface of samples exposed to a non-enzymatic PBS hydrolytic medium for a similar period (Figure 8a). High magnification images (Figures 8c and 8d) also reveal that enzymatic degradation eroded the samples without retention of degradation products, suggesting their release in the media.

Figure 9 shows the weight loss evolution of 1L6 electrospun scaffolds that were fully immersed in the degradation media. In all cases, degradation progressed very fast during the first three days of exposure (*e.g.*, weight loss was higher than 60%) and subsequently a steadily evolution at a lower degradation rate was detected (*e.g.,* weight loss was close to 90-95% after

10 days). Minor differences were observed between samples exposed to the three different enzymatic media. Polymers logically appeared to be more easily degraded in microfiber than in film form, especially at the beginning of exposure.

**Figure 8.** Scanning electron micrographs of 1L6 films after 19 days of exposure to PBS (a), α-chymotrypsin (b,d) and lipase (c) media at 37 ºC.

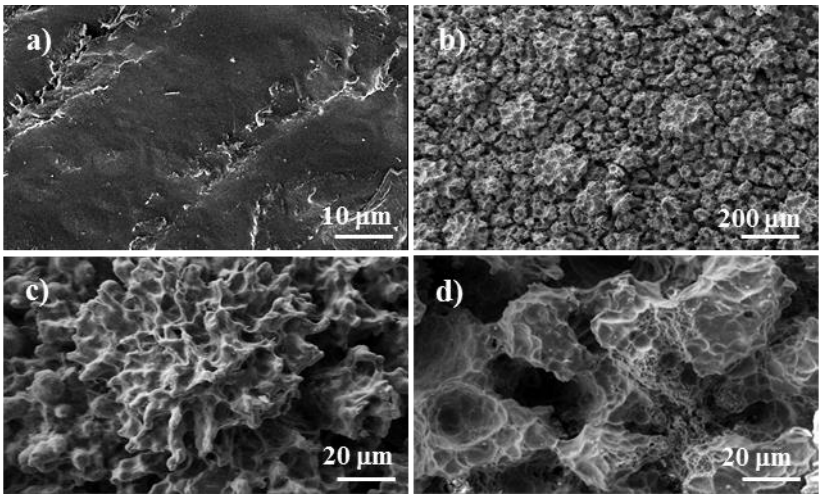




**Figure 9.** Plots of weight loss versus exposure time for 1L6 scaffolds exposed to proteinase K (▲) α-chymotrypsin (●) and lipase (♦) media. For comparative purposes degradation data in a proteinase K medium are also given for a 1L6 film (-) and a not fully immersed 1L6 scaffold (■).

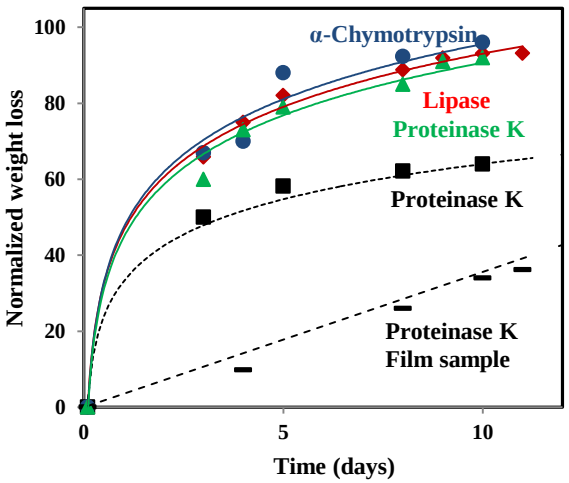

Figure 10 shows SEM micrographs of the scaffold during the enzymatic attack. It is clear that only the fibers placed on the surface of the scaffold were degraded at the beginning (Figure 10a) due to the high hydrophobicity of the sample that prevented the access of the aqueous medium to the inner parts of the scaffold, which remained practically unaltered. Obviously, the internal fibers become accessible to enzymes as the fibers placed on the surface were degraded (Figure 10b), being this process slower than the initial step concerning the outer fibers. A practically complete degradation was reached after 10 days as shown in Figure 10c.

High magnification micrographs revealed some differences on the texture of degraded fibers. Note for example that fibers exposed to proteinase K seemed to retain more degradation products (Figure 10f), a feature that may be related to the slightly lower weight loss observed in this medium. These products were less evident during exposure to lipase medium and specifically a clear erosion of minority beads was detected (Figure 10e). It is interesting to note that scaffolds tend to float on the medium and consequently degradation could be clearly delayed by the wettability effect as shown in Figure 9 for a scaffold exposed to proteinase K medium without a forced immersion.



### 4. Poly(ester urea) 1L6 electrospun scaffolds loaded with α-chymotrypsin as a degrading enzyme

The high solubility of 1L6 allowed the choice of the appropriate combination of solvents to perform the electrospinning process and dissolve potentially degrading enzymes without a remarkable inactivation/denaturation effect. α-Chymotrypsin was selected as the degrading enzyme on account of its higher effectiveness, as found in the degradation experiments with film samples. To avoid protein denaturation, methanol was preferred to ethanol; specifically a $CHCl_3$:$CH_3OH$ 9:4 *v*/*v* mixture and a polymer concentration of 13 wt-% were used. A high enzyme concentration (1.5 *w*/*v*-%) was also employed to ensure incorporation of a reasonable proportion of enzymes (*i.e.,* 10 wt-%) with a suitable activity within nanofibers. Electrospinning conditions were optimized under these new values and some parameters should be significantly varied, as indicated in Table 2. The most drastic change affected the flow rate, which had to be significantly

decreased to obtain continuous and homogeneous fibers (Figure 5c). Solvent evaporation was enhanced and the average value of fiber diameters (*i.e.,* 458 nm) was lower than of ethanol containing mixtures and higher flow rates. In this case, contact angle measurements (Figure 6) indicated a slight decrease in hydrophobicity compared to the unloaded scaffold. The large amount of loaded enzyme and the significant reduction in fiber diameter are worth noting.

**Figure 10.** Scanning electron micrographs of 1L6 scaffolds after exposure to α-chymotrypsin (a,b,c,d), lipase (e) and proteinase K (f) media at 37 ºC for 3 (a,d,e,f), 6 (b) and 8 (c) days.

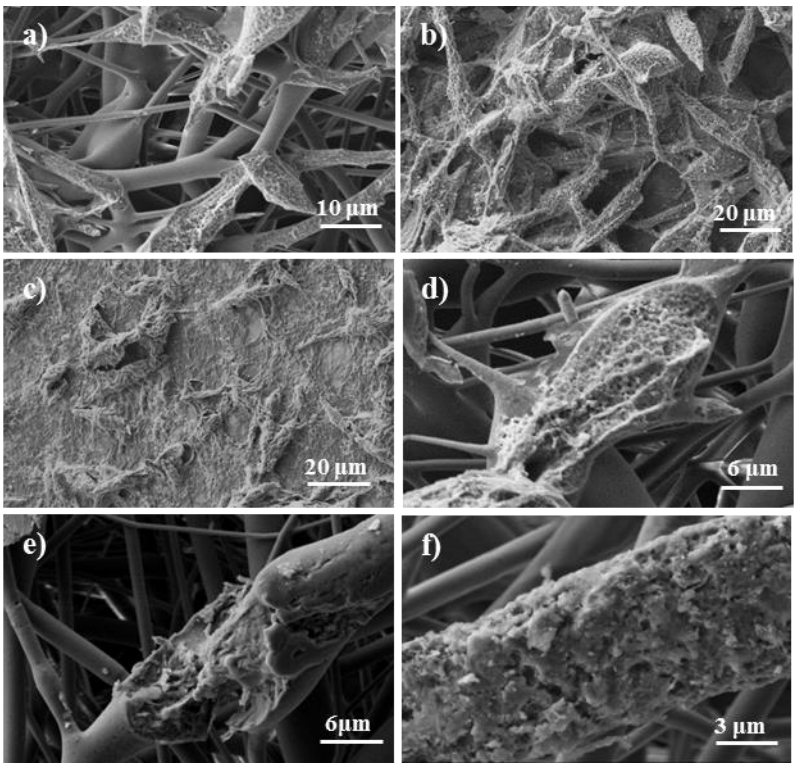




New scaffolds appear highly interesting because of their incorporation of agents, which could accelerate the degradation process and tissue regeneration. Cell colonization could be enhanced by the formation of a more porous structure and loss of the supporting synthetic polymer. Since electrospun nanofibers have good characteristics (*e.g.*, size and surface morphology) to be enzyme immobilization supports, several works have focused on achieving enzyme immobilization via covalent attachment.[58] The simpler approach consisting in the

incorporation of enzymes (including α-chymotrypsin and lipase) into the polymers was previously demonstrated for α-amino acid-based poly(ester amide)s.[59] The present approach is similar because the enzyme is directly incorporated into 1L6 during the electrospinning process.

Micrographs in Figure 11a reveal the degradation of scaffolds exposed to a pH 7.4 sodium phosphate buffer at 37 ºC without a forced immersion and after only 2 days of exposure. More interestingly, only nanofibers on the outer surface of the scaffold (*i.e.,* those in direct contact with the aqueous medium) are degraded. Furthermore, the process mainly affects the inner part of fibers, where the maximum amount of enzyme is loaded. As can be seen in the higher magnification image (Figure 11b), fibers appear longitudinally cracked or even as if they had exploded and only their skin remained. The SEM micrograph clearly demonstrated that enzymatic attack took place by simple exposure of the α-chymotrypsin loaded fiber to the aqueous medium in contrast with the low erosion detected when unloaded fibers were exposed to PBS (not shown). The micrograph shows also that degradation products seemed to be partially retained in the fibers due to their high insolubility. UV absorbance measurements (282 nm) indicate that no α-chymotrypsin was released to the PBS degradation medium after 3 days of exposure. Thus, enzymes were effectively retained in the scaffold when exposed to a hydrophilic medium. Also interesting is the high hydrophobicity of the scaffold surface (Figure 6), which caused a progressive degradation that should evolve from the outer to the inner surface. Thus, the scaffold should retain its structural function for longer than expected when all fibers were equally accessible to water molecules and started to degrade at the same time.



**Figure 11.** Scanning electron micrographs at different magnifications of 1L6 scaffolds loaded with 10 wt-% of α-chymotrypsin after exposure to a PBS medium at 37 ºC for 2 days.

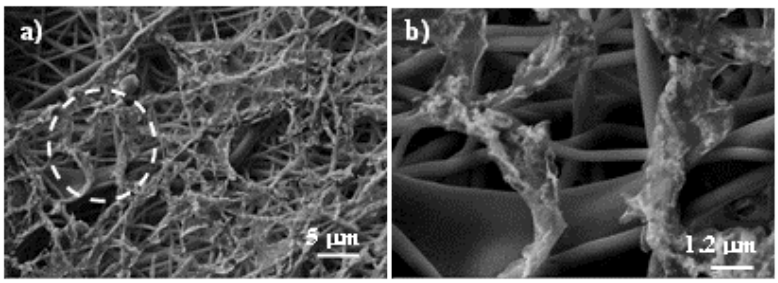

### 5. Biguanide release from 1L6 scaffolds

The release of biguanide compounds from an electrospun matrix is intimately related to the morphology and structure of constituent fibers and to the release environment. In fact, the rate of diffusion-controlled drug release depends on three main factors: a) Solubility of the drug in the release medium, b) Ability of the medium to penetrate the polymer matrix, and c) Physical interactions between polymer and drug.[60]

The release of CHX and PHMB from 1L6 scaffolds was studied in media with different hydrophobicity/hydrophilicity ratios (*i.e.,* PBS and PBS-EtOH 3:7 *v*/*v* mixture). Specifically, ethanol is more hydrophobic than water and has higher affinity with 1L6. PBS-EtOH may also have a swelling effect that facilitated drug delivery. The release behavior of both drugs in the two media was clearly different, *i.e.,* a maximum release of 3% in PBS (data not shown) versus 91% in the mixture of solvents after an exposure of only 90 h (Figure 12).



**Figure 12.** Drug release profiles of 1L6 scaffolds loaded with 0.05 wt-% of CHX (○) and 0.015 wt-% of PHMB (●) in PBS-EtOH 3:7 *v*/*v*.

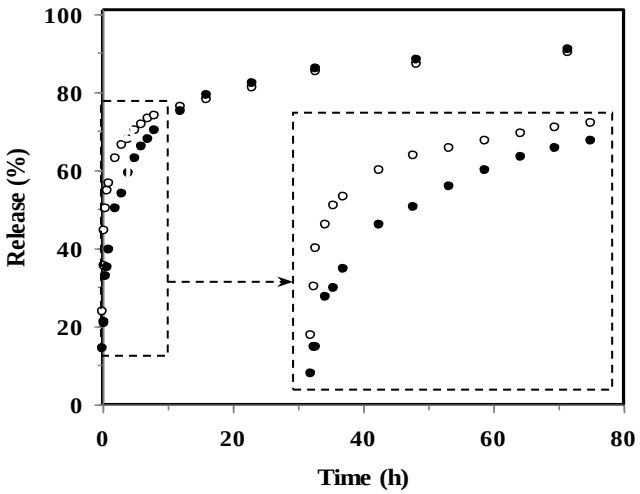

Logically, differences in release behavior between CHX and PHMB were insignificant in the more hydrophobic medium. In fact, the release of PHMB was slightly delayed during the first 10 h of exposure, probably due to its higher molecular weight, which hindered diffusion through the microfiber, and even to its slightly higher hydrophilicity. Nevertheless, measurements indicate a rapid release of both drugs from electrospun scaffolds in a media with similar hydrophobicity than physiological serum-containing medium, and consequently a rapid antibacterial effect should be expected.

### 6. Antibacterial assays of biguanide loaded 1L6 scaffolds

The antibacterial effect of CHX and PHMB released from microfiber scaffolds was determined by studying bacterial growth inhibition in broth culture. Unloaded 1L6 scaffolds appeared highly susceptible to bacterial colonization, with bacterial growth levels similar to that of the positive control (polystyrene plate), as can be seen in Figure 13. Colonization can be effectively avoided by loading a low PHMB and CHX ratio, as also shown in Figure 13. Thus, a significant decrease in the number of both Gram-positive (*M. luteus*) and Gram-negative (*E. coli*) bacteria was observed in drug loaded scaffolds compared to the control and the unloaded scaffold. The greatest decrease was found for the high molecular weight PHMB (*i.e.* 97-95% versus 76-79% for PHMB and CHX, respectively).



It should be pointed out that the number of active biguanide groups in the CHX and PHMB loaded scaffolds was similar because drug content was specifically selected to this end. Furthermore, differences cannot be attributed to a different release behavior, as above explained, and even a slightly lower release rate was observed for PHMB. This suggests a higher antimicrobial activity of biguanides in polymeric form, as has also been reported.[51] In fact, the high effectiveness has been related to a novel mechanism of action based on the interaction of PHMB with nucleic acids that led to co-precipitation. At low bacteriostatic concentrations, the damage caused by this interaction could be tolerable and the antibacterial effect would be due to disruption of the cell membrane, as usually expected. However, because the binding between PHMB and DNA is highly cooperative, a slightly higher drug dose can cause massive

perturbation of DNA function and/or precipitation leading to cell death. An additional advantage of PHMB over CHX is that a lower weight-% is required for similar biguanide contents. Logically, the electrospinning conditions should be less affected, and moreover drug activity can be increased by loading a higher amount of PHMB (*e.g.*, just that corresponding to CHX wt-%).

The effect of CHX and PHMB on studied bacteria was similar due to the wide antibacterial spectrum of both drugs (Figure 13). It is highly interesting that CHX and PHMB could be loaded into the 1L6 microfibers by electrospinning without loss of antimicrobial activity. Hence, solvent or high voltage did not cause any adverse effect, allowing easy preparation of scaffolds with an added value (*e.g.*, antibacterial activity).

**Figure 13.** *Escherichia coli* and *Micrococcus luteus* bacterial growth in 1L6 scaffolds loaded with CHX and PHMB and the positive control. The bars are mean ± SD (n=4). * $p < 0.05$ vs. control, ANOVA followed by Tukey test.



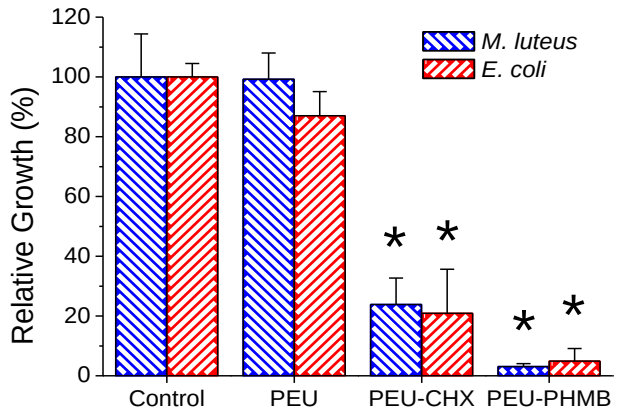


### 7. Biocompatibility of films and scaffolds of the poly(ester urea) 1L6

Adhesion and proliferation tests of epithelial (Vero) and fibroblast (Cos-7) cells were performed on 1L6 films and scaffolds. These assays are useful in following cell development because adhesion is an early cellular event and proliferation is an evidence of metabolic cell

activity. While adhesion of both cell lines on scaffolds and the control was rather similar, significant differences were detected between scaffolds and films (Figure 14a). Viability was significantly lower for films, especially Vero cell line ones. This result is interesting because it reflects the effect of increased porosity of the scaffold sample (*i.e.,* a 3D-structure more favorable for rapid cell colonization), which is even sufficient to counterbalance the negative effect of its higher hydrophobicity. Proliferation assays gave similar results, as depicted in Figure 14b, although enhancement of cell proliferation compared to the film was similar for both Cos-7 and Vero cell line scaffolds.

**Figure 14.** Biocompatibility of the 1L6 matrices determined by cell adhesion (a) and proliferation (b) of Cos-7 cells (fibroblast) and Vero cells (epithelial). The bars are mean ± SD (n=4). * $p < 0.05$, scaffold vs. film, ANOVA followed by Tukey test.

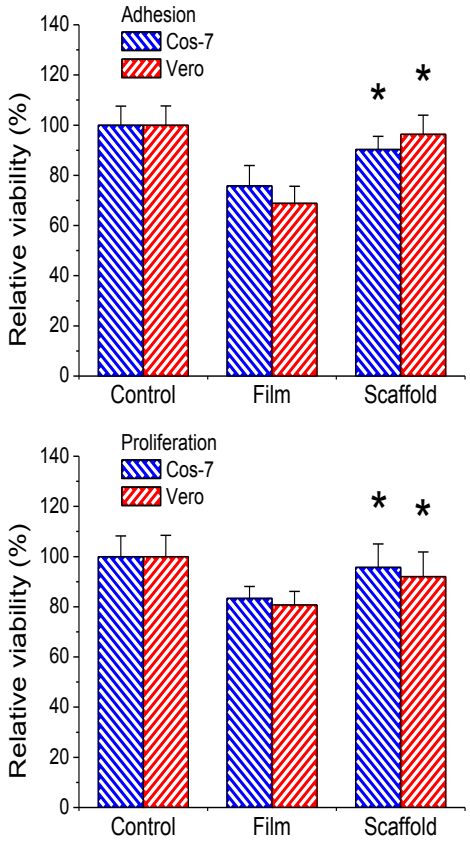

Representative micrographs of morphological characteristics of cell growth on 1L6 films are shown in Figure 15. Fibroblast (Cos-7) and epithelial (Vero) cells formed monolayers on the 1L6 film surface (Figures 15a and 15e) structured with close interactions between neighboring cells to form a tissue (see arrows in Figures 15b and 15f). Furthermore, cell adhesion on the film surface promoted the formation of intercellular bridges (see double arrows in Figures 15c and 15g). These bridges correspond to filopodia developed from an early attachment (h), as evidenced by the rounded shape of cells. Moreover, the free surface of the material made it possible to obtain a broad extension of cell cytoplasm through lamellipodia (named cell spreading), which are auxiliaries for cell attachment onto the material surface through filopodia (see arrows in Figures 15d and 15i).

Micrographs in Figures 16a and 16g show that both types of cells were also competent to form monolayers over the fiber matrices. Fiber tracks can be clearly seen below the Cos-7 cell monolayer (Figure 16a) whereas the tile morphology of Vero cells hinders their observation (Figure 16g). Cos-7 cells demonstrated ability to invade the pores between fibers, forming a tissue-like structure (arrows in Figure 16b) where cells were connected to each other by small filopodia (arrows in Figure 16c). Material colonization occurred locally, as evidenced by the formation of interconnected cell clusters (arrows in Figure 16d). The 1L6 scaffolds facilitated guided cell growth (Figure 16e) and the establishment of cell connections through extensions of filopodia that cross over the pores of the matrix (arrows in Figure 16f). Vero cells also grew over the polymer matrix in a guided manner through the fibers (arrows in Figure 16h).

**Figure 15.** Morphological characteristics of cell growth (fibroblast (Cos-7) cells (a-d) and epithelial (Vero) cells (e-i)) in 1L6 films.

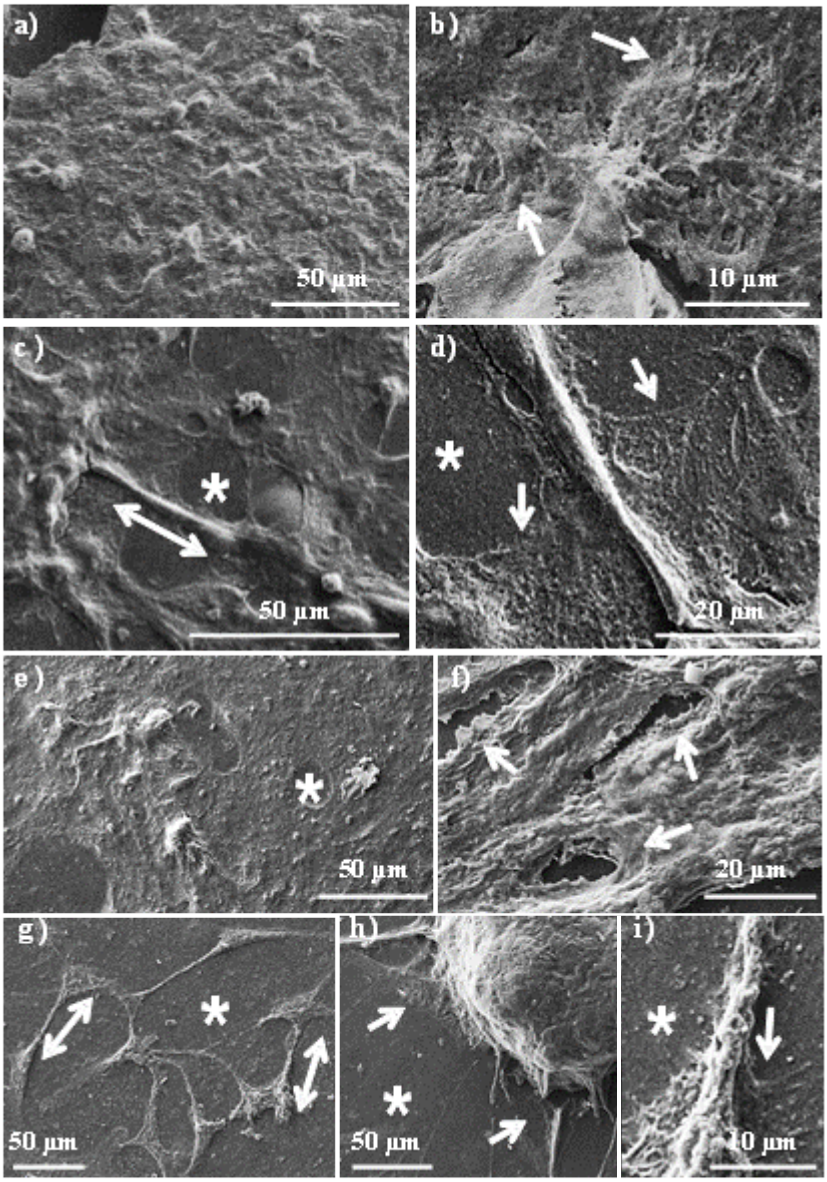

**Figure 16.** Morphological characteristics of cell growth (fibroblast (Cos-7) cells (a-f) and epithelial (Vero) cells (g-h)) in 1L6 matrices.

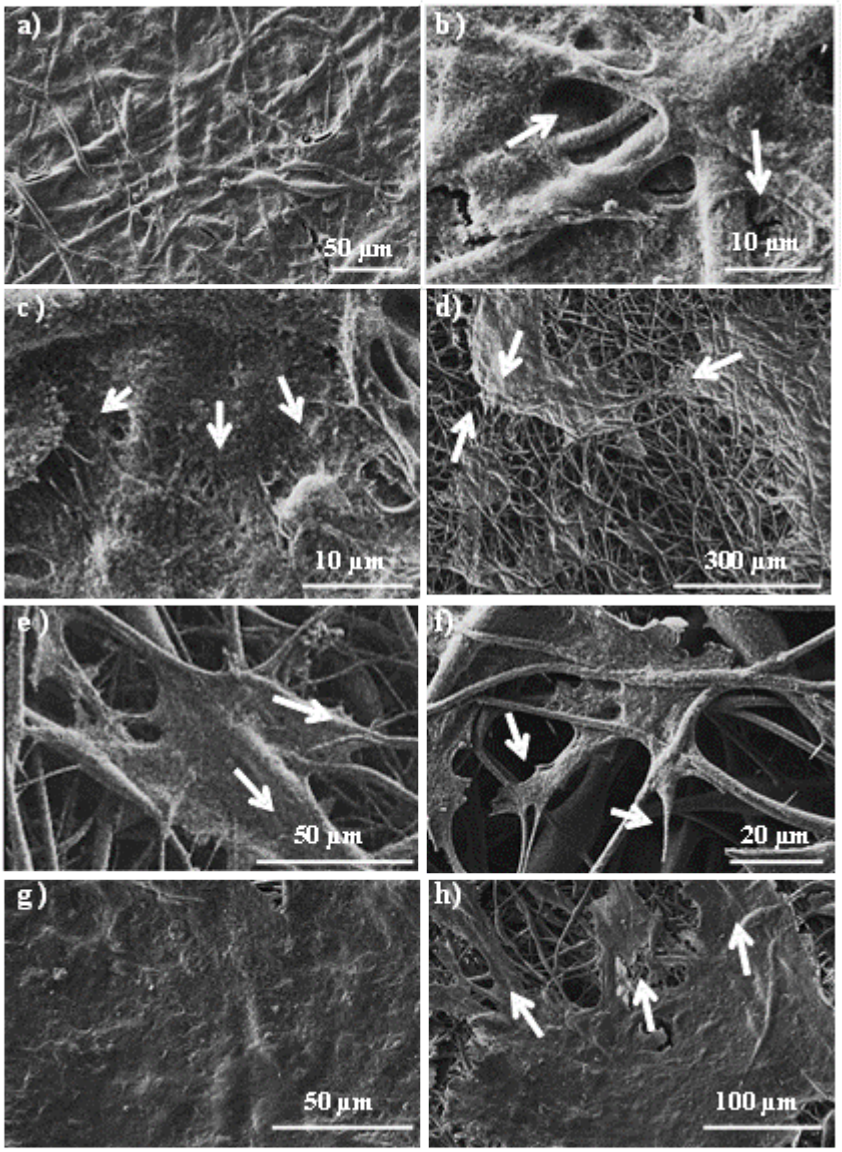

## IV. Conclusions

A new α-amino acid containing poly(ester urea) was successfully electrospun to form microfiber scaffolds. Continuous fibers with a monomodal diameter distribution and slightly rough surface were formed under a wide range of electrospinning conditions. The high solubility of the PEU derived from L-leucine, 1,6-hexanediol and carbonic acid allowed the use of appropriate solvents to load different antibacterial drugs and even enzymes without being denatured.

The 1L6 poly(ester urea) films were more susceptible to enzymatic attack by proteases than by lipases because the latter mainly involved hydrolysis of ester groups. Despite these minor differences, both enzymes led to rapid degradation of film samples. 1L6 scaffolds degraded faster than films due to the greater surface area of constitutive fibers. The high hydrophobicity of 1L6 scaffolds had repercussions on enzymatic degradability since different weight loss rates were found depending on how samples were exposed to the medium (*e.g.,* forced or non-forced immersion). In any case, hydrophobicity caused that inner fibers were well-preserved at least during the first three days of exposure.



Monomeric (CHX) and polymeric (PHMB) biguanide compounds were effectively loaded into the electrospun scaffolds. Slight differences in fiber morphology and antibacterial properties were found depending on the loaded drug. Specifically, PHMB led to narrow fibers and had an increased antibacterial effect against Gram-positive and Gram-negative bacteria. α-Chymotrypsin could also be loaded into the 1L6 scaffolds, giving rise to materials with enzymes that could accelerate degradation and tissue regeneration.

Adhesion and proliferation of epithelial (Vero) and fibroblast (Cos-7) cells on 1L6 films and scaffolds demonstrated the biocompatibility of the new poly(ester urea). Slight differences in cell viability were found, with films exhibiting the lower values. The effect of increased porosity of scaffold samples appears sufficient to counterbalance the negative effect of its higher hydrophobicity.

## V. References


1. Huang SJ, Bansleben DA, Knox JR. J Appl Polym Sci 1979;23:429.
2. Yoneyama M, Hashimoto T, Arai K. Polym Prepr Jpn 1994;43:177.
3. Kartvelishvili T, Tsitlanadze G, Edilashvili L, Japaridze N, Katsarava R. Macromol Chem Phys 1997;198:1921.
4. Gomurashvili ZD, Katsarava R, Tugushi D. Poly(ester urea) polymers and methods of use. WO 2007050415 A2: 2007.
5. Katsarava R, Beridze V, Arabuli N, Kharadze D, Chu CC, Won CY. J Polym Sci Part A: Polym Chem 1999;37:391.
6. Reneker DH, Chun I. Nanotechnology 1996;7(3):216.
7. Frenot A, Chronakis IS. Curr Opin Colloid In. 2003;8:64.
8. Dzenis Y. Science 2004;304:1917.
9. Jayaraman K, Kotaki M, Zhang Y, Mo X, Ramakrishna S. J Nanosci Nanotechnol 2004; 4:52.
10. Dhakate SR, Singla B, Uppal M, Mathur RB. Adv Mater Lett 2010;1:200.
11. Sharma S. Adv Mater Lett 2013;*4*:522.
12. Wu Y, Gao M, Li X, Liu Y, Pan H. J Alloy Compd 2014;608:220.
13. Kim H, Che L, Ha Y, Ryu W. Mater Sci Eng C 2014;40:324.
14. Guo Q, Liu D, Zhang X, Li L, Hou H, Niwa O, You T. Anal Chem 2014;86:5898.
15. Li WQ, Ma SY, Luo J, Mao YZ, Cheng L, Gengzang DJ, Xu XL, Ya SH. Mater Lett 2014;132:338.
16. Shahverdi S, Hajimiri M, Esfandiari MA, Larijani B, Atyabi F, Rajabiani A, Dehpour AR, Gharehaghaji AA, Dinarvand R. Int J Pharm 2014;473:345.
17. Shirazi MJA, Bazgir S, Shirazi MMA. Biofuel Research Journal 2014;1:39.
18. Shirazi MMA, Kargari A, Bazgir S, Tabatabaei M, Shirazi MJA, Abdullah MS, Matsuura T, Ismail AF. Desalination 2013;329:1.
19. Shirazi MJA, Bazgir S, Shirazi MMA, Ramakrishna S. Desalination and Water Treatment 2013;51:5974.
20. Mirtalebi E, Shirazi MMA, Kargari A, Tabatabaei M, Ramakrishna S. Desalination and Water Treatment 2014:1.
21. Dersch R, Steinhart M, Boudriot U, Greiner A, Wendorff JH. Polym Adv Technol 2005;16:276.
22. You Y, Min BM, Lee SJ, Lee TS, Park WH. J Appl Polym Sci 2005;95:193.

23. Cao S, Hu B, Liu H. Acta Polym Sin 2010;20:1193.
24. Thomas V, Jose MV, Chowdhury S, Sullivan JF, Dean DR, Vohra YK. J Biomat Sci-Polym E 2006;17:969.
25. Sell SA, McClure MJ, Garg K, Wolfe PS, Bowlin GL. Adv Drug Deliver Rev 2009;61:1007.
26. Chen Z, Mo X. Mater Lett 2007;61:3490.
27. Homayoni H, Ravandi SAH, Valizadeh M. Carbohyd Polym 2009;77:656.
28. Gao Y, Truong YB, Zhu Y, Kyratzis IL. J Appl Polym Sci 2014;131:40797.
29. Del Valle LJ, Camps R, Díaz A, Franco L, Rodríguez-Galán A, Puiggalí J. J Polym Res 2011;18:1903.
30. Kayaci F, Umu OCO, Tekinay T, Uyar T. J Agric Food Chem 2013;61:3901.
31. Chen L, Bromberg L, Hatton TA, Rutledge GC. Polymer 2008;49:1266.
32. Gliscinska E, Gutarowska B, Brycki B, Krucinska I. J Appl Polym Sci 2013;128:767.
33. Liu X, Lin T, Gao Y, Xu Z, Huang C, Yao G, Jiang L, Tang Y, Wang X. J Biomed Mater Res Part B 2012;100B :1556.
34. Mei Y, Yao C, Fan K, Li X. J Membr Sci 2012;417:20.
35. Ren X, Kocer HB, Worley SD, Broughton RM, Huang TS. J Appl Polym Sci 2013;127:3192.
36. Spasova M, Manolova N, Paneva D, Rashkov I. E-Polymers 2004;4:1.
37. Heunis T, Bshena O, Klumperman B, Dicks L. Int J Mol Sci 2011;12:2158.
38. Del Valle LJ, Roa M, Díaz A, Casas MT, Puiggalí J, Rodríguez-Galán A. J Polym Res 2012;19:9792.
39. Del Valle LJ, Díaz A, Royo M, Rodríguez-Galán A, Puiggalí J. Express Polym Lett 2012;6:266.
40. Llorens E, Del Valle LJ, Ferrán R, Rodríguez-Galán A, Puiggalí J. J Polym Res 2014;21:360.
41. Fernandes JG, Correia DM, Botelho G, Padrão J, Dourado F, Ribeiro C, Lanceros-Méndez S, Sencadas V. Polymer Testing 2014;34:64.
42. Ben-Knaz R, Pedahzur R, Avenir D. Adv funct mater. 2010;20:2324.
43. Green D, Fulghum T, Nordhaus MA. Immobilized Antimicrobial Agents: A Critical Perspective. Science agains microbial pathogens: communicating current research and technological advances. Méndez-Vilas, Editor. Formatex Microbiology books Series. Badajoz. España. 2011. pp. 84-98

44. Vasilev K, Cook J, Griesser H. Expert Rev Med Devic 2009;6(5):553.
45. Charnley M, Textor M, Acikgoz C. React Funct Polym 2011;71(3):329.
46. Milstone A, Passaretti C, Perl T. Clin Infect Dis 2008;46(2):274.
47. Lim K, Kam P. Anaesth Intens Care 2008;36(4):502.
48. De Paula G, Netto G, Mattoso L. Polymers 2011;3:928.
49. Roth B, Brill FHH. Physiol. 2010;23:4.
50. Allen MJ, White GF, Morby AP. Microbiology 2006;152:989.
51. Gilbert P, Pemberton D, Wilkinson DE. J Appl Bacteriol 1990;69:593.
52. Llorens E, Del Valle LJ, Díaz A, Casas MT, Puiggalí J. Macromol Res 2013;21:775.
53. Fridrikh SV, Yu JH, Brenner MP, Rutledge GC. Phys Rev Lett 2003;90:144502
54. McKee MG, Elkins CL, Long TE. Polymer 2004;45:8705.
55. Luo CJ, Nangrejo M, Edirisinghe M. Polymer 2010;51:1654.
56. Wenzel R. Ind Eng Chem 1936;28:988.
57. Cassie ABD, Baxter S. Trans Faraday Soc 1944;40:546
58. Jia H. “Enzyme-carrying electrospun nanofibers” in Methods in molecular biology Clifton, N. J. Editor. 2011. p. 205-212.
59. Tsitlanadze G, Machaidze M, Kviria T, Djavakhishvili N, Chu CC, Katsarava R. J Biomater Sci Polym Ed 2004;15:1.
60. Liu H, Leonas K, Zhao Y. J Eng Fiber Fabr 2010;5(4):10.
61. Liu X, Lin T, Gao Y, Xu Z, Huang C, Yao G, Jiang L, Tang Y, Wang X. J Biomed Mater Res Part B 2012;100B:1556.

# *Incorporation of bacteriophages in electrospun fibres of a poly(ester urea) derived from L-leucine.*

Infection by pathogenic organisms and multidrug resistant organisms are nowadays a major problem for modern medicine since they are responsible of significant morbidity and mortality. Therefore, great efforts have been focused to reduce antibacterial resistance, being considered different solutions: Development of new antibacterial compounds, education for consumers, standardized treatment protocols by physicians, regularization of the market, prevention of the marketing of counterfeit and adulterated antimicrobials, etc. Alternatively, and for over 70 years it has been proposed and applied the use of bacteriophages for the treatment of bacterial infections. In particular, this therapeutic alternative has been driven in various countries of the East Europe.

Bacteriophages are viruses that infect bacteria in species-specific manner. After the bacteriophage enters to the bacterium, it makes use of the metabolic machinery of bacterium for its replication. Multiple copies of the bacteriophage are quickly generated and finally the excessive load of new particles produces bacterial lysis. The released new viral particles are competent to produce again the bacteria infection. Phage therapy appears nowadays highly interesting for the treatment of bacterial infections that are resistant to common antibiotics. Phages are considered as a new tool in clinical research and molecular biology. Especially, if we take into account that there are bacteriophages isolated against pathogenic bacteria such as *Pseudomonas, Staphylococcus, Escherichia and Mycobacterium*, which are resistant to antibiotics.

The main focus of this section is an advance on the results concerning the incorporation of bacteriophages into fibers prepared by electrospinning. Electrospinning technique has been widely used for encapsulation of drugs and proteins.[1-3] However, there is a reduced number of

works that have explored this technique as a tool for encapsulating biological systems such as bacteria and viruses.[4,5] In this chapter, the electrospinning technique has been used with the aim of encapsulate two preparations of bacteriophages: *Pyophages* (Pyo) and *Staphylophages* (Staph). Pyophages are a mixture of lytic bacteriophages with activity against *Pseudomonas aeruginosa, Staphylococcus aureus, Escherichia coli, Streptococcus and Proteus;* while Staphylophages has only lytic activity against *Staphylococcus aureus* bacterium.

## 1. Lytic activity of Pyophages and Staphylophages

Bacteriophage activity was evaluated before their incorporation in the electrospinning solution. Phages were provided in a carbonate adsorbed form for stability reasons. Bacterial growth tests were performed with three different concentrations (0.02 g/mL, 0.05 g/mL and 0.1 g/mL) of Pyophages and Staphylophages adosorbed in carbonate. In case of Pyophages the activity was studied in an *Escherichia coli* medium, while Staphylophages was studied in *Staphylococcus aureus* medium.



In both cases (Figures 1a and 1b) a cyclical effect of bacterial growth and inhibition was observed when the concentration was low (e.g. 0.02 g(mL), whereas at higher concentration bacterial growth could suppressed (e.g. 0.1 g/mL for Staphylophages. This result is expected for bacterial populations when are infected by bacteriophages. The decrease of the bacterial population after reaching its maximum growth clearly indicates the lytic activity. The subsequent bacterial growth at low concentration is due to the time required for a new phage to infect bacteria and replicate. The behavior observed for the control (brain heart infusion, BHI, medium) was clearly different since in this case the relative bacterial growth increases until a constant value.

TEM analysis of the Pyophages (Figure 2) shows the structure of a complex bacteriophage, with the structure defined by its envelope protein which consists on different parts: head, neck, tail and caudal fibers.

**Figuras 1.** Growth curves of the bacterium *Escherichia coli* (a), *Staphylococcus aureus (b)* in the presence of different concentrations of Pyophages and Staphylophages, respectively.

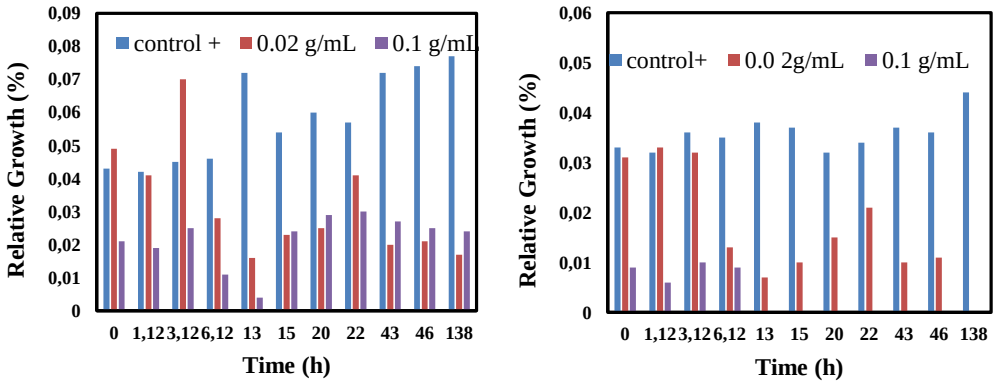


**Figure 2.** Transmission electron microscopy (TEM) micrograph of Pyophages.

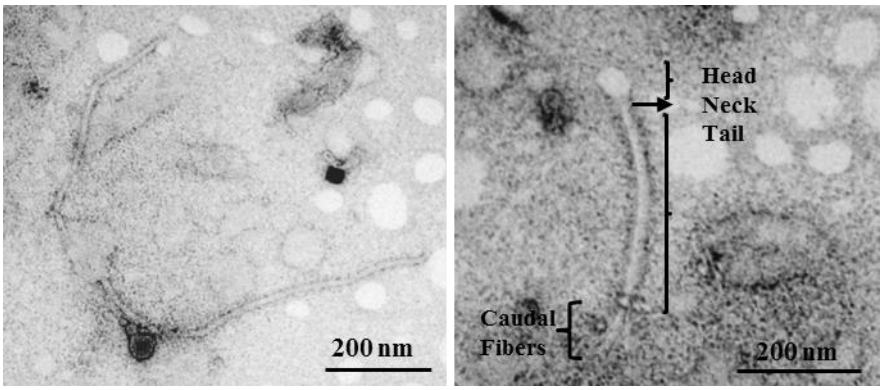




### 2. Electrospinning of poly(ester urea) 1L6 loaded with bacteriophages.

The poly(ester urea) derived from L-leucine, named 1L6, was chosen as the polymer fibrous matrix for encapsulation of pyophages and staphylophages by electrospinning. Basically, the following procedure was applied: bacteriophages adsorbed in sodium carbonate were suspended in a chloroform-ethanol (10:1 *v/v*) solution of 1L6 at a concentration of 10% (*w/v).* The weight of carbonate particles was 25 % of 1L6. The suspension was homogenized by magnetic

stirring and then mobilized with a peristaltic pump to get the selected flow rate for the electrospinning process. Alternatively electrospinning was also carried out using bacteriophages that were previously desorbed from the carbonate. For this purpose the carbonate was incubated in phosphate buffer saline (PBS, pH 7.2-7.4) with stirring at 37 ºC for 30 min. The supernatant was recovered and frozen at -80ºC for 24 h and then lyophilized. Finally, the freeze dried phage was suspended in a chloroform-ethanol (10:1 v/v) solution of 1L6 at the concentration of 10% (*w*/*v*). In all cases, the amount of loaded phages corresponded to that obtained by desorption of a weight of carbonate particles equivalent to 25% of dissolved 1L6. The resulting homogeneous solution was in this case mobilized with an injection pump.

The first process is named “electrospinning of adsorbed phages”, while the second procedure corresponds to “electrospinning of purified phages”.

It is widely known that the fibers produced by electrospinning depend on the characteristics of the solution (*e.g.,* polymer concentration, volatility of the solvent, etc.), and operational parameters (*e.g.,* electric field, needle-collector distance and solution flow). In the Table 1 are shown the optimal operational parameters to obtain fibers of 1L6 loaded with bacteriophages from both procedures. It is clear that the flow rate was the most sensitive parameter, being required low and high values when purified or adsorbed phages were used, respectively.



**Table 1.** Optimal operational parameters for electrospinning of 1L6 loaded with pyophagues (Pyo) and staphylophages (Staph).

| Sample | Voltage (kV) | Flow (mL/h) | Needle-collector distance (cm) |
|---|---|---|---|
| 1L6 | 30 | 1.5 | 24.5 |
| 1L6-Pyo/$CaCO_3$ | 30 | 6.7 | 24.5 |
| 1L6-Pyo | 30 | 1 | 24.5 |
| 1L6-Staph/$CaCO_3$ | 30 | 5 | 24.5 |
| 1L6-Staph | 30 | 0.8 | 24.5 |

Figures 3a and 3b show the surface morphology of electrospun fibers prepared from bacteriophages adsorbed on carbonate. The fibers clearly show deformations that correspond to aggregates of carbonate particles. Furthermore, it can be observed that these aggregates are well encapsulated into fibers that exhibit an smooth texture. Round shaped protuberations appear randomly located along the fibers that constitute the porous scaffold.

Fiber diameters of bacteriophage loaded samples were in the micrometric range and higher than unloaded fibers. Thus, fibers incorporating Pyo and Staph adsorbed in carbonate had average diameters of 3.49 ± 0.91 µm and 4.07 ± 0.49 µm, respectively (Figure 3a and 3b), whereas an average diameter of 2.80 ± 0.41 µm was found for the unloaded sample. The indicated increase is basically a consequence of the increase of the flow rate (i.e, 6.7 and 5 mL/h for Pyo and Staph, respectively, and 1 mL/h for the unloaded sample). Some differences were also found in the fiber diameter distribution and specifically the narrow range was found for fibers loaded with Staph (from 3.14 to 4.91 µm, 95% CI) in contrast with the wider range of Pyo loaded fibers (from 1.33 to 5.48 µm, 95% CI).



**Figure 3.** SEM micrographs showing electrospun 1L6 scaffolds loaded with Pyo/$CaCO_3$ (a), Staph/$CaCO_3$ (b) Diameter distributions are shown in each case in the right.

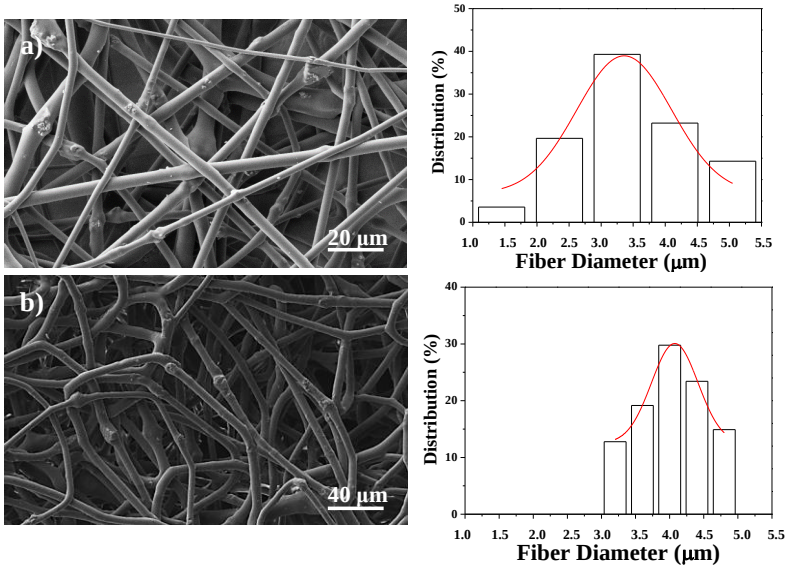

Figures 4a and 4b show the SEM images of the matrices of 1L6 loaded with purified Pyo and Staph, respectively. It can be clealry observed in the images that the fibers show smooth surfaces, circular cros-sections and rather similar diameters in the micrometric scale. Thus, average diameters of 2.29 ± 0.38 µm and 2.54 ± 0.43µm were determined for electrospun 1L6 fibers loaded with purified Pyo and Staph, respectively. Both values are very similar to the diameter found for the unloaded 1L6 fibers (2.80 ± 0.41 µm) as presumable from the highly similar operational parameters employed for the three samples (Table 1).

**Figure 4.** SEM micrographs showing electrospun 1L6 scaffolds loaded with Pyo (a) and Staph (b). Diameter distributions are shown in the right.

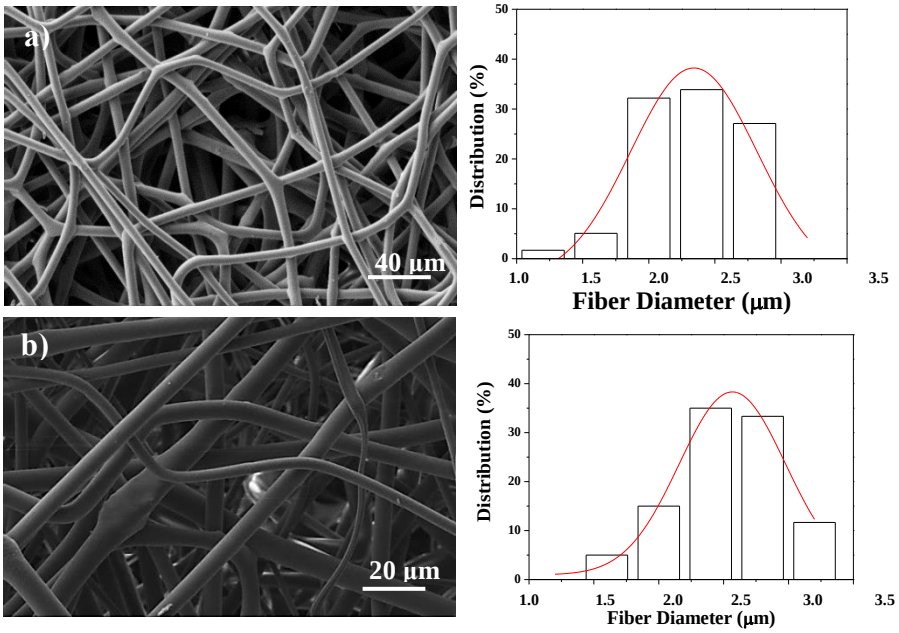




### 3. Hydrophobicity of the electrospun samples

The surface properties of 1L6 microfiber matrices unloaded and loaded with bacteriophages were studied using the measurements of contact angles. These were determined at room temperature applying the sessile drop method and using an OCA-15 plus Contact Angle

Microscope (Dataphysics, USA) and SCA20 software. Contact angle values of the right and left sides of distilled water drops were measured and averaged. Measurements were performed 10 s after the drop (0.5 µL) was deposited on the sample surface. All CA data were an average of six measurements on different surface locations.

A 1L6 film sample was used as a reference, being determined a contact angle of 93.4º ± 1.4°. This angle increased drastically for electrospun scaffolds (132.8º ± 2.5°) as a consequence of the increased rugosity and the presence of air pockets. Scarce variations were found when samples were directly loaded with purified Pyo and Staph bacteriophages or with the carbonate particles. Thus, contact angles were 124.2º ± 0.7° and ± 132.2º ±1 .3° for matrices loaded with pyophages, and 133.0º ± 1.1 and 134.9º ° ± 0.5 ° for matrices loaded with staphylophages (Figures 5a and 5b). Greater values were observed in each group when carbonate particles were incorporated as a consequence of the small increase on roughness and porosity.



It is relevant that spreading of water drops on the scaffold surface was not observed. This feature logically indicates and hydrophobic interaction between water and the polymer matrix and particularly a good encapsulation of the hydrophilic carbonate particles.

### 4. Antibacterial assays of electrospun 1L6 scaffolds loaded with bacteriophages

The antibacterial activity of the 1L6 matrix loaded with bacteriophages was assessed by quantitative measure of inhibition of bacterial growth in broth. As it was previously indicated, the pyophage corresponds to a mixture of phages with specific antibacterial activity against *Staphylococcus aureus, Streptococcus, Pseudomonas aeruginosa, Proteus* and *Escherichia coli,* while staphylophage is an isolated phage with specific antibacterial activity against *Staphylococcus aureus*.

**Figure 5.** Contact angles for unloaded electrospun 1L6 scaffolds and scaffolds loaded with Pyophages (a) and Staphylophages (b). For the sake of completeness values of 1L6 films are also given.

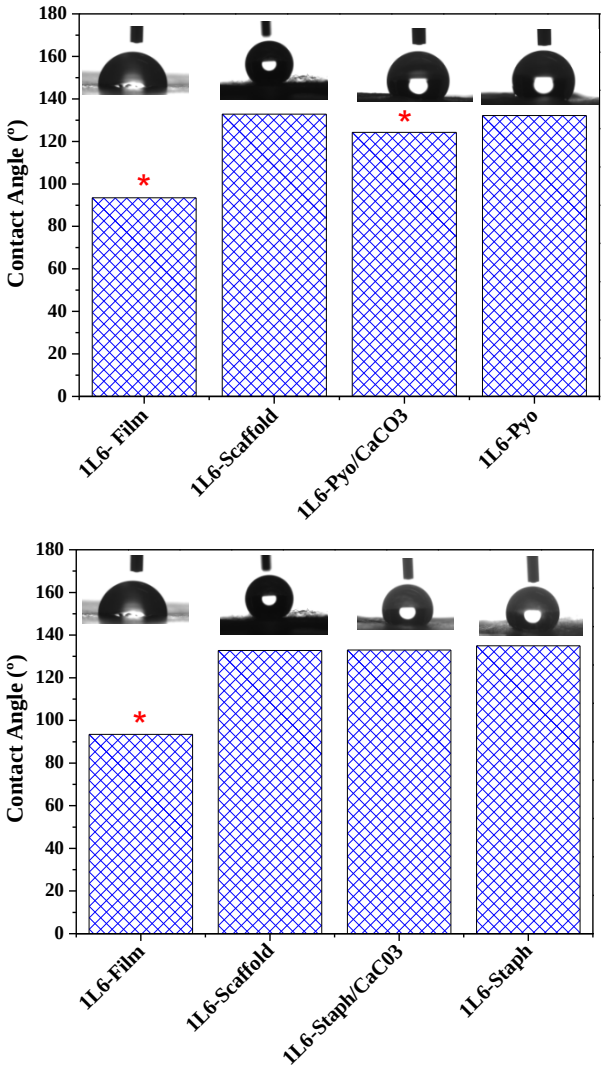




In brief, *Escherichia coli* (*E.coli*) and *Staphylococcus aureus* (*S,aureus*) bacteria were selected to evaluate the antimicrobial effect of electrospun 1L6 scaffolds loaded with pyophages and staphylophages, respectively. The bacteria were previously aerobically grown to exponential

phase in broth culture (brain heart infusion medium, BHI). Growth experiments were performed in polystyrene tubes using 5 mL of broth. Square pieces (10x10x0.1 mm) of the electrospun scaffold were place into each tube. Then, 1 mL of broth culture containing $10^3$ CFU was seeded on the electrospun fiber mats. The cultures were incubated at 37 ºC and agitated at 200 rpm. Aliquots of 100 µL were taken at predetermined time intervals for absorbance measurement at 650 nm in a plate reader. Thus, turbidity was directly related to bacterial growth. All assays were conducted in triplicate and the values averaged.

Figure 6 shows the bacterial growth curves for *E.coli* in contact with scaffolds loaded with either purified pyophages or pyophages adsorbed in carbonate. Typical bacterial growth dynamics were found with the control sample and the unload 1L6 scaffold. Thus, curves showed the initial lag phase (first 6 h), the exponential growth or logarithmic phase (up to 30 h) and finally the stationary phase that prolongs up to 98 h.

The inhibitory effect of scaffolds loaded with pyrophages was clearly detected after 72 h of culture. The relative growth decreased to 30% and 42% considering the scaffolds loaded carbonate particles and the purified pyophages, respectively. The inhibition was similar although a slightly higher effect was observed when the purification process was avoided. Thus, particles with adsorbed phages were equally active, being not detected a decrease caused by a slower release. After the inhibition period, a new episode of bacterial growth took place as can be inferred from the change on the slope of the curve. This feature is good agreement with the previously described cyclical growth of bacteriophages.



Figure 7 shows the bacterial growth curves for *Staphylococcus aureus* in contact with scaffolds loaded with either purified staphylophages or staphylophages adsorbed in carbonate. In this case the lag phase extended up to 8h, the exponential phase up to 30 h and the stationary phase up to 98 h. The inhibition effect was also detected after 72 h and specifically the relative growth decreased to 70% for both loaded samples. After this period, a new episode of bacterial growth took place.

**Figure 6.** Growth curves of the bacterium *Escherichia coli* in the presence of electrospun 1L6 scaffold loaded with pyophages.

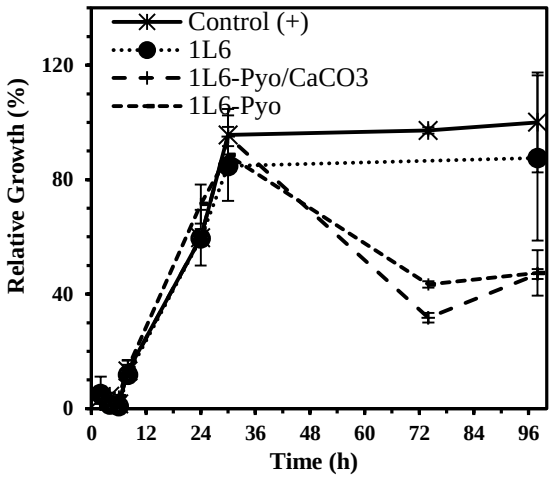




**Figure 7.** Growth curves of the bacterium *Staphylococcus aureus* in the presence of electrospun 1L6 scaffold loaded with staphylophages.

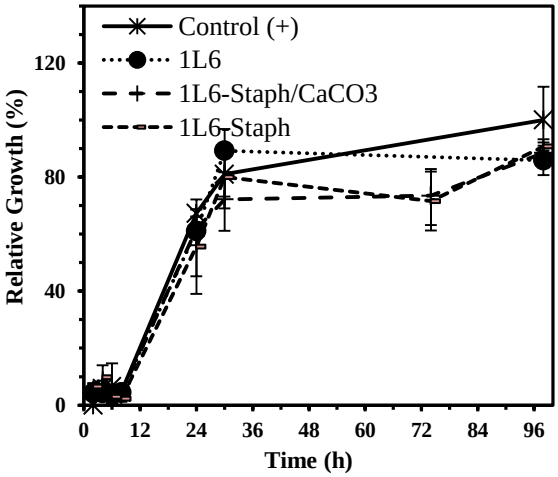

### 5. Biocompatibility of electrospun 1L6 scaffolds loaded with bacteriophages

Adhesion and proliferation tests were performed as a measure of the biocompatibility of the 1L6 scaffolds loaded with bacteriophages. Vero cells were cultured in Dulbecco's modified Eagle medium (DMEM) as previously reported.[6] Unloaded and bacteriophage loaded 1L6 scaffolds were placed into the wells of a multiwell culture plate. Samples were fixed in the wells with a small drop of silicone (Silbione® MED ADH 4300 RTV, Bluestar Silicones France SAS, Lyon, France) and then sterilized by UV-radiation in a laminar flux cabinet for 15 min. For the cell adhesion assay, aliquots of 50-100 µL containing $5x10^4$ cells were seeded onto the electrospun samples in each well and incubated for 24 h for adhesion assay, while $2x10^4$ cells were cultured by 72 h for the proliferation assay.

The cellular viability was evaluated by the standard method of MTT using five replicates and the results were averaged. Samples with adhered and grown cells on the mats were fixed with 2.5% *w/v* of glutaraldehyde at 4 ºC overnight. They were subsequently dehydrated and processed for observation by scanning electronic microscopy.



1L6 scaffolds prepared by electrospinning had a tridimensional pore structure that turns out to be an excellent support for the adhesion and growth of eukaryotic cells. Figures 8a and 9a show that the adhesion percentages for Vero cells (epithelial cells) were higher for 1L6 scaffolds than for control (2D surface of the culture plate). The Vero cells proliferated on unloaded 1L6 and 1L6 matrices loaded with pyophages and staphylophages (Figures 8b and 9b, respectively). Growth percentages were significantly ($p<0.05$) higher than those determined for the control. This led to the conclusion that new scaffolds were fully biocompatible provided that bacteriophages encapsulated were not cytotoxic for Vero epithelial cells.

**Figure 8.** Biocompatibility of 1L6 matrices loaded with Stahpylophages by means of cell adhesion (a) and proliferation (b) assays using ephitelial Vero cells. The bars are mean ± SD (n=4). * $p < 0.05$, scaffold vs. film, ANOVA followed by Tukey test.

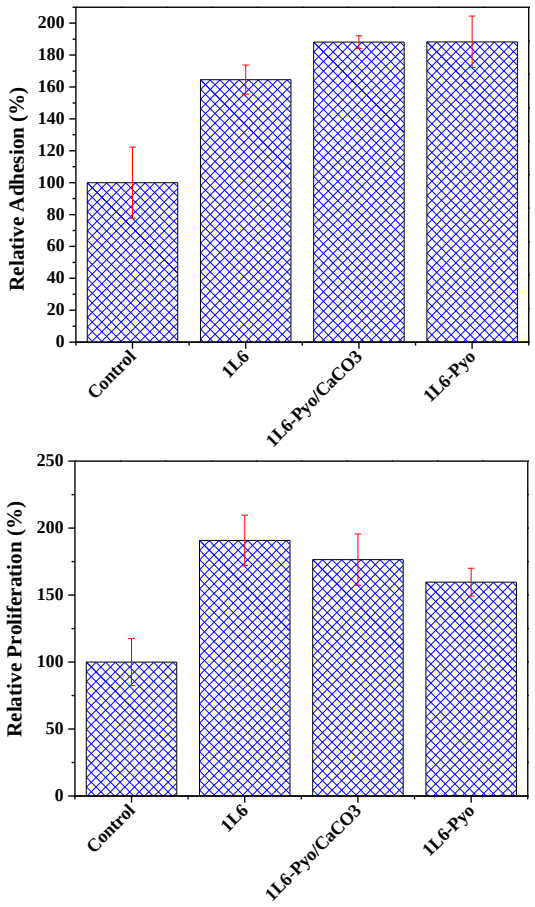

**Figure 9.** Biocompatibility of 1L6 matrices loaded with Stahpylophages by means of cell adhesion (a) and proliferation (b) assays using ephitelial Vero cells. The bars are mean ± SD (n=4). * $p$ < 0.05, scaffold vs. film, ANOVA followed by Tukey test.

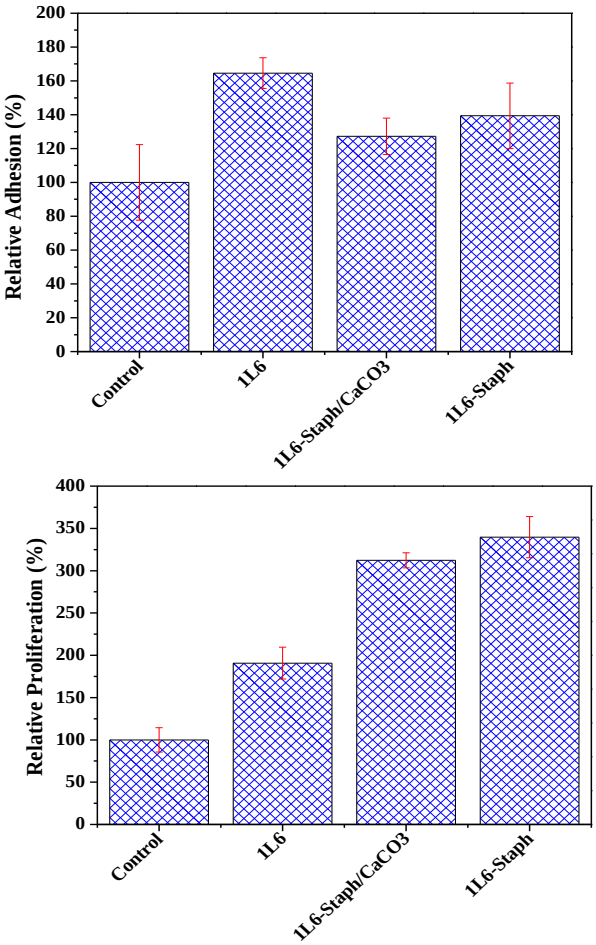


Micrographs of cellular monolayers grown onto the scaffolds loaded with pyophages and staphylophages are given in Figure 10. The SEM images clearly demonstrated that loaded bacteriophages did not cause a cytophatic effect in Vero cells. The cells monolayer was well formed as shown by the intimate contact between cells, besides cell spreading is able to colonize the scaffold through its porous structure.

**Figure 10.** Morphological characteristics of epithelial-like Vero cells growth in 1L6 fiber matrices loaded with Staphylophages (a, b) and Pyophages (c, d) in adhesion (a,c) and proliferation(b,d) assays.

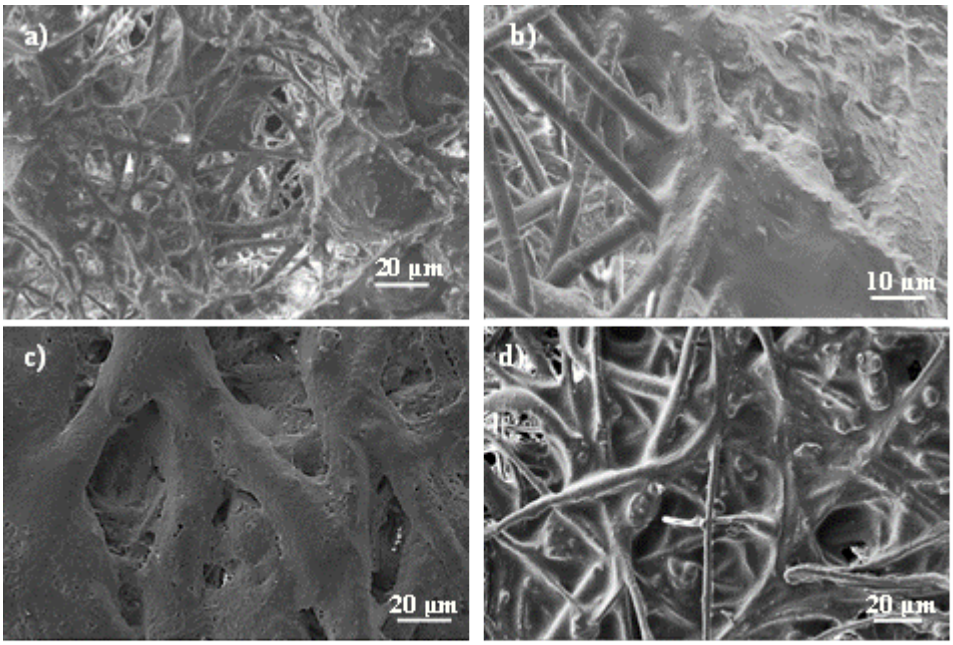




## I. Conclusions

Phages can be incorporated by means of the electrospinning technique and without losing their activity into microfibers of the poly(ester urea) derived from L-leucine, 1,6-hexanediol and carbonic acid. Both free and carbonate adsorbed bacteriophages can be employed, having the resulting loaded scaffolds a similar bactericide activity. Results are promising since up to now electrospun scaffolds were usually loaded by a simple adsorption process that was performed after processing.

The selected poly(ester urea) had solubility characteristics that allowed loading phages in the electrospun solution without causing a decrease on their activity. Processing conditions were different when free or carbonate adsorbed phages were employed and consequently resulting fiber morphologies depended on the way as phages were incorporated. The use of

carbonate particles required a higher flow rate that caused an increase on the microfiber diameter. In this case, fibers showed abundant protuberances that were randomly distributed along the fiber. Carbonate particles were well encapsulated in the electrospun fibers and consequently the hydrophobicity of the scaffolds did not decrease after the incorporation of the inorganic salt particles. Scaffolds loaded with phages were fully biocompatible unlike usual bactericide drugs that could produce a cytopatic effect at high doses.

## II. References

1. Llorens E, Del Valle LJ, Ferrán R, Rodríguez-Galán A, Puiggalí J. J Polym Res 2014;21:360.
2. Yang D, Li Y, Nie J. Carbohydr Polym 2007;69:538.
3. Kenawy ER, Bowlin GL, Mansfield K, Layman J, Simpson DG, Sanders EH, et al. J Control Release 2002;81:57.
4. Lee SW, Belcher AM. Nano Lett 2004;4:387.
5. Salalha W, Kuhn J, Dror Y, Zussman E. Nanotechnology 2006;17:4675.
6. Llorens E, Del Valle LJ, Díaz A, Casas MT, Puiggalí J. Macromol Res 2013;21:775.

# Chapter 5.2

## *Anhydric maleic functionalization and polyethylene glycol grafting of lactide-co-trimethylene carbonate copolymers.*

Lactide and trimethylene carbonate copolymers were successfully grafted with polyethylene glycol via previous functionalization with maleic anhydride and using *N*,*N*´-diisopropylcarbodiimide as condensing agent. Maleinization led to moderate polymer degradation. Specifically, the weight average molecular weight decreased from 36,200 to 30,200 g/mol for the copolymer having 20 molar-% of trimethylene carbonate units.

Copolymers were characterized by differential scanning calorimetry, thermogravimetry and X-ray diffraction. Morphology of spherulites and lamellar crystals was evaluated with optical and atomic force microscopies, respectively. The studied copolymers were able to crystallize despite the randomness caused by the trimethylene carbonate units and the lateral groups. Contact angle measurements indicated that PEG grafted copolymers were more hydrophilic than parent copolymers. This feature justified that enzymatic degradation in lipase medium and proliferation of both epithelial-like and fibroblast-like cells were enhanced. Grafted copolymers

were appropriate to prepare regular drug loaded microspheres by the oil-in-water emulsion method. Triclosan release from loaded microspheres was evaluated in two media.

## I. Introduction

Polylactide (PLA) is currently the main biobased thermoplastic polymer that can be manufactured at a more competitive price than petroleum based polymers. Furthermore, polylactide has suitable properties for both commodity and specialty applications.[1] For example, low toxicity and environmentally benign characteristics have made PLA an ideal material for food packaging and film wrap, as well as for other consumer products.[2,3] PLA has also been widely used for biomedical applications such as medical implants in the form of screws, pins, rods, and meshes,[4,5] bioabsorbable sutures,[6-8] tissue engineering scaffolds[9] and drug-delivery systems[10] because of its ability to biodegrade into innocuous lactic acid under physiological conditions and its exceptional qualities, like biocompatibility, FDA approval for clinical use, low immunogenicity and good mechanical properties. Despite these advantages, its hydrophobicity may hinder certain biological and biomedical applications. In this sense, different PLA-based amphiphilic block copolymers (*e.g.*, those constituted by poly(ethylene glycol) (PEG)) have been designed and synthesized[11] from maleic anhydride grafted PLA, a method first reported by Carlson *et al*.[12] Moreover, modification with polar groups to increase hydrophilicity has been proved to improve cell adhesion without any harmful effect.



Polyethylene glycol grafted polylactides (PEG-*g*-PLA) have also been considered to improve the ductility of PLA. In fact, PEG has excellent plasticizing abilities, although the amount introduced in PLA must be lower or equal to 20 wt% to avoid phase separation.[11,13-15] Reactive blending of a maleic anhydride grafted PLA with hydroxyl functionalized PEG has been proposed as an easy way to prepare PEG-*g*-PLA copolymers, which should create more interactions between the so-functionalized polyester matrix and non-grafted PEG.[16] In situ reactive grafting of hydroxy terminated poly(ethylene glycol) (PEG) plasticizer onto maleic anhydride modified PLA in PLA/PEG blends had a positive impact on mechanical properties and lowered the glass transition temperature significantly compared to the blends where no grafting could occur (neat PLA + PEG).

Polytrimethylene carbonate (PTMC) is a well-known biodegradable polymer with rubbery characteristics and suitable properties as a biomaterial for biomedical applications.[17] In fact, segmented copolymers constituted by glycolide-*co*-trimethylene carbonate, and even glycolide-*co*-caprolactone-*co*-trimethylene carbonate soft segments, have been widely employed for preparation of monofilament surgical sutures since stiffness of polyglycolide hard blocks can be reduced.[18,19] In the same way, efforts to improve the mechanical properties (*e.g.*, ductility) of PLA for use in a wide range of applications have been conducted; specifically, random and sequential copolymerizations of lactide and trimethylene carbonate have been considered.[20-22]

The aim of the present work is to prepare PEG grafted poly(lactide-*r*-trimethylene carbonate) (PLA-*r*-PTMC) copolymers via maleic acid functionalization and evaluate the effect of PEG chains on properties, degradability and cytotoxicity. Potential applications of the new biodegradable systems as drug delivery nanospheres are also considered.



## II. Experimental Section

### 1. Materials

Grafted copolymers were synthesized following the scheme in Figure 1. All solvents, triclosan, *N*,*N*'-diisopropylcarbodiimide, 3-(4,5-dimethylthiazol-2-yl)-2,5-diphenyl-2H-tetrazolium bromide (MTT) and cell culture labware were purchased from Sigma-Aldrich (Spain). L-lactide, polyvinyl alcohol (PVA) and polyethylene glycol (550 g/mol) were purchased from Sigma-Aldrich, whereas trimethylene carbonate (1,3-dioxane-2-one) and maleic anhydride were purchased from Boehringer and Fluka, respectively. All solvents, polymers and reagents were used as received.

The enzyme used in the degradation studies (*i.e.*, lipase from *Rhizopus oryzae*) and Dulbecco's phosphate buffered saline medium were also purchased from Sigma Aldrich.

**Figure 1.** Synthesis scheme for PEG grafted polymers derived from lactide and trimethylene carbonate.

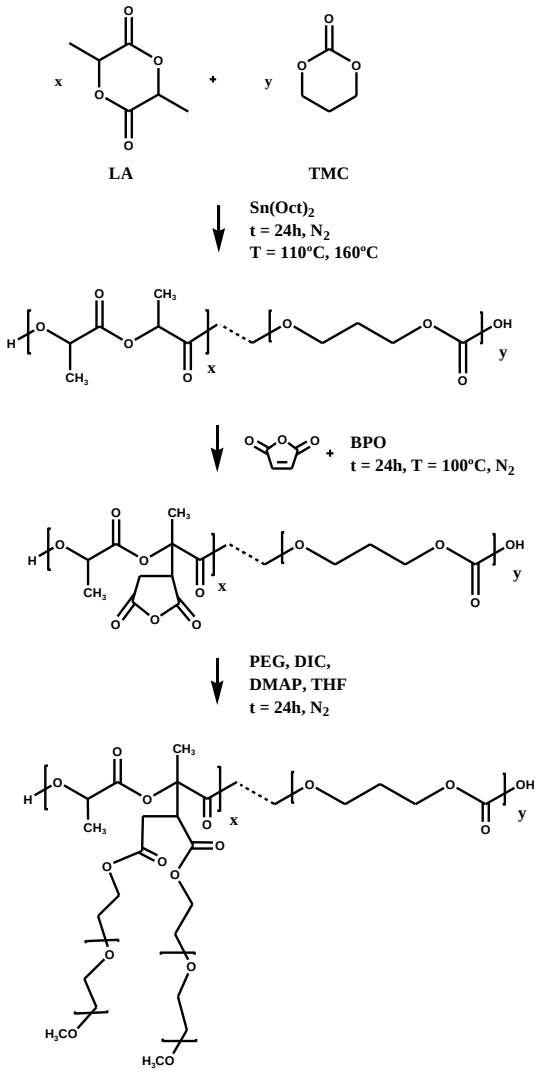




## 2. Synthesis of PLA and PLA-r-PTMC samples

PLA and PLA-*r*-PTMC were synthesized by bulk ring-opening polymerization of L-lactide (LA) and its mixture with appropriate amounts of trimethylene carbonate (TMC). $Sn(Oct)_2$ (0.05*M* solution in dry chloroform) was used as a catalyst, with the monomer/catalyst

ratio always close to 5,000. The monomers and initiator were mixed in a silanized glass flask equipped with a magnetic stirrer and gas inlet and outlet tubes. Chloroform was subsequently removed under vacuum. Polymerizations were performed under a nitrogen atmosphere at temperatures of 140 ºC and 160 ºC for the homopolymer and the trimethylene carbonate copolymers, respectively, for 24 h. Temperature was increased for the preparation of the copolymer due to the lower reactivity of TMC. Reported synthesis data of the PTMC homopolymer indicated that temperatures around 160 °C were appropriate for reaction times close to 24 h.[23,24] Samples were purified by precipitation from dichloromethane solutions with methanol and stored under vacuum.

### 3. Maleic anhydride functionalization

One gram of the appropriate polymer or copolymer sample in powder form was mixed evenly with benzoyl peroxide (BPO), which was used as an effective radical initiator reported in the literature for the functionalization of polymers based on lactide and ε-caprolactone.[25–27] The mixture was introduced in a round bottom flask and vacuum dried at room temperature for at least 4 h. Toluene (5 mL) was added to dissolve the sample, purged with pure nitrogen and then heated to 100 ºC. Maleic anhydride (MA) was dissolved in toluene (2 mL) in a second flask, purged with nitrogen, heated to 100 ºC and finally added to the first polymer or copolymer solution. Reaction was performed at 100 ºC for 24 h, the ratios (*w/w*) of polymer/copolymer to MA and BPO being 1:1 and 18:100, respectively. The solution was then dialyzed against chloroform using a membrane (Zellu Trans, Roth) with a nominal M*w* cut-off of 1,000g/mol for 48 h. The final product was recovered from the dialysis bag solution by rotavaporation and then stored under vacuum.



### 4. Grafting with polyethylene glycol

One gram of the maleinized sample and 1 mmol of 4-dimethylaminopyridine (DMAP) were completely dissolved in 4 mL of anhydrous tetrahydrofurane (THF) and kept at room

temperature for 30 min. PEG (1 mmol) and diisopropylcarbodiimide (DIC) (1.3 mmol) were mixed in 2 mL of THF and slowly transferred into the polymer solution using a syringe. The solution was stirred at room temperature for 24 h. At the end of the reaction time, the solution was concentrated by removing most of the solvent. The new polymer was dissolved in dichloromethane and precipitated in cold methanol.

## 5. Measurements

Molecular weight was estimated by size exclusion chromatography (GPC) using a liquid chromatograph (Shimadzu, model LC-8A) equipped with an Empower computer program (Waters). A PL HFIP gel column (Polymer Lab) and a refractive index detector (Shimadzu RID-10A) were employed. The polymer was dissolved and eluted in 1,1,1,3,3,3-hexafluoroisopropanol containing $CF_3COONa$ (0.05 M) at a flow rate of 0.5 mL/min (injected volume 100 µL, sample concentration 2.0 mg/mL). Number and weight average molecular weights were calculated using polymethyl methacrylate standards.



$^1$H-NMR spectra were acquired with a Bruker AMX-300 spectrometer operating at 300.1 MHz and 75.7 MHz, respectively. Chemical shifts were calibrated using tetramethylsilane as an internal standard. Deuterated chloroform was used as the solvent.

Infrared absorption spectra were recorded with a Fourier Transform FTIR 4100 Jasco spectrometer in the 4000-600 $cm^{-1}$ range. A Specac model MKII Golden Gate attenuated total reflection (ATR) cell with a heated Diamond ATR Top-Plate was used.

Calorimetric data were obtained by differential scanning calorimetry with a TA Instruments Q100 series equipped with a refrigerated cooling system (RCS). Experiments were conducted under a flow of dry nitrogen with a sample weight of approximately 5 mg while calibration was performed with indium.

X-ray powder diffraction patterns were acquired with a PANalytical X´Pert diffractometer with Cu $K_\alpha$ radiation ($\lambda$ = 0.1542 nm) and a silicium monocrystal sample holder. Operating voltage and current were 40 Kv and 50 mA, respectively.

Spherulitic morphologies were prepared from both solution and bulk crystallization from the melt state and then analyzed by optical microscopy. A Zeiss Axioskop 40 Pol light polarizing microscope equipped with a Linkam temperature control system configured by a THMS 600 heating and freezing stage connected to an LNP 94 liquid nitrogen pump cooling system. A first-order red tint plate was employed to determine the sign of spherulite birefringence under crossed polarizers. Micrographs were taken with a Zeiss AxioCam MRc5 digital camera. In order to study melt crystallized spherulites, thin films were previously prepared from the evaporation of dilute solutions of the polymer in 1,1,1,3,3,3-hexafluoroisopropanol (0.5 mg/mL). Small sections of these films were pressed or smeared between two cover slides, inserted in the hot stage, melted at approximately 20 ºC above their melting point for 5 min to wipe sample history effects and quickly cooled to the selected crystallization temperature. Solution crystallized spherulites were more easily obtained by slow evaporation of dilute (40 mg/mL) chloroform solution drops placed between two cover slides.



For AFM studies, drops of highly diluted solutions in formic acid (0.05 mg/mL) were deposited on cover slides. Height and amplitude images of spherulites were obtained with a Molecular Imaging PicoSPM using a NanoScope IV controller in ambient conditions and a scan window size of 10 x 10 $\mu m^2$. Tapping mode AFM was operated at constant deflection (*i.e.*, constant vertical force with triangular gold-coated silicon nitride cantilever). The row scanning frequency was set to 1 Hz and the physical tip-sample motion speed was 10 μm/s.

Thermal degradation was studied at a heating rate of 20 ºC/min with around 10 mg samples in a Q50 thermogravimetric analyzer of TA Instruments and under a flow of dry nitrogen. The analysis was performed in the 25 to 600 ºC temperature range.

Contact angles (CA) were measured at room temperature with sessile drops using an OCA-15 plus Dynamic Contact Angle measuring device (Dataphysics, USA). SCA20 software was used. Contact angle values of the right and left sides of distilled water drops were measured (10 s after the drop (5 μL) was deposited on the sample surface) and averaged over six measurements on different locations of the surface.

### 6. Degradation studies Materials

Samples for degradation studies were cut from regular films of 0.5 × 0.5 $cm^2$ and 120 µm in thickness prepared by melt pressing 300 mg of the appropriate polymer at a temperature of 10 °C above the melting peak temperature and then led to slowly cool to room temperature in order to keep their semicrystalline character.

Enzymatic degradation was conducted at 37 °C by using a *Rhizopus oryzae* lipase (56-60 units/mg). The enzymatic medium, 1 L, consisted of a pH 7.4 sodium phosphate buffer (PBS) containing sodium azide (0.03 wt-%) and 1 g of lipase. All enzymatic solutions were renewed every 48 h because of enzymatic activity loss. After immersion, samples were rinsed with water, dried to constant weight under vacuum and stored over $P_4O_{10}$ before analysis. Weight retention was then calculated. Hydrolytic degradation was evaluated in the same way but using PBS medium without enzyme. Degradation studies were performed in triplicate, with given data corresponding to the average values.



Inspection of the morphology of degraded films was conducted by scanning electron microscopy using a Focused Ion Beam Zeiss Neon 40 instrument (Carl Zeiss, Germany). Carbon coating was performed using a Mitec K950 Sputter Coater fitted with a *k*150x film thickness monitor. Samples were visualized at an accelerating voltage of 5 kV.

### 7. Cell adhesion and proliferation assays

Fibroblast-like Cos-7 and epithelial-like Vero cells from kidney of African green monkey were cultured in Dulbecco's modified Eagle medium (DMEM) as previously reported.[28] These cell lines are interesting since these represent two of the main human tissues for which biocompatibility is interesting to be tested.

Square pieces (0.5×0.5×0.12 $mm^3$) of the press-molded films were placed into each well of a multiwell culture plate. Samples were fixed in the wells with a small drop of silicone (Silbione® MED ADH 4300 RTV, Bluestar Silicones France SAS, Lyon, France) and then sterilized by UV-radiation in a laminar flux cabinet for 15 min. For the cell adhesion assay,

aliquots of 50-100 µL containing $5x10^4$ cells were seeded onto the molded samples and incubated for 24 h (adhesion assay) or 4 days (proliferation assay).

Samples were evaluated by the standard adhesion and proliferation method[23] using three replicates and the results were averaged. Results were normalized with a positive control (100% of cell adhesion and cell proliferation) that consisted on the polystyrene tissue plate. Samples with adhered and grown cells on their surface were fixed overnight in 2.5% *w*/*v* formaldehyde at 4 ºC. They were subsequently dehydrated and processed for observation by scanning electronic microscopy.

### 8. Preparation of microspheres and release study

0.25 g of the grafted copolymer and 0.0075 g of triclosan (*i.e.*, 3 wt% with respect to the polymer) were dissolved in methylene dichloride (6 mL). The resulting homogeneous solution was dropwise added to 42 mL of a stirred (1000 rpm) aqueous solution of PVA (1%, *w*/*v*) for 1 h. The resulting oil-in-water emulsion was further stirred at 42ºC for 5 h in order to completely evaporate the organic solvent. The formed microspheres were collected by centrifugation, washed five times with water and finally freeze dried. Drug loading was determined by UV spectroscopy using a Shimadzu 3600 spectrometer. About 20 mg of triclosan loaded microspheres were accurately weighed, dissolved in methylene chloride and finally brought to 5 mL volume. Triclosan was quantified by means of the absorbance measured at 281 nm and the calibration linear plot obtained from standard solutions. Measurements were conducted in triplicate and controlled release measurements were made with triclosan loaded samples. These were weighed and incubated at 37 ºC in an orbital shaker at 200 rpm in tubes of 50 mL for 24 h. PBS (hydrophilic medium) and alternatively its mixture with ethanol (*i.e.*, 3:7 *v*/*v* ratio) as a more hydrophobic component were employed as release media. Samples were withdrawn from the release medium at predetermined time intervals and drug concentration was evaluated by UV spectroscopy, as above indicated. The volume of the release medium was kept constant by addition of fresh buffer or PBS/ethanol mixture. All drug release tests were carried out using three replicates and the results were averaged.

## III. Results and Discussion

Ring-opening polymerization conditions were selected in order to minimize a preferential reaction of lactide that could lead to the formation of polylactide blocks.[21,23,24] $^1$H NMR spectra (Figure 2a) were used to determine the lactide comonomer content in the polymer chain, which was always in good agreement with the feed ratio (Table 1). Specifically, signals at 5.20-5.00 ppm (methine protons of lactoyl units) and 4.20 ppm (α-methylene protons of trimethylene carbonate units) were selected to estimate the molar composition:

$$\text{TMC (mol-\%)} = 100 \times 0.5 \times A_{4.20} / (0.5 \times A_{4.20} + A_{5.20\text{-}5.00}) \quad (1)$$

Data in Table 1 also point out that polymerization yields were always high (80-85%) and that final molecular weights determined by GPC were similar for all studied samples (*i.e.*, $M_n$ ranged between 20,100 and 22,100 g/mol).



**Table 1.** Synthesis data of homopolymers and copolymers prepared by ring opening polymerization.

| Polymer[a] | Yield (%) | $f_x$ [b] | $M_n$ [c] (g/mol) | $M_w$ [c] (g/mol) | PDI[c,d] |
|---|---|---|---|---|---|
| PLA | 80 | - | 20,500 | 48,500 | 2.4 |
| LA-*r*-TMC 5 | 85 | 4.2 | 22,100 | 52,900 | 2.4 |
| LA-*r*-TMC 20 | 80 | 19.8 | 20,100 | 36,200 | 1.8 |

[a]The number in the abbreviation indicates the lactide weight percentage in the reaction monomer mixture.

[b]Trimethylene carbonate molar fraction determined from $^1$H NMR spectra.

[c]From GPC.

[d]Polydispersity index.

A great excess of maleic anhydride was used to ensure sufficient functionalization of all the polymers. This option was preferred because it allowed easy removal of polyanhydride by products due to their high solubility in chloroform. Furthermore, the PEG derivatives, which could hypothetically be produced in the subsequent reaction step, were highly soluble in both chloroform and methanol (*i.e.,* the solvent-precipitation system for the purification of the grafted samples).

**Figure 2.** $^{1}$H-NMR spectra of LA-*r*-TMC 20 (a) and (LA-*r*-MC 20)-*g*-PEG (b).

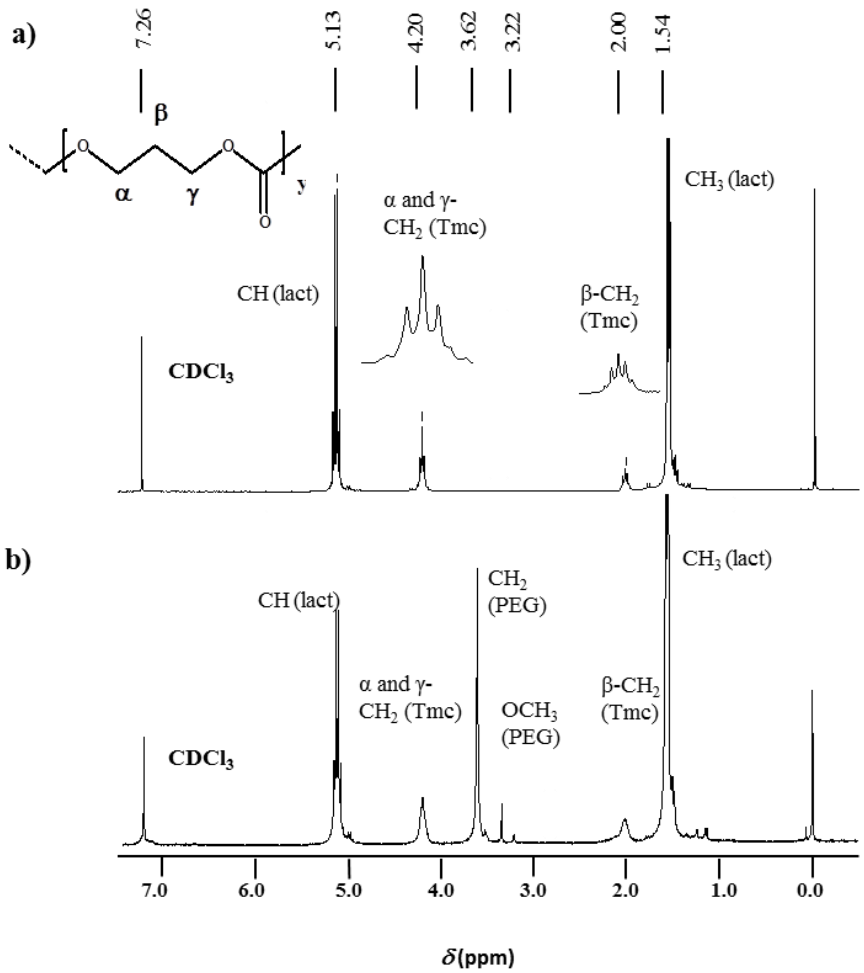

Figure 3a shows the IR spectrum of maleic anhydride functionalized samples, which evidenced the presence of a carboxylic acid band (1730 $cm^{-1}$) derived for MA hydrolysis along a typical anhydride band at 1856 $cm^{-1}$. This hydrolysis occurred easily during storage, as shown in Figure 3b since the intensities of indicated anhydride and carboxylic acid bands decreased and increased, respectively. Consequently, the final polyethylene glycol grafting was performed by a condensation reaction using a typical agent such as *N*,*N*'-diisopropylcarbodiimide. After grafting, the carboxylic acid group signal (*i.e.,* 1720 $cm^{-1}$) disappeared completely and gave rise to a single band at 1747 $cm^{-1}$, indicating that condensation was successful for both acid groups of the open anhydride and that the corresponding ester group was formed.

**Figure 3.** FTIR spectra (1950-1600 $cm^{-1}$ region) of maleic anhydride functionalized LA-*r*-TMC 20 sample (blue trace) and the corresponding PEG grafted copolymer (red trace) taken immediately after reaction (a) or after storage for 4 h (b).



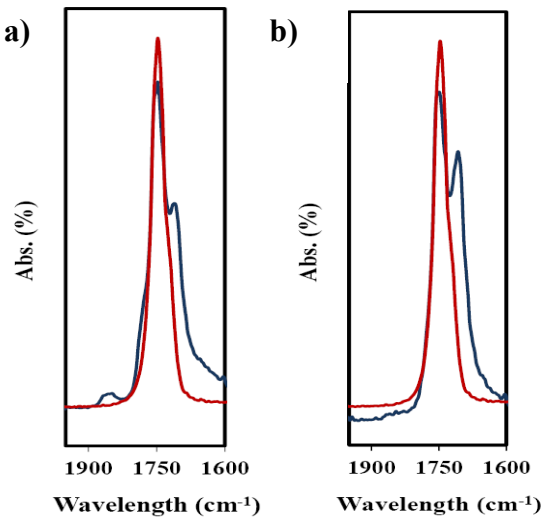


The $^{1}H$ NMR spectrum of the grafted polymers only showed the expected signals of the main chain, together with the signal corresponding the methylene group of polyethylene glycol units (3.62 ppm) and a singulet corresponding to its terminal methyl group at 3.22 ppm (Figure 2b for a representative sample). Logically, the ratio between methylene and methyl signals was in

agreement with the molecular weight of the PEG used (*i.e.*, 550 g/mol). Furthermore, PEG content was easily determined (Table 2) from the area of signals representative of lactide (5.20-5.00 ppm), polyethylene glycol (3.61 ppm) and trimethylene carbonate (4.20 ppm) units according to the equation:

$$\text{PEG (mol\%)} = 100 \times A_{3.61} / (A_{3.61} + 0.5 \times A_{4.20} + A_{5.20\text{-}5.00}) \quad (2)$$

Only the signals corresponding to main chain carbon atoms and those assigned to the grafted chains were observed with significant intensity in the $^{13}$C NMR spectra. In contrast, maleic units were hard to detect, in agreement with the low functionalization yield. $^{13}$C NMR spectra also corroborated the existence of heterosequences indicative of a random monomer distribution. Thus, complex lactoyl signals were detected due to triad and dyad sensitivities of methine and methyl groups (inset of Figure 4).



**Figure 4.** $^{13}$C-NMR spectra of LA-*r*-TMC 20. Inset shows signals indicative of triad and dyad sequences.

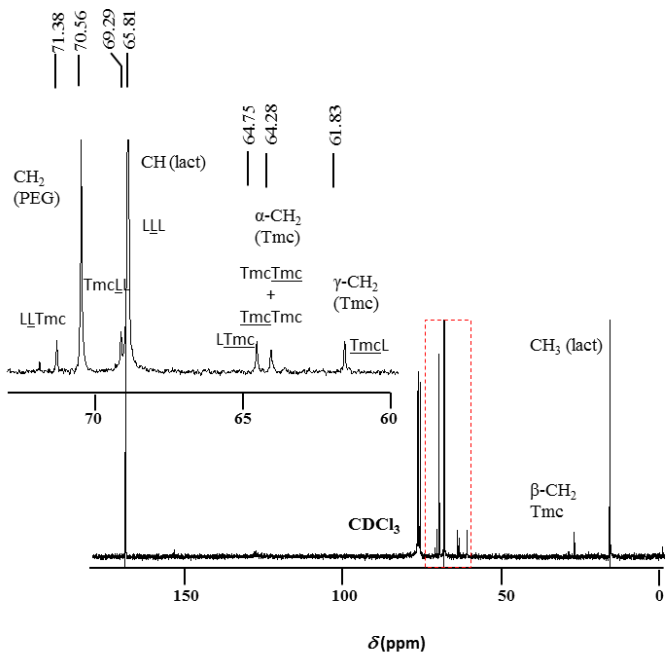

Table 2 summarizes the main data concerning the synthesis of polyethylene glycol grafted samples. Maleinization reaction led to some degradation but it is worth noting that the decrease in the molecular weight was lower than 35% for the two trimethylene carbonate derivatives. It is also interesting to indicate that incorporation of polyethylene glycol was successful and specifically a molar percentage close to 15-17% could be achieved, although the reaction yields were moderate, probably as a consequence of the above chain breakages. Grafting was similar for the two synthesized copolymers as deduced from the determined molar percentage of PEG (15–17 mol%) and only a slight decrease was detected for the polylactide homopolymer (*i.e.*, 10 mol%). When the molecular weight decrease (Table 2) is taken also into account the functionalization and grafting process seems clearly more favorable for the copolymers of lactide and trimethylene carbonate.

**Table 2.** Synthesis data of poly(ethylene glycol) grafted samples.

| Polymer | Yield (%) | PEG (mol-%) | $M_n$[a] (g/mol) | $M_w$[a] (g/mol) | PDI[a,b] |
|---|---|---|---|---|---|
| PLA-*g*-PEG | 65 | 10 | 10,943 | 28,572 | 2,6 |
| (LA-*r*-TMC 5)-*g*-PEG | 50 | 15 | 17,200 | 37,300 | 2.2 |
| (LA-*r*-TMC 20)-*g*-PEG | 55 | 17 | 15,900 | 30,200 | 1.9 |

[a]From GPC; [b]Polydispersity index.



### 1. Thermal properties of polyethylene glycol grafted copolymers

The effect of polyethylene glycol grafting on thermal properties of neat polymers was investigated by DSC analysis. Figure 5 shows the typical four run protocol used to characterize the main thermal properties of grafted and non-grafted samples (Table 3). Specifically, melting

and crystallization data of as-synthesized, melt crystallized and melt quenched samples are determined.

**Figure 5.** DSC calorimetric traces obtained with PLA-*g*-PEG: (a) Heating run (20 ºC/min) of the as-synthesized sample, (b) Cooling run (10 ºC/min) of a melted sample, (c) Subsequent heating run (20 ºC/min) of the sample crystallized from the melt, (d) Heating run (20 ºC/min) of a melt quenched sample.

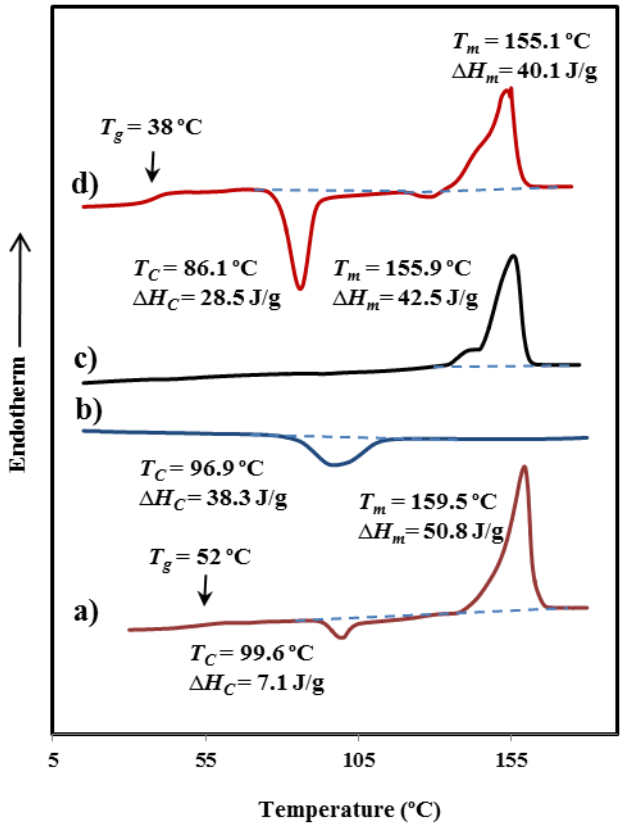


The third heating run gave more information about the studied semicrystalline samples; specifically, glass transition temperature, cold crystallization and melting data were obtained. Figure 6 shows the effects of PEG chain grafting, which can be summarized as follows: a) Decrease of the glass transition temperature due to the presence of more flexible PEG chains

and slight decrease in the molecular weight; b) phase separation between PEG and the lactide rich copolymers could not be detected because a single glass transition temperature was always observed even if samples were quenched to -60 ºC (not shown); c) no melting or crystallization peaks associated with PEG could be detected in any of the studied samples; d) decrease of the melting and crystallization enthalpy of polylactide blocks due to hindered crystallization caused by grafted PEG chains; e) Increase in the complexity of the melting peak for high TMC contents, probably because of the presence of a new population of more defective lamellar crystals; f) decrease of the cold crystallization temperature due to enhanced nucleation induced by the presence of functional groups, as previously reported for related grafted polycaprolactone samples.[29]

**Figure 6.** DSC calorimetric traces corresponding to the heating run of quenched samples of LA-*r*-TMC 5 (a), (LA-*r*-TMC 5)-*g*-PEG (b), LA-*r*-TMC 20 (c) and (LA-*r*-TMC 20)-*g*-PEG (d).



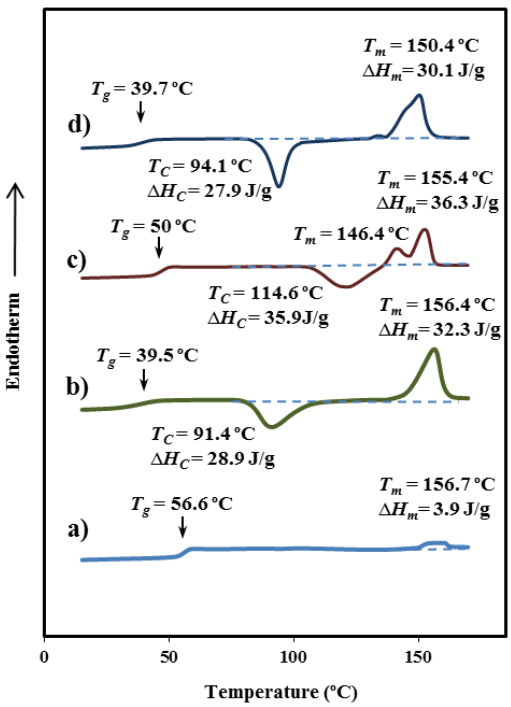

**Table 3.** Main calorimetric of grafted and non-grafted samples.

| Sample | First Heating | | Cooling | | Second Heating | | | | | Third Heating | | | |
|---|---|---|---|---|---|---|---|---|---|---|---|---|---|
| | $T_f$ (ºC) | $\Delta H_f$ (J/g) | $T_c$ (ºC) | $\Delta H_c$ (J/g) | $T_c$ (ºC) | $\Delta H_c$ (J/g) | $T_f$ (ºC) | $\Delta H_f$ (J/g) | $T_g$ (ºC) | $T_c$ (ºC) | $\Delta H_c$ (J/g) | $T_f$ (ºC) | $\Delta H_f$ (J/g) |
| PLA | 173.2 | 56 | 105.9 | 41.9 | 110.3 | 8.9 | 172.81 | 56.9 | 57.6 | 111.5 | 56.6 | 172.4 | 55.7 |
| LA-*r*-PMC 5 | 151.7 | 33.4 | 96.2 | 5.9 | | | 160.3 | 6.1 | 56.6 | | | 156.7 | 3.9 |
| LA-*r*-TMC 20 | 155.9 | 38.7 | 97.3 | 8.3 | 107 | 23.1 | 146.4 155.7 | 37.5 | 50 | 114.6 | 35.9 | 146.4 155.4 | 36.3 |
| PLA-*g*-PEG | 159.5 | 50.6 | 97.1 | 38.1 | | | 155.7 | 40.1 | 38.7 | 86.1 | 35.5 | 155.1 | 40.2 |
| (LA-*r*-TMC 5)-*g*-PEG | 157.1 | 31.9 | 85.9 | 8.7 | 93.5 | 20.7 | 159.8 | 32.6 | 39.5 | 91.4 | 28.9 | 156.4 | 32.3 |
| (LA-*r*-TMC 20)-*g*-PEG | 152.1 | 31.7 | 81.5 | 20 | 89.8 | 9.7 | 151.1 | 32.3 | 39.7 | 94.1 | 27.9 | 150.4 | 30.1 |

## 2. Structure and crystalline morphology of polyethylene glycol grafted copolymers

X-ray diffraction profiles of polyethylene glycol grafted copolymers and of copolymers before maleic anhydride functionalization always showed the typical polylactide diffraction peaks. Thus, the strongest Bragg peaks were observed at 0.542, 0.472, and 0.403 nm and could be indexed as the (200) + (110), (203) and (015) reflections of the α-form of polylactide[30-33] (molecules with a $10_7$ helical conformation arranged according to a $P2_12_12_1$ orthorhombic space group with $a$ = 1.078-1.075 nm, $b$ = 0.645-0.604 nm, and $c$ (chain axis) = 2.880-2.780 nm. Patterns were also characterized by an amorphous halo at 0.506 nm, which was clearly more intense for the grafted samples (Figure 7). The degree of crystallinity, $X_c$, was deduced from the areas of crystalline peaks ($\Sigma A_B$) and the amorphous halo ($A_A$) of the deconvoluted profiles (*i.e.*, $X_C = 100 \times \Sigma A_B / ( \Sigma A_B + A_A )$ ). Grafting caused a decrease in the degree of crystallinity; in particular, a change from 54% to 44% was determined for the sample having the highest molar fraction of TMC (*i.e.*, 20%).



**Figure 7.** X-ray powder diffraction profiles of LA-*r*-TMC 20 (red) and (LA-*r*-TMC 20)-*g*-PEG (blue). Inset shows the deconvoluted profile of the PEG grafted sample.

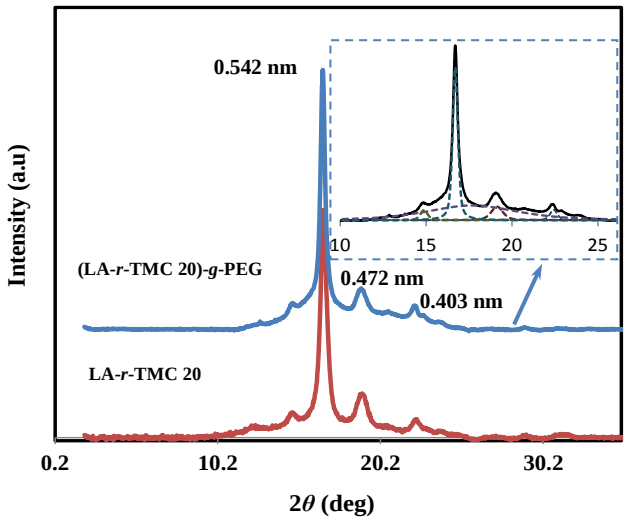

It is interesting to note that no diffraction peaks corresponding to the polyethylene glycol structure could be observed. As a result, the grafted chains were not able to arrange in crystalline domains, as also deduced from DSC data. The structure of PEG is defined by a $P2_1/a$ space group and a unit cell with parameters $a$ = 0.805 nm, $b$ = 1.304 nm, $c$ (fiber axis) = 1.948 nm and $\beta$= 125.4º, [34] the expected strongest peaks being those at 0.462 nm (120 reflection) and 0.386-0.377 nm (112, 032, $13\bar{2}$ and $21\bar{2}$ reflections).

Grafted copolymers crystallized from the melt state as negative spherulites with a fibrillar texture, as depicted in Figure 8a for the (LA-*r*-TMC 20%)-g-PEG sample. In fact, negative spherulites constituted by edge-on lamellae are characteristic of PLA crystallized at temperatures close to 120 ºC.[35] In general, spherulites grow until impingement, and consequently grafted chains become included within the spherulites rather than occluded. For this reason, the degree of perfection of the observed aggregates was limited.

Ringed negative spherulites were also obtained by evaporation of dilute chloroform solutions (Figure 8b). The spacing between consecutive rings became close to 7 μm and indicated a lamellar twisting that led to domains constituted by flat-on lamellae. These crystals should have a positive birefringence,[36-37] as envisaged in some bands of the spherulites in Figure 8b (see arrow).



Grafted copolymers were also able to crystallize from evaporation of dilute formic acid solutions, giving rise to aggregates of lamellar crystals (Figure 9). These aggregates had maximum dimensions of around 2 μm and well-defined lateral edges in some cases, and were formed by a stack of small crystals with a thickness of about 11-12 nm, as determined from AFM measurements (Figure 9c). A spindle shape was generally detected for the individual crystals, as reported for lactide copolymers when the growth rate along the [010] direction becomes enhanced.[38] Results obtained with (LA-*r*-TMC 20%)-g-PEG are interesting because they show its capability to rend crystalline structures despite the certain degree of randomness caused by the incorporation of TMC units and even the presence of pegylated chains, which should logically be excluded from the crystals and incorporated into the amorphous crystal surfaces.

**Figure 8.** Spherulitic morphologies of (PLA-*r*-PTMC 20%)-g-PEG prepared by crystallization from the melt state at 115 ºC (a) or evaporation of a chloroform diluted solution (b). Insets show details of micrographs taken using a first-order red tint plate. White arrow points to domains with a positive birefringence.

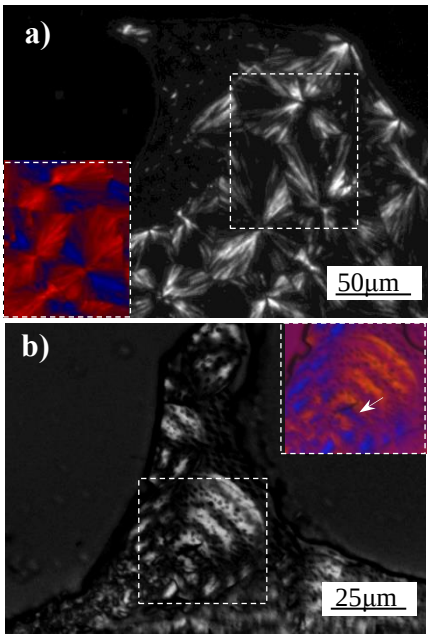




**Figure 9.** Atomic Force Microscopy topographic (left) and height (middle) images, and corresponding height profile (right) for (LA-*r*-TMC 20)-*g*-PEG. Crystals were obtained from slow evaporation of a diluted chloroform solution at 25 ºC.

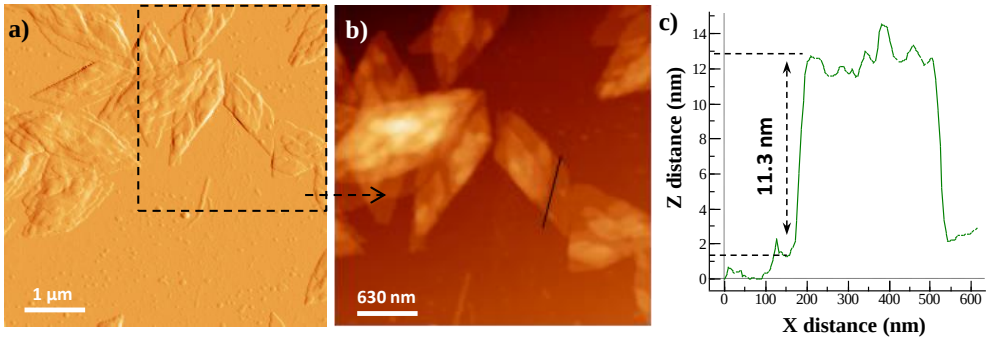

### 3. Thermal stability of polyethylene glycol grafted copolymers

TGA and DTGA curves of LA-*r*-TMC copolymers before and after grafting with polyethylene glycol are compared in Figure 10, whereas the main decomposition data are summarized in Table 4. Decomposition of the LA-*r*-TMC copolymer is peculiar since a well-defined single decomposition process is observed at 286 ºC, which is in agreement with the characteristic peak observed for PTMC (288 ºC) and far from that detected for PLA (379 ºC). Thus, degradation of the predominant component sequences seemed to be determined by the decomposition of the less stable component despite it being in a minority ratio. Copolymer decomposition could therefore not be associated with a simple combination of the characteristic degradation curves of the two constituent homopolymers, as also previously reported in the study of PTMC/PLA blends.[39]

**Table 4.** Characteristic TGA and DTGA data for the decomposition of the studied copolymers.



| Polymer | $T_{onset}$ (ºC) | $T_{10\%}$ (ºC) | $T_{20\%}$ (ºC) | $T_{40\%}$ (ºC) | $T_{max}$ [a] (ºC) |
|---|---|---|---|---|---|
| LA-*r*-TMC 5 | 186 | 261 | 270 | 280 | 292 |
| LA-*r*-TMC 20 | 214 | 267 | 274 | 281 | 286 |
| (LA-*r*-TMC 5%-*g*-PEG | 262 | 307 | 318 | 332 | **341,** 410 |
| (LA-*r*-TMC 20)-*g*-PEG | 240 | 292 | 304 | 319 | **329,** 405 |

[a] When two peaks were detected the most intense is indicated by bold characters.

Polyethylene glycol grafted samples were more thermally stable than the parent non-grafted copolymers because DTGA peaks appeared at higher temperatures. However, $T_{onset}$ was lower, probably as a consequence of the higher terminal group concentration (*i.e.,* lower molecular weight). Grafted samples also showed a complex degradation process with multiple DTGA peaks, with the highest temperature one (ca. 400 ºC) being probably related to decomposition of grafted polyethylene glycol chains. Decomposition clearly occurred in a wider temperature range than in non-grafted samples, as expected considering the complexity of the

molecular structure. Char yields were similar (ca. 5%) for all samples except for the LA-*r*-TMC copolymer, which decomposed completely.

**Figure 10.** TGA and DTGA traces of (LA-*r*-TMC 20) (red solid lines), (LA-*r*-TMC 20%)-*g*-PEG (blue dashed lines).

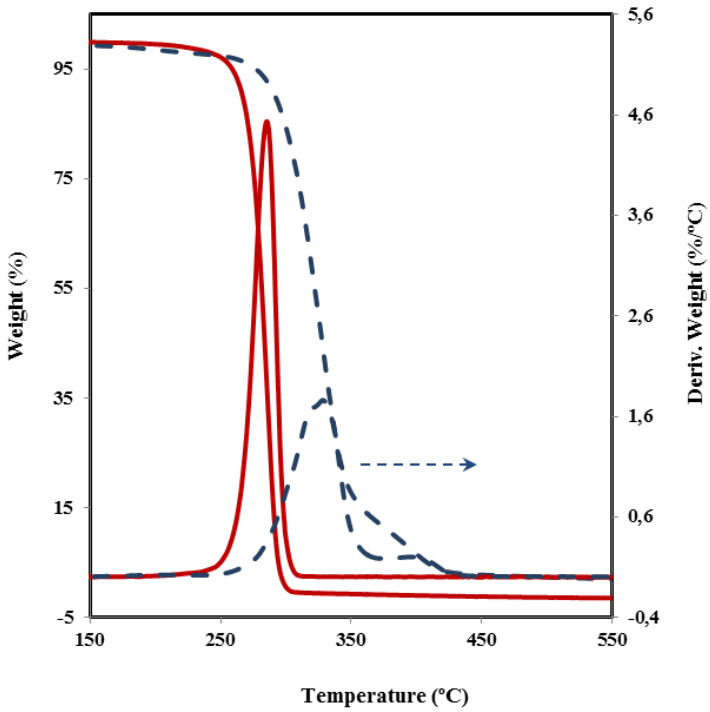




## 4. Hydrophilicity of polyethylene glycol grafted copolymers and enzymatic degradability

Figure 11 shows the water contact angles values determined for films of representative samples. (LA-*r*-TMC 20%)-*g*-PEG was statistically significantly different, indicating the increase in hydrophilicity caused by pegylation. Thus, contact angle values decreased to 60º while the value for the parent copolymer (*i.e.*, LA-*r*-TMC 20) was 92º. The effect of PEG was logically clearer for the copolymer with the highest degree of functionalization. Despite similarities in contact angle

values for the other studied samples, it seems that incorporation of trimethylene carbonate units increased the hydrophobicity of the sample. Note that the contact angle determined for PLA was 87º, a value slightly lower than those found for the random copolymers.

**Figure 11.** Contact angles for the indicated PEG grafted and non-grafted samples (* p<0.05 vs non-grafted samples, Tukey's test).

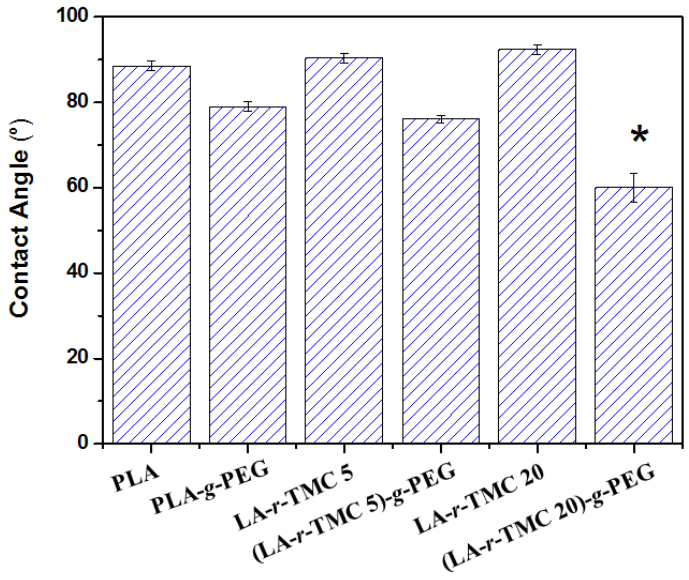




The evolution of weight loss during enzymatic degradation is plotted in Figure 12 for the melt-processed film of (LA-*r*-TMC 20)-*g*-PEG. As can be seen, the sample degraded steadily at a slow rate, with a loss value slightly higher than 20% after 34 days of exposure to lipase medium. Degradation was also evaluated in PBS control solution because in this case only hydrolytic attack was expected. Results indicated a weight loss of less than 2.5% after 34 days of exposure.

**Figure 12.** Weight loss of PLA-*g*-PEG and (LA-*r*-TMC 20)-*g*-PEG samples during exposure to lipase medium at 25 ºC. For the sake of completeness data corresponding to (LA-*r*-TMC 20)-*g*-PEG sample during exposure to the PBS control solution at 25 ºC are also plotted.

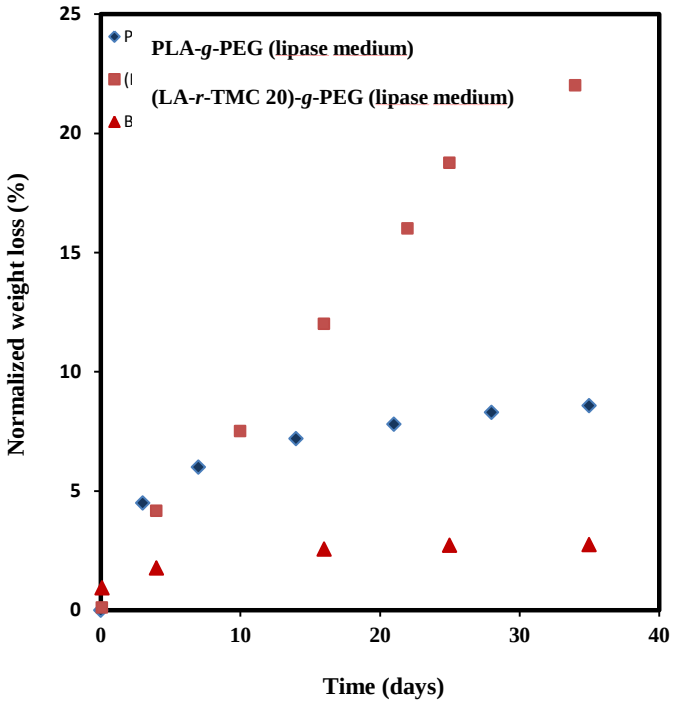




SEM micrographs taken after and before immersion to the medium showed a change in the surface texture as a consequence of degradation (Figure 13). Thus, abundant formation of deep cracks (*e.g.*, Figure 13b) was detected, in contrast with the smooth surface of the molten films and even with the practically unaltered surface of samples exposed to non-enzymatic PBS hydrolytic medium for a similar period (Figure 13a). High magnification images (inset of Figure 13b) also revealed that enzymatic degradation eroded the samples, with some retention of degradation products, which appeared as small granules.

**Figure 13.** Scanning electron micrographs of (LA-*r*-TMC 20)-*g*-PEG exposed to PBS (a) and lipase (b) media at 25 ºC for 34 days, respectively. Inset shows a magnification of the enzymatically degraded sample.

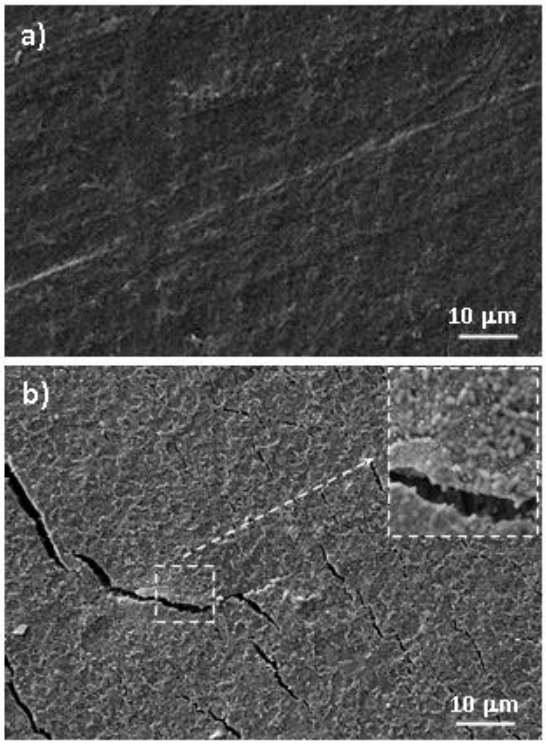




For the sake of completeness, Figure 12 also shows the degradation profile for the PLA-*g*-PEG sample. In this case, enzymatic attack progressed at a clearly slower rate because the sample was more hydrophobic (contact angle of 79º as opposed to 60º) due to the lower degree of pegylation attained (Table 2). It must also be taken into account that enhanced degradation should be expected for (LA-*r*-TMC 20)-*g*-PEG due to the chain randomness and higher amorphous content of the processed sample.

### 5. Cell adhesion and proliferation on polyethylene glycol grafted copolymers

Figures 14a and 14b compare cell viability on PLA, LA-r-TMC 20 and (LA-*r*-TMC 20)-*g*-PEG films after 24 h and 7 days of exposure. Results point out significantly higher viability ($p<0.05$) on the copolymer samples compared to PLA for cell adhesion assays performed with both fibroblast-like and epithelial-like cell lines. Specifically, relative viability increases close to 30% and 20% were determined, the higher value corresponding to the PEG grafted sample. Nevertheless, differences between the two copolymer samples were not statistically significant ($p>0.05$) (Figure 14a). On the other hand, cell proliferation assays revealed significantly higher cell growth on the grafted copolymer than on the other two samples. The increment in relative viability reached a value between 20 and 30% depending on the cell line (Figure 14b). Viability was very similar for PLA and non-grafted copolymer sample (p › 0.005).

These results demonstrated that PEG grafting is an interesting structural modification since surface properties are maintained, allowing high cell adhesion. Furthermore, the pegylated material has a prolonged activity, as shown by the improved rate of cell growth.



Observation of cultures by SEM microscopy revealed morphological characteristics associated with cell adhesion and proliferation onto the film surfaces (Figures 15 and 16). At the observation period, no noticeable differences in the morphology of fibroblast-like and epithelial-like cells (*i.e.*, Cos-7 and VERO cells) cultured on LA-*r*-TMC 20 and (LA-*r*-TMC 20)-*g*-PEG films were detected. Cells attached and spread out on the film surfaces (Figures 15a and 15b) after a 24 h seeding period. Also, they exhibited large areas of cytoplasm extending on the film surface and favoring cell adhesion onto the material. High magnification micrographs showed that these cells were anchored on film surfaces via cytoplasmic projections such as typical filopodia (Figures 15c and 15d). Cells proliferated and reached confluence after 7 days of culture. The material was colonized; specifically cells formed a monolayer with close contact between them. Cell growth occurred in stratified form, mimicking the organization of tissues, as could be clearly observed (Figures 15e and 15f).

**Figure 14.** Adhesion (a) and proliferation (b) of fibroblast-like cells (Cos-7) and epithelial-like cells (VERO) on PLA, LA-*r*-TMC 20 and (LA-*r*-TMC 20)-*g*-PEG surfaces. Viability for adhesion and proliferation assays was evaluated after 24 h and 7 days of culture, respectively. Measurements of the control (*i.e.*, without films) are set to 100% for each time point. Data ($n$=4) were expressed in percentages compared against the control. (*) indicates significant difference ($p<0.05$, ANOVA follows Tukey's test) compared to PLA.

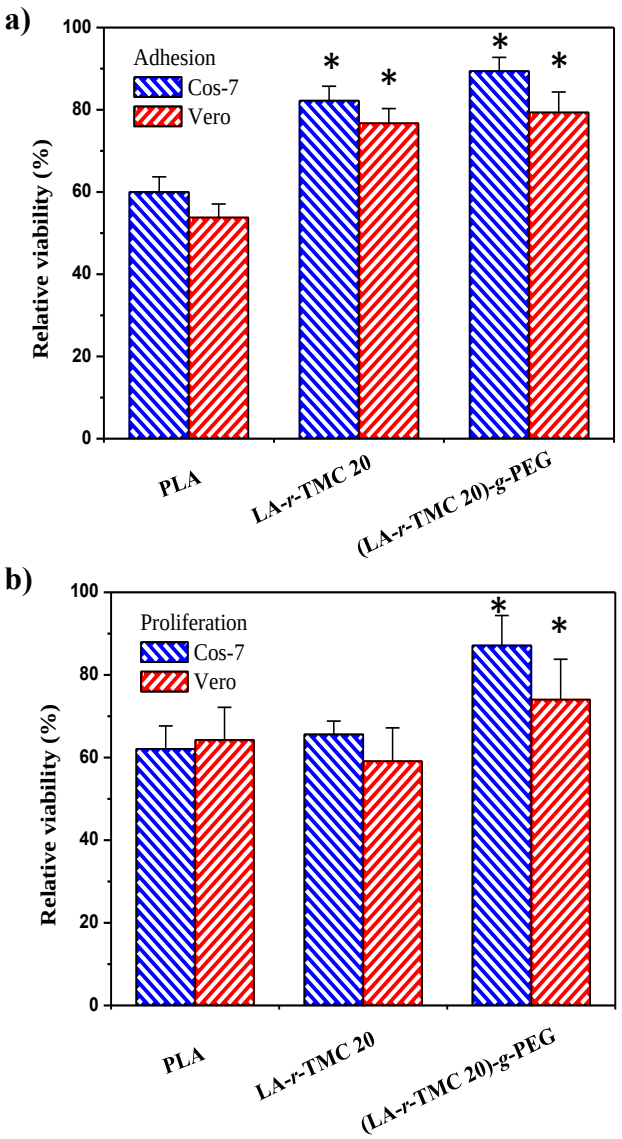

**Figure 15.** SEM micrographs of fibroblast-like (Cos-7) cells on the surface of LA-*r*-TMC 20 (a, c, e) and (LA-*r*-TMC 20)-*g*-PEG (b, d, f) films after 24 h (a-d) and 7 days (e, f) of culture. Low (a, b) and high (c, d) magnification images show cell attachment and spreading onto the material surface (*) and the presence of filopodia (arrows) that extend over the surface. Complete spreading can be observed after 7 days of exposure (e, f). Cell growth occurred in stratified form, mimicking the organization of a tissue.

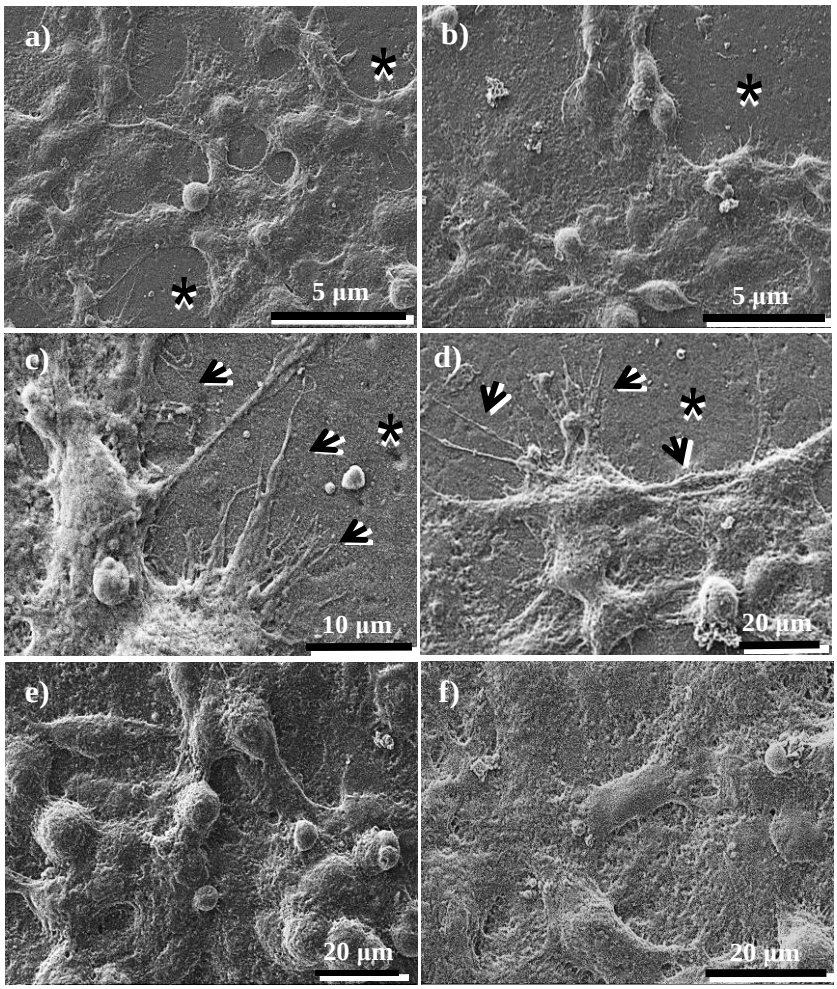




Figure 16 shows representative micrographs of adhesion and proliferation of VERO cells onto the two polymer films (*i.e.*, LA-r-TMC 20 and (LA-r-TMC 20)-g-PEG samples). These images demonstrated the formation of cell monolayers and also the development of small filopodia that

form junctions between cells. It is interesting to note that after 7 days of culture the cell number clearly increased aswell as the cell–cell interactions in the monolayer.

**Figure 16.** SEM micrographs of epithelial-like Vero cells onto the surface of LA-*r*-TMC20 (a, c, e) and (LA-*r*-TMC20)-*g*-PEG (b,d,f) films after 24 h (a-b) and 7 days (c-f) of culture. Low (a-d) and high (e, f) magnification images show the cell monolayer onto the material surface (*) and the presence of very much small filopodia around of the cell to formed intimal junctions (arrows). The increase in the cell number after 7 days of culture shows smaller cells and more cell-cell interactions in the monolayer.

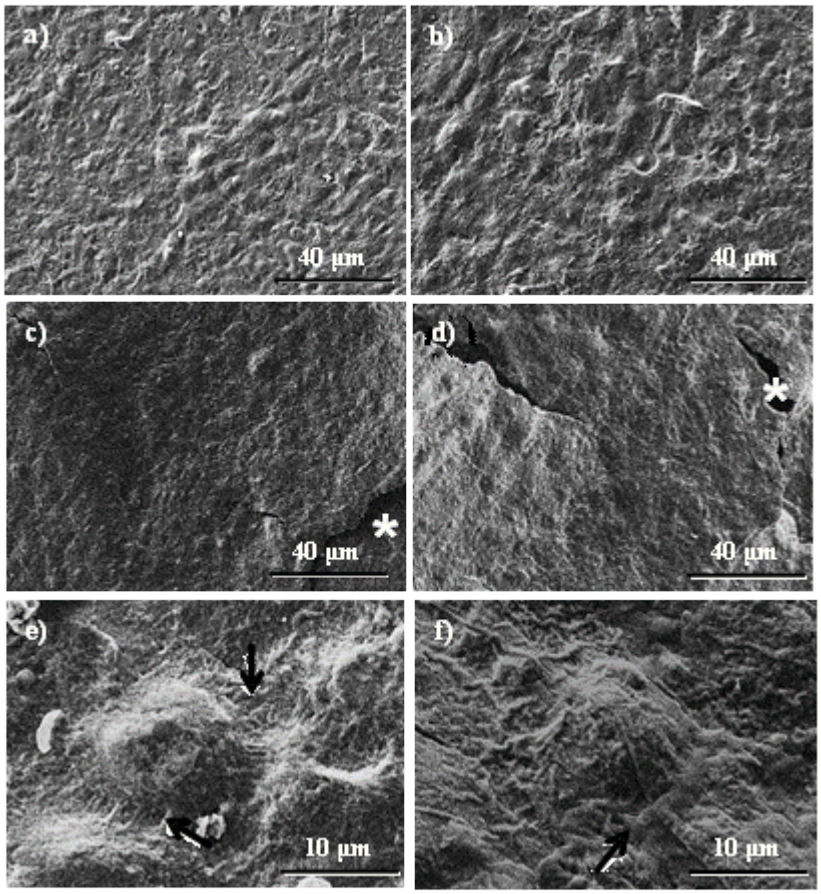

## 6. Nanospheres of polyethylene glycol grafted copolymers and release behavior of triclosan loaded samples

Triclosan loaded microparticles of (LA-*r*-TMC 20)-*g*-PEG grafted copolymer were obtained with an 83% yield (*i.e.*, weight of microparticles / (weight of triclosan + weight of polymer)) by the oil-in-water emulsion method. Microparticles were spherical and rather homogeneous in size (Figure 17a), with the predominant diameter being close to 35 µm and its range of variation between 16 and 45 µm. Microspheres showed a relatively smooth texture and many small pores on their surface. Drug loading and encapsulation efficiency were close to 2.3% and 48%, respectively.

The release of triclosan from microspheres is shown in Figure 17b for the hydrophilic PBS medium and the ethanol/PBS mixture. Clear differences can be observed since the rate of diffusion-controlled drug release depends on three main factors: a) Solubility of the drug in the release medium, b) ability of the medium to penetrate the polymer matrix, and c) physical interactions between polymer and drug.[40]



Triclosan was entrapped in the microspheres when the aqueous PBS medium was employed because a maximum release of 35% was attained. The concentration of released triclosan was lower than the corresponding solubility limit (10-17 mg/mL), suggesting that good interactions could be established between the drug and the hydrophobic polymer matrix. In fact, the establishment of an equilibrium defined by a partition coefficient has been reported for triclosan release into aqueous buffers.[41]

The release profile changed drastically when ethanol was added to the medium; in particular, practically complete release (98%) was observed for the 3:7 (*v*/*v*) mixture after 1200 min of exposure. The profile was characterized by a fast release at the beginning of exposure (*e.g.*, 80% was determined after only 300 min), which could be associated with the drug entrapped near the surface of microparticles. Complete release seems in agreement with a decrease in the hydrophilicity of the medium and also with a swelling of the polymer matrix caused by the incorporation of ethanol in the medium.

**Figure 17.** (a) SEM micrographs of triclosan loaded (LA-*r*-TMC 20)-*g*-PEG microspheres. Inset corresponds to a magnification of the surface texture. (b) Triclosan release profiles of loaded (LA-*r*-TMC 20)-*g*-PEG microspheres in PBS/EtOH 3:7 *v*/*v* (■) and PBS (●).

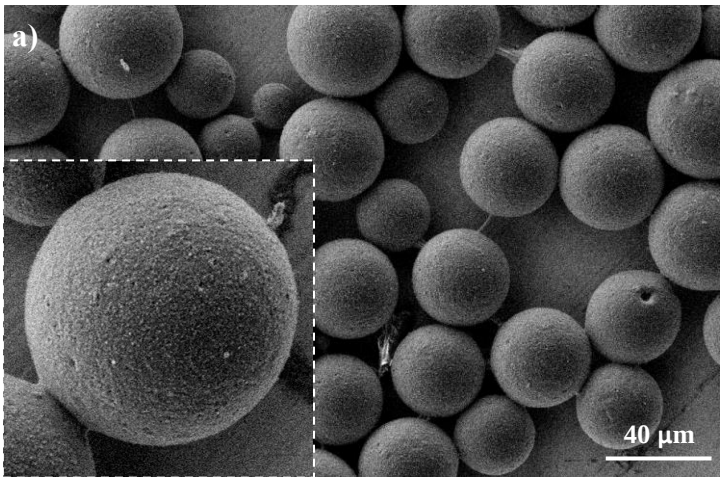


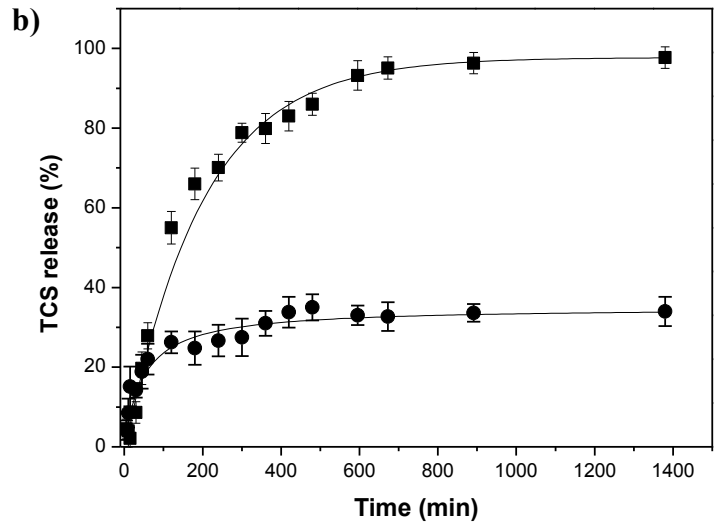

## IV. Conclusions

Copolymers of lactide and trimethylene carbonate could be effectively grafted with polyethylene glycol by a two-step synthesis that firstly involved functionalization with maleic anhydride and then condensation reaction with polyethylene glycol. A certain degree of hydrolysis of the anhydride was observed, and consequently a condensing agent like *N*,*N*´-diisopropylcarbodiimide was required to ensure complete pegylation of functional groups. Moderate degradation was detected but grafted copolymers could be obtained with a relatively good yield and a high PEG content (*e.g.*, 17 wt%). Thus, copolymers with a number average molecular weight of 19,900 g/mol were able to incorporate up to five PEG grafted chains with $M_n$ equal to 550 g/mol.

Incorporation of PEG led to a decrease in the melting enthalpy and greater complexity of the melting peak, which was only associated with polylactide. Nevertheless, samples were able to crystallize, rendering negative spherulites and thin lamellar crystals despite the presence of up to 17 mol-% of PEG and the randomness of the main chain caused by the incorporation of up to 20 mol-% of TMC units. Thermal stability and hydrophilicity of copolymers became enhanced by their grafting with PEG chains.



All copolymers were biocompatible because they supported adhesion and proliferation of both fibroblast-like and epithelial-like cells. However, results were more favorable for the grafted copolymers which, in addition, had higher enzymatic degradability. Grafted copolymers were appropriate to prepare microspheres by the oil-in-water emulsion method. These were obtained with a high yield and had good encapsulation efficiency for drugs like triclosan.

## V. References


1. Nampoothiri KM, Nair NR, John RP. Bioresour Technol 2010;101:8493.
2. Auras R, Harte B, Selke S. Macromol Biosci 2003;4: 835.
3. Weber CJ, Haugaard V, Festersen R, Bertelsen G. Food Addit Conta 2002;19:172.
4. Shuko S, Suzuki, Ikada Y. "Poly(Lactic Acid): Synthesis, Structures, Properties, Processing, and Applications, Medical applications. John Wiley & Sons, Inc; 2010. Chapter 27, p. 443.
5. Gilding DK, Williams DF, Editor. In Biocompatibility of Clinic Implant Materials. CRC Press: Boca Raton, FL; 1982. p. 9.
6. Conn J, Oyasu R, Welsh M, Beal JM. Am J Surg 1974;128:19.
7. Schmitt EE, Polistina RA, American Cynamid Co. Surgical Sutures, United States patent 3 297 033. 1967.
8. Burger C, Kabir K, Rangger C, Mueller M, Minor T, Tolba RH. Arch Orthop Trauma Surg 2006;126:695.
9. Dhandayuthapani B, Yoshida Y, Maekawa T, Kumar DS. Int J Polym Sci 2011, Article ID 290602. doi:10.1155/2011/290602
10. Heller J. CRC Crit Rev Ther Drug Carrier Syst 1985;1:39
11. Oh JK. Soft Matter 2011;7:5096.
12. Carlson D, Nie L, Narayan R, Dubois P. J Appl Polym Sci 1999;72:477.
13. Jacobsen S, Fritz HG. Polym Eng Sci 1999;39:1303.
14. Hu Y, Hu YS, Topolkaraev V, Hiltner A, Baer E. Polymer 2003;44:5681.
15. Hu Y, Rogunova M, Topolkaraev V, Hiltner A, Baer E. Polymer 2003;44:5701.
16. Hassouna F, Raquez JM, Addiego F, Dubois P, Toniazzo V, Ruch D. Eur Polym J 2011;47: 2134.
17. Pego AP, Vleggeert-Lankamp CLAM, Deenen M, Lakke EAJF, Grijpma DW, Poot AA, Marani E, Feijen J. J Biomed Mater Res A 2003;67A:876.
18. Katz AR, Mukherjee DP, Kaganov AL, Gordon S. Surg Gynecol Obstet 1985;161:213.
19. Oberhoffner S, Planck H. Surgical suture material from triblockterpolymer, its use in surgery and process for its preparation. EP 0835895. 1997.
20. Pego AP, Siebum B, Van Luyn MJA, Van Seijen XJGY, Poot AA, Grijpma DW, Feijen J. Tissue Eng 2003;9:981.
21. Franco L, Bedorin S, Puiggalí J. J Appl Polym Sci 2007;104:3539.

22. Guerin W, Helou M, Carpentier JF, Slawinski M, Brusson JM, Guillaume SM. Polym Chem 2013;4:1095.
23. Zurita R, Puiggalí J, Franco L, Rodríguez-Galán A. J Polym Sci A Polym Chem 2006;44:44.
24. Díaz-Celorio E, Franco L, Rodríguez-Galán A, Puiggalí J. Eur Polym J 2012;48:60.
25. Pan J, Wang Y, Qin S, Zhang B, Luo Y. J Biomed Mater Res B Appl Biomater 2005;74:476.
26. Gomez d'Ayala G, di Pace E, Laurienzo P, Pantalena D, Somma E, Nobile MR. Eur Polym J 2009;45: 3217.
27. Mangiacapra P, Raimondo M, Tammaro L. Vittoria V. Biomacromolecules 2007:8:773.
28. Llorens E, Del Valle LJ, Díaz A, Casas MT, Puiggalí J. Macromol Res 2013;21:775.
29. Gomez G, d'Ayala, Di Pace E, Laurienzo P, Pantalena D, Somma E, Nobile M. Eur Polym J 2009;45:3217.
30. De Santis P, Kovacs AJ. Biopolymers 1968;6:299.
31. Hoogsteen W, Postema AR, Pennings AJ, Ten Brinke G, Zugenmaier P. Macromolecules 1990;23:634.
32. Miyata T, Masuko T. Polymer 1997;38:4003.
33. Kobayashi J, Asahi T, Ichiki M, Okikawa A, Suzuki H, Watanabe T, Fukada E, Shikinami Y. J Appl Phys 1995;77:2957.
34. Takahashi Y, Tadokoro H. Macromolecules1973;6:672.
35. Ye HM, Xu J, Freudenthal J, Kahr B. J Am Chem Soc 2011;133:13848.
36. Xu J, Guo BH, Zhou JJ, Li L, Wu J, Kowalczuk M. Polymer 2005;46:9176.
37. Ying J, Wei W, Zhaohui S. Appl Spectrosc 2011;65:454.
38. Casas MT, Puiggalí J, Raquez JM, Dubois P, Córdova ME, Müller AJ. Polymer 2011;52: 5166.
39. Márquez Y, Franco L, Puiggalí J, Thermochim Acta 2012;550:65.
40. Liu H, Leonas K, Zhao Y. J Eng Fibers Fabr 2010;5:10.
41. Zurita R, Puiggalí J, Rodríguez-Galán A. Macromol Biosci 2006;6:58.

# Chapter 5.3

## *Study on the crystallization of multiarm stars with a poly(ethyleneimine) core and poly(ε-caprolactone) arms of different length.*

Crystallization of multiarm star systems constituted by a core of poly(ethyleneimine) (PEI) and arms of poly(ε-caprolactone) (PCL) was studied by electron microscopy, calorimetry and optical microscopy techniques. Three systems differing on the degree of polymerization of PCL were studied as well as binary mixtures constituted by systems differing on the length of PCL arms. Samples were able to crystallize from both diluted solutions and the melt state giving rise to well-formed lamellae and spherulites, respectively. Lamellae of samples with large PCL arms were highly regular and corresponded to elongated hexagonal crystals with an aspect ratio that decreased with the length of PCL arms.

A significant decrease on equilibrium melting temperatures, degree of crystallinity and glass transition temperature was detected for samples having short PCL arms. Crystallization kinetics was also highly influenced by the length of PCL arms, being both primary nucleation density and secondary nucleation constant increased as the length of PCL arms decreased. Crystallization of star mixtures having different PCL lengths was determined by the larger arms since they initiated the process and subsequently shorter arms were progressively incorporated. A thermal nucleation was characteristic of multiarm star mixtures due to the different crystallization temperature ranges of samples with large and short PCL arms, whereas samples with a homogeneous arm length rendered an athermal nucleation.

## I. Introduction

The use of polymers having dendritic structures like hyperbranched or star-like topologies may lead to a significant improvement of mechanical properties of polymer matrices without affecting their thermomechanical behavior.[1-4] These structures prevent also chain entanglement and consequently low viscosity formulations can be derived.[5] Star modifiers provide advantageous technological applications in different fields as for example the development of epoxy coatings. Interesting properties like low shrinkage can also be achieved by the use of hyperbranched structures.[6,7] In addition, the use of arms with labile groups (*e.g.,* the ester linkages of poly(ε-caprolactone)) may provide the capability to get thermally reworkable materials.[1,8]

Multiarm stars can be synthesized following the ‘‘core-first’’ approach that consist on a living polymerization of a monomer from a multifunctional core.[9-11] Systems based on commercial poly(ethyleneimine) (PEI) (Lupasol$^{TM}$) having poly(ε-caprolactone) (PCL) arms of different lengths (Figure 1a) can be easily prepared at a low cost. Previous studies demonstrated that arms with a degree of polymerization of only 10 could effectively reduce the formulation viscosity and maintain a final $T_g$ of the derived material higher than measured in matrices modified with the corresponding linear polyester.[12,13]



Control of the arm length is in general interesting to improve solubility of the multiarm modifier in the corresponding polymer matrix. This feature has for example a crucial influence in thermal curing processes which became decelerated when more soluble systems having short arms were employed.[14] In addition, chain flexibility and hydrophobic character of PCL arms provided a good miscibility in most epoxy resins[15,16] and an improvement of toughness through crazing and shear yielding mechanisms to absorb energy locally.[17]

The attachment of regular linear units to a fully amorphous dendritic core may enable a crystallization process that rendered semicrystalline materials. Nevertheless, a minimum length of the arms seems to be required since units close to the amorphous core may be unable to crystallize and even the presence of the core could make chain fold less tight.[18]

Star polymers having PCL arms showed a lower degree of crystallinity than linear PCL as a logical consequence of the steric restrictions imposed by dendritic or hyperbranched cores.[18] It was also found that the typical lamellar rearrangement of PCL was less pronounced in star polymers respect to the linear ones since amorphous cores constituted an obstacle to the molecular reordering and the lamellar thicknening process. Interestingly, equilibrium melting temperature was higher in star polymers due the reduccion of entropy and positional freedom of the melt caused by the presence of the hyperbranched cores.[18]

Morphology of single crystals of multiarm polymers has been scarcely studied but in general lamellar structures were reported for systems based on nylon 6[19] and PCL[20] arms. However, these crystals were more irregular than those obtained from the linear analogues. Specifically, crystals of star-branched PCL derivatives were characterized by the presence of many irregular steps on the lateral crystal growth faces, which were related to the high fold surface free energy and the constrained character of the star-branched polymers.[20] In the case of PCL derivatives it was also detected that the crystal aspect ratio decreased when the length of the arms was increased. This ratio was also significantly greater for linear polymers with respect to star-branched and increased with crystallization temperature as it was well established for polyethylene.[21] The capability to render well-defined lamellar structures has been interpreted as a exclusion of the central cores from the crystalline regions. These cores should be located at the lamellar surface and the bounded arms should be integrated in the derived lamellae (Figure 1b).



Another relevant point that has recently been evaluated concerns the influence of the number of arms of a multistar polymer on the crystal morphology. Thus, sugar alcohols like glycerol, erythritol and xylitol have been employed as initiators of the ring opening polymerization of ε-caprolactone to get multistar polymer with three, four and five arms of similar lenght, respectively.[22] A decrease of both melting enthalpy and crystallization rate was observed as the number of PCL arms was increased. It was interpreted as a consequence of the limiting effect of the central core on the chain mobility.

In this work we want to insist on the influence of the arm length on factors that determine the crystallization process like crystal morphology, primary nucleation density, crystal growth and

secondary nucleation constant. Specifically, the system derived from commercial Lupasol and ε-caprolactone (PEI-PCL) has been considered. Furthermore, coexistence of multiarm systems having different PCL arm lengths could be usual and therefore it becomes important to evaluate the implications of heterogeneous multiarm systems on thermal properties and the crystallization process.

**Figure 1.** (a) Chemical structure of multiarm star PEI-PCL *x* copolymers. (b) Model of lamellar crystals grown from multiarm star PEI-PCL copolymers.

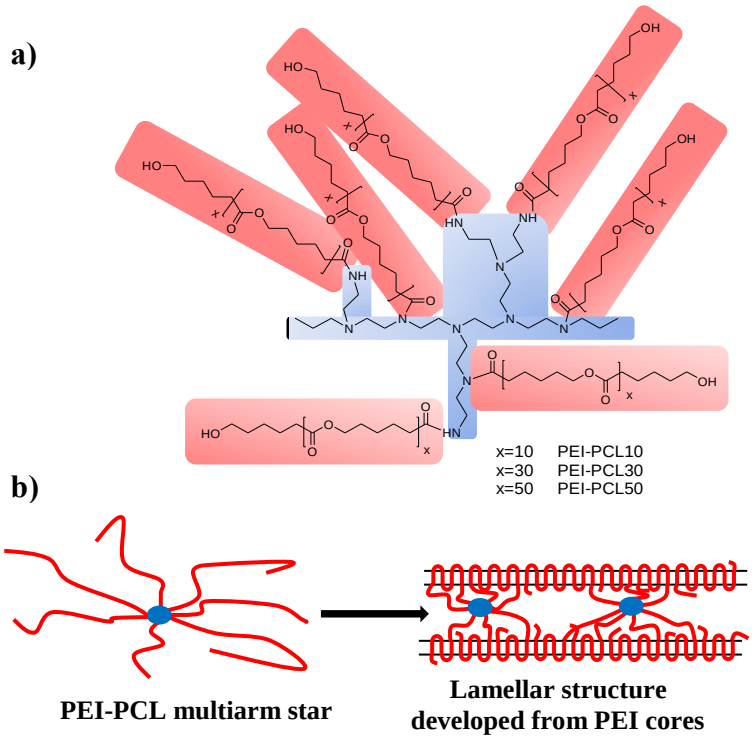




## II. Experimental Section

### 1. Materials

Poly(ethyleneimine) (PEI) Lupasol® FG (800 g/mol) was purchased from BASF and used without further purification. The ($NH_2$/NH/N) relationship of this polymer was reported to be

1/0.82/0.53, which corresponds to an equivalent number of primary, secondary and tertiary amines of 0.010, $8.37 \times 10^{-3}$, and $5.3 \times 10^{-3}$ eq/g. ε-Caprolactone (Sigma-Aldrich) was distilled under vacuum, whereas tin (II) 2-ethylhexanoate (Sigma-Aldrich, 98%) was used without further purification.

Multiarm star PEI-PCL copolymers were synthesized as previously described.[23] Basically, PEI and the appropriate amount of ε-caprolactone were placed at room temperature in a two-necked flask equipped with a magnetic stirrer and a gas inlet to fill the flask with argon. After addition of a small amount of tin (II) 2-ethylhexanoate (*i.e.,* 0.3 mmol respect to 0.625 mmol of PEI), the flask was immersed in an oil bath thermostatized at 130 ºC during 48 h. The crude product was subsequently dissolved in chloroform and the polymer was isolated by precipitation in methanol. Finally, the sample was recovered by filtration and dried at 45 ºC under vacuum for two days.

Degree of polymerization of PCL arms was controlled by means of the feed ratio between ε-caprolactone monomer and the number of active NH groups. Specifically, ratios of 10, 30 and 50 were selected to get polymers with rather different arm lengths. These samples will be named with the acronym PEI-PCL *x*, where *x* accounts for the degree of polymerization. Number average molecular weights were 20,000, 42,400 and 85,500 g/mol as determined by $^{1}$H-NMR spectroscopy[23] for PEI-PCL 10, PEI-PCL 30 and PEI-PCL 50 samples, respectively. Spectroscopic data also revealed that experimental degrees of polymerization of PCL arms were 12, 26 and 53 (*i.e.,* very close to those expected from the selected feed ratios).



Mixtures of star samples having two different arm lengths were obtained by slow evaporation of a chloroform solution containing equal weights of both selected multiarm polymers. Mixtures will be named with the acronym PEI-PCL *x*/*y* where *x* and *y* indicate the caprolactone degrees of polymerization of the involved multiarm stars.

## 2. Measurements

The spherulite growth rate was determined by optical microscopy using a Zeiss Axioskop 40 Pol light polarizing microscope equipped with a Linkam temperature control system

configured by a THMS 600 heating and freezing stage connected to a LNP 94 liquid nitrogen cooling system. Spherulites were grown from homogeneous thin films prepared from the melt. Next, small sections of these films were pressed or smeared between two cover slides and inserted into the hot stage, giving rise to samples with thicknesses close to 10 μm in all cases. Samples were kept at approximately 20 ºC above the polymer melting point for 5 minutes to eliminate sample history effects (when mixtures were studied the final temperature was determined from the component with the greatest melting temperature). For isothermal crystallization experiments, samples were quickly cooled to the selected crystallization temperature. The radius of growing spherulites was monitored during crystallization with micrographs taken with a Zeiss AxiosCam MRC5 digital camera at appropriate time intervals. A first-order red tint plate was employed to determine the sign of spherulite birefringence under crossed polarizers.

A Philips TECNAI 10 electron microscope was used and operated at 80 kV and 100 kV for bright field and electron diffraction modes, respectively. Selected area electron diffraction patterns were taken with a SIS MegaView II digital camera and internally calibrated with gold ($d_{111}$ = 0.235 nm).



Calorimetric data were obtained by differential scanning calorimetry with a TA Instruments Q100 series equipped with a refrigerated cooling system (RCS) operating at temperatures from -90 ºC to 550 ºC. Experiments were conducted under a flow of dry nitrogen with a sample weight of approximately 5 mg and calibration was performed with indium. $T_{zero}$ technology required a calibration based on two experiments: the first was performed without samples while sapphire disks were used in the second. Thermal characterization was performed following a four run protocol consisting on a heating run (20 ºC/min) of the multiarm polymer, a cooling run (10 ºC/min) after keeping the sample in the melt state for three minutes to wipe out the thermal history, a subsequent heating run (20 ºC/min) of the sample crystallized from the melt and finally a heating run (20ºC/min) of a sample quenched from the melt by immersion in liquid nitrogen. Isothermal crystallization studies were performed with samples previously heated (20 ºC/min) up to 25 ºC above their melting temperature (in the case of mixtures this was determined

by the component with the highest melting point), subsequently held for 5 min at this temperature and finally cooled to the selected temperature at a rate of 50 ºC/min. Samples were kept at the isothermal temperature until baseline was attained.

## III. Results and Discussion

### 1. Thermal properties of PEI-PLC x multiarm stars

DSC scans performed with samples having the shortest and the largest PCL arms are given in Figure 2 as representative examples, whereas properties determined for the three PEI-PCL *x* samples are summarized in Table 1. The most distinctive behaviour respect to linear PCL was logically found for PEI-PCL 10. Thus, a double melting peak near 43 and 49 ºC was determined for the multiarm star (quenched sample) in contrast with the single peak reported for PCL within the 59-64 ºC range. The appearance of the double peak changed with the crystallization process and specifically the relative intensity of the lower temperature peak increased in the order solution crystallized > melt crystallized > quenched sample as expected from a typical lamellar thickening process (i.e., 48-49 ºC is associated to lamellae that are reordered/thickened during the heating process). Melting enthalpies indicated a degree of crystallinity of 56.7% for the PEI-PCL 10 melt crystallized sample that was significantly lower than the value determined for PEI-PCL 50 (i.e., 67.1%). Crystallinities were estimated taking into account the enthalpy of 135 J/g that was reported for a 100% PCL crystalline sample[24,25] and also the contribution of the PEI core to the total weight of the sample (i.e., 4% and 1% for PEI-PCL 10 and PEI-PCL 50, respectively). Crystallinities of the stars were nevertheless similar to the value close to 60% that was reported for PCL.[26] Glass transition temperatures were between -62 and -57 ºC, decreasing as the PCL arms became shorter and in any case comparable with the typical value given for linear PCL (-60 ºC).

**Table 1.** Main thermal properties determined by DSC for PEI-PCL *x* samples.

| Sample | 1st Heating scan | | Cooling scan | | 2nd Heating scan | | | 3rd Heating scan | |
|---|---|---|---|---|---|---|---|---|---|
| | $T_f$ (ºC) | $\Delta H_f$ (J/g) | $T_c$ (ºC) | $\Delta H_c$ (J/g) | $T_f$ (ºC) | $\Delta H_f$ (J/g) | $T_g$ (ºC) | $T_f$ (ºC) | $\Delta H_f$ (J/g) |
| PEI-PCL 10 | **44.8**, 48.3 | 74.5 | 19.5 | 76.9 | **44.7**, 48.2 | 76.6 | -62.0 | **43.1**, 48.6 | 75.2 |
| PEI-PCL 30 | **62.7**, 63.9 | 125.7 | 32.2 | 93.8 | 53.7 | 97.7 | -57.0 | 53.2 | 97.3 |
| PEI-PCL 50 | **62.4** | 117.1 | 32.7 | 89.7 | 54.6 | 90.5 | -57.0 | **54.1**, 55.5 | 90.5 |

[a]When multiple melting peaks are observed the most intense one is indicated in bold numbers.

**Figure 2.** DSC traces obtained with PEI-PCL 10 (a) and PEI-PCL 50 (b) samples, corresponding from down to up to the heating run (20 ºC/min) of the as-synthesized sample, the cooling run (10 ºC/min) after keeping the sample in the melt state for three minutes, the subsequent heating run (20 ºC/min) of the non-isothermally crystallized sample (c) and the heating run (20 ºC/min) of a sample previously cooled from the melt state at the maximum rate allowed by the equipment. Insets show the glass transition temperatures detected in the third heating run.

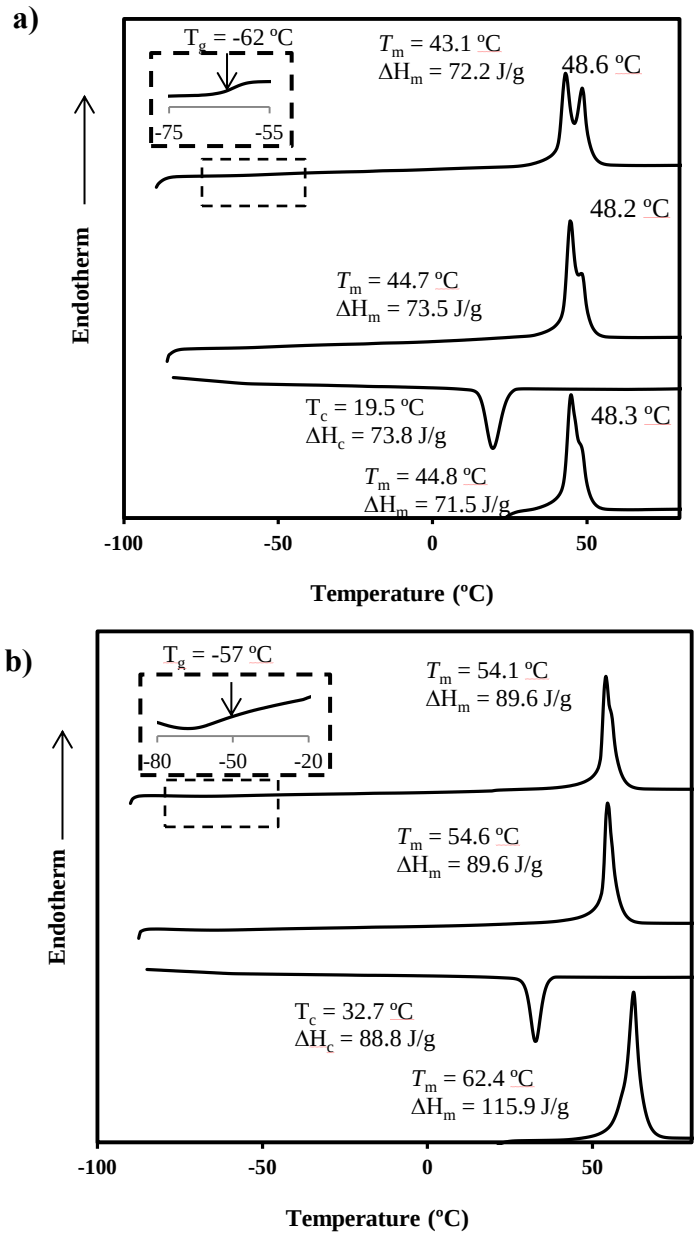

## 2. Equilibrium melting temperature of PEI-PLC *x* multiarm stars

Equilibrium melting temperature ($T_m^0$) is a crucial parameter for determining crystal growth rate and specifically degree of supercooling ($T_m^0 - T_c$). The Hoffman-Weeks extrapolation[27] is a commonly accepted method to estimate the equilibrium temperature due to its simplicity and straightforward implementation, although it is subject to criticism[28] and improvements have been proposed.[29] The method is based on equation 1, which was deduced from a combination of the well-known Gibbs-Thomson equation and secondary nucleation theory.[30] This equation relates the melting temperature, $T_m$, of a crystal formed at a temperature $T_c$ , the equilibrium melting temperature and the thickening coefficient, $\gamma$, defined as the ratio between the thickness of the grown crystal, $l_c$, and the initial thickness of a "virgin lamella", $l_g^*$:

$$T_m = T_m^0 (1 - 1/\gamma) + T_c / \gamma \quad (1)$$

A straight line is obtained by plotting $T_m$ as a function of $T_c$, with the equilibrium temperature corresponding to the intersection of this line with the $T_m = T_c$ line. The validity of equation 1 implies that lamellar crystals thicken at a specific crystallization temperature which also influences the thickening parameter.



Figure 3 shows as a single melting peak was detected for the three types of multiarm stars, even for the PEI-PCL 10 sample, and that it increased as the crystallization temperature did. An unambiguous estimation of an equilibrium melting temperatures could therefore be deduced from the Hoffman-Weeks plots (Figure 4). Equilibrium melting temperatures increased with the length of the PCL arms, being determined values of 58.4, 73.1 and 74.7 ºC. These values were larger than those determined for linear PCL samples having similar molecular weights (*i.e.*, 45, 57, 64 and 67 ºC were estimated for samples having molecular weights of 578, 1,750, 6,590 and 15,700 g/mol, respectively[31]) as expected from the above indicated decrease of the melt entropy for hyperbranched cores[15].

It is also worth pointing out that the slope of the plots, $1/\gamma$, can be regarded as a measure of the stability of crystals undergoing the melting process and that significant differences are found. Thus, short PCL arms clearly decreased the slope, suggesting a greater difference between $l_c$ and $l_g^*$.

**Figure 3.** DSC heating scans (20 ºC/min) of PEI-PCL 10 (a), PEI-PCL 30 (b) and PEI-PCL 50 (c) samples isothermally crystallized at the indicated temperatures.

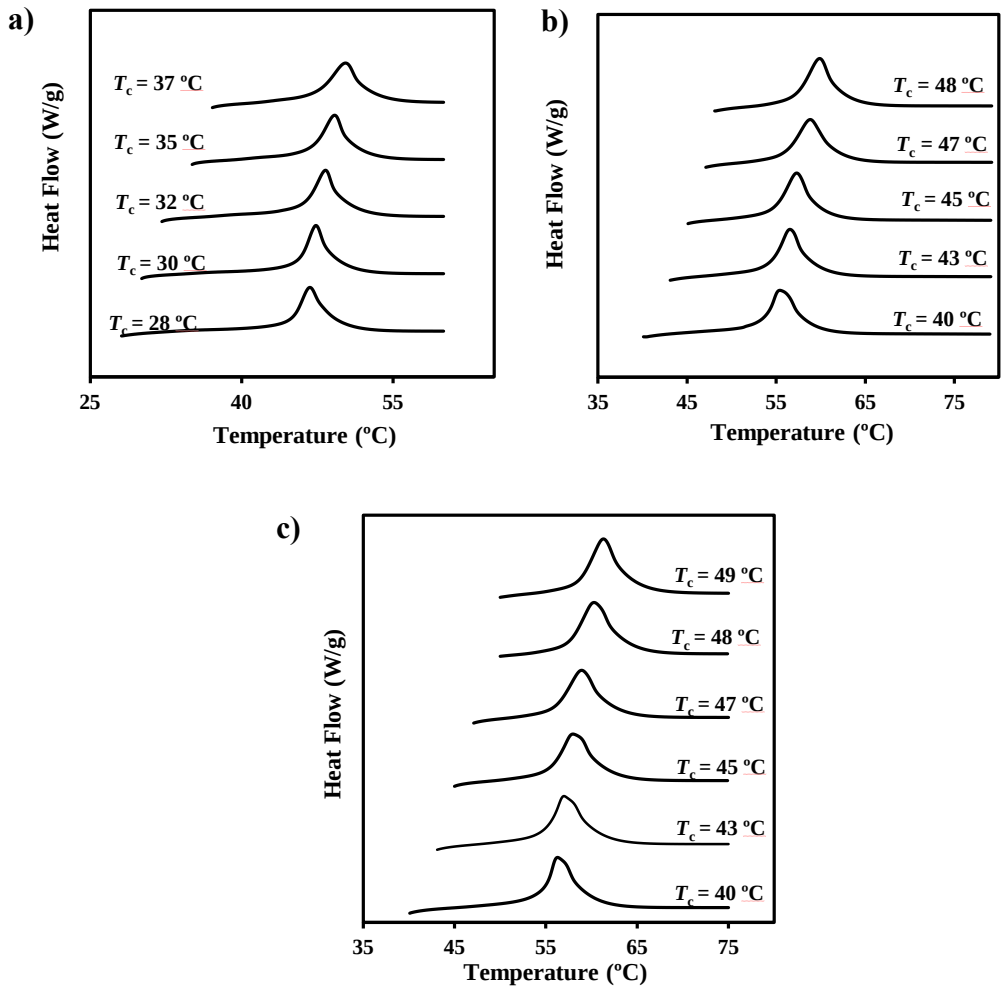




### 3. Lamellar and spherulitic morphologies of PEI-PCL x multiarm stars

Typical poly(ε-caprolactone) lamellar crystals were obtained from PEI-PCL 30 and PEI-PCL 50 multiarm star samples (Figures 5b and 5c) by isothermal crystallization at 40-60 ºC from dilute solutions in *n*-hexanol. In general, multilayered crystals were developed from helicoidal dislocations, being the thickness of individual lamellae close to 10 nm as determined by

measuring their shadows in the electron micrographs. Morphology of crystals corresponded to truncated rhombic crystals with different aspect ratios depending on the sample and the crystallization temperature. Highly irregular crystals were obtained by contrast at the lower crystallization temperature (40 ºC) from the sample with the shortest PCL arms (i.e., PEI-PCL 10). These had a lanceolate appearance, irregular edges and frequent striations on their surface. In fact, multifacets seem to be developed on the curved faces as was also reported for other multiarm systems having in this case long PCL arms and a core consisting on a third-generation hyperbranched polyester with approximately 32 terminal hydroxyl groups (Boltorn, Perstorp AB, Sweden).[20] Surface striations is a common feature of linear PCL crystals that have received different explanations (*e.g.,* presence of microcrystals along the crystal growth direction[32] or non-planar structure of crystals[33]) but remains nowadays non completely understood. In any case, results clearly demonstrated the ability to crystallize of the star samples despite the relatively high bulk dimensions of the core and even the short length of crystallizable arms (*i.e.*, PEI-PCL 10).



**Figure 4.** Hoffman-Weeks plot of temperatures corresponding to endothermic melting peaks versus crystallization temperature for PEI-PCL 10, PEI-PCL 30 and PEI-PCL 50. Equilibrium melting temperatures are explicitly indicated at the intersection point with the $T_m = T_c$ line.

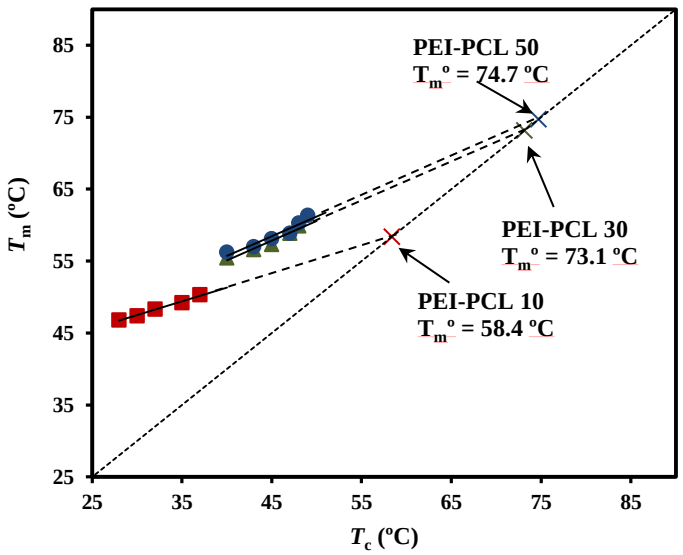

The electron diffraction patterns of PEI-PCL *x* lamellar crystals are practically identical, being mainly characterized by four strong spots at spacing of 0.414 nm and two strong spots at 0.374 nm (Figure 6). These are indexed as the (110), ($1\bar{1}0$) and (200) reflections of a rectangular unit cell with $a = 0.747$ nm, $b = 0.498$ nm. Patterns showed reflections up to 0.186 nm and systematic absences only for *h*00 and 0*k*0 reflections with *h* or *k* odd. These data are fully consistent with the reported structure of PCL that obeys to a $P2_12_12_1$ orthorhombic space group with cell dimensions of $a = 0.747$ nm, $b = 0.498$ nm and $c$ (fibre axis) = 1.705 nm. The crystalline structure of PCL was reported to be an arrangement of molecules with a practically all trans molecular conformation.[34-36]

Correlation between bright field micrographs and the electron diffraction patterns showed that the crystallographic *b* axis (or the reciprocal b* axis) was parallel to the truncated face or the elongation direction of PEI-PCL 10 crystals. Therefore, the well-formed and truncated rhombic crystals were constituted by four {110} faces and two {100} faces, being the angles between two consecutive {110} faces and between {110} and {100} faces of 112 º and 124 º. Namely, very close to the theoretical values (i.e., those deduced from unit cell dimensions) of 113º and 124º, respectively. It is well known that crystallization temperature influences the morphology of polyester single crystals, being characteristic an increase of the aspect ratio with crystallization temperature.[37-39] This feature is not observed when truncated PEI-PCL 30 and PEI-PCL 50 crystals are compared since the aspect ratio (i.e., determined by the ratio of the dimensions of {100} and {110} faces) decreased from 3.5 to 1.7 despite the crystallization temperature was higher for the second sample (60 ºC respect to 40 ºC). It seems that the aspect ratio decreased also when the size of PCL arms increased[20] as can also be inferred when morphologies of PEI-PCL 10 and PEI-PCL 30 crystals obtained at the same temperature are compared.

PEI-PCL samples easily crystallized from the melt rendering typical spherulitic morphologies with a negative birefringence as depicted in Figure 7. Main differences concern to nucleation, which as will further discussed, is lower for samples having larger arms and a lower ratio of PEI cores that could act as primary nucleating agents.

**Figure 5.** Transmission electron micrographs of PEI-PCLX 10 (a), PEI-PCLX 30 (b) and PEI-PCLX 50 (c) samples isothermally crystallized from *n*-hexanol at 40, 40 and 60 ºC, respectively. The arrows indicate the *b* crystallographic axis direction for the different crystals. The inset of (a) shows more clearly the lanceolate/lenticular morphology of PE-PCL 10 single crystals.

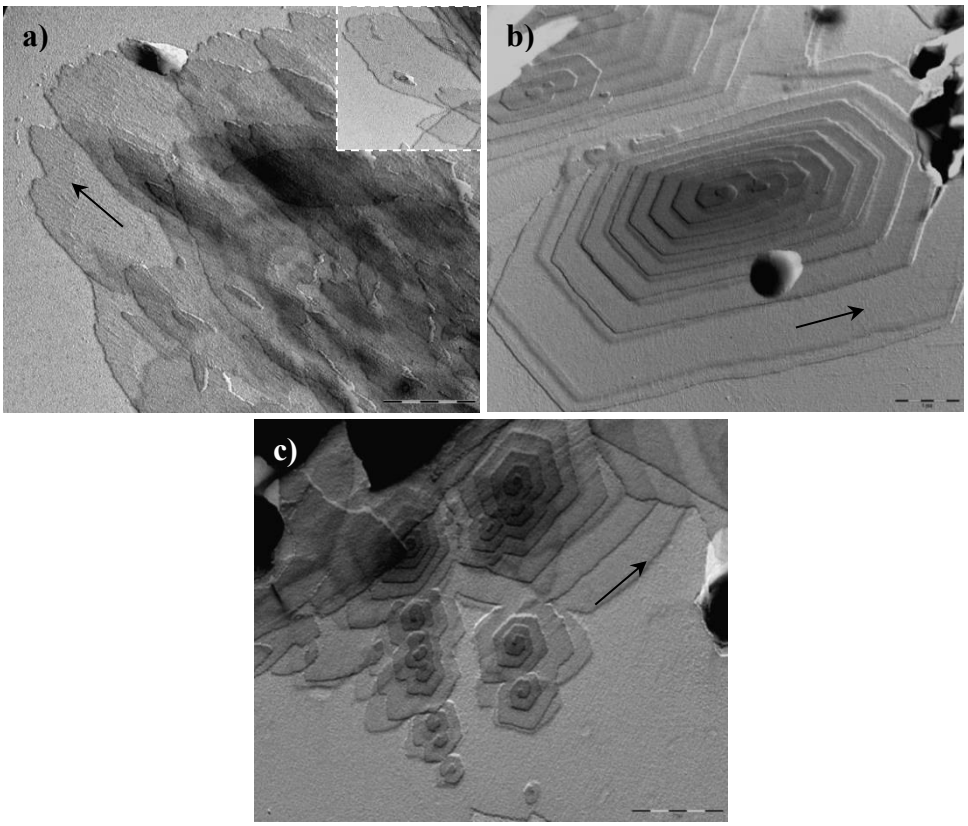




**Figure 6.** Electron diffraction pattern taken from PEI-PCL 10 (a), PEI-PCL 30 (b) and PEI-PCL 50 (c) lamellar crystals obtained as above indicated.

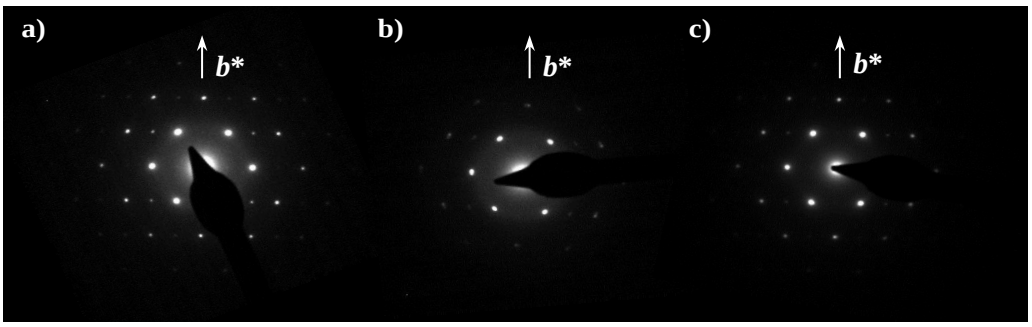

**Figure 7.** Polarized optical micrographs of PEI-PCL 10 (a), PEI-PCL 30 (b) and PEI-PCL 50 (c) isothermally crystallized at 40 ºC, 48 ºC and 49 ºC, respectively.

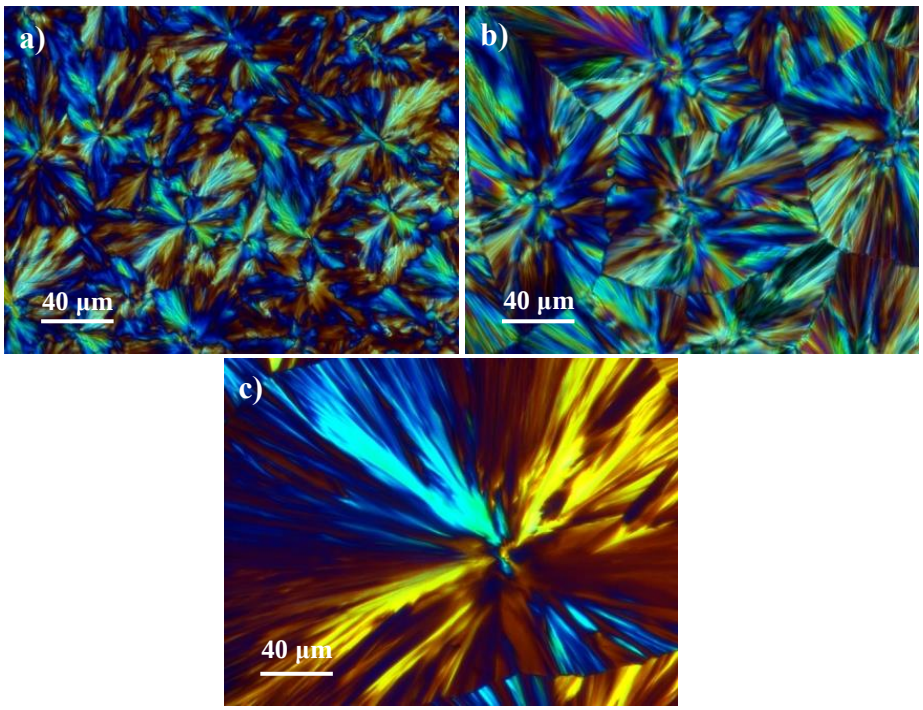




### 4. Isothermal crystallization analysis of PEI-PCL x multiarm stars

Kinetic analysis of multiarm polymers was only performed for melt crystallization processes because of the impossibility to obtain amorphous samples by cooling the melted polymer at the maximum rate allowed by the equipment.

Crystallization experiments were therefore carried out in narrow temperature intervals due to experimental limitations. These covered the range between 28 and 37 ºC for samples having the shortest PCL arms (*i.e.*, PEI-PCL 10) and the ranges between 40 and 48 or 49 ºC for PEI-PCL 30 or PEI-PCL 50 samples, respectively. The time evolution of the relative degree of crystallinity, $\chi(t)$, was determined from crystallization exotherms (*e.g.*, Figure 8a for PEI-PCL 10) through the ratio area of the exotherm up to time *t* divided by the total exotherm area:

$$\chi(t) = \int_{t0}^{t} (dH/dt)dt \; / \; \int_{t0}^{\infty} (dH/dt)dt \qquad (2)$$

where d*H*/d*t* is the heat flow rate and $t_0$ the induction time. The development of crystallinity always showed a characteristic sigmoidal dependence on time for the five melt crystallization experiments performed for the different samples (*e.g.*, Figure 8b for PEI-PCL 10). These data were analyzed assuming the well-known Avrami equation[41,42] for primary crystallization:

$$1 - \chi(t-t_0) = \exp[-Z\,(t-t_0)^n] \qquad (3)$$

where $Z$ is the temperature-dependent rate constant and $n$ the Avrami exponent whose value varies according to the crystallization mechanism. A normalized rate constant, $k = Z^{1/n}$, is usually evaluated for comparison purposes since its dimension (time$^{-1}$) is independent of the value of the Avrami exponent.

Table 2 summarizes the main kinetic parameters of the primary crystallization process, as deduced from the plots of log{-ln[1-$\chi$ $(t- t_0)$]} against log $(t - t_0)$ (Figure 8c). The values of the Avrami exponent for PEI-PCL 10 remained in a narrow range, from 2.19 to 2.47, 2.37 being the average value. This suggests the occurrence of predetermined (heterogeneous) nucleation with spherical growth under high geometric constraints since the theoretical value should be equal to 3. Both sporadic (heterogeneous) and homogeneous nucleation can be clearly discarded as a higher exponent, close to 4, should be derived. Furthermore, homogeneous nucleation usually requires high undercooling, which is not the case. It can be indicated that the Avrami exponents tended to decrease with decreasing the crystallization temperature, suggesting a higher geometrical constrain. Specifically, at a temperature of 28 ºC crystallization approaches to a two-dimensional growth. Samples with longer arms showed a similar behaviour, being the average Avrami exponents of 2.22 and 2.23 for PEI-PCL 30 or PEI-PCL 50 samples. Exponents of these samples were found to vary without a well-defined trend within slightly larger intervals (*i.e.*, 1.60-2.48 and 1.81-2.64 for lengths of 30 and 50, respectively).

**Figure 8.** (a) Exothermic DSC peaks corresponding to isothermal crystallizations of PEI-PCL 10 at temperatures between 28 and 37 ºC. (b) Development of the relative degree of crystallinity of PEI-PCL 10 at different crystallization temperatures. (c) Avrami plots corresponding to isothermal crystallization of PEI-PCL 10 at the above indicated temperatures.

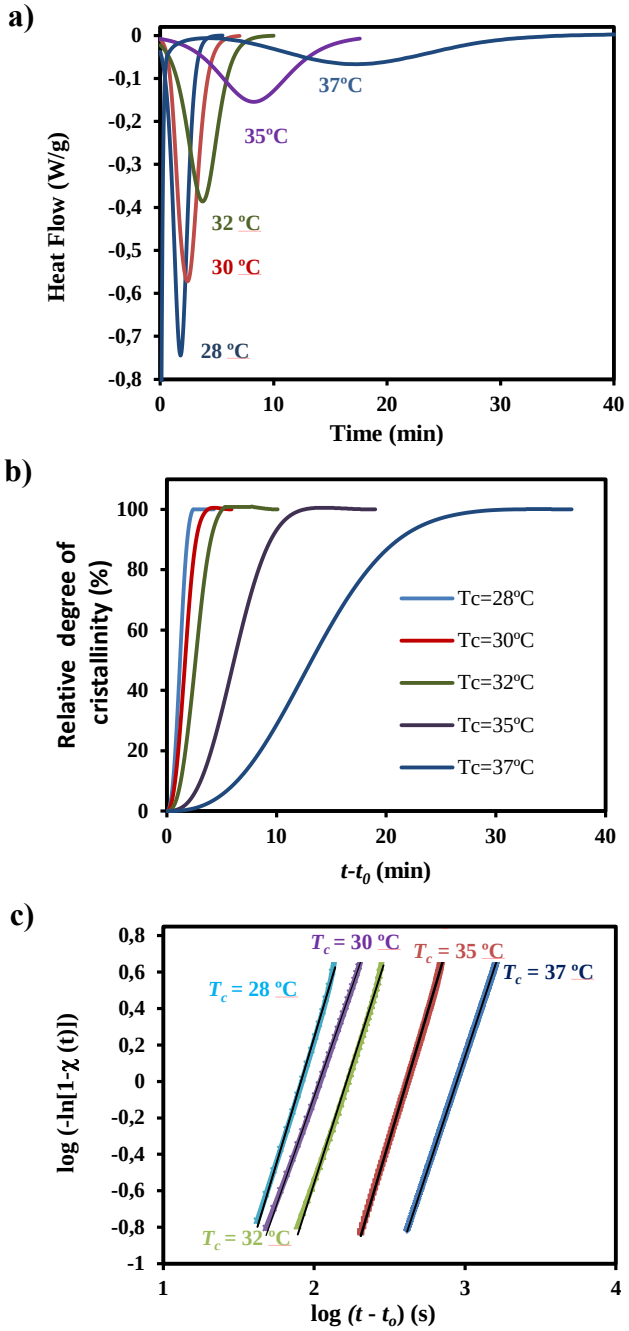

The values corresponding to reciprocal crystallization half-times ($1/\tau_{1/2}$), calculated as the inverse of the difference between crystallization start time and half-crystallization time, are also given in Table 2. This parameter is a direct measure of the crystallization process, and can therefore be used to check the accuracy of Avrami analysis by comparison with the theoretical kinetic value (*i.e.*, $1/\tau_{1/2} = (Z / \ln 2)^{1/n}$). Values reported in Table 1 showed a good agreement between values deduced from both methods. Summarized data allows also evaluating the variation of the overall rate constant with temperature for the different samples, as then will be discussed.

**Table 2.** Main crystallization kinetic parameters determined by DSC for PEI-PCL *x* samples.

| Sample | *T* (ºC) | $Z \cdot 10^6$ ($s^{-n}$) | *n* | $k \cdot 10^3$ ($s^{-1}$) | $1/\tau_{1/2} \cdot 10^3$ ($s^{-1}$) | $(Z/\ln 2)^{1/n} \cdot 10^3$ ($s^{-1}$) |
|---|---|---|---|---|---|---|
| PEIPCL 10 | | | | | | |
| | 28 | 39.40 | 2.19 | 9.69 | 11.43 | 11.46 |
| | 30 | 10.57 | 2.34 | 7.46 | 8.70 | 8.72 |
| | 32 | 1.534 | 2.47 | 4.40 | 5.09 | 5.10 |
| | 35 | 0.3179 | 2.40 | 1.94 | 2.27 | 2.29 |
| | 37 | 0.0527 | 2.47 | 1.13 | 1.31 | 1.31 |
| PEIPCL 30 | | | | | | |
| | 40 | 517.13 | 1.60 | 8.87 | 11.55 | 11.16 |
| | 43 | 1.4564 | 2.22 | 2.33 | 2.77 | 2.75 |
| | 45 | 0.2078 | 2.35 | 1.44 | 1.68 | 1.68 |
| | 47 | 0.0059 | 2.46 | 0.45 | 0.52 | 0.52 |
| | 48 | 0.0012 | 2.48 | 0.26 | 0.29 | 0.30 |
| PEIPCL 50 | | | | | | |
| | 40 | 34.522 | 2.37 | 13.14 | 15.34 | 15.29 |
| | 43 | 11.738 | 2.16 | 5.18 | 6.21 | 6.18 |
| | 45 | 24.333 | 1.81 | 2.90 | 3.57 | 3.57 |
| | 47 | 1.4454 | 2.10 | 1.63 | 1.91 | 1.94 |
| | 48 | 0.0800 | 2.31 | 0.85 | 0.99 | 0.99 |
| | 49 | 0.0012 | 2.64 | 0.42 | 0.53 | 0.48 |

## 5. Secondary nucleation constant for the isothermal crystallization of PEI-PCL x multiarm stars

Crystallization kinetics from the melt state was also studied for the three PEI-PCL *x* samples by optical microscopy. Spherulite radii grew linearly in all cases with time until impingement, as shown in Figure 9a for the representative and less crystalline PEI-PCL 10 sample. Figure 9b compares the temperature dependence of the crystal growth rate for the three PEI-PCL samples, being found a similar evolution than the overall crystallization rate ($k = Z^{1/n}$) determined from DSC experiments. The relatively high growth rate allowed collecting only experimental data over a narrow temperature range where crystallization was mainly governed by secondary nucleation. This interval was clearly shifted to lower temperatures for the sample with shorter arms but corresponded to a similar degree of supercooling (i.e., higher than 8 ºC) than found for samples with larger arms (i.e., higher than 13 ºC ).

Final spherulitic radii varied between 17 and 200 µm and logically decreased for a given multiarm sample when primary nucleation density was higher (i.e., samples obtained at lower crystallization temperatures). Nucleation was very low at the highest crystallization temperature where spherulites with diameters up to 200 µm could be obtained. The number of nuclei remained practically constant during crystallization for all isothermal experiments, suggesting that it proceeded according to an athermal nucleation. This feature can justify the observed proportionality between *G* and *k* as reported for different authors.[42-45] As can be seen in Figure 10a, the temperature evolution of primary nucleation revealed a single exponential dependence. It is remarkable that the number of active nuclei was high (e.g., 4,000 nuclei/mm$^2$ for the less crystalline PEI-PCL 10 sample crystallized at a such low temperature as 28 ºC). This feature is a clear indication of the effectiveness of cores to start crystallization. The maximum measured nuclei density varied also with the arm length, being found that this density decreased when stars had longer arms probably as a consequence of their lower ratio of PEI cores that may act as primary nuclei.

The radial growth rate ($G$) of polymer crystals is usually described by the Lauritzen and Hoffman equation,[47] which is based on the Turnbull–Fisher expression[48] suitable for the crystallization process of homopolymers. The Lauritzen and Hoffman equation is formulated as:

$$G = G_0 \exp[-U^*/(R(T_c - T_\infty))]\exp[-K_g/(T_c(\Delta T)f)] \quad (4)$$

where $G_0$ is a constant preexponential factor, $U^*$ represents the activation energy characteristic of the transport of the crystallizing segments across the liquid–crystal interface, $T_\infty$ is the temperature below which such motion ceases, $T_c$ is the crystallization temperature, $R$ is the gas constant, $K_g$ is the secondary nucleation constant, $\Delta T$ is the degree of supercooling measured as $T_m^0 - T_c$, and $f$ is a correction factor accounting for the variation in the bulk melting enthalpy per unit volume with temperature ($f = 2T_c/(T_m^0 + T_c)$).

It is advisable to rearrange Eq. (4) in a logarithmic form:

$$\ln G + U^*/R(T_c - T_\infty) = \ln G_0 - K_g/[T_c(\Delta T)f] \quad (5)$$



and plot the left-hand side of the equation versus $1/[T_c(\Delta T)f]$. Straight lines with slopes equal to $-K_g$ should be obtained.

The Lauritzen-Hoffman plot was fitted for the three considered PEI-PCL $x$ copolymers with straight lines ($r^2 > 0.98$) when the "universal" values reported by Suzuki and Kovacs[49] (*i.e.*, $U^* = 1500$ cal/mol and $T_\infty = T_g - 30$ K) were used in the calculation (Figure 10b). Kinetic features at low supercoolings are basically governed by the nucleation term, and consequently crystallization rates could become relatively insensitive to the $U^*$ and $T_\infty$ parameters. The plot was used to estimate secondary nucleation constants of $0.66 \times 10^5$, $0.51 \times 10^5$ and $0.26 \times 10^5$ $K^2$ for PEI-PCL 10, PEI-PCL 30 and PEI-PCL 50 samples, respectively. These values clearly indicate a greater difficulty for crystallization as the length of the PCL arm decreased.

**Figure 9.** (a) Plots of the radius of PEI-PCL 10 spherulites versus crystallization time for isothermal cold crystallizations performed between 28 and 40 ºC. (b) Experimental spherulitic growth rates (solid lines and full circles) and overall crystallization rates (dashed lines and open symbols) of PEI-PCL 10, PEI-PCL 30 and PEI-PCL 50 samples.

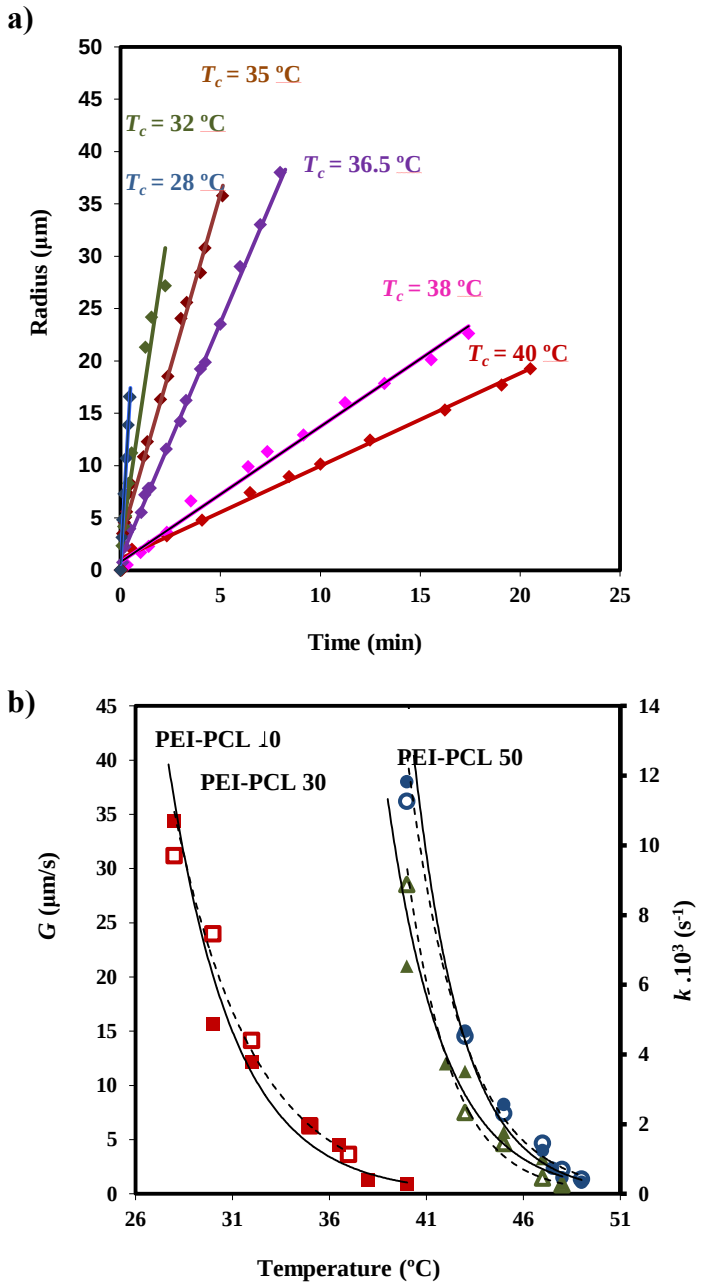

**Figure 10.** (a) Change in the nucleation density with isothermal crystallization temperature for PEI-PCL 10, PEI-PCL 30 and PEI-PCL 50 samples. (b) Plot of ln $G + U^* / R(T_c-T_\infty)$ versus $1 / T_c(\Delta T) f$ to determine the $K_g$ secondary nucleation constant of PEI-PCL 10, PEI-PCL 30 and PEI-PCL 50 samples.

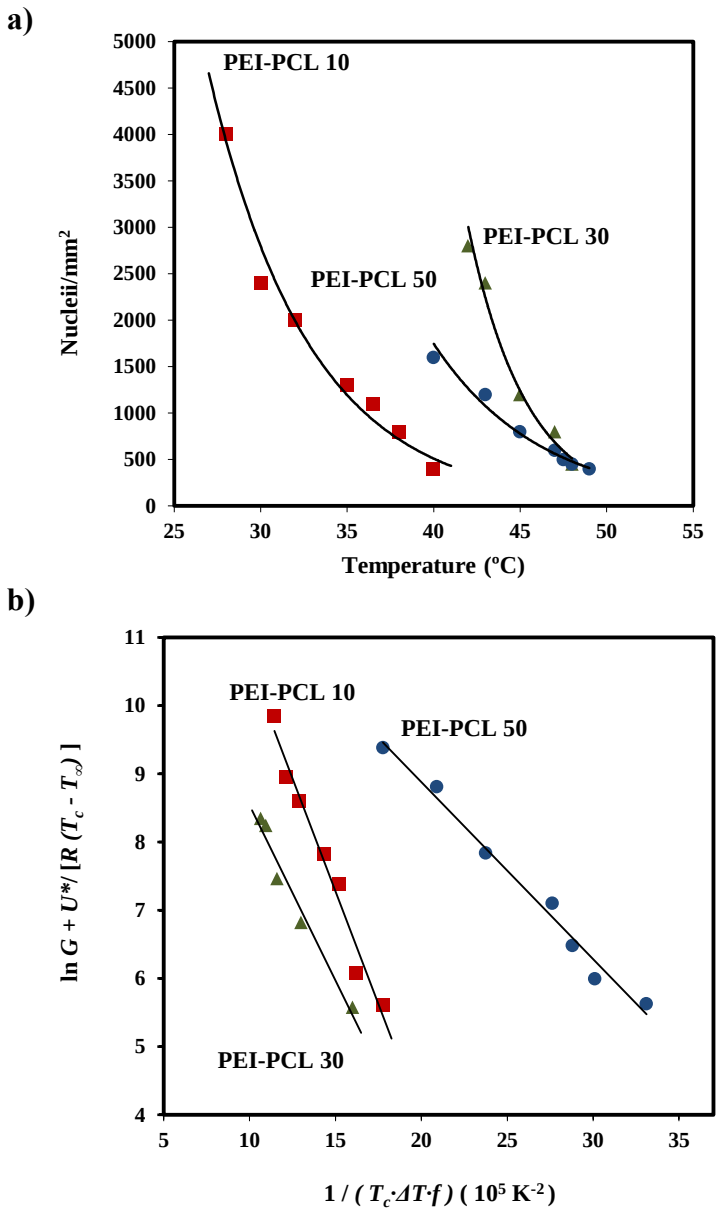

### 6. Thermal behavior of PEI-PLC x/y multiarm star mixtures

Figure 11 shows the calorimetric runs performed with the PEI-PCL 10/50 mixture as a sample having the largest difference between the lengths of constitutive PCL arms. Several points deserve attention when runs are compared with those obtained from each multistar system:

a) Melting point of the mixture becomes similar to that determined for the individual PEI-PCL 50 component, indicating that shortest PCL arms were mainly incorporated into lamellae constituted by the sample with the larger arms. Namely, the characteristic crystals observed for PEI-PCL 10 (predominant melting peak at 44.8 ºC) were not developed since only a very small shoulder could be detected near 49 ºC.

b) Crystals became less perfect since a population of thin crystals were detected for solution crystallized samples in disagreement with results attained with PEI-PCL 50 (i.e., melting peaks at 58.1 and 61.3 ºC were observed for the mixture in contrast with the single peak at 62.4 ºC observed for PEI-PCL 50).



c) A complex melting peak was observed for melt crystallized or quenched samples, being temperatures again similar to those determined for PEI-PCL 50 crystals prepared under identical procedures.

d) Melting and crystallization enthalpies were lower than measured for the individual PEI-PCL 10 and PEI-PCL 50 components and obviously for than expected from a simple mixture of spherulites, a feature that it is again in agreement with an effective incorporation of short PCL arms into lamellae of the PEI-PCL 50 sample. Note for example that melting enthalpy of melt crystallized PEI-PCL 10/50 mixture is 74.1 J/g (once the experimental enthalpy was corrected taking into account the mass of the PEI core), whereas a value of 83.6 J/g could be expected for the mixture (i.e., the average of 76.6 and 90.5 J/g enthalpies determined for the individual components).

e) Crystallization of PEI/PCL 10/50 from the melt was slightly delayed with respect to PEI/PCL 50 (i.e., 28.1 with respect to 32.7 ºC) but took place clearly faster than PEI-PCL 10 (i.e., 28.1 with respect to 19.5 ºC).

f) Glass transition temperature of the mixture became on the contrary closer to that observed for PEI-PCL 10 suggesting that the amorphous phase was enriched on the shortest PCL arms.

**Figure 11.** DSC traces obtained with PEI-PCL 10/50 samples following the same protocol indicated in Figure 2.

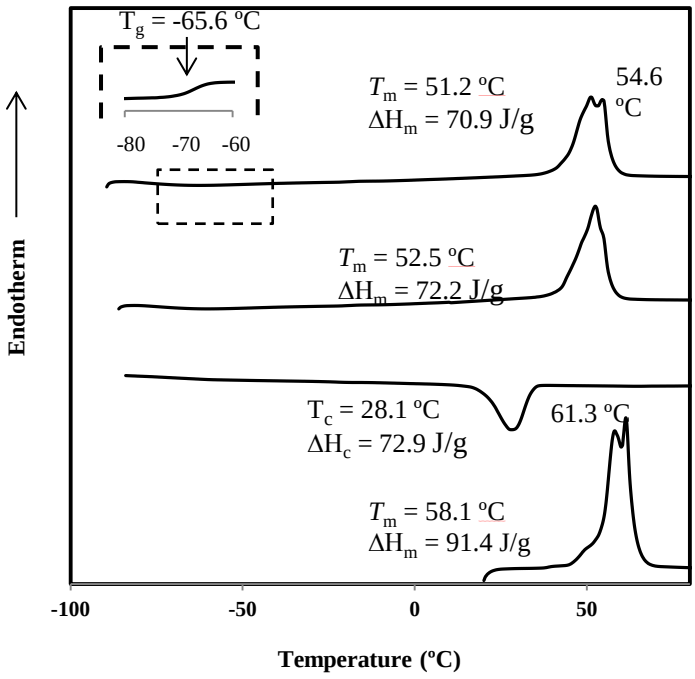


Figure 12 shows the equilibrium melting points determined for PEI-PCL 10/50, 30/50 and 30/50 mixtures according to the Hoffmann-Weeks plot.[27] Values were similar (65.2-67.6 ºC) but slightly decreased as the average length of PCL arms did (i.e., the order of $T_m^0$ values was PEI-PCL 30/50 > PEI-PCL 10/50 > PEI-PCL 10/30). It should be pointed out that these temperatures demonstrated again a worse degree of lamellar perfection than found for samples with larger PCL arms (i.e., PEI-PCL 50 and PEI-PCL 30 with temperatures higher than 73 ºC).

Nevertheless, temperatures were significantly greater than detected for PEI-PCL 10 (i.e., 58.4 ºC) as presumably for a crystallization driven by the largest PCL arms.

**Figure 12.** Hoffman-Weeks plot of temperatures corresponding to endothermic melting peaks versus crystallization temperature for PEI-PCL 10/30, PEI-PCL 10/50 and PEI-PCL 30/50 samples. Equilibrium melting temperatures are explicitly indicated at the intersection point with the $T_m = T_c$ line.

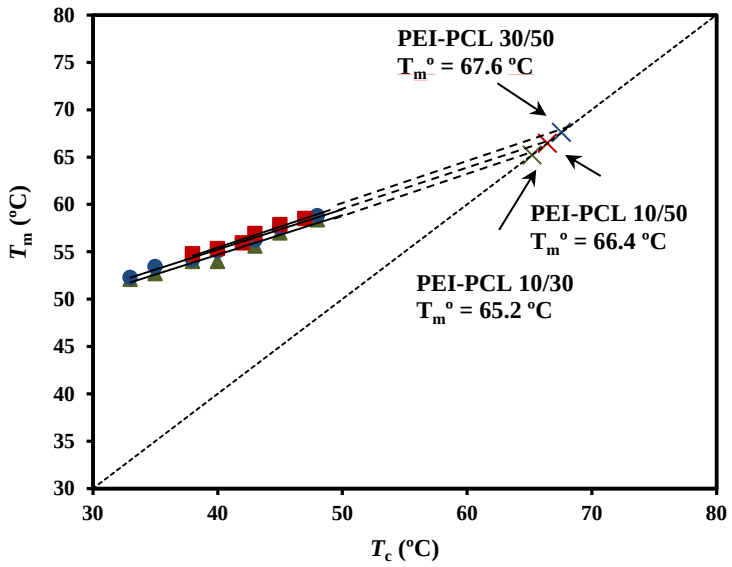




Crystallization from the melt gave rise to typical spherulites with a negative birefringence. Morphology of spherulites obtained at a given temperature was similar but with a wide range of diameter sizes for PEI-PCL 10/50 and PEI-PCL 10/30 samples (Figure 13). In fact, the number of nuclei increased during crystallization for all isothermal experiments, suggesting a thermal nucleation that could be related with the great difference between maximum temperatures at which crystallization of PEI-PCL 10 and PEI-PCL-30 or PEI-PCL 50 multiarm samples is possible (Figure 9b).

**Figure 13.** Polarized optical micrographs of PEI-PCL 10/50 isothermally crystallized at 35 ºC.

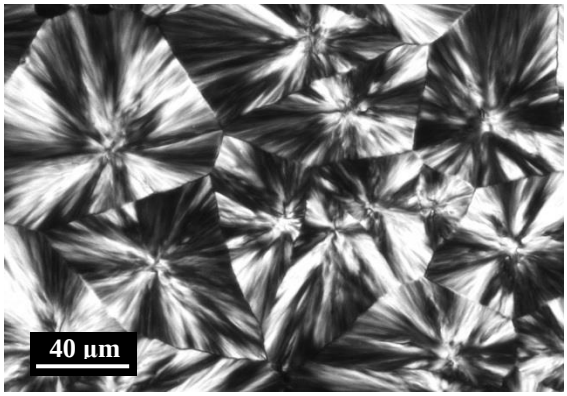


### 7. Influence of the coexistence of different PCL arm lengths on spherulitic growth rates, primary nucleation density and secondary nucleation constant



Figure 14a shows the evolution of the crystal growth rate for the different studied multiarm mixtures. Measurements could be performed in different temperature intervals but in this case the highest temperature was always similar (48-49 ºC) as a consequence of the presence of a ratio of PCL arms with a degree of polymerization equal or greater than 30, which initiated the crystallization process. The lowest crystallization temperature was related to the presence of arms with the lowest degree of polymerization and specifically corresponded to the PEI-PCL 10/30 sample. Similar conclusions could be obtained when the evolution of primary nuclei with temperature (Figure 14b) was considered. Namely, the highest temperature at which nuclei were formed was similar. Logically an exponential dependence with decreasing temperatures was found and the number of nuclei became lower than determined for the parent samples with uniform arm lengths.

Lauritzen-Hoffmann plots (Figure 15) showed a slight difference between slopes from the three studied mixtures, being the corresponding secondary nucleation constants $0.92 \times 10^5$, $0.99 \times 10^5$ and $1.16 \times 10^5$ $K^2$ for PEI-PCL 10/50, PEI-PCL 30/50 and PEI-PCL 10/30, respectively. Note that only the sample with the lowest average PCL length had a significantly

higher value. It should also be pointed out that nucleation constants were clearly higher than determined for the corresponding samples with PCL lengths of 10, 30 and 50, demonstrating a hindered crystallization process for samples with heterogeneous sizes.

**Figure 14.** (a) Experimental spherulitic growth rates (solid lines, full symbols) of PEI-PCL 10/30, PEI-PCL 10/50 and PEI-PCL 30/50. For the sake of completeness experimental overall crystallization rates (dashed lines and open symbols) are also plot for PEI-PCL 10/50 and PEI-PCL 30/50 samples. (b) Change in the nucleation density with isothermal crystallization temperature for PEI-PCL 10/30, PEI-PCL 10/50 and PEI-PCL 30/50 samples.

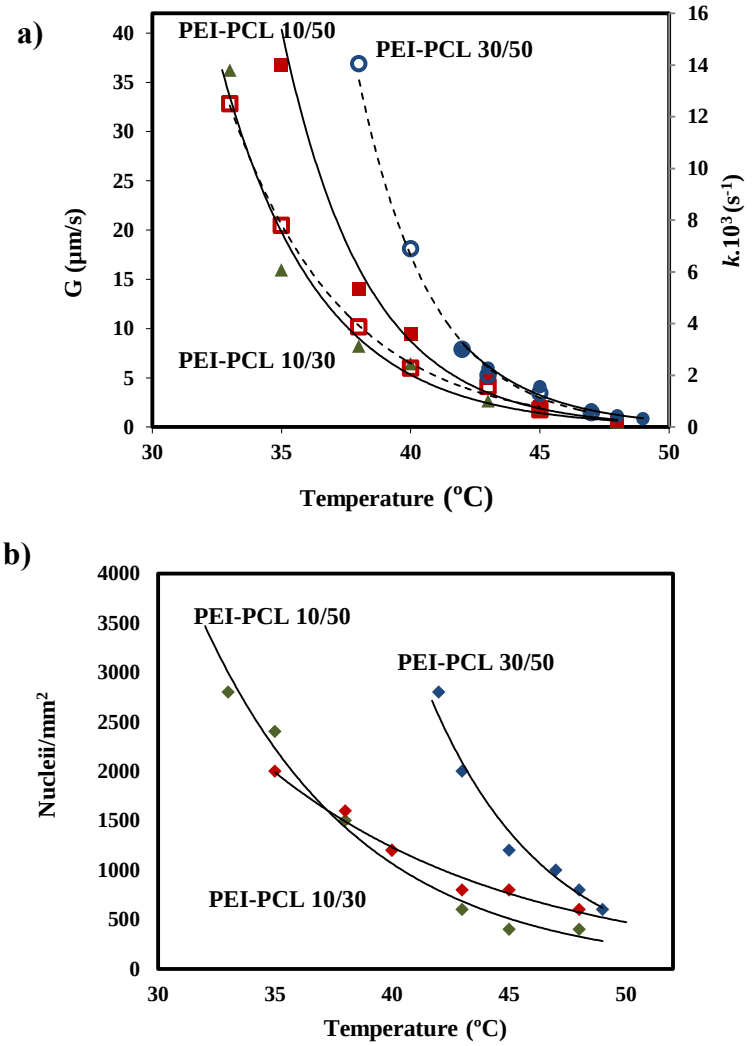

Crystallization process was also evaluated from calorimetric experiments as summarized in Table 3. In this case, the Avrami constant seems to increase for all mixtures when the crystallization temperature decreased, a feature that contrast with previous observations on samples having homogeneous arms. In this way, nucleation may follow a different mechanism that implied some sporadic or homogeneous nucleation, which agrees with the thermal nucleation process previously pointed out for mixtures of PEI-PCL stars having different PCL lengths. This process seems more important when crystallization temperature decreased. It is also remarkable that the overall crystallization rates (Table 3) were not proportional to the crystal growth rates for mixtures having PCL arms with the lowest degree of polymerization as shown in Figure 14a for PEI-PCL 10/50. Note, on the contrary the good agreement between temperature evolution of *k* and *G* for the PEI-PCL 30/50 mixture.

**Figure 15.** Plot of ln $G + U^*$ / $R(T_c\text{-}T_\infty)$ versus 1 / $T_c(\Delta T)$ $f$ to determine the $K_g$ secondary nucleation parameter of PEI-PCL 10/30, PEI-PCL 10/50 and PEI-PCL 30/50 samples.



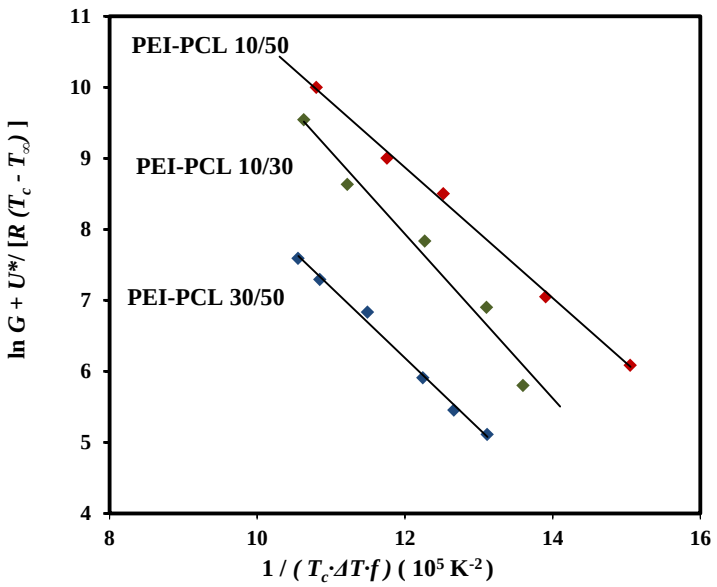

**Table 3.** Main crystallization kinetic parameters determined by DSC for PEI/PCL *x*/*y* samples.

| Sample | *T* (ºC) | *Z*. $10^6$ ($s^{-n}$) | *n* | *k*. $10^3$ ($s^{-1}$) | 1 / $\tau_{1/2}$ .$10^3$ ($s^{-1}$) | $(Z/\ln 2)^{1/n}$ .$10^3$ ($s^{-1}$) |
|---|---|---|---|---|---|---|
| PEI-PCL 10/30 | | | | | | |
| | 33 | 2.4774 | 2.94 | 12.54 | 14.16 | 14.03 |
| | 35 | 0.5113 | 3.03 | 8.38 | 9.43 | 9.46 |
| | 38 | 6.8328 | 2.44 | 7.58 | 8.62 | 8.87 |
| | 40 | 6.0534 | 2.19 | 4.21 | 5.04 | 4.90 |
| | 43 | 1.2879 | 2.10 | 1.59 | 1.88 | 1.87 |
| | 45 | 0.1025 | 2.30 | 0.92 | 1.07 | 1.07 |
| PEI-PCL 10/50 | | | | | | |
| | 33 | 7.4148 | 2.69 | 12.50 | 14.28 | 14.19 |
| | 35 | 6.9214 | 2.44 | 7.80 | 9.09 | 8.92 |
| | 38 | 0.5138 | 2.61 | 3.87 | 4.46 | 4.48 |
| | 40 | 0.0963 | 2.65 | 2.27 | 2.69 | 2.58 |
| | 43 | 3.6542 | 1.94 | 1.57 | 1.89 | 1.90 |
| | 45 | 0.0691 | 2.26 | 0.67 | 0.79 | 0.79 |
| PEI-PCL 30/50 | | | | | | |
| | 38 | 1.3664 | 3.16 | 14.05 | 15.58 | 15.65 |
| | 40 | 0.0696 | 3.31 | 6.89 | 7.70 | 7.69 |
| | 42 | 0.0095 | 3.18 | 3.01 | 3.39 | 3.37 |
| | 43 | 0.0175 | 2.87 | 2.00 | 2.26 | 2.25 |
| | 45 | 0.4102 | 2.22 | 1.32 | 1.09 | 1.52 |
| | 47 | 0.2445 | 2.03 | 0.56 | 0.65 | 0.66 |



## IV. Conclusions

Multiarm star systems constituted by a commercial core of poly(ethyleneimine) and poly(ε-caprolactone) arms with degrees of polymerization of 50, 30 and 10 were able to crystallize from both the melt state and diluted *n*-hexanol solutions. In the last case, lamellae with the typical PCL structure were attained, being demonstrated the capability to crystallize even when samples had a degree of polymerization as low as 10. Morphologies of single crystals were variable, being found the lower degree of perfection when sample had the shortest PCL arms. Thermal properties showed also a differentiated behaviour for PEI-PCL 10 in terms of low melting and glass transition temperatures and reduced crystallinity. The length of PCL arms had also a

remarkable influence on the crystallization kinetics. Specifically, the primary nucleation density and the second nucleation constant increased when the length decreased as consequence of the increase of the nucleation effect caused by a major ratio of PEI cores and the hindered crystal growth due to the existence of short PCL arms.

Crystallization of PEI-PCL *x*/*y* mixtures from the melt was basically determined by the larger PCL arms. These were the first to crystallize determining the final thermal properties (e.g. melting and equilibrium melting points) and subsequently the shorter arms were progressively incorporated into the lamellae. A thermal nucleation was characteristic of multiarm star mixtures due to the different crystallization temperature of samples with large and short PCL arms, a feature that contrasts with the athermal nucleation determined for samples with a homogeneous arm length.

## V. References


1. Morell M, Erber M, Ramis X, Ferrando F, Voit B, Serra A. Eur Polym J 2010;46:1498.
2. Yang JP, Chen ZK, Yang G, Fu SY, Ye L. Polymer 2008;49:3168.
3. Morell M, Ramis X, Ferrando F, Yu Y, Serra A. Polymer 2009;50:5374.
4. Zhang J, Guo Q, Fox B. J Polym Sci Part B: Polym Phys 2010;48: 417.
5. Zagar E, Zigon M, Prog Polym Sci 2011;36: 53.
6. Klee JE, Schneider C, Hölter D, Burgath A, Frey H, Mülhaupt R. Polym Adv Technol 2001;12:346–354.
7. Francos XF, Salla JM, Mantecón A, Serra A, Ramis X. J Appl Polym Sci 2008;109:2304.
8. Foix D, Erber M, Voit B, Lederer A, Ramis X, Mantecón A, Serra A. Polym Degrad Stab 2010;95:445.
9. Liu C, Zhang Y, Huang J. Macromolecules 2008;41:325.
10. Gao H, Matyjaszewski K, Macromolecules 2008;41:1118.
11. Mendrek B, Trzebicka B, Walach W, Dworak A. Eur Polym J 2010;46:2341.
12. Morell M, Lederer A, Ramis X, Voit B, Serra A. J Polym Sci Part A: Polym Chem 2011:49:2395.
13. Morell M, Ramis X, Ferrando F, Serra A. Polymer 2011;52:4694.
14. Morancho JM, Cadenato A, Ramis X, Morell M, Fernández-Francos X, Salla JM, Serra A. J Therm Anal Calorim 2013;114:409.
15. Fan W, Wang L, Zheng S. Macromolecules 2009;42:327.
16. Hameed N, Guo Q, Hanley T, Mai YW. J Polym Sci Part B: Polym Phys 2010;48:790.
17. Sperling LH. Introduction to Physical Polymer Science. Wiley Interscience, Hoboken, 2006. p. 573.
18. Núñez E, Ferrando C, Malmström E, Claesson H, Werner PE, Gedde UW. Polymer 2004;45:5251.
19. Risch BG, Wilkes GL, Warakomski JM. Polymer 1993;34:2330.
20. Núñez E, Gedde UW. Polymer 2005;46:5992.
21. Organ SJ, Keller A, J Mater Sci 1985;20:1571.
22. Xie W, Jiang N, Gan Z. Macromol Biosci 2008;8:775.

23. Acebo C, Fernández-Francos X, Ferrando F, Serra A, Salla JM, Ramis X. React Funct Polym 2013;73:431.
24. Crescenzi V, Manzini G, Calzolari G, Borri C. Eur Polym J 1972;8:449.
25. Nakagawa S, Kadena K, Ishizone T, Nojima S, Shimizu T, Yamaguchi K, Nakahama S. Macromolecules 2012;45:1892.
26. Muñoz-Bonilla A, Cerrada ML, Fernández-García M, Kubacka A, Ferrer M, Fernández-García M. Int J Mol Sci 2013;14:9246.
27. Hoffman JD, Weeks JJ. J Res Natl Bur Stand 1962;66:13.
28. Strobl G. Eur Phys J 2000:E3:165.
29. Marand H, Xu J, Srinivas S. Macromolecules 1998;31:8219.
30. Hoffman JD, Davies GT, Lauritzen JI. Treatise in Solid State Chemistry, N.B. Hannay (Ed.), New York: Plenum Press; 1976, Chapter 7, p. 497-614.
31. Huang JP, Xu X, Luo XL, Ma CDZ, Chinese J Polym Sci 2002;20:45.
32. Núñez E, Gedde UW. Polymer 2005;46:5992.
33. Furuhashi Y, Sikorski P, Atkins E, Iwata T, Doi Y. J Polym Sci Polym Phys 2001;39:2622.
34. Pouget E, Almontassir A, Casas MT, Puiggalí J. Macromolecules 2003;36:698.
35. Chatani Y, Okita Y, Tadokoro H, Yamashita Y. Polymer 1970;1:555.
36. Hu H, Dorset DL. Macromolecules 1990;23:4604.
37. Iwata T, Doi Y. Polym Int 2002;51:852.
38. Gestí S, Almontassir A, Casas MT, Puiggalí J. Biomacromolecules 2006;7:799.
39. Gestí S, Casas MT, Puiggalí J. Polymer 2007;48:5088.
40. Gestí S, Almontassir A, Casas MT, Puiggalí J. Polymer 2004;45:8845.
41. Avrami M. J Chem Phys 1939;7:1103.
42. Avrami M. J Chem Phys 1940;8:212.
43. Chan TW, Isayev AI, Polym Eng Sci 1994;34:461.
44. Fatou JG, Marco C, Maldelkern L. Polymer 1990;31:890.
45. Lu H, Qiao J, Yang Y. Polym Int 2002;51:1304.
46. Kenny JM, Maffezzoli A, Nicolais R. Thermochim Acta 1993;227:83.
47. Lauritzen JI, Hoffman JD. J Appl Phys 1973;44:4340.
48. Turnbull D, Fisher JC. J Chem Phys 1949;17:71.
49. Suzuki T, Kovacs AJ. Polym J 1970;1:82.

# Chapter 6.

# Conclusions

The results reported in this work can be summarized as follows:

**Study of Copoly(alkylene dicarboxylate)s derived from diacid units with different parity and length of the polymethylene segments.**

a. Thermal polycondensation using titanium tetrabutoxyde as a catalyst was successfully used to obtain copolyesters constituted by 1,9-nonanediol and different ratios of azelaic and pimelic acid units. Final copolymer compositions were always in good agreement with the feed molar ratio and the attained molecular weights were typical of polycondensation reactions involving monomers with different functionality.
b. The copolymer with the intermediate composition (i.e. PE9,7/9-0.5) had lowest melting temperature and melting enthalpy. However, the crystallinity of this sample was still high. It seemed possible to incorporate comonomer units into the crystalline structure of each homopolymer.
c. Homopolymers and copolymers crystallized according to a spherulitic growth and a heterogeneous primary nucleation. Significant differences were found between the spherulitic textures (i.e. fibrilar or ringed) and even on the crystallization kinetics of PE97 and PE99 homopolymers. Specifically, non-isothermal crystallization from the melt was less favourable for the PE97 sample and consequently the PE9,7/9-0.5 copolymer started to crystallize by the arrangement of azelate moieties.
d. X-ray diffraction data indicated that crystallization always occurred according to a lamellar insertion mechanism. Significant differences were observed between crystal lamellar and amorphous layer thicknesses of homopolymers and the copolymer with intermediate composition. Optical microscopy, DSC, SAXS and FTIR data suggested that this copolymer crystallized, giving rise to lamellar cores with a predominant PE99 structure, and that pimelate units were mainly located on the amorphous interlamellar regions.

e. Poly(nonamethylene pimelate) and poly(nonamethylene azelate) crystallize according to an orthorhombic $P2_1ab$ space group and unit cells with parameters $a$ = 0.500 nm, $b$ = 1.480 nm and $c$ (chain axis) = 2.25 or 2.50 nm. Molecules adopt an all-trans conformation and the packing is defined by a setting angle respect to the $a$ axis close to ±50º. Morphology of lamellar crystals is variable and specifically the aspect ratio increases as the degree of supercooling decreases.

f. Single crystals of the three studied samples were easily degraded by enzymes, which initiated the attack on the amorphous lamellar surfaces in such a way that crystals edges remain practically unaltered until the late stages of degradation. Crystal edges are also more stable during annealing processes performed in the crystallization medium at temperatures close to dissolution. Unusual framed crystals with rhombic and hexagonal morphologies can be obtained by this thermal treatment.



g. Thermal polycondensation of mixtures of azelaic and succinic acids with an excess of 1,4-butanediol rendered copolyesters with a variable composition, high yield, relatively high molecular weights and melting points within a wide temperature range (i.e. 36 ºC-113 ºC).

h. Despite their random distribution, all studied copolymers are semicrystalline and the crystalline morphologies of copolymers are highly different depending on the predominant structures of PE44 and PE49 homopolymers: small negatively birefringent axialitic morphologies for PE49 and large banded spherulites with concentric extinction rings for PE44.

i. Minimum distortion of the unit cell occurs with increasing comonomer content due to exclusion of foreign units from the crystalline phase. Crystallization from the melt first involved the succinate rich segments, resulting in a peculiar behavior for copolymers having an intermediate composition since crystallization of butylene azelate could be

enhanced by rapid cooling. No phase separation between azelate and succinate rich domains occurred in the amorphous phases.

j. Equilibrium melting temperatures, determined by the Hoffman-Weeks plot, were found to decrease compared to those of parent polyesters with increasing the comonomer content. The stability of crystals undergoing the melting process also decreased with the incorporation of comonomer units, the effect being more significant for azelate rich copolymers. A melting point depression which fitted the Baur exclusion model was clearly observed for all copolyesters.

k. Secondary nucleation constants increased with the comonomer content being the effect less significant when the copolymer was rich on azelate units. Thus, incorporation of succinate units had a slight influence on the energy barrier for overall crystallization of polybutylene azelate, probably as a consequence of the previous arrangement of butylene succinate rich segments.

l. Enzymatic degradability of polyesters constituted by azelate or succinate units differs considerably. Thus, samples having distinctive, controlled biodegradability can be easily generated by copolymerization. Copolymers have significant amorphous domains that facilitate enzymatic attack and lead to post-exposure surface textures that are clearly different from those developed in the more crystalline homopolyester samples. Constituent spherulites can become highlighted during degradation if they have the appropriate size and are surrounded by significant amorphous zones.



***Micro-molded exfoliated clay nanocomposites and functionalized silica micro and nanoparticles by means of ultrasonic technology.***

a. Ultrasonic micro-molding has been probed as a new and effective method to get nanocomposites with good clay dispersion and exfoliated structures.

b. Two biodegradable polymer matrices coming from renewable resources as well as both neat and organo-modified clays were considered and gave always rise to

positive results. Control of processing parameters allowed getting samples with a minimum degradation being best results attained when compatibilizer compounds were not employed. Nevertheless, polylactide nanocomposites with unaltered molecular weights could always be prepared independently of the selected clay.

c. Ultrasonic technology appears as a promising method to get directly molded nanocomposite specimens without modifying the clay or performing a subsequent processing as in the case of nanocomposites prepared by solvent casting, melt mixing or in situ polymerization.

d. Exfoliated C25A clays had a peculiar influence on the crystallization of polylactide as also previously reported for PLA/C30B nanocomposites. Thus, the exfoliated clay displayed an antinucleating effect but at the same time enhanced the crystal growth rate. The influence of exfoliated clays on the crystallization of poly(nonamethylene azelate) was on the contrary in agreement with a typical behavior where the silicate layers favoured the primary nucleation and hindered molecular transport. In this way, the effect of the clay on the overall crystallization rate was dependent on the crystallization temperature since the two indicated effects point to opposite behaviors.



e. Poly(nonamethylene azelate) and its mixtures with functionalized silica micro/nanoparticles can be micro-molded by means of ultrasonic energy and using similar time, amplitude and force processing parameters. Minimum polymer degradation was detected in the molded specimens as well as a good dispersion of the added particles.

f. Thermal stability was slightly improved by the addition of silica particles. The decomposition of grafted functional groups was only detected at the end of the thermal degradation process.

g. Silica nanoparticles had a significant influence on the crystallization process even at the low content of 3 wt-%. Avrami exponents slightly decreased with respect to the

neat polymer as a probe of the geometrical constrains caused by the incorporation of the well dispersed nanospheres. The overall crystallization rate of nanocomposites was always greater than that determined for the neat polymer being the ratio of the respective constants between 1.4 and 2.5.

h. Negative and ringed spherulites were obtained at the different assayed temperatures following an athermal nucleation. Furthermore, agglomeration of silicate particles can be discarded from morphological observations.

i. Primary nucleation was significantly enhanced when silica nanoparticles were added, being expected that the functionalized surface of silica nanoparticles favoured the adsorption of polyester molecules. In addition, the enhanced PE99/$SiO_2$ interfacial interaction favours molecular deposition on the existing crystal surfaces causing a decrease on the secondary nucleation constant and an increase on the crystal growth rate.



***New poly(ester urea) derived from L-leucine: Electrospun scaffolds loaded with antibacterial drugs, enzymes and Incorporation of bacteriophages.***

a. A new α-amino acid containing poly(ester urea) was successfully electrospun to form microfiber scaffolds. Continuous fibers with a monomodal diameter distribution and slightly rough surface were formed under a wide range of electrospinning conditions.

b. The high solubility of the PEU derived from L-leucine, 1,6-hexanediol and carbonic acid allowed the use of appropriate solvents to load different antibacterial drugs and even enzymes without being denatured.

c. The 1L6 poly(ester urea) films were more susceptible to enzymatic attack by proteases than by lipases because the latter mainly involved hydrolysis of ester groups. Despite these minor differences, both enzymes led to rapid degradation of film samples. 1L6 scaffolds degraded faster than films due to the greater surface area of constitutive fibers. The high hydrophobicity of 1L6 scaffolds had

repercussions on enzymatic degradability since different weight loss rates were found depending on how samples were exposed to the medium (e.g. forced or non-forced immersion). In any case, hydrophobicity caused that inner fibers were well-preserved at least during the first three days of exposure.

d. Monomeric (CHX) and polymeric (PHMB) biguanide compounds were effectively loaded into the electrospun scaffolds. Slight differences in fiber morphology and antibacterial properties were found depending on the loaded drug. Specifically, PHMB led to narrow fibers and had an increased antibacterial effect against Gram-positive and Gram-negative bacteria.

e. α-Chymotrypsin could also be loaded into the 1L6 scaffolds, giving rise to materials with enzymes that could accelerate degradation and tissue regeneration.

f. Adhesion and proliferation of epithelial (Vero) and fibroblast (Cos-7) cells on 1L6 films and scaffolds demonstrated the biocompatibility of the new poly(ester urea). Slight differences in cell viability were found, with films exhibiting the lower values. The effect of increased porosity of scaffold samples appears sufficient to counterbalance the negative effect of its higher hydrophobicity.



g. Phages can be incorporated by means of the electrospinning technique and without losing their activity into microfibers of the poly(ester urea) derived from L-leucine, 1,6-hexanediol and carbonic acid.

h. Both free and carbonate adsorbed bacteriophages can be employed, having the resulting loaded scaffolds a similar bactericide activity. Results are promising since up to now electrospun scaffolds were usually loaded by a simple adsorption process that was performed after processing.

i. The selected poly(ester urea) had solubility characteristics that allowed loading phages in the electrospun solution without causing a decrease on their activity. Processing conditions were different when free or carbonate adsorbed phages were employed and consequently resulting fiber morphologies depended on the way as

phages were incorporated. The use of carbonate particles required a higher flow rate that caused an increase on the microfiber diameter. In this case, fibers showed abundant protuberances that were randomly distributed along the fiber. Carbonate particles were well encapsulated in the electrospun fibers and consequently the hydrophobicity of the scaffolds did not decrease after the incorporation of the inorganic salt particles. Scaffolds loaded with phages were fully biocompatible unlike usual bactericide drugs that could produce a cytopatic effect at high doses.

***Anhydric maleic functionalization and polyethylene glycol grafting of lactide-co-trimethylene carbonate copolymers.***

a. Copolymers of lactide and trimethylene carbonate could be effectively grafted with polyethylene glycol by a two-step synthesis that firstly involved functionalization with maleic anhydride and then condensation reaction with polyethylene glycol. A certain degree of hydrolysis of the anhydride was observed, and consequently a condensing agent like N,N´- diisopropylcarbodiimide was required to ensure complete pegylation of functional groups. Moderate degradation was detected but grafted copolymers could be obtained with a relatively good yield and a high PEG content (*e.g.*, 17 wt%). Thus, copolymers with a number average molecular weight of 19,900 g/mol were able to incorporate up to five PEG grafted chains with Mn equal to 550 g/mol.
b. Incorporation of PEG led to a decrease in the melting enthalpy and greater complexity of the melting peak, which was only associated with polylactide. Nevertheless, samples were able to crystallize, rendering negative spherulites and thin lamellar crystals despite the presence of up to 17 mol-% of PEG and the randomness of the main chain caused by the incorporation of up to 20 mol-% of TMC units. Thermal stability and hydrophilicity of copolymers became enhanced by their grafting with PEG chains.

c. All copolymers were biocompatible because they supported adhesion and proliferation of both fibroblast-like and epithelial-like cells. However, results were more favorable for the grafted copolymers which, in addition, had higher enzymatic degradability.

d. Grafted copolymers were appropriate to prepare microspheres by the oil-in-water emulsion method. These were obtained with a high yield and had good encapsulation efficiency for drugs like triclosan.

***Multiarm stars with a poly(ethyleneimine) core and poly(ε- caprolactone) arms of different length.***

a. Multiarm star systems constituted by a commercial core of poly(ethyleneimine) and poly(ε-caprolactone) arms with degrees of polymerization of 50, 30 and 10 were able to crystallize from both the melt state and diluted n-hexanol solutions. In the last case, lamellae with the typical PCL structure were attained, being demonstrated the capability to crystallize even when samples had a degree of polymerization as low as 10.



b. Morphologies of single crystals were variable, being found the lower degree of perfection when sample had the shortest PCL arms.

c. Thermal properties showed also a differentiated behaviour for PEI-PCL 10 in terms of low melting and glass transition temperatures and reduced crystallinity.

d. The length of PCL arms had also a remarkable influence on the crystallization kinetics. Specifically, the primary nucleation density and the second nucleation constant increased when the length decreased as consequence of the increase of the nucleation effect caused by a major ratio of PEI cores and the hindered crystal growth caused by the existence of short PCL arms.

e. Crystallization of PEI-PCL x/y mixtures from the melt was basically determined by the larger PCL arms. These were the first to crystallize determining the final thermal

properties (*e.g.* melting and equilibrium melting points) and subsequently the shorter arms were progressively incorporated into the lamellae.

f. A thermal nucleation was characteristic of multiarm star mixtures due to the different crystallization temperature of samples with large and short PCL arms, a feature that contrast with the athermal nucleation determined for samples with a homogeneous arm length.